Automated Patient-Specific Modeling of Blood Flow and Vessel Wall Mechanics in Aortic Pathology

Zur Erlangung des akademischen Grades eines

Doktors der Ingenieurwissenschaften

der Fakultät für Informatik

der Universität Fridericiana zu Karlsruhe (TH)

genehmigte

Dissertation

von

Dilana Hazer

aus Beirut

Tag der mündlichen Prüfung:	14.12.2009
Erster Gutachter:	Prof. Dr.-Ing. Rüdiger Dillmann
Zweiter Gutachter:	Prof. Dr. med. Götz-Martin Richter

Acknowledgment

This thesis was conducted during my work as a research assistant at the Institute of Anthropomatics - University of Karlsruhe (TH), chair Prof. R. Dillmann and at the Department of Diagnostic Radiology - University Hospital Heidelberg, under the direction of Prof. G.M. Richter. It was performed within the setting of the Research Training Group 1126 - Intelligent Surgery and partly funded by DI 330/22, both founded by the German Research Foundation (DFG). Further, I conducted a research internship at the Biomedical Engineering Department - Carnegie Mellon University (CMU) in Pittsburgh, PA, which was supported by InterACT and KHYS. I thank everyone who provided support and encouragement through the pursuit of this project.

First of all, I would like to express my deep gratitude to Prof. Dr.-Ing. R. Dillmann and Prof. Dr. med. G.M. Richter for being my supervisors. Thank you for your invaluable guidance and precious support and for providing me the opportunity and the freedom to explore the fascinating world of medical engineering. Thank you for your interest in my work; you gave me the tools to build this thesis. I also thank Prof. Dr. rer. nat. W. Juling and Prof. Dr.-Ing. R. Stiefelhagen for being involved as examiners in my doctoral defense.

Deep appreciation to Dr. E.A. Finol for offering me the opportunity in conducting a research internship in your group at CMU in Pittsburgh. I will never forget our weekly meetings and all the useful discussions and invaluable advices about computational biomechanics. Thank you for this great experience.

Grateful thanks to Dr. med. M. Kostrzewa for being so closely involved in completing this thesis and for your extensive contributions in the experimental validation. Thank you for the great effort you put in teaching me all about the mysteries of medicine. I appreciated the time working with you.

I extend my deep thanks to Dr.-Ing. R. Kröger for your constructive criticisms, for sharing your views and thoughts with me, for being a great source of inspirational ideas, insight and enthusiasm. Great appreciation for the help at late hours, reading, understanding and reviewing this thesis. Thank you for giving your time so generously no matter how busy you were.

Sincere thanks are dedicated to my students Markus Stoll, Eduard Schmidt, Lukasz Rytel, Bettina Phu, Maria Kopaigorenko, Miriam Bauer, Dennis Prill, Vignesh Rammohan and Oleksandr Bondarenko for being involved within the setting of diploma and student projects. Particularly, I would like to thank my HiWis Eduard Schmidt and Markus Stoll for their precious contribution, especially in the development of MoDiSim.

Not to forget is the secretary team, Claudia Grünewald in Heidelberg and Christine Brand and Isabelle Wappler in Karlsruhe. I thank you for your great support and your unremitting readiness to help without hesitation.

Thanks also to all my friends -without listing- for your motivation, each one on his own way! Especially, thank you Steffi for sharing our conference rooms, for our sportive activities, for our travel adventures and for the thesis' review in Beirut... Thank you for everything, during but also after the thesis time!

I owe grateful thanks to Dr. M. Schwehn for all the encouragement you provided me in the last months. Thanks for your listening and your patience. I believe, without the strength you gave me I could not have done it.

There are no words to describe how grateful I am to you Matthias for all the distances you travelled and the hours you spent on the highways. You supported me and motivated me to never give up, you contributed to make it happen. Thank you for your love, for your acceptance and for being there for me - no matter where and what time or day or week.

And finally, my deepest thanks to my mom, my dad and to my brothers 'Schumi' and 'Mickel' for always standing by me and guiding my efforts. You started all this, thanks for giving me the opportunity to finish it. Thank you for your assistance and for your faith in me.

Dilana Hazer

Contents

1 Introduction **1**
1.1 Motivation 1
1.2 State of the Art 3
1.3 Objective and Contribution 6
1.4 Chapters Layout 8

2 Medical Background **9**
2.1 Cardiovascular System 9
2.1.1 Heart and Blood Circulation 10
2.1.2 Cardiac Cycle 11
2.1.3 Blood Vessels 12
2.1.4 The Aorta 14
2.2 Vascular Pathologies 16
2.2.1 Arteriosclerosis 16
2.2.2 Aneurysms 18
2.2.3 Dissections 19
2.3 Diagnosis and Therapy of Aneurysms 19
2.3.1 Symptoms and Diagnosis 20
2.3.2 Risks and Therapy 20
2.4 Endovascular Therapy 22
2.4.1 Stents and Stent-Grafts 23
2.4.2 Healing Process 25
2.4.3 Risks and Complications 26

3 Simulation Workflow **27**
3.1 Introduction: Approach & Requirements 27
3.2 Process Chain for CSM, CFD and FSI 28
3.2.1 Segmentation of the CT/MRI images 29
3.2.2 3D Model Generation and Preprocessing 30
3.2.3 Mesh Generation and Processing 32
3.2.4 Physical Modeling 32
3.2.5 Initial and Boundary Conditions 33

3.2.6 Mathematical Modeling . . . 34
3.2.7 Representation and Evaluation . . . 35
3.3 Numerical Stability . . . 35
3.3.1 Mathematical Stability . . . 36
3.3.2 Physical Stability . . . 36
3.4 System Integration into *MoDiSim* . . . 36
3.4.1 Automation of the Modeling . . . 37
3.4.2 The MoDiSim Simulation System . . . 37
3.4.3 Modeling Components . . . 38
3.4.4 Expandability of the System . . . 41
3.4.5 Optimization of the Models . . . 41
3.4.6 Individualization of the Simulations . . . 41
3.5 Processed 3D Aortic Models . . . 42
3.6 Summary . . . 46

4 Mesh Generation & Processing 47
4.1 Introduction: Meshing Requirements . . . 47
4.2 Mesh Quality . . . 48
4.2.1 Quality Checking . . . 48
4.2.2 Quality Metrics . . . 48
4.3 Mesh Control Functions . . . 50
4.3.1 Boundary Layers . . . 50
4.3.2 Surface Size Function . . . 52
4.3.3 Volume Size Function . . . 54
4.4 Mesh Independency . . . 55
4.4.1 Methods . . . 55
4.4.2 Results . . . 57
4.5 Mesh Generation Approaches . . . 60
4.5.1 Surface and Interface Meshing . . . 60
4.5.2 Volume Blood Meshing . . . 61
4.5.3 Volume Wall Meshing . . . 61
4.6 Meshing Results . . . 62
4.6.1 Surface and Interface Meshing . . . 63
4.6.2 Volume Blood Meshing . . . 65
4.6.3 Volume Wall Meshing . . . 67
4.7 Mesh Processing . . . 69
4.7.1 Conversion . . . 69
4.7.2 FE-sets . . . 70
4.8 System Integration in *Mesh-Gen* and *Mesh-Pro* . . . 70
4.8.1 Automation of Mesh Generation . . . 72
4.8.2 Automation of Mesh Processing . . . 73
4.9 Summary . . . 76

5 Vessel Wall Modeling 77
5.1 Introduction 77
5.2 Continuum Structure Mechanics 78
5.2.1 Lagrangian and Eulerian Configurations 78
5.2.2 Deformation and Displacement 79
5.2.3 Strain Analysis 82
5.2.4 Forces and Euler-Cauchy Principle 85
5.2.5 Stress Analysis 86
5.2.6 Virtual Work Principle 89
5.3 Physical Constitutive Laws 90
5.3.1 Elasticity Theory 91
5.3.2 Anisotropy 94
5.3.3 Compressibility 95
5.3.4 Hyperelastic Models 97
5.4 Finite Element Method 99
5.4.1 Galerkin's Formulations 99
5.4.2 Geometric Discretization 100
5.4.3 Incremental Approach 103
5.4.4 Time Integration 106
5.4.5 Implicit Iteration Methods 107
5.5 CSM Simulation Models 109
5.5.1 Physical and Constitutive Modeling 110
5.5.2 Initial and Boundary Conditions 113
5.5.3 Mathematical and Numerical Modeling 114
5.5.4 Numerical Stability - Discussion 115
5.6 System Integration in *CSM-Sim* 117
5.6.1 Automation 118
5.6.2 Optimization 120
5.6.3 Individualization 121
5.7 CSM Simulation Results 122
5.7.1 Effects of transient pressure and material nonlinearity using CT-AAA 122
5.7.2 Effects of Wall Thickness using MR-AAA 125
5.7.3 Effects of Stent and Stent-Graft using CT-TAA 128
5.7.4 Cross-sectional Strain Analysis using 4D-CT-AA 133
5.8 Summary 134

6 Blood Flow Modeling 135
6.1 Introduction 135
6.2 Continuum Fluid Dynamics 136
6.2.1 Configuration Formulations 136
6.2.2 Substantial Derivative 138

6.2.3 Mass Conservation . . . 139
6.2.4 Momentum Conservation . . . 141
6.2.5 Energy Conservation . . . 143
6.2.6 Numerical Equations Form . . . 145
6.3 Physical Properties and Constitutive Laws . . . 146
6.3.1 Incompressibility . . . 146
6.3.2 Viscosity . . . 147
6.3.3 Laminar and Turbulent Flow . . . 148
6.3.4 RANS Equations and Turbulence Models . . . 150
6.4 Finite Volume Method . . . 153
6.4.1 FVM versus FEM . . . 153
6.4.2 Spatial Discretization . . . 154
6.4.3 Interpolation and Differentiation . . . 157
6.4.4 Pressure-based Formulation . . . 159
6.4.5 Time Integration . . . 163
6.4.6 Iterative Algorithms . . . 164
6.5 CFD Simulation Models . . . 166
6.5.1 Physical and Constitutive Modeling . . . 167
6.5.2 Initial and Boundary Conditions . . . 169
6.5.3 Mathematical and Numerical Modeling . . . 172
6.5.4 Numerical Stability - Discussion . . . 173
6.6 System Integration in *CFD-Sim* . . . 175
6.6.1 Automation . . . 176
6.6.2 Optimization . . . 178
6.6.3 Individualization . . . 179
6.7 CFD Simulation Results . . . 180
6.7.1 Wall Shear Stresses using CT-AA . . . 180
6.7.2 Pathological Aneurysm Conditions using CT-AAA . . . 183
6.7.3 Effects of non-Newtonian Blood using CT-AAA . . . 183
6.7.4 Effects of Stent-Graft Implantation using CT-TAA . . . 187
6.8 Summary . . . 190

7 Blood-Wall Interaction 191
7.1 Introduction . . . 191
7.2 Fluid-Structure Interaction . . . 191
7.2.1 Arbitrary Lagrangian-Eulerian Formulation . . . 192
7.2.2 Interface Definition . . . 193
7.2.3 Equilibrium Conditions . . . 194
7.2.4 Iteration Convergence . . . 195
7.2.5 FEM Coupled Equations . . . 196
7.2.6 Time Integration Consistency . . . 197
7.2.7 Coupling Approaches . . . 197

7.2.8 Solution Methods 203
7.3 FSI Simulation Models 205
7.3.1 Physical and Constitutive Modeling 206
7.3.2 Initial and Boundary Conditions 207
7.3.3 Mathematical and Numerical Modeling 210
7.3.4 Numerical Stability - Discussion 211
7.4 System Integration in *FSI-Sim* 214
7.4.1 Automation 215
7.4.2 Optimization 218
7.4.3 Individualization 219
7.5 FSI Simulation Results 220
7.5.1 Coupled vs. Decoupled Results using MR-AAA 220
7.5.2 FSI from in-vivo Experiment using 4D-CT-P2 222
7.5.3 FSI from in-vivo Experiment using 4D-CT-P3 224
7.6 Summary 226

8 Experimental Validation 227
8.1 Introduction 227
8.2 Experimental Setting and Data 228
8.2.1 Dynamic 4D-CT with Contrast Medium 230
8.2.2 Catheter-based in-vivo Pressure Measurements 231
8.2.3 Ultrasound-based Flow Measurements 232
8.3 Simulations and Evaluation Approach 233
8.3.1 Wall Deformation Simulations 233
8.3.2 Blood Pressure Simulations 237
8.3.3 Blood Flow Simulations 237
8.4 Experiments vs. Simulations 239
8.4.1 4D-CT-P1 (Experiment 1 with CSM) 239
8.4.2 4D-CT-P2 (Experiment 2 with FSI) 241
8.4.3 4D-CT-P3 (Experiment 3 with FSI) 243
8.5 Discussion 245
8.5.1 Wall Deformation Results 245
8.5.2 Blood Pressure Results 246
8.5.3 Blood Flow Results 246
8.6 Summary 246

9 Conclusions 247
9.1 Summary and Discussion 247
9.2 Future Developments 249

References XI

I am sorry for such a long letter; I lacked the time to write a shorter one!

Blaise Pascal

Chapter 1

Introduction

1.1 Motivation

Cardiovascular pathologies are prevalent causes leading to high mortality every year [PPR+05]. Stenosis, aneurysms, dissections and long-term endurance result amongst others from complex blood flow patterns and fatigue of the vessel wall. Aortic aneurysms for instance, are associated with a dilatation of a highly fatigued vessel and represent one of the most dangerous cardiovascular pathologies on the event of rupture. If left untreated, the aneurysm may enlarge and eventually rupture. A rupture of the vessel results in serious internal bleeding and leads to death unless treated rapidly. Only 10 % of the patients survive an aortic rupture. Cardiovascular diseases occur with increasing incidence in patients above the age of 50.

Due to the high mortality and in order to intervene duly, it is essential to identify reliable predictors for the development and the growth of the pathologies. The currently used primary indicators for the evaluation of the associated risks are based on the disease shape and stage as well as on the experience of the physician [LWJ+02; Par98]. These observations are usually obtained from routine tomography scans. For an aortic aneurysm, the risk of rupture is positively correlated with the diameter of the vessel and the aneurysm expansion rate. An aneurysm diameter that is larger than 5 cm or an expansion rate of more than 1 cm per year are considered to be risky and require a surgical intervention. Lower diameters and expansion rates are usually classified as still-non-risky and do not require the patient to undergo a surgery. Instead, these patients are treated conservatively, for instance with anti-hypertensiva, in order to avoid the risks and later complications associated with a surgical intervention. However, recent research shows that these predictors related to the extent of dilatation are not always sufficient enough and thus do not present a reliable tool [VG05]. In fact, small aneurysms are also subject to rupture, whereas larger ones sometimes may not. Previous studies indicate that the risk for an abdominal aortic aneurysm (AAA) with a diameter less than 5 cm to rupture ranges between 12.8 % and 23.23 % [VG05]. This is an indication that aortic aneurysms are still not fully understood and that more reliable predictors and further development of better patient-specific models are necessary. Furthermore, the currently used predictors do not consider individual characteristics such as shape, material, physiology or biomechanics. Various studies report that age, smoking and hypertension are factors which also identify patients exposed to vascular risk [SvdLK+06].

Several studies have demonstrated that minimally invasive endovascular procedures are advantageous over conventional surgery in treating cardiovascular pathologies [SvdLK+06; FMRK03]. However, several unsolved issues in this field are still pertinent [VRW98]. An individual and efficient treatment requires the knowledge of image-based physiological parameters that help the interventional radiologist in evaluating his decisions during patient diagnosis and assist the surgeon during surgical intervention. Thus, it is of primary importance to be able to non-invasively identify parameters that individually contribute to the development and growth of the pathologies.

Cardiovascular diseases tend to occur at sites with pathological hemodynamics and elastomechanics. High wall stresses often correlate with regions of fatigued vessel represented by decreasing wall strength. Wall stresses are the forces which arise from the intraluminal pressure and the wall shear stresses (WSS) acting on the inner wall surface. Abnormal blood flow parameters and high stress distributions may therefore be causative and hence predictive factors for the growth of a vascular pathology. In presence of abnormal vessel wall conditions, the blood flow patterns take complex forms. Complex flow alterations result in high pressure and WSS gradients. The involved flow patterns and the associated high intraluminal pressure weaken the vessel and lead in turn to pathological conditions of its elastomechanical functioning. Due to alterations in its structural constitution, the fatigued wall starts to expand and may then rupture. A dilatation of the vessel is therefore mainly due to a highly fatigued wall. Ruptures occur when the mechanical stresses acting on the inner wall exceed the failure strength of the diseased vascular tissue.

Patient-specific computational modeling of cardiovascular biomechanics from medical images may be helpful for patients with cardiovascular pathologies to predict the associated risks and thus to evaluate the necessity of a surgical intervention. Image-based *Computational Structure Mechanics* (CSM) and *Computational Fluid Dynamics* (CFD) based on the Finite Element/Volume

Methods (FEM/FVM) have become efficient tools in modeling the blood flow and the wall mechanics in human vessels. They allow to non-invasively simulate the individual hemodynamics and elastomechanics needed for an efficient minimally invasive treatment. A realistic modeling can be achieved by coupling both CFD and CSM simulations. The so called *Fluid Structure Interaction* (FSI) is a numerical approach that allows computing patient-specific blood flow and wall mechanics parameters in order to understand the underlying factors affecting the interaction between hemodynamics and elastomechanics.

By simulating the pathological biomechanical conditions, CSM, CFD and FSI allow to identify individual parameters such as high shear stress gradients or weak spots and sites of excessive mechanical strain that contribute to the development and growth of the disease. Simulations are needed to understand the role of flow and pressure distributions in characterizing regions of stressed vessels. Based on these predictions, a realistic insight into the pathological vessel parameters may be provided and predictive simulations of disease growth, state of fatigue and assessment of risk may be evaluated for a given patient. The focus of this work is therefore to establish a simulation-based tool for the computation of biomechanics to non-invasively help the diagnosis of patients with vascular pathologies on an individual basis.

1.2 State of the Art

Various research approaches demonstrated that biomechanical analysis of the vessels is a valuable tool in risk evaluation and therapy follow up. In a structural study conducted by Fillinger et al., wall stresses calculated using solid models based on static homogeneous intraluminal pressure showed that the peak wall stress is 12 % more accurate than the AAA diameter in evaluating the aneurysm risk of rupture [FMRK03]. Further, the following factors, amongst others, influence the hemodynamics and the elastomechanics: beside the pulsatile blood pressure acting on the inner wall, the pathology shape and size [VRW98], the wall thickness, the asymmetry, the presence of thrombus [WMWV02; DMV03] as well as the wall and blood constitutive properties and flow behavior. These factors are therefore essential for an accurate evaluation.

Venkatasubramaniam et al. [VFM$^+$04] showed that the peak stress computed in ruptured AAA is significantly higher than that in non-ruptured models. They also found the wall stresses to be more sensitive to wall thickness than to asymmetry and obtained a 20 % increase in stress for a 25 % reduction of wall thickness. Sankar et al. [SL09] investigated the effects of asymmetry of stenoses on the flow dynamics. Based on 5 idealized models with various degrees of asymmetry, they showed that increasing asymmetry significantly influences the WSS and has therefore to be modeled accurately. Also Scotti et al. [SSMF05] studied the effects of asymmetry and wall thickness on the wall mechanics in 10 idealized models of AAA based on FSI and CSM simulations. They found that the wall stresses increase with increasing asymmetry and that a correct modeling of the variable wall thickness plays a significant role on the computations. Their results report that homogeneous thickness assumption underestimates the wall stresses by 77 % compared to variable thickness.

Di Martino et al. [DMGF$^+$01] were the first to present results of a patient-specific fully coupled FSI simulation and suggested that the elastomechanics of the wall are affected by the blood flow field. Scotti et al. [SSMF05] compared their FSI and CSM results and showed that CSM underestimates the peak stress by $\approx 9.2\,\%$ with homogeneous thickness and by $\approx 29.4\,\%$ with variable thickness. The effects of both FSI and CSM modeling were also investigated by Leung et al. [LWC$^+$06]. In contrast to Scotti et al., the authors found that the difference between the FSI and the CSM was less than 1 %, thus suggesting that CSM is sufficient for a pure prediction of stress distributions.

Leung et al. [LWC$^+$06] also examined the influence of AAA geometries on the wall stress in three patients with similar diameters (57 mm, 53 mm, 50 mm) and showed that the diameter has less influence on the peak stress than the patient-specific geometry. Vorp et al. [VRW98] found that the wall stress increases with bulge diameter and asymmetry and hence is affected by the aneurysm shape and size. Li et al. [LBBJ$^+$07] conducted a numerical analysis on the effects of different degrees of stenoses (30 %, 50 %, 70 %) on the blood flow and vessel wall mechanics and reported that the degree alone is not enough to predict the risk of plaque rupture.

Various turbulent models have been used in CFD modeling to simulate the turbulent flow behavior [YB04; TBM$^+$09]. Other investigations assumed the blood flow to be laminar [QTV00]. Li et al. [LBBJ$^+$07] simulated the blood flow with laminar and turbulent models and showed that for stenoses degrees larger than 30 %, the differences in the shear and radial (hoop) stresses between the laminar and turbulent models become considerable with significantly smaller recirculation zones in the turbulent flow. Also Berguer et al. [BBK06] studied the influence of blood flow turbulences on the wall stresses. They considered an idealized axis-symmetric AAA model for their computations in which the turbulent results demonstrated much higher pressure than the laminar results. The authors suggested therefore that turbulences should be accurately included into the modeling, while Khanafer et al. [KBB07] declared that since the flow is only turbulent over a small cardiac cycle time period, these results do not apply for the whole cardiac cycle. Furthermore, for simplicity most of the CFD simulations consider the blood as a Newtonian fluid with a constant viscosity. Various investigations on the blood constitutive behavior proposed however that blood should be actually modeled as a non-Newtonian fluid [GvdVJ99; ABH05; KGBB06].

Scotti et al. [SF07] considered additionally the intraluminal thrombus (ILT) in their work to simulate the wall forces. They showed that the presence of the ILT reduces the stresses on the wall and that the peak moves to the thinner thrombus location. The simulations were performed on a real patient with FSI and CSM and the results show that taking into account the blood flow does not have significant influence on the position of the peak wall stress. However, the CSM method leads to a significant underestimation of the wall stresses, which proves the conclusion proposed by the same authors 2 years before in [SSMF05]. Similar computations and results on the effects of thrombus were also reported by Wang et al. Many other studies simulated the effects of stents and stent-grafts on the flow dynamics and the wall mechanics [LK05a; LK05b; LK06b]. Prakash et al. [PE01] conducted research on the mesh resolution requirements in 3D computational methods.

In summary, all current research approaches demonstrate that the simulation of pathological biomechanical conditions is helpful in identifying individual parameters such as high pressure and shear stress gradients or weak spots and sites of excessive mechanical strain that contribute to the development and growth of the pathologies. They also show how significant the effects of patient-specific geometry and pathology shape, of accurate physics and of coupled (FSI) and decoupled (CSM, CFD) modeling are on the simulation results. However,

1. The computational models are rarely optimized in terms of all significant aspects.
2. The simulations are usually restricted to one application pathology or vessel region.
3. Mathematical and physical stability essential for reliable modeling are mostly not considered.
4. High-quality meshes confining to the simulation requirements with mesh optimization algorithms are rarely included in the generation process.
5. Due to the specific characteristics and the complexity of patient-specific data, most of the studies manually create and process their mesh and simulation models.
6. Experimental validation with real measurements and in-vivo data is rarely conducted.

A clinically implementable system requires the accounting for all these aspects simultaneously for reliable modeling. In spite of all technological advancements in computational methods this remains unsolved to this day.

1.3 Objective and Contribution

The primary objective of the present work is to establish a numerical approach to non-invasively help the diagnosis of patients with vascular pathologies on an individual basis. The aim is therefore to generate a reliable and easy-to-use simulation tool for the computation of blood flow and vessel wall mechanics. In this work, a patient-specific FEM-/FVM-based system, *MoDiSim*[1], has been designed, developed and evaluated to automatically simulate the hemodynamics and the elastomechanics as well as their interaction within image-based vessel models. MoDiSim provides an individual computational analysis for the detection of regions with pathological conditions and for the evaluation of associated risks. For the computation of blood flow and vessel wall biophysical parameters, individual numerical models for CSM, CFD and FSI have been generated and implemented based on CT/MRI images and on in-vivo measured flow and pressure data. MoDiSim puts together commercial codes for mesh generation, CSM, CFD and FSI in an easy-to-use way with automated and hidden data transfer between the codes. Thus, through the automation of the individual modeling steps, generating and running the simulations may be performed directly in MoDiSim, without any knowledge about the operation of the individual codes.

The specific goals and contribution of this work are defined as follows:

- **Mesh Generation:**
  Finite-based simulations require accurate patient-specific mesh models. For the generation of different modeling applications, various mesh generation processes are necessary and have been created and examined [HBK$^+$07; HSU$^+$08].
- **Vessel Wall Modeling:**
  Computational Structure Mechanics simulation models have been developed and implemented to simulate the response of the vessel wall to intraluminal forces in order to understand the role of the elastomechanics in characterizing regions of fatigued vessels [HSU$^+$08; HFK$^+$09]. The simulations are based on a continuum structure mechanics approach and the computations are thereby based on the finite element method.

---

[1] Modeling and Simulation framework for patient-specific vessels

- **Blood Flow Modeling:**
  Computational Fluid Dynamics simulation models have been developed and implemented to describe the blood flow features and to simulate the hemodynamics in individual vascular pathologies [HUK+06b; HUK+06a; HKU+07]. The modeling is based on a continuum fluid dynamics approach and the computations are based on the finite volume method.
- **Blood-Vessel Interaction:**
  More accurate and realistic modeling may be achieved by quantifying the influence of flow alterations and non-uniform hemodynamic forces on the wall strain and stress distributions. Fully coupled Fluid Structure Interaction models have been developed and implemented to simulate the physical interaction between the hemodynamics and the elastomechanics.
- **Experimental Validation:**
  The validation of the simulations is necessary for a clinical implementation and was therefore performed using in-vivo pressure and ultrasound-based velocity measurements, as well as 4D-CT images obtained from individual experiments conducted on porcine aortas [HFK+09].

Further, an important feature of the modeling is to be able to reproduce the patient-specific flow and structural fields in a stable and accurate way. The aim is to develop a modeling framework to facilitate a clinical implementation of such computational methods. For each of the above mentioned modeling applications (Mesh, CSM, CFD and FSI), this includes:

- **Simulation Workflow:**
  Building the elements of the individual process chain.
- **Numerical Stability:**
  Attaining physical and mathematical stability for reliable simulations.
- **Automation:**
  Automation of the modeling process by integrating all individual modeling steps into the *MoDiSim* system.
- **Optimization:**
  Optimization of the integrated components and implemented models.
- **Individualization:**
  Individualization of the simulations in terms of imaging source, patient geometry, vessel region or pathology shape and stage.
- **Expandability:**
  Expandability of the system by allowing a flexible modular structure to further include the simulation of different vessels or endovascular devices.

1.4 Chapters Layout

The present work consists of 9 chapters. The individual chapters have the following content:

Chap.2 describes the medical background behind the modeling. Particularly, the anatomy and physiology of the cardiovascular system as well as an overview on various aortic pathologies will be presented.

Chap.3 illustrates the simulation workflow for CSM, CFD and FSI simulations in general, to be applied to the different applications. Building the individual elements of the process chain, the MoDiSim system developed in this work as well as the processed aortic models are described.

Chap.4 discusses the generation and processing of the meshes. After introducing the meshing quality and control functions necessary to obtain high-quality and stable meshes, the mesh independency analysis performed in this work is presented. Then, various meshing and processing approaches for the different applications as well as the resulting meshed models are presented. Finally, the integration of this step into MoDiSim will be described.

Chap.5 is devoted to the vessel wall modeling. The chapter includes a theoretical part dealing with the fundamental principles of continuum structure mechanics, the elasticity theory and the finite element method, and an applied part consisting of a description of the CSM simulation models used, the system integration into MoDiSim as well as examples on the achieved results.

Chap.6 addresses the blood flow modeling. An overview on the theoretical principles of continuum fluid dynamics, the blood constitutive modeling and the finite volume method are first described. Following, the applied CFD simulation models and the system integration are presented. The chapter is also concluded by some of the obtained numerical results.

Chap.7 is dedicated to the blood-wall interaction simulations. After introducing the field of fluid-structure interaction and various coupling techniques and solution approaches, the underlying physical interaction between the blood flow and the vessel wall will be presented. Thereby, the applied FSI physical and mathematical models, the system integration as well as some of the simulation results will be illustrated.

Chap.8 describes the experimental validation. The performed experiments and the data acquired for the validation of the simulations as well as the evaluation technique and the quantified validation results are thereby presented.

Chap.9 concludes finally the whole work with a summarized discussion and gives an overview on possible future developments in this field.

Chapter 2

Medical Background

2.1 Cardiovascular System

The cardiovascular system is a closed system consisting of the heart, the blood and the blood vessels. It is responsible for the convective transport of substances within the body. It supplies all organs with blood which in turn supplies the cells with nutrients and oxygen and disposes the body from carbon dioxide and wastes. Thereby, the blood contributes in the integration of the organs in a complete *body* system and contains components of the immune and coagulation systems which defend the body from exogenic substances and loss of blood. Further, a network of blood vessels connected partly in parallel and partly in series is responsible for the entire circulatory system, divided into the systemic (big) circulation and the pulmonary (small) circulation. Both circulation parts involve the same blood vessel types which allow to take the blood away from and back to the heart. Thereby, the pulmonary circulation transports deoxygenated blood away from the heart to the lungs and returns oxygenated blood back to the heart. Whereas, the systemic circulation transports oxygenated blood away from the heart to the rest of the body and returns deoxygenated blood back to the heart. Furthermore, the oriented blood flow direction necessary for the convection is achieved thanks to a pressure gradient that is generated by the cardiac valves in the heart [SL00].

In the present section, the anatomy and physiology of the cardiovascular system will be presented. After introducing the heart and the blood circulation, the cardiac cycle and its physiological phases will be described. Then, the blood vessels including the three main wall layers affecting the mechanical behavior of the vessels will be presented. Finally, the main artery in the body, *the aorta*, will be also described.

2.1.1 Heart and Blood Circulation

The heart is a muscle hollow organ consisting of four chambers: two *ventricles* and two *atriums*. Due to their cyclic and synchronic movement, the heart represents the functional pump of the blood circulation. While the left ventricle passes the blood from the lungs into the large systemic circulation, the right ventricle returns the blood from the systemic circulation back to the lungs. The left and the right ventricles are separated from the blood circulation system with the two *semilunar* valves: the *aortic* and the *pulmonary* valves, respectively [Sch07]. Furthermore, the left and the right atriums support the filling of the ventricles. The atriums are connected to the ventricles through the *mitral* and the *trikuspid* valves, also known as the *atrioventricular* valves, allowing the blood to pass only in one direction.

The circulation of the blood begins in the right atrium, from which it flows into the right ventricle through the tricuspid valve as shown in Fig.2.1. From there the blood is pumped through the pulmonary valve into the pulmonary artery which conducts it to the lungs. In the lungs, the blood gets oxygenated before it flows back through the pulmonary vein to the left atrium. Through the mitral valve, the blood passes then to the left ventricle where, under high pressure, it gets pressed into the largest vessel, the *aorta*. The blood in the aorta is branched out to reach and supply all cells in the body. After the exchange with the cells, the deoxygenated blood returns back into the two *vena cavas* which direct the blood back to the right atrium [SL00].

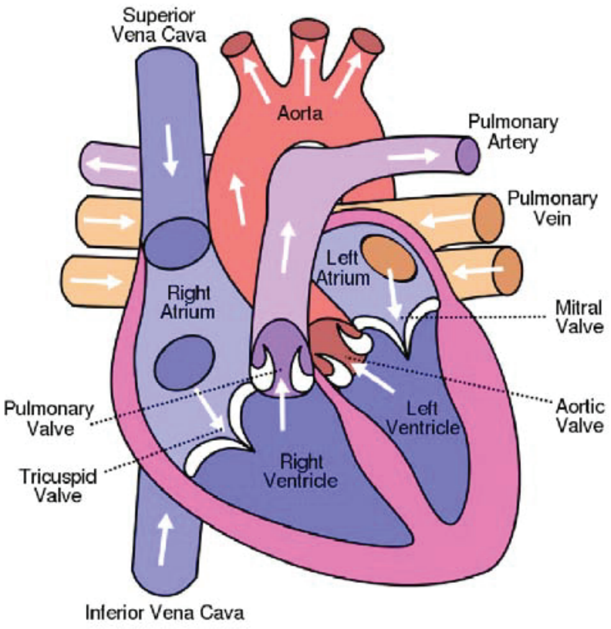
Superior Vena Cava
Aorta
Pulmonary Artery
Pulmonary Vein
Left Atrium
Right Atrium
Mitral Valve
Aortic Valve
Pulmonary Valve
Left Ventricle
Tricuspid Valve
Right Ventricle
Inferior Vena Cava

Figure 2.1: Heart and blood circulation.

2.1.2 Cardiac Cycle

The pumping function of the heart is coordinated based on rythmetic and spontaneous sequences of contraction and relaxation. The frequency of the cardiac cycle depends on various factors such as rest, fatigue or emotions. Under normal conditions, the frequency varies between 60 and 80 beats per minute. In contrast to skeletal muscles, the cardiac muscle is composed of special *myocytes* which regulate its own function without the help of external nerves. These myocytes are located within the *sinoatrial* (SA) and the *atrioventricular* (AV) nodes responsible for the stimulation of a series of electrical impulses. An action potential is first created by a wave of electrical stimulation sent by the SA node which initiates the atrial contraction. With a delay, allowing for the blood in the atriums to fill the respective ventricles, the wave reaches the AV node leading to a contraction of the ventricles. The electrical activity of the heart over time may be detected by skin electrodes and recorded using *electrocardiography* (ECG). The cardiac cycle may be divided into four phases [Sch07] as illustrated in Fig.2.2:

- **Isovolumetric Contraction:**
  The cardiac cycle begins with an electrical stimulation signal leading to an isovolumetric contraction of the heart under closed valves. Thereby, the pressure in the ventricles increases up to the level in the aorta and the atrioventricular valves close.

- **Ejection:**
  As soon as the intraventricular pressure exceeds the aortic and pulmonary pressure, the aortic and pulmonary valves open and the heart ejects the blood out into the arteries. In the ejection phase, the pressure in the ventricles increases further until it reaches its systolic maximum.

- **Isovolumetric Relaxation:**
  Then, the pressure in the ventricles decreases below the pressure in the aortic and pulmonary arteries and the aortic and pulmonary valves close. Here starts the phase in which an isovolumic relaxation of the ventricles takes place.

- **Filling:**
  When the intraventricular pressure becomes lower than that in the atriums, the atrioventricular valves open and the blood flows from the atriums into the ventricles filling them again, while the pressure in the ventricles stays almost constant.

Then follows the contraction phase again. Contraction and ejection build the *systole*, while the *diastole* consists of the relaxation and the filling phases.

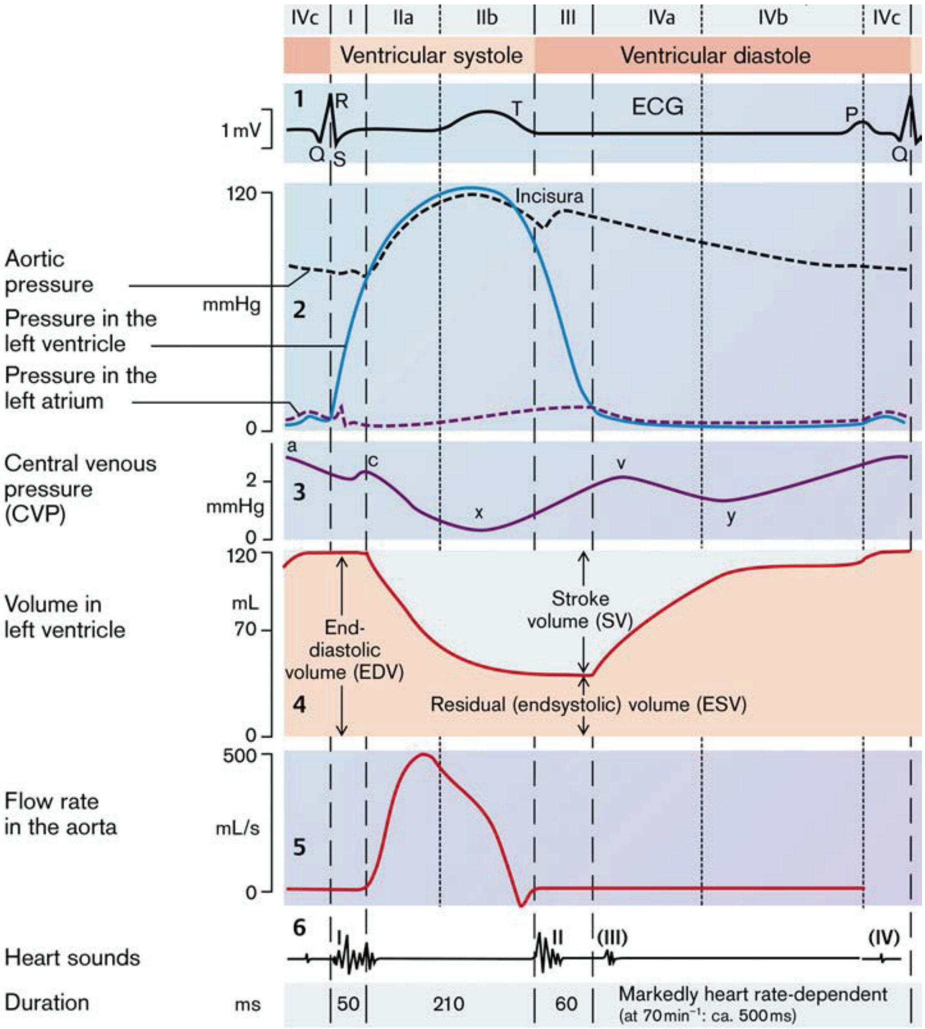

Figure 2.2: Cardiac cycle: Systole with isovolumetric contraction (I) and ejection (IIa and IIb) phases; Diastole with isovolumetric relaxation (III) and filling (IVa and IVb) phases [SL00].

2.1.3 Blood Vessels

Blood vessels are responsible for the transport of the blood through the body within the circulatory system. There are various types of blood vessels, split in mainly three categories: arteries and arterioles, capillaries, veins and venoles. Arteries are derived from the aorta, which in turn are branched out into arterioles and finally into capillaries. Arteries and arterioles are also known as high-pressure vessels and take the oxygenated blood away from the heart. In the capillaries, the exchange of substances between the blood and the tissues takes place. The capillaries unify then into the venoles, which in turn join the veins and finally reach the two large vena cavas. Veins and venoles belong to the low-pressure system and transport the deoxygenated blood from the capillaries back to the heart.

Vessel walls consist in general of three layers: the *tunica intima*, the *tunica media* and the *tunica adventitia*, shown in Fig.2.3.

- **Tunica Intima:**
  The *tunica intima* is the thinnest and innermost layer consisting of a single section of smooth endothelial cells that are in contact with the flowing blood. They are carried by a thin basal membrane surrounded by a subendothelial layer of connective tissue containing fine collagen fibers and elastic bands called the *elastica interna*. The endothelial cells have an elongated form and are in general directed parallel to the flow direction [SK07]. The young, healthy intima is usually very thin and has small influence on the mechanical properties of the vessel [HO03].

- **Tunica Media:**
  The *tunica media* is the middle and thickest layer. It consists of circularly arranged elastic laminae involving mainly elastic fibers. The individual laminae are connected together through a complex network of thin elastic fibrils, collagen fibrils and smooth muscle cells [HO03]. The vascular smooth muscle, especially in the arteries, controls the caliber of the vessel. The number of elastic layers, and hence the elasticity, decreases with decreasing vessel size so that these are hardly present in muscular arteries [BDZ07]. In the arteries toward the periphery, the elastic layers are only present at the boundary sides of the media, known as *elastica interna* and *elastica externa*. On the other hand, a thicker layer of elastic material is present in the aorta, providing a high compliance necessary to stand the high pressure pumped from the heart [RLD96], [Rem99]. In average, 52 elastic laminae are present in the thoracic aorta. The media has the largest effect on the mechanical properties of healthy vessels [HO03]. The direct mechanical influence of the smooth muscle cells is thereby small; these are rather responsible for the production of other, non-cellular structures.

- **Tunica Adventitia:**
  The *tunica adventitia* is the outermost layer of the vessel. It is surrounded by connective tissue and mainly consists of collagen fibrils arranged in helical structures. It also contains nerves that supply the muscular layer, as well as nutrient capillaries (*vasa vasorum*) in the larger blood vessels. It acts as a cylindrical shell [HO03] which reinforces the vessel wall from overexpanding and rupturing, especially at high pressure [SBRH02]. The adventitia is directly exposed and anchored to the surrounding tissue and organs.

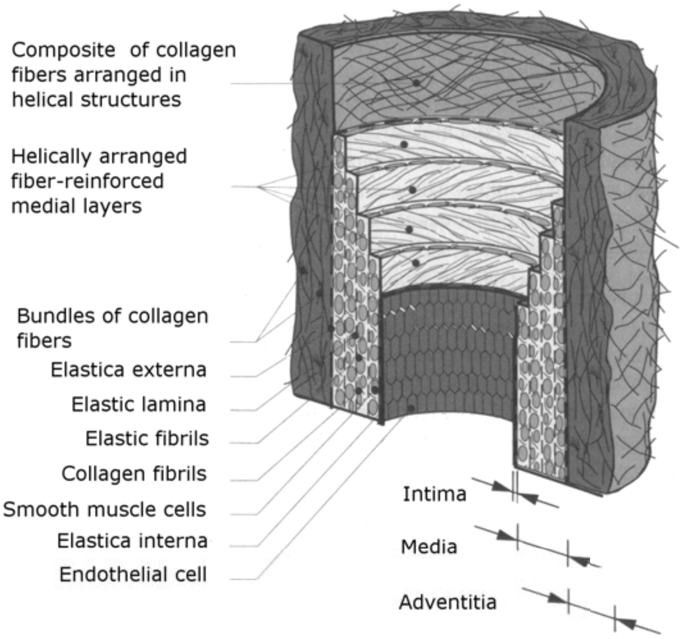
Composite of collagen fibers arranged in helical structures
Helically arranged fiber-reinforced medial layers
Bundles of collagen fibers
Elastica externa
Elastic lamina
Elastic fibrils
Collagen fibrils
Smooth muscle cells
Elastica interna
Endothelial cell
Intima
Media
Adventitia

Figure 2.3: Vessel wall layers: Intima, media and adventitia [HO03].

2.1.4 The Aorta

The *aorta* is the largest artery in the cardiovascular system. It has an average diameter of 2.5 cm and is directly connected to the left ventricle of the heart. The aorta is classified in two parts (Fig.2.4): the thoracic part located above the *diaphragma* and the abdominal part located underneath. The *aorta ascendens* denotes the short ascending part at the beginning of the thoracic aorta and includes the arterial branches to the coronary arteries. Then, follows the *aortic arch*, which represents the transition to the descending part, known as the *aorta descendens*. The aortic arch includes the branches for the supply of the head and the arms. The aorta descendens is divided into the *aorta thoracica descendens* and *aorta abdominalis descendens*.

As the large arteries proximal to the heart, the aorta is elastically deforming and has therefore a *Windkessel* function. In a healthy adult under normal conditions, the blood is ejected intermittently with a frequency of 60 to 80 beats per minute from the left ventricle into the aorta. The ejected stroke volume in the systole is thereby partly absorbed through the elastic deformation of the vessel wall. The elasticity in this context is denoted as *compliance*. As a result of this compliant behavior, the peak pressure in the systole as well as the strong pressure drop in the diastole may be smoothed through compensation. In addition, over the diastolic duration, the blood volume may be further transported thanks to the restored forces. Consequently, the cyclic blood flow from the heart takes a continuous form [Sch07].

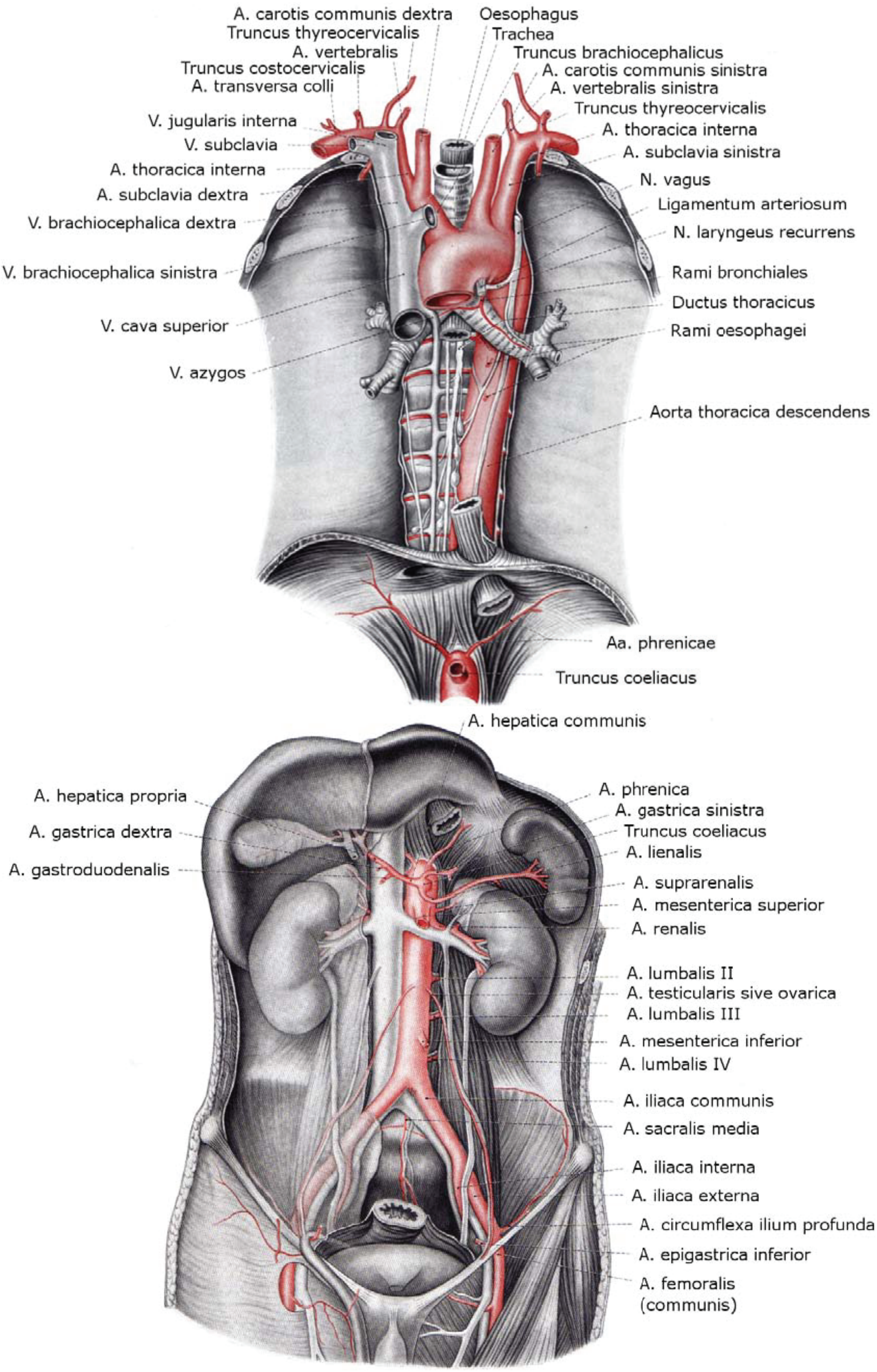
A. carotis communis dextra
Truncus thyreocervicalis
A. vertebralis
Truncus costocervicalis
A. transversa colli
V. jugularis interna
V. subclavia
A. thoracica interna
A. subclavia dextra
V. brachiocephalica dextra
V. brachiocephalica sinistra
V. cava superior
V. azygos
Oesophagus
Trachea
Truncus brachiocephalicus
A. carotis communis sinistra
A. vertebralis sinistra
Truncus thyreocervicalis
A. thoracica interna
A. subclavia sinistra
N. vagus
Ligamentum arteriosum
N. laryngeus recurrens
Rami bronchiales
Ductus thoracicus
Rami oesophagei
Aorta thoracica descendens
Aa. phrenicae
Truncus coeliacus
A. hepatica communis
A. hepatica propria
A. gastrica dextra
A. gastroduodenalis
A. phrenica
A. gastrica sinistra
Truncus coeliacus
A. lienalis
A. suprarenalis
A. mesenterica superior
A. renalis
A. lumbalis II
A. testicularis sive ovarica
A. lumbalis III
A. mesenterica inferior
A. lumbalis IV
A. iliaca communis
A. sacralis media
A. iliaca interna
A. iliaca externa
A. circumflexa ilium profunda
A. epigastrica inferior
A. femoralis
(communis)

Figure 2.4: Anatomy of the thoracic (top) and the abdominal (bottom) aorta [HRL66].

2.2 Vascular Pathologies

The cardiovascular system is subject to various pathologies with different origins and effects. In the event of a vascular disease, the cardiovascular system cannot function properly as the blood and nutrients distribution system for the body. Depending on the severity and the stage of the pathology, this may have fatal consequences for the patient. Pathologies of the blood vessels are of particular importance in this work. The most common vascular pathologies are *arteriosclerosis*, *aneurysms* and *dissections*.

In this section an overview on these three pathologies will be presented. Particularly, the origin and classification of the diseases will be described. Particular attention in the description is given to the aorta, to which most of the application examples in this work are associated.

2.2.1 Arteriosclerosis

The most common pathology of the blood vessels is the arteriosclerosis. The term arteriosclerosis describes vascular pathologies that lead to a stiffening of the vessel wall. The most common form of arteriosclerosis is the atherosclerosis. It represents a degenerative disease and is also known as arterial calcification as illustrated in Fig.2.5. More precisely, atherosclerosis is associated with a development of *atheromatous plaques* in the tunica intima which lead after a certain time to a weakening and degeneration of the arterial tissue. The risk factors to initiate an atherosclerosis are manifold and vary from arterial hypertension, overweight, diabetes mellitus to stress and nicotine abuse [Geb07], as well as genetic predisposition, age, gender or various infections.

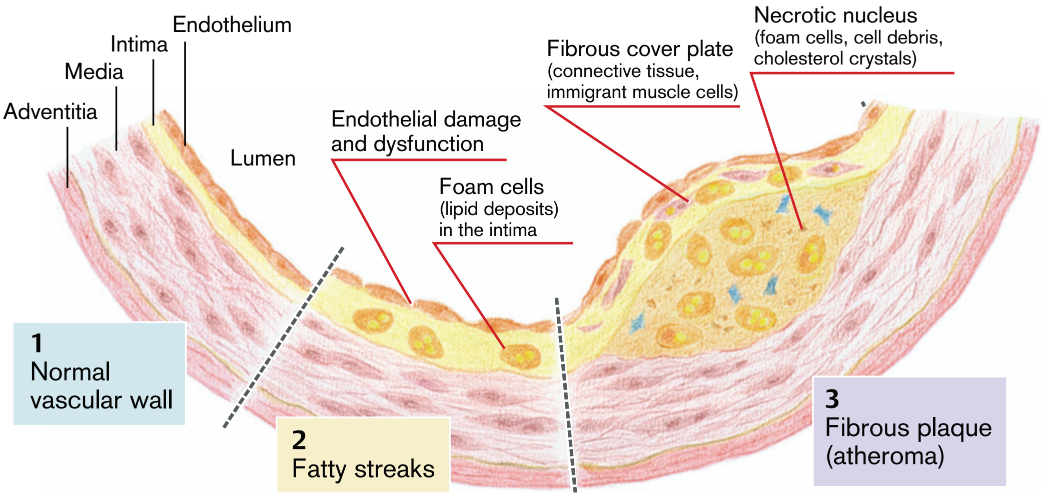
Endothelium
Intima
Media
Adventitia
Lumen
Endothelial damage and dysfunction
Foam cells (lipid deposits) in the intima
Fibrous cover plate (connective tissue, immigrant muscle cells)
Necrotic nucleus (foam cells, cell debris, cholesterol crystals)
1 Normal vascular wall
2 Fatty streaks
3 Fibrous plaque (atheroma)

Figure 2.5: Atherosclerotic change of the vessel wall [SL00].

The disease starts with a perturbation in the substance exchange of the vessel wall due to a *dysfunction* in the endothelial tissue. As a result, fats, proteins, calcifications and other substances are stored and settled. This occurs due to the building of special adhesion molecules by the endothelial cells which lead to the migration of monocytes and T-lymphocytes into the subendothelial space. The latter produce a large number of proinflammatory substances which stimulate the migration of smooth muscle cells from the media into the intima. Further, fibrous capsules are formed that enclose the accumulated cells which in turn build the central necrotic core of the atheromatous plaques [SL00].

As a result of this process, arterioclerosis leads to a weakening of the intima and to a destruction of the elastic fibrils in the muscle layers of the media increasing its stiffness. The loss of elasticity is particularly dangerous for the vessels near the heart. Through this effect, various other pathologies such as the building of *thrombos* or the development of *stenosis* take place (Fig.2.6.a). Stenosis is associated with a narrowing of the blood vessels and thus a perturbation of the blood flow due to the *deposit* of various substances. The increasing size of the plaques may lead at a certain advanced level to a restriction in blood supply, *ischemia*, of the related vessels, and thus influencing the whole blood circulation in a serious negativ way. Furthermore, through the high flow velocity in the narrowed vessel regions, the atherosclerotic plaques may rupture, leading to a development of a so called thrombos, which in turn presents a risk of an accute occlusion or a pulmonary embolism.

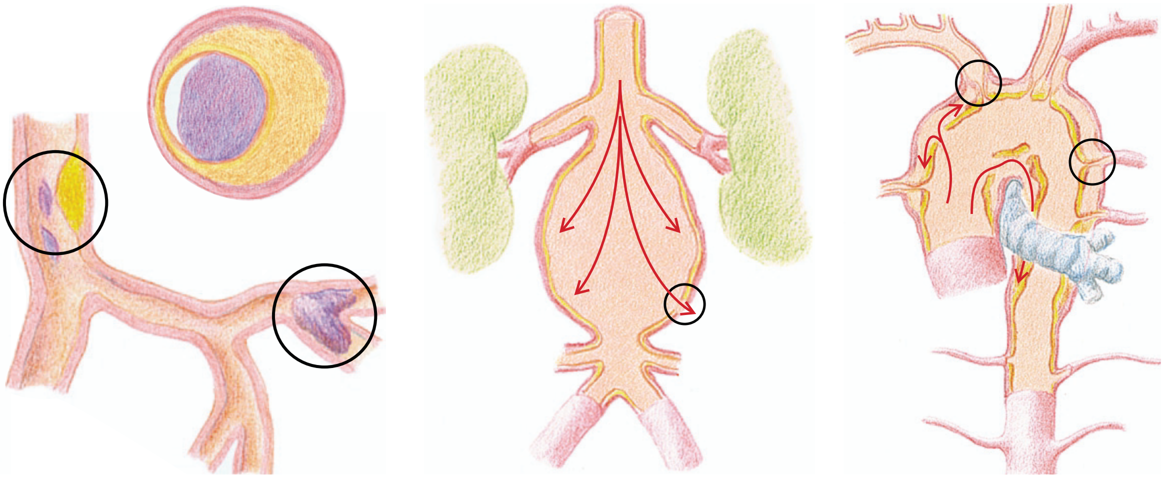

(a) Thrombus and Stenosis (b) Aneurysm (c) Dissection

Figure 2.6: Vascular pathologies: Consequences of atherosclerosis [SL00].

2.2.2 Aneurysms

A further consequence of the weakening of the vessel wall and the changes in its elastic properties is the development of aneurysms, shown in Fig.2.6.b. An aneurysm is a pathological dilatation of the vessel in which the diameter becomes larger than 1.5 times the original diameter. This abnormal dilatation of the vessel wall layers is locally restricted and permanent and is due to either inherent or acquired vessel wall change. Over 90 % of the aneurysms are at the origin of an atherosclerosis. Through an atherosclerosis, the continuous damage of the vessel wall may promote its dilatation. In few cases, an aneurysm originates from inflammation or infections due to fungus or bacterium. Also, inherited weakness of the collagen fibrils (Marfan syndrome) may lead to an aneurysm [Sch07]. In general, the locations of the vessel wall at which an aneurysm arises are not statistically distributed, but are especially present at regions where the blood flow is disturbed. The crucial problem thereby is that once an aneurysm has been developed, the high pressure produced by the blood within the expanded aneurismal bulge leads in turn to further dilatation.

An aneurysm may be *fusiform* with a homogeneous dilatation in radial direction, or *saccate* with a sac-like excrescence. Aneurysms are classified in *aneurysma verum* (real), and *aneurysma spurium* (wrong). The most common aneurysms are the aneurysma verum, in which the vessel dilatation affects all local wall layers. On the other hand, an aneurysm spurium originates from a damage of the vessel wall in the form of lesions, for instance due to a complication after a surgery or an arterial punctuation. Thereby, as a result of the lesion, blood is emitted in the wall leading to an extravasal pulsating hematoma.

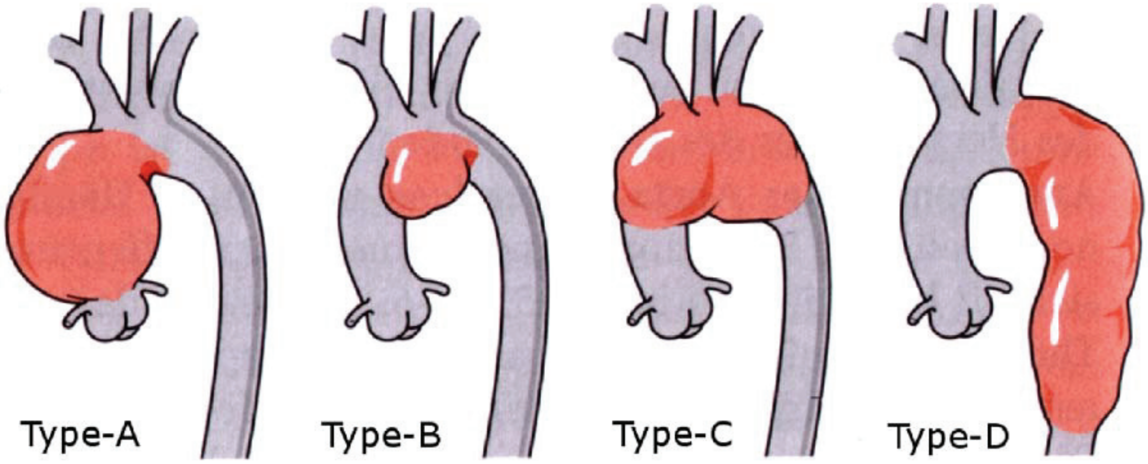

Figure 2.7: Aneurysms classification after their position [BE08].

Aneurysms may also be classified after their location; in the aorta this involves thoracic (TAA), thoracic-abdominal and abdominal (AAA) aneurysms. For these three types of aneurysms, there exist further classification approaches. For instance, the *Cooley* classification represented in Fig.2.7 assigns four types for the thoracic aorta [EKH$^+$07]: Type-A = ascending, Type-B = aortic arch, Type-C = aortic arch to descending and Type-D = descending.

2.2.3 Dissections

A dissection is associated with a longitudinal or transversal tearing in the innermost tunica intima layer which leads to the development of a subendothelial wrong canal between the intima and the media, as illustrated in Fig.2.6.c. As a result, the vessel wall is split up and the blood flows between the layers. The blood flowing into this second wrong canal may lead to a narrowing and hence to a collapse of the actual vessel lumen, known as *true lumen collapse* effect. In addition, a *reentry* effect arises when a further tearing of the intima occurs yielding a new connection of the wrong lumen to the true lumen. Beside the atherosclerosis, *autosomal* inherited connective tissue diseases such as the Marfan syndrome present also risk factors for the development of a dissection.

Aortic dissections are classified after the *Stanford* classification in Type-A and Type-B. Type-A describes dissections in which the tearing of the intima is located *prior* the left arteria subclavia in the aortic arch and/or in the aorta ascendens, while Type-B represents dissections *below* the left arteria subclavia. Consequently, Type-A dissections are quite dangerous leading to an urgent *relocation* of the vessel outlets. They present a surgical emergency and require an aortic repair, since if left untreated they lead in 90 % of the cases to death. Type-B dissections are less crucial and depending on their stage may be treated either in a conservative (medicinal) way or if required with an endovascular surgery (stent implantation).

2.3 Diagnosis and Therapy of Aneurysms

Although the conducted work applies to any vessel type, shape or pathology, aortic aneurysms have been the main application example in this work. Therefore, this section is dedicated to aneurysm specific symptoms and diagnosis as well as to the related risks and therapy options.

2.3.1 Symptoms and Diagnosis

A large number of patients, especially at the beginning stage of the aneurysm, do not show clinical symptoms. These usually show up at a late stage, when the large dilated vessel starts to disturb its environment. The missing symptoms make the diagnosis of aneurysms a difficult task. When present, noticeable symptoms of AAA are mostly expressed in terms of back and diffuse abdominal pain. Further symptoms are diffused pain in the legs, strangury and alteration of diarrhea and obstipation. TAA show difficulties in swallowing, cough, hoarseness, perturbation in the blood circulation in the arms and the brain or even shortness of breath, mostly due to the high pulsating pressure in the aneurysm. In few cases, signs of pulsating swelling may also indicate a possible aneurysm.

Aneurysms are mostly discovered accidently in a routine inspection. For asymptomatic patients, an ultrasound-based inspection is usually used being the cheapest scanning way. As mentioned before, the currently used way to evaluate the risk of rupture is based on the maximum diameter and on the expansion rate of the aneurysm. A more accurate diagnostic inspection is obtained via a tomographic CT- or MRI-scan to identify the exact diameter of the vessel.

2.3.2 Risks and Therapy

Aneurysms have a high potential of rupture, as a result of the decrease in wall strength due to the dilatation. A rupture of an AAA leads to serious bleeding and is associated with 80-90 % lethality, while 45-60 % of the patients die due to an hypovolemic shock before reaching the hospital. However, not every aneurysm holds the same risk potential. Further, only 50 % of the patients survive an emergency surgery of a ruptured aneurysm. Since an aortic surgery is related to various risks and complications, the advantages of the intervention must be well evaluated and a surgery is only conducted when the risk of a rupture overtakes those of the surgery itself.

The risk of rupture increases exponentially with the aortic diameter. In fact, the risk of rupture for an infrarenal aortic aneurysm with a diameter of 5-6 cm is 10 %, of 6-7 cm is 20 % and of a diameter more than 7 cm is 40 % per year. Based on this, therapy suggestions are derived as follow: an AAA diameter of 4.5 to 5.5 cm should be subject to an indication control for an intervention, while an AAA with a diameter larger than 5.5 cm or an expansion rate larger than 1 cm per year is an absolut indication for undergoing a surgical therapy [SSMF05].

Various therapy options are possible. These may be classified in two areas: the *conservative* medicinal therapy and the surgical intervention in the form of an open *conventional* or a *minimally invasive* endovascular surgery.

- **Conservative Medicinal Therapy:**
  Goal of this conservative therapy is to control the high blood pressure, the malfunction of substance exchange or even the related overweight through the adoption of medicaments. Although thereby, since a developed aneurysm is associated with an irreversible dilatation, the aim is not to *eliminate* the aneurysm but rather to positively affect the disease growth by preventing further development and dilatation of the aneurysm and thus reduce the high risk of rupture. This may be achieved for instance by decreasing the blood pressure using *anti-hyperthensiva* which in turn leads to a reduction in the loads applied at the vessel wall and consequently lowers the risk factor for further dilatation.

- **Conventional Open Surgery:**
  In the open conventional surgery, the diseased aneurismal part of the aorta is replaced through a vessel prothesis. The access gate to the infrarenal aorta is usually conducted *retroperitoneal*, that is situated behind the peritoneum, while the thoracic access occurs through the left *intercostal* space. In order to replace the diseased part, it is necessary to separate the vessel from the blood circulation. This usually leads to a strong increase in pressure that may be reduced using pressure decreasing agents or other surgical procedures such as a connection to a cardiopulmonary bypass. Thereby, the blood is exhausted from the right atrium through a canula, arterialized and then pumped again through a canula into the body. After separating the diseased vessel part from the blood circulation, the aneurysm sac is opened and depending on the dilatation of the aneurysm, a cylindrical or a bifurcating prothesis is interposed [BE08]. For the prophylaxis of infection, the aneurysm sac is used to coat the prothesis.

- **Minimally Invasive Surgery:**
  Another form of surgery is the minimally invasive intervention using endovascular procedures. This advantageous approach is described in detail in the next section.

2.4 Endovascular Therapy

Due to its high invasiveness, the conventional surgery is often accompanied by subsequent risks and complications especially in old patients. An alternative form of the intervention with various advantages is in the field of the minimally invasive surgery using endovascular procedures. Hereby, the diseased vessel part is not replaced, but protected from the inside (endovascular) through the implantation of a vessel prothesis (Fig.2.8). The intervention occurs under angiographic control. Thereby, a *stent* or a *stent-graft* is inserted into the vessel through an artery, for instance the *arteria femoralis* for the abdominal aorta. The position of the stent i.e. stent-graft is adjusted using a guide wire. Once the right position has been found in the angiography, the stent i.e. stent-graft in the diseased part may be deployed. If required, the contact with the wall is adjusted afterwards using an inflatable balloon (*balloon dilatation*). The stent diameter around the necks, below and above the aneurysm where the stent-graft is in touch with the healthy aorta, must be about 1 to 2 mm larger than the aortic diameter in order to prevent *migration* [Medb].

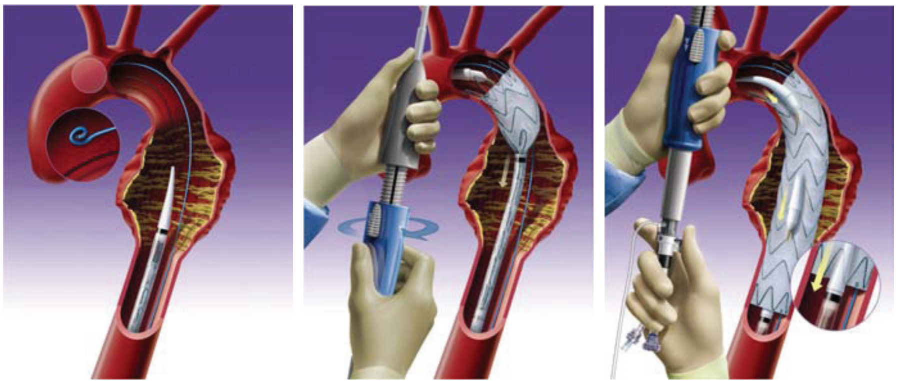

Figure 2.8: Endovascular intevention: Stent-graft implantation [Medb].

Compared to a conventional open surgery, an endovascular intervention holds mainly advantages in terms of the minimal invasiveness with a shorter stay at the hospital and a faster convalescence of the patients. Furthermore, many studies have demonstrated that endovascular therapies has lower morbidity and lethality [Bec91]. The lethality rate decreases thereby from 50 % to 20-30 % [Lut07]. However, an endovascular therapy can only be conducted under special morphological requirements. Especially, the availability of a sufficient long healthy aortic part *cranial* and *caudal* to the aneurysm with about 15 mm overlapping space [DB00], is required for the fixation of the endovascular prothesis. After *Allenberg*, an endovascular therapy of infrarenal aneurysms may only be conducted for types I, IIA and IIB as illustrated in Fig.2.9. Consequently, only about 30 % of all AAA patients may be treated with endovascular procedures.

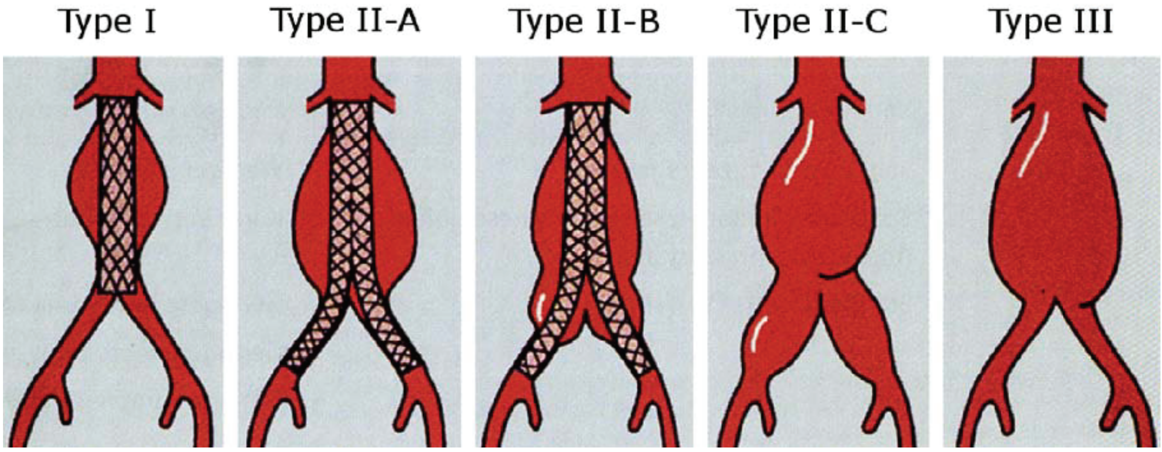

Figure 2.9: Endovascular therapy for AAA [Sie06].

2.4.1 Stents and Stent-Grafts

Endovascular devices are expandable mesh tubes designed to be inserted into the diseased vessel. For obvious reasons, they are inserted in their undeployed state through a catheter in the artery and navigated until they reach the right position at which the device is deployed. A *stent-graft* is an endovascular prothesis consisting of a mesh tube *stent* which surface is covered with an elastic material called *graft*, as illustrated in Fig.2.10.

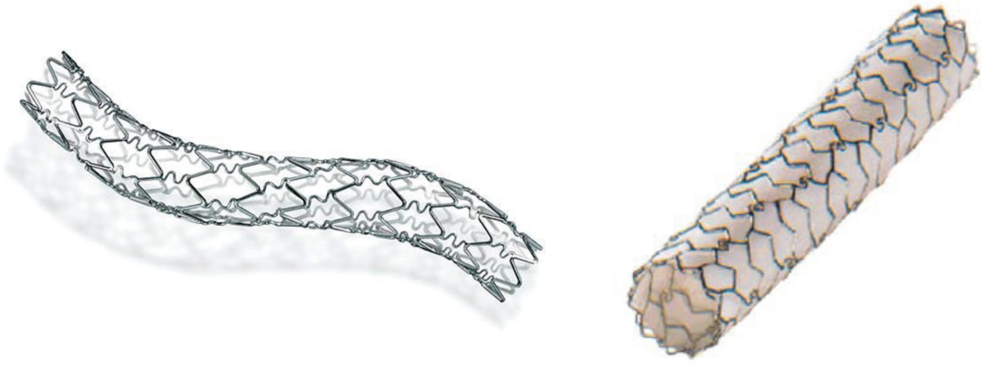

(a) Curved stent (b) Cylindrical stent-graft

Figure 2.10: Endovascular devices: Stent and stent-graft.

In the case of an aneurysm, a stent-graft is used in order to restore and stabilize the normal pathway of the blood and to protect the fatigued vessel wall from high intraluminal pressure. The blood should thereby flow only inside the stent-graft. Consequently, the aneurysm is functionally shut off as in the open surgery and the rupture risk is reduced.

The field of stent-graft design is currently a popular research area. Since the first implantation in the nineties, many types have been developed. The individual stent-grafts differ in the type of fixation at the deployment area or in the type of material used for both the stent and the graft and in the design of the stent geometry. The design of a stent-graft is also related to its application area. On one side, through its stiffness it must be able to overcome all loads. On the other hand, it must be so flexible such to allow all deflections which comes on its way during insertion [CSM02].

A stent without a graft is adopted in the therapy of stenosis to support the vessel wall by expanding and preventing it from closing. When used in a stent-graft, the stent serves the anchoring of the stent-graft in the healthy aortic wall above and below the aneurysm. It also enforces the graft in the area of the aneurysm and helps thereby to avoid a bending. Furthermore, by pressing the graft towards the wall, the stent improves the building of new tissue in the inbetween areas and hence enforces the healing process [WF99]. Possible stent designs include the cylinder geometry, the mesh structure, the raised wires and rings as well as the combination of various geometry-specific designs [CSM02]. Current implanted stents are especially made of *nitinol* or *steel* materials [Cow07] and include zig-zag patterns. Others are made of alloyment based on *cobalt*, *tantalum* or *drug-eluting* and biocompatibel materials, which are degraded by the body after a certain time. For the fixation, there exist *balloon-expandable* and *self-expandable* stents, while *balloon dilatation* is only adopted to conduct small placement corrections.

Most adopted grafts for the stent-grafts consist of *polyethylene terephthalate* (PET) or *polytetrafluorethylene* (PTFE). PET is a solid plastic material used in a woven or knitted textile form. Especially, woven textiles that may be produced with a very low wall strength of 0.1 mm or less are adopted. PET-tissue is very soft, though almost completely non-elastic. Its compliance is equivalent to only 0.0016 % diameter increase per mmHg, in contrast to the thoracic aorta in which, depending on the age, a 0.14 % to 0.27 % diameter increase per mmHG is obtained at the same diameter [WF99]. Compared to PTFE, PET provides the advantage of larger stability, while ePTFE has better compatibilty exciting less defence mechanisms. PTFE is a plastic polymer of fluorine and carbon. It is used as a graft material in its expanded form (ePTFE) at which it behaves plastically even at high pressures. During the implantation, the diameter of the graft may get changed through the balloon dilatation. ePTFE is more elastic than PET-tissue with a diameter increase of 0.016 % per mmHg, however still much less elastic than the aorta [WF99].

2.4.2 Healing Process

The first reaction to the metallic stent after an endovascular therapy is the development of thrombus due to the pressure against the wall and to the negative charge of the metal surface. Few days post the implantation, the body starts to change this thrombus. Thereby, the smooth muscle cells migrate into the thrombus and build there new regeneration tissue, the *neointima*, mainly consisting of collagen and which origin is still not fully understood. These developments are concentrated on the stent but may also extend to the graft [DB00]. A current hypothesis for this effect is based on the observation that, since the cells responsible for repairing the arteries originate from the media, this layer could also be the origin for the development of the neointima. The hypothesis assumes that the damage of the smooth muscle cells of the media leads to a high production of the structure elements *elastin* and *collagen* and that the smooth cells start to migrate into the intima [MGF01].

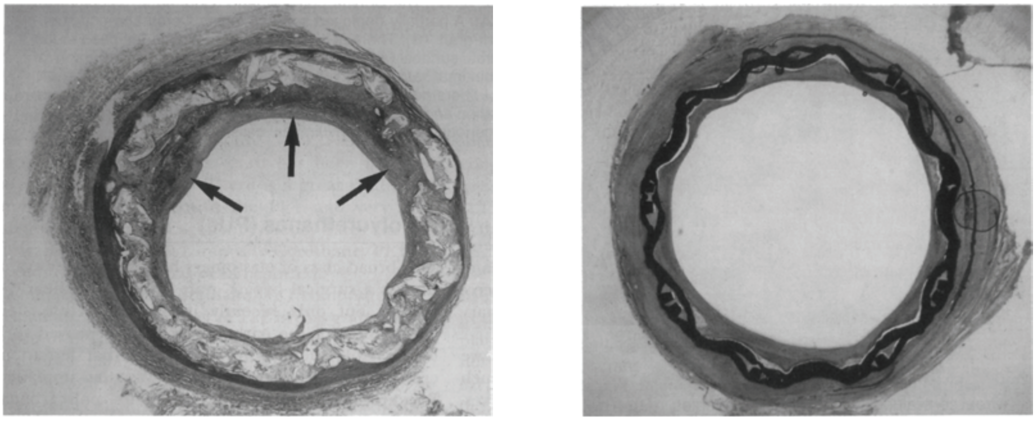

(a) PET Graft with stenosis (b) ePTFE graft with weaker reaction

Figure 2.11: Reactions on grafts with PET and ePTFE materials [DB00].

A common post-implantation syndrome with pain and fever occurs when PET-grafts are used and requires an accurate investigation to prevent possible infections. Hereby, the development of thrombus is particularly dominated, mostly including also cells of the immune system, which effect is known as the *neointimal stenosis* (Fig.2.11.a). Therefore, grafts made of PET should only be implanted in large vessels with diameters larger than 10 mm. The higher resilience compared to ePTFE may be here an advantage (Fig.2.11.b).

In case the stent is *outside* the graft, then a thin layer of neointima is developed, with a thicker non-completely developed layer between the stent and the graft. When the stent is *inside* the graft, thus directly facing the blood, then the grown neointima is relatively thick yielding in a better healing. Further, the graft permeability also plays an important role in the healing process [DB00].

2.4.3 Risks and Complications

As mentioned before, compared to open surgery, endovascular therapies are minimally invasive presenting various advantages. Especially, the lethality rate and the recovery period for the patients decreases with a stentgraft implantation. Minimally invasive surgeries may therefore be applied to old patients who cannot undergo an open surgery anymore. However, various complications may arise during an endovascular implantation, imposing for instance the removal and the replacement of the stent-graft with a new one.

The most frequent complication in the treatment of stenosis, especially in the coronary arteries, is *restenosis*. A restenosis describes an occlusion of the vessel through a tissue *excrescence* that originates from an inflammation of the vessel wall that arises due to the dilatation of the vessel. It can also originate from an atherosclerosis which arises due to a change in the hemodynamics compared to the old form of the aorta. This risk may be reduced through a *drug-eluting* stent (DES) [SDW$^+$07].

In the treatment of aneurysms with a stentgraft implantation, *endoleaks* are the most frequent complication and occur in 10 % of the interventions. An endoleak is a persistent blood flow outside the stent-graft lumen but inside the treated aneurysm sac [SL00]. It mostly originates at the ends of the stent-graft due to a deficient sealing of the vessel wall. It may also occur at intersection regions between two overlapping stent-grafts or due to a porous material structure or simply a failure of the stent-graft material. As a result of an endoleak, the high pressure in the aneurysm sac is maintained and the risk of rupture is preserved. Endoleaks may also lead to a stent-migration. Persistent endoleaks are dangerous and require an endovascular intervention, such as balloon dilatation or implantation of a second stent-graft. In few cases, they even require a treatment through an open surgery. Fortunately, in most of the cases they just disappear alone few days after they arise without the necessity of an intervention [IN01].

In few cases, the stent-graft cannot stand the existent forces and breaks. However, also here a further intervention is not always required. Further, stent-migration may occur especially in the descending thoracic aorta and concerns 2 % of the treated patients. In a stent-migration, the device leaves its original position and migrates in the blood flow direction, and hence misses its application location. Stent-migration is mainly due to shear stresses arising from the pulsatile flowing blood and may in turn lead to endoleaks.

Finally, a strong dilatation of the neck is also possible. This mainly arises in old patients with arteriosclerosis and may also lead to stent migration or endoleaks. Also complications at the gate artery may lead to a prolongation of the healing time for the patient [IN01].

Chapter 3

Simulation Workflow

3.1 Introduction: Approach & Requirements

Patient-specific computational modeling of cardiovascular disease is a complex process consisting of several stages. Careful and adequate processing of all steps beginning with the tomographic image data and ending with clinically applicable and valid simulations must be performed and is indispensable for the generation of accurate and individual results. The aim is therefore to develop a reliable modeling process as well as to facilitate a clinical implementation of such computational methods in the field of minimally invasive cardiovascular diagnosis and endovascular therapy. Such a modeling provides a potential to aid the diagnosis of aortic disease and their collateral risks, and represents a promising milestone toward optimal planning and controlling the efficiency of endovascular treatments.

Procedural Approach

The procedural approach for computational modeling involves the definition of four aspects: problem, physics, mathematics and evaluation. In the *problem definition*, the issues to be solved must be first formulated. In the *physics definition*, physical models that satisfy the problem definition must be established. Then follows the *mathematics definition*, in which mathematical methods appropriate to solve the defined physics have to be determined. Finally, the *evaluation definition* is concerned with representation forms that adequately and clearly reflect the results. Corresponding to these aspects, four main questions arise and have to be addressed: What parameters to solve? Which equations to solve? How to solve these equations? And how to evaluate and represent the results?

Modeling Requirements

With regards to a clinical implementation, the following requirements must be fulfilled: First of all, the modeling must be reliable in terms of *accuracy* and *numerical stability.* Therefore, the results must be interpretable on the basis of physical fundamentals and mathematical theories. Beside reliability, an *automation* of the process is indispensable for the radiologist and the surgeon to save time, complexity and unnecessary interaction during intervention. The automation is achieved via *system integration* of all simulation components into a single program to facilitate the interaction efficiency and usability. Further, important features of the workflow are the *optimization* and *individualization*, that is, generating simulations that are able to reproduce the patient-specific physical parameters in an accurate way. Finally, the *expandability* of the system is useful to enhance flexibility, by easily allowing an extension to include further applications and pathologies as well as the integration of endovascular devices or surrounding organs into the modeling process.

Taking into account the above described approach and requirements, the main focus of the present chapter includes the following:

- Building the elements of the process chain in an accurate and stable way.
- Automation of the process via integration of the individual steps into an extendable simulation system.
- Optimization and individualization of the modeling in terms of patient geometry, pathology shape and vessel region.

3.2 Process Chain for CSM, CFD and FSI

Processing image-based computational modeling consists of the stages represented in Fig.3.1. The simulation workflow is a chain that begins with the segmentation of the patient-specific tomographic images after 3D reconstruction. From the segmented data, an initial geometrical model is created and has to be preprocessed. Then, high-quality meshes required for running and converging the simulations are generated. Reliable physical models must be defined in order to determine the system of equations to be solved. Realistic initial and boundary conditions, based on individual and physiological measured data, are required for the solution of the system of partial differential equations. Mathematical models based on appropriate numerical methods need to be defined in order to discretize the system of equations and perform the simulations. Finally, proper representation and evaluation of the results is necessary to visualize, analyze and quantify the parameters of interest.

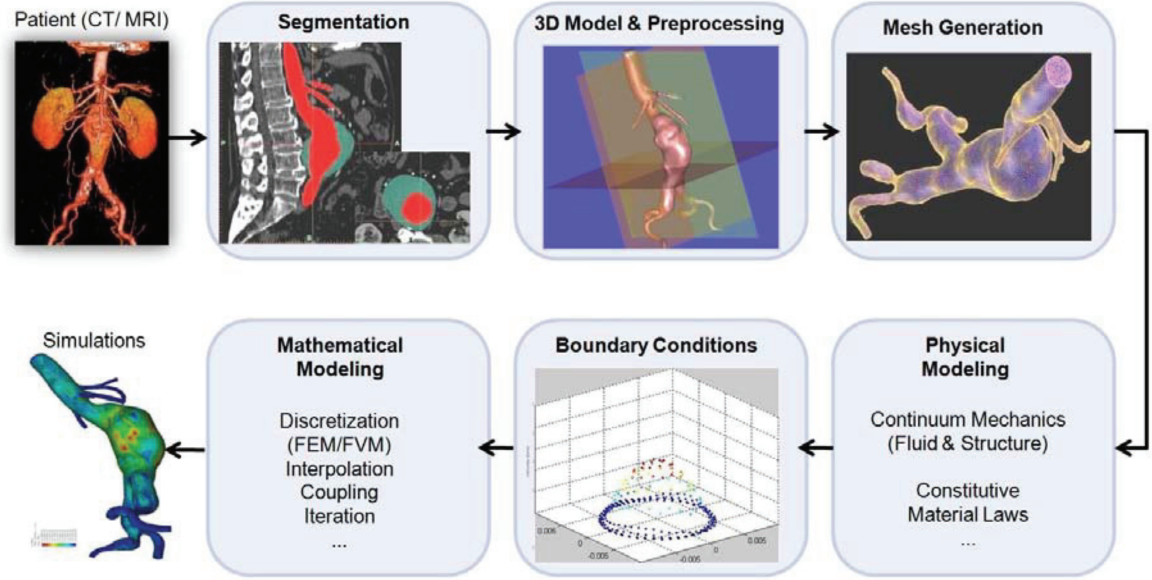
Patient (CT/ MRI)
Segmentation
3D Model & Preprocessing
Mesh Generation
Physical Modeling
Continuum Mechanics (Fluid & Structure)
Constitutive Material Laws
...
Boundary Conditions
Mathematical Modeling
Discretization (FEM/FVM)
Interpolation
Coupling
Iteration
...
Simulations

Figure 3.1: Simulation workflow.

The individual elements of the process chain are described in the next sections.

3.2.1 Segmentation of the CT/MRI images

Patient-specific modeling is based on morphological data derived from either computed tomography (CT) or magnetic resonance imaging (MRI) scans. For patient-specific biomechanical simulations, great care has to be taken when generating the three-dimensional (3D) description of the geometry of interest. The CT data are therefore accurately segmented, extracting the region of interest limited by the vessel wall. An initial approximation of the boundary surface is first generated from the 3D scan based on the region growing approach. The output of the 3D segmentation usually shows many artifacts, inaccurate boundary contours and inhomogeneous lumen domain (Fig.3.2.a). A fine and adequate segmentation is a prerequisite to achieve accurate and stable numerical results. For this reason, a manual correction of the 2D slices, usually in axial direction, is further required to improve the 3D segmentation by removing pixels outside, or filling in pixels inside the lumen (Fig.3.2.b). The final segmentation shows good results (Fig.3.2.c) though it is time-consuming.

Due to limitations in the quality of the CT and MRI images, the detection of the wall thickness is not directly possible. The region of interest is therefore represented by the inner wall of the model. In order to determine the wall volume, a thickness is defined and assigned to the inner wall as described in

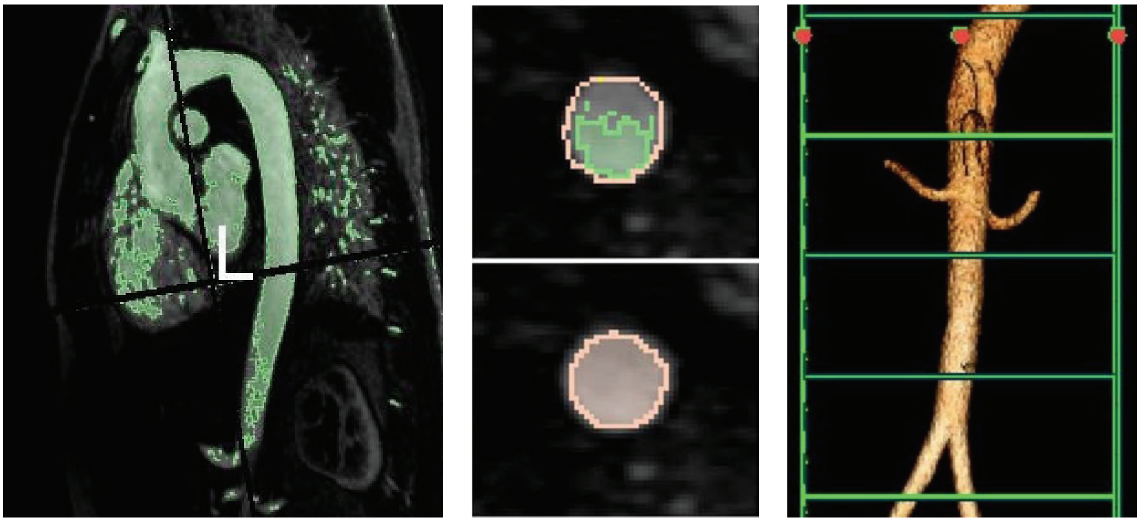

(a) Initial approximation (b) 2D-correction (c) Final result

Figure 3.2: Patient-specific segmentation step.

Chap.4. Alternatively, the segmented lumen is dilated by a certain number of pixels n to additionally derive the outer wall surface. n is chosen depending on the resolution of the images, so that the desired wall thickness is obtained. In this way, a homogenous thickness is assumed. In all cases, the knowledge of the wall thickness is a crucial issue for accurate modeling. The segmentation is performed using the software package Mimics (Materialize Inc.).

3.2.2 3D Model Generation and Preprocessing

The generation and the preprocessing of the three-dimensional geometrical model is performed based on the segmented patient images.

Generation of the 3D Geometrical Model

From the segmented *Dicom* slices, an initial 3D geometrical model is created by combining all 2D slices into one dataset. Then, using a surface triangulation based on the marching cubes method [LC87], an initial boundary surface is constructed from the volume model. The algorithm generates isosurfaces from the volume based on a minimum/maximum specified scalar range. The generation of the 3D model and the extraction of the boundary surface made for the inner wall are also performed for the dilated outer wall, in case this latter is used for the determination of the wall volume.

Preprocessing of the 3D Geometrical Model

The processing of the obtained 3D geometrical model is performed using the software Paraview, an open source vtk/itk based scientific application developed by Kitware Inc for medical image processing.

Prior the mesh generation step, the boundary surface of the segmented model must be preprocessed and optimized. Thereby, the obtained geometry is first idealized using Laplacian smoothing to adjust the vertices distribution and the cells shape. Then a surface-cleaning filter is applied to merge duplicate points within a specific tolerance as well as to remove unused points. Further, in order to ensure simulations free of oscillations, the blood must flow orthogonal to the inlet and outlet faces. Therefore, a clip filter is applied, to cut and readjust the inlet and outlet boundary faces such that their normal is parallel to the flow direction. Finally, the resulting aortic wall surface is extracted and exported into an .stl or a .vtk file consisting of 3D triangles.

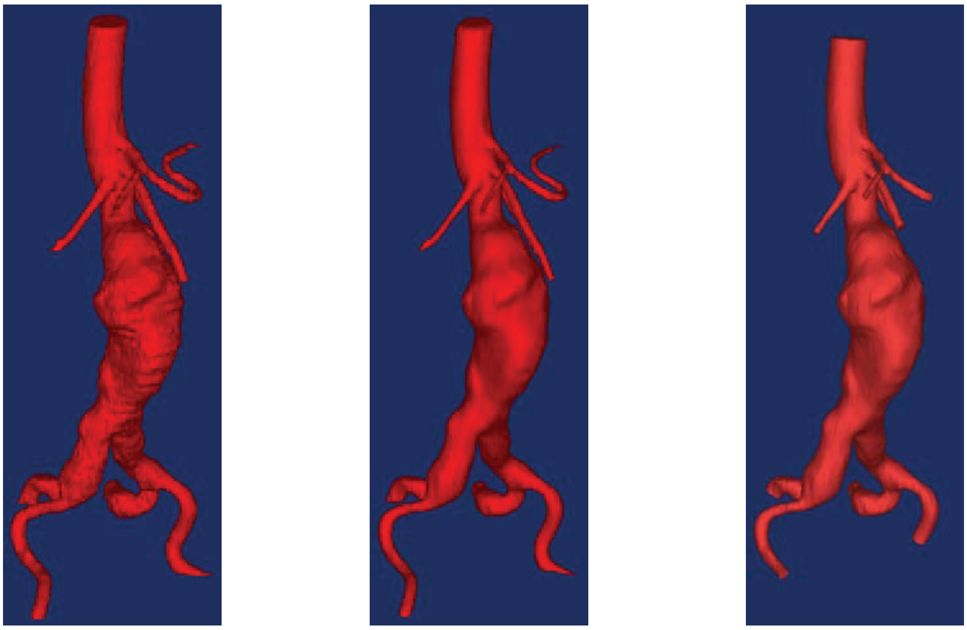
(a) Generated model (b) Surface optimization (c) Boundary clipping

Figure 3.3: 3D model generation and preprocessing steps.

Fig.3.3 shows the generation and preprocessing of the segmented geometrical model. The concatenation of all 2D slices into one dataset and the triangulation of the set of points representing the image file is shown in (a). The smoothing and cleaning filter effects are illustrated in (b) and show a clear improvement of the surface quality. Finally the clipped surface, which allows the blood to flow in normal direction to the inlet and out of the outlet faces, is shown in (c) and is a necessary prerequisite for simulations free of backflows.

3.2.3 Mesh Generation and Processing

Blood flow and vessel wall computations based on the Finite Element and Volume Methods require the generation of finite cells to represent the blood and the wall elements. The computation of the parameters then occurs on those discrete elements before it is integrated over the whole volume domain. Furthermore, to enhance numerical stability, which in turn affects the convergence and the accuracy of the simulations, high-quality three dimensional surface and volume mesh models have to be created. At this point, the obtained and preprocessed vessel surface does not yet guarantee the stability of the simulations. A high quality surface mesh must be free of high-skewness cells. This is achieved by integrating a variety of mesh control functions which allow the generation of high quality and controlled meshes. Quality controlling is based on mesh functions accounting for

- the curvature at the boundary surface,
- the distribution of the cell size near the wall boundary, and
- the propagation of the mesh from the surfaces into the volume.

Triangular and quadratic elements are generated for the surface meshes. As for the volume meshes, they consist of tetrahedral, hexahedral and wedge cells. Depending on the application, various meshing processes had to be developed to generate suitable mesh models. These may be summarized by:

- *Boundary Surface* meshing for wall and blood-wall interaction simulations
- *Blood Volume* meshing for blood and blood-wall interaction simulations
- *Wall Volume* meshing for blood-wall interaction simulations

Details on the mesh generation processes depending on the different applications and on the used control functions will be described in Chap.4.

3.2.4 Physical Modeling

An indispensable issue for a reliable interpretation of patient-specific computational modeling in medical applications is to be based on realistic physical theories. Physical modeling involves two aspects: describing the fundamental mechanical behavior through the fundamental equations, and taking into account the material constitutive properties based on physical material laws.

Fundamental Equations

Simulating the hemodynamics and the elastomechanics within vessel models is equivalent to solving the time-dependent fundamental equations governing the blood flow and the vessel wall domains. These are represented by physical conservation laws and principles. For the blood domain, they represent a mathematical relationship between the main fluid variables, flow velocity and pressure, together with the fluid physical properties in the lumen region. For the wall domain, the fundamental equations are equivalent to mathematical expressions relating the mechanical forces to the wall deformation through the structure physical properties in and along the wall region.

Material Laws

Another important aspect while simulating the blood flow and the vessel wall is to accurately describe the physical nature of the materials being modeled. Thus, beside the fundamental fluid and structure mechanics conservation equations, the properties of the blood as a fluid and the wall as a solid must be physically defined. Physical properties are described through the flow type and through material laws which represent the material behavior in terms of constitutive equations. Essential fluid constitutive models are those describing the viscosity and the compressibility of the blood. For the structure, constitutive behavior mainly includes the modeling of the elasticity, the isotropy and the compressibility of the wall.

Details on the derivation and the application of the fundamental equations and the material laws are described in Chap.5 and Chap.6 for the structure and the fluid domains, respectively.

3.2.5 Initial and Boundary Conditions

For each computational point, a finite approximation of the partial differential equations will be established. In order to solve the resulting system of equations governing the blood flow and the vessel wall domains, information about the initial and the boundary solutions need to be defined. Model boundaries are for instance the inlet, the outlets, the inner wall, the blood-wall interface, the thrombos-blood or stent-wall faces. Choosing proper initial and boundary conditions is indeed essential to successfully solve a given problem. The required conditions depend on the type of the computational domain and on the governing equations used. In general, boundary conditions are given in terms of [FP08]:

- The value of the variable, known as the *Dirichlet* boundary condition
- The gradient of the variable, usually derived in normal direction to the boundary, known as the *Neumann* boundary condition
- A combination of the Dirichlet and the Neumann conditions

For realistic simulations and to keep the model patient-specific, individual physiological data, when available, are used to set the conditions at the boundaries of the vessel model. Boundary conditions are usually expressed in terms of data based on steady or unsteady flow and pressure profiles along the cardiac cycle, or in terms of degrees of freedom (DOF) constraints. The profiles are obtained either via direct measurements at specific locations, or via indirect derivation based on physical and/or physiological laws. Examples are the derived inhomogeneous Womersley spacial profiles and the conservation-based pressure-specific or outflow-rate boundary conditions. All profiles are preprocessed to avoid undesirable oscillations later in the simulations. Finally, a good initialization of the model from appropriate locations or values increases stability and enforces convergence as well as reduces the simulation time.

All these conditions will be described and discussed in Chap.5, Chap.6 and Chap.7, according to their respective application.

3.2.6 Mathematical Modeling

The resulting set of equations consists of a nonlinear complex system of partial differential equations. Analytical algebraic methods have limitations solving such elaborate systems. Numerical approaches are needed instead to solve analytically non-solvable problems. The Finite-Element Method (FEM) and Finite-Volume Method (FVM) are numerical approaches with high-potential in solving time-dependent complex systems of nonlinear partial differential equations. The FEM and FVM methods are based on the discretization of the governing equations using a numerical finite mesh. The use of a finite mesh with a large number of elements and the integration of the conservation equations over the individual cells, result in exact solutions of the FEM and FVM methods. Not to forget the fundamental feature of finite methods being based on physical theories, indispensable for reliable interpretation of patient-specific medical results.

Applying appropriate FEM- and FVM-based numerical solvers depends on many factors such as the desired accuracy, the time available but also on the physical problem such as dealing with static or dynamic domains. Thus, depending on the application, appropriate spatial and temporal discretization techniques may be applied. Further, coupling algorithms for fluid-solid variables, interpolation methods, contact algorithms for solid-solid problems, iteration solution methods etc. should be defined to numerically solve the conservation equations. The main focus thereby is to achieve numerically stable solutions.

The formulation and the application of FEM- and FVM-based solutions are presented in Chap.5 and Chap.6, respectively. Further mathematical aspects concerning the interaction of coupled problems are described in Chap.7.

3.2.7 Representation and Evaluation

Once the entire process is compiled and the simulations are performed, the results may be finally visualized and quantified in a comprehensible way.

In general, quantifying the simulation results is a time intensive and complex task especially when large number of data is considered. Further, evaluation approaches depend on the desired precision and mainly on the time available. Forms of presentation also depend on the problem definition, goals and the results themselves. Therefore, in order to facilitate this task, relevant evaluation parameters such as velocity vectors and magnitudes, pathlines, blood pressure, displacement fields or various wall stress distributions are defined, depending on the application, at various regions and times of interest. Evaluation regions and times are chosen such as to support the radiologist and the surgeon in their decisions. Considerable locations representing a potential help in diagnosis and risk prediction concern areas with formation of recirculation zones, development of vortices, reversed flows or high pressure, stresses and strains. These usually occur within the cardiac cycle at the peak and late systole and at the early diastole, where the wall stresses are too high or the recirculation zones grow to large 3D vortices with reversed flow at the outlet boundaries.

3.3 Numerical Stability

Numerical stability of the simulations is an essential aspect for realistic and accurate patient-specific biomechanical modeling. Demonstration of numerical stability is computationally expensive and time-consuming. Consequently, most of the investigations carried out in this domain do not consider this aspect. However, provided that accuracy is an indispensable step for a reliable evaluation of surgical procedures and planning of optimal therapies which lead to much more efficient treatments, numerical stability was cautiously investigated in this work.

> *The precision of the approximation improves with the level of discretization and the degree of interpolation chosen, while the detriment of the necessary computation time and memory size* [Zie89].

3.3.1 Mathematical Stability

Mathematical stability is attained by ensuring individual converged solutions of the numerical computations. It is characterized by small residuals and moderate number of iterations leading to fast convergence. It is also represented by results that are independent on the size of the timesteps used. Mathematically stable simulations are achieved through the integration of the conservation equations based on appropriate mathematical models. In particular, the integration of optimized algorithms, discretization schemes and numerical solvers, compatible choice of various settings as well as definition and adaptation of suitable parameters are of major importance.

3.3.2 Physical Stability

While the mathematical stability is characterized by the convergence, physical stability is represented by the accuracy. It is ensured by applying reliable physical models and realistic and consistent boundary conditions. Physical stability is also enhanced by generating results that are independent on the mesh configuration of the model. This is achieved by performing a computational grid analysis in which the properties of the meshes required for stable results are determined. Thereby, several resolution refinements are performed via iterative simulating until mesh-independent computations are reached.

3.4 System Integration into *MoDiSim*

A patient-specific simulation system has been developed to automatically simulate and analyze the blood flow and the vessel wall as well as their interaction in the aorta. The primary goal thereby is to attain a numerical tool to aid the diagnosis of aortic pathologies and predict associated risks and which after all:

- operates automatically with minimal effort and interaction
- holds an expandable structure
- is optimized in terms of integrated models
- allows individual computations

These issues are determining requirements and were realized in this work. They are presented in the following sections.

3.4.1 Automation of the Modeling

Manual processing of the individual steps of the workflow chain is a time consuming and expensive task. Further, beside the time and complexity aspects, it also requires that the user is familiar with the individual application programs, their technical components and especially, not unimportant, the physical and mathematical background of the modeling. Keeping in mind that for clinical applications, the primary target user is a medical doctor, whose time should be rather concentrated on the patient and whose interaction capability with complex software components as well as physical and mathematical knowledge are limited. Therefore, besides reliability, an automation of the simulation process is necessary for the radiologist and the surgeon to save time and complexity and to reduce effort and unnecessary interaction during intervention.

Automatic processing with individual awareness in terms of geometry and conditions is a prerequisite for performing fast, accurate and realistic finite-element computations of the hemodynamics and the elastomechanics in the arteries and is therefore included in this work. The automation is realized via integration of all individual modeling steps into a single simulation system to facilitate the interaction efficiency and usability. Strategy for dealing with complex geometries depends on time available, desired quality and accuracy [Gam06]. The automatic approach developed in this work has a trade-off between computational cost and complexity, mesh size and accuracy, quality and physics, with minimal interaction and processing effort.

3.4.2 The MoDiSim Simulation System

The MoDiSim system encloses the whole process for the generation of stable patient-specific simulation models. It allows automatic processing of the individual steps of the simulation workflow. All algorithms and approaches related to each individual step are integrated into an independent component. Furthermore, the system offers a flexible simulation environment with interfaces to the mesh generators Gambit and TGrid, to the structure mechanics FEM-program Abaqus, to the fluid dynamics FVM-program Fluent and to the FEM-program Adina, which indeed includes Fluid-Structure interaction capabilities.

All components are represented within an interface through which the user interacts with the program. Each component operates in its own dialog interface, so that it can be processed apart, independent from the other. For each application the user specifies through the interface the specific models, parameters and various conditions associated to the defined problem. The program generates then automatically the necessary input files and models, gives them to the specific programs, performs all necessary checks, and executes the simulations. A visualization part is also included within each interface, which allows to visualize and analyze various parameters of the simulation results in 3D at any instant of time.

3.4.3 Modeling Components

In total, the simulation process is integrated within the MoDiSim system into five main components (Fig.3.4). These include mesh generation, mesh processing, vessel wall simulations, blood flow simulations and blood-wall interaction simulations, respectively. Each modeling component represents an independent and individual application.

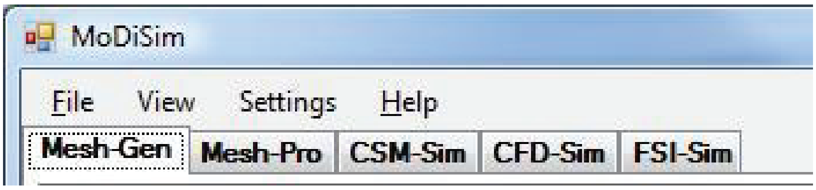

Figure 3.4: MoDiSim: Components in the main interface.

A diagram representing the system architecture and the components overview is sketched in Fig.3.5. The modeling components are described in the following:

1. **Mesh-Gen:**
   The mesh generation step is integrated into this component. *Mesh-Gen* was developed to automatically generate complex patient-specific mesh models from CT and MRI image-based segmented geometries of healthy and diseased vessels. The mesh generation includes various processes for the creation of optimized surface mesh models for the vessel wall and the interface surfaces as well as volume mesh models for the blood and the wall domains. The meshing is executed based on the mesh generators Gambit and TGrid. More details on the *Mesh-Gen* component are presented in Chap.4.

2. **Mesh-Pro:**
   This component includes the automatic processing of the generated meshes. *Mesh-Pro* consists of a conversion library for various finite mesh models (.vtk, .stl, .neu, .msh, .inp, .in) required for CSM, CFD and FSI simulations within patient-specific vessels. Further, the converted models include, depending on the modeling application, predefined FE sets necessary for the definition of individual boundary conditions. More details on the *Mesh-Pro* component is also described in Chap.4.

3. **CSM-Sim:**
   The Computational Structure Mechanics (CSM) simulation part is integrated into this component. *CSM-Sim* was developed to automatically define, perform and analyze vessel wall simulations in patient-specific aortic models. It includes continuum structure mechanics modeling, constitutive formulation of the vessel elasticity, definition of appropriate boundary conditions, integration of FEM-based discretizations and representation of the results. The computations are automatically executed based on the FEM program Abaqus. The *CSM-Sim* component is presented in details in Chap.5.

4. **CFD-Sim:**
   The Computational Fluid Dynamics (CFD) simulation part is integrated into this component. *CFD-Sim* was developed to automatically define, perform and analyze patient-specific blood flow simulations in the aorta. Hereby, continuum fluid dynamics modeling, constitutive blood behavior, various boundary conditions, FVM-based solution approaches as well as quantification of the simulations are integrated. The automatic computations are based on the FVM program Fluent. The *CFD-Sim* component is described in details in Chap.6.

5. **FSI-Sim:**
   The Fluid-Structure Interaction (FSI) modeling is integrated into this component. *CFD-Sim* and *CSM-Sim* allow separate simulations of blood flow and vessel wall assuming rigid walls and predefined loads, respectively. To achieve more realistic computations, *FSI-Sim* was developed to automatically perform, quantify and visualize patient-specific blood-vessel interaction simulations. It basically consists of two subcomponents for CFD and CSM modeling which are coupled together through their interface. The automatic coupled computations are thereby performed using the FEM program Adina. A detailed description of *FSI-Sim* is included in Chap.7.

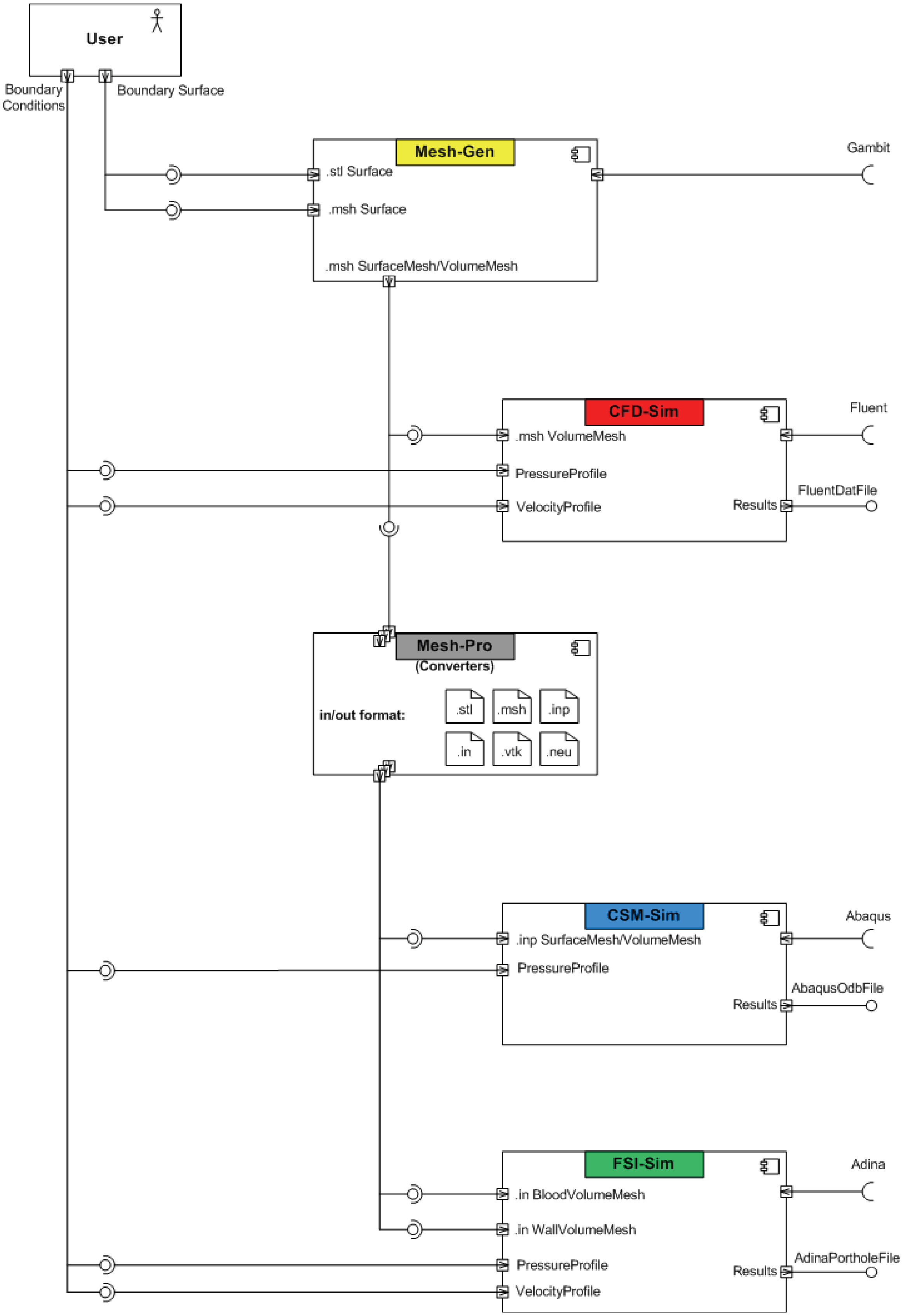
User
Boundary Conditions
Boundary Surface
Mesh-Gen
.stl Surface
.msh Surface
.msh SurfaceMesh/VolumeMesh
Gambit
CFD-Sim
.msh VolumeMesh
PressureProfile
VelocityProfile
Results
Fluent
FluentDatFile
Mesh-Pro
(Converters)
in/out format:
.stl
.msh
.inp
.in
.vtk
.neu
CSM-Sim
.inp SurfaceMesh/VolumeMesh
PressureProfile
Results
Abaqus
AbaqusOdbFile
FSI-Sim
.in BloodVolumeMesh
.in WallVolumeMesh
PressureProfile
VelocityProfile
Results
Adina
AdinaPortholeFile

Figure 3.5: MoDiSim: Components overview.

3.4.4 Expandability of the System

Further, expandability is another important factor necessary when developing systems for medical applications. The system must be extendable to match the actual needs of the user. Thanks to its flexible structure, the MoDiSim system developed in this work can be easily extended to include modeling of various vessel parts, new pathologies, surrounding organs or implantable endovascular devices. This can be achieved via integration of further components, sub-components or simply new objects within the existing system modules. Examples would be for instance the integration of new physical models to simulate different vessels, dissections and stenoses, intraluminal thrombos or even implanted stents and stent-grafts. In this case, the mesh generation and conversion steps can be extended as well to match the new modeling aspects.

3.4.5 Optimization of the Models

In the next step, the components of the process chain were further developed and the individual elements were optimized. Therefore, the effect of appropriate physical models on the patient-specific modeling were investigated. Thereby, the effects of various blood viscosity and flow turbulence on the hemodynamics, the effects of static and dynamic simulations, of linear and nonlinear elasticity, of various wall thicknesses and of stent-implantation on the biomechanics were evaluated. Also, various numerical methods were integrated to ensure stable solutions and optimized parameters enhancing the convergence course were determined. Since the stability of the computations is significantly influenced by the choice of the mesh model and its cells decomposition, the effects of various mesh configurations on the convergence of the simulations were also investigated. Thereby, universal mesh parameters for aortic geometries that ensure numerical stability were also extracted based on mesh refinement analysis. Furthermore, numerical tools were developed for the acquisition of accurate boundary conditions. This includes the derivation and the implementation of special flow and pressure conditions based on physical and physiological laws.

3.4.6 Individualization of the Simulations

Individual-awareness in terms of geometry and conditions as well as improved physical properties presents another essential aspect. Individualization is demonstrated by allowing the simulation of different individual applications: different patient geometries, different vessel regions and different pathological states.

The system independency, also in terms of the imaging source, can be represented as follow:

- **CT- and MRI- based images:**
  The models originate from either CT or MRI scans, making the system valid for both imaging techniques. In fact, this is obvious, since the key difference lies in the segmentation step. And as long as the segmented 3D model is available, whether it originates from CT or MRI images, the remaining steps of the simulation workflow can be processed in the same way.

- **Abdominal and thoracic aortas:**
  Further, both abdominal and thoracic parts of the aorta are presented. The modeling was made possible through the integration of various associated physical models and by ensuring that the mesh generation and conversion steps are independent on the shape of the 3D geometry. Six abdominal and one thoracic aortas are processed within this work. The thoracic model was simulated indeed in a post stent-graft implantation state and the effects of the stent-graft design on the elastomechanics and on the hemodynamics were evaluated.

- **Healthy and diseased, human and porcine aortas:**
  Simulation independency in terms of the patient and in terms of the shape of the disease is presented by modeling healthy and diseased as well as human and porcine aortas. This was mainly achieved through the integration of various constitutive material models for the blood and the wall with specific appropriate parameters. Four healthy and three diseased aortas were modeled. Four of the seven models originate from human and three from porcine aortas.

3.5 Processed 3D Aortic Models

In total, ten individual simulations were processed within the MoDiSim system. These arise from seven subject-specific, abdominal and thoracic, healthy and diseased, human and porcine aortic models. The individual geometries originate from morphological data derived from CT or MRI scans. A total number of slices n_s was acquired to reconstruct an aortic model from about the renal arteries to the aortic bifurcation for the abdominal part, and from above the aortic valve down to the renal arteries for the thoracic part. The 2D image size was $x_i * y_i$ mm^2 and the slice thickness was d_s mm, resulting in a voxel size of $x_v * y_v * z_v$ mm^3 at a resolution of $x_p * y_p$ pixels.

All models information are summarized in Tab.3.1, including number of slices, image size, slice thickness, image resolution and voxel size.

Table 3.1: Summary of all processed models.

Model	n_s	$x_i * y_i$	d_s	$x_p * y_p$	$x_v * y_v * z_v$	**Origin**
CT-AA	210	128*128	1.0	512*512	0.25*0.25*1.0	Human
CT-AAA	109	256*256	3.0	512*512	0.50*0.50*3.0	Human
CT-TAA	210	128*128	1.0	512*512	0.25*0.25*1.0	Human
MR-AAA	41	471*353	7.5	256*192	1.84*1.84*7.5	Human
4D-CT-P1	182	294*294	0.9	512*512	0.57*0.57*0.9	Porcine
4D-CT-P2	275	77*77	0.9	512*512	0.15*0.15*0.9	Porcine
4D-CT-P3	222	102*102	1.0	512*512	0.20*0.20*1.0	Porcine

All three-dimensional geometrical models are accurately reconstructed via segmentation and preprocessing as described in Sec.3.2. For CT-AAA, MR-AAA and CT-TAA the intraluminal thrombus (ILT) and the stent were additionally included. The patient-specific segmentation, the extraction of the 3D geometrical models and the preprocessing of the boundary surfaces prior to meshing are shown in Fig.3.7 to Fig.3.12.

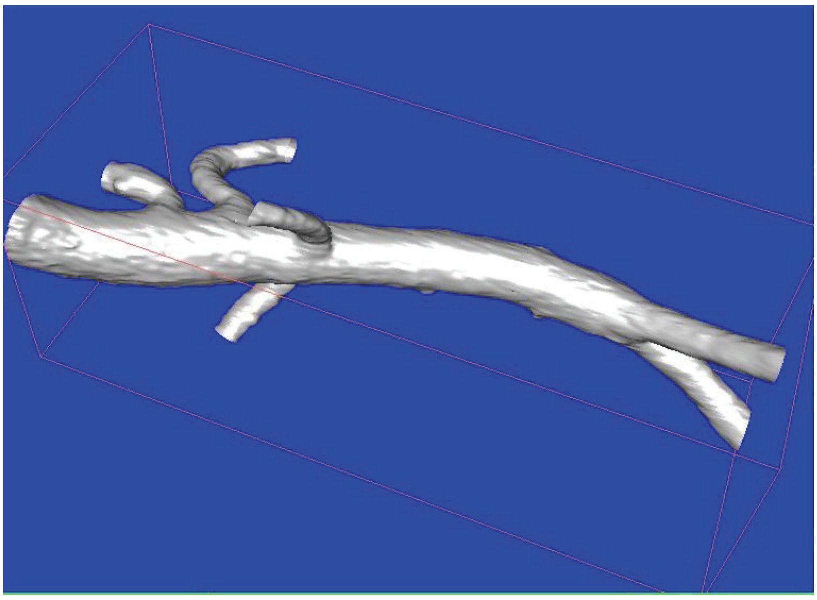

Figure 3.6: CT-AA: Patient CT-based Abdominal Aorta.

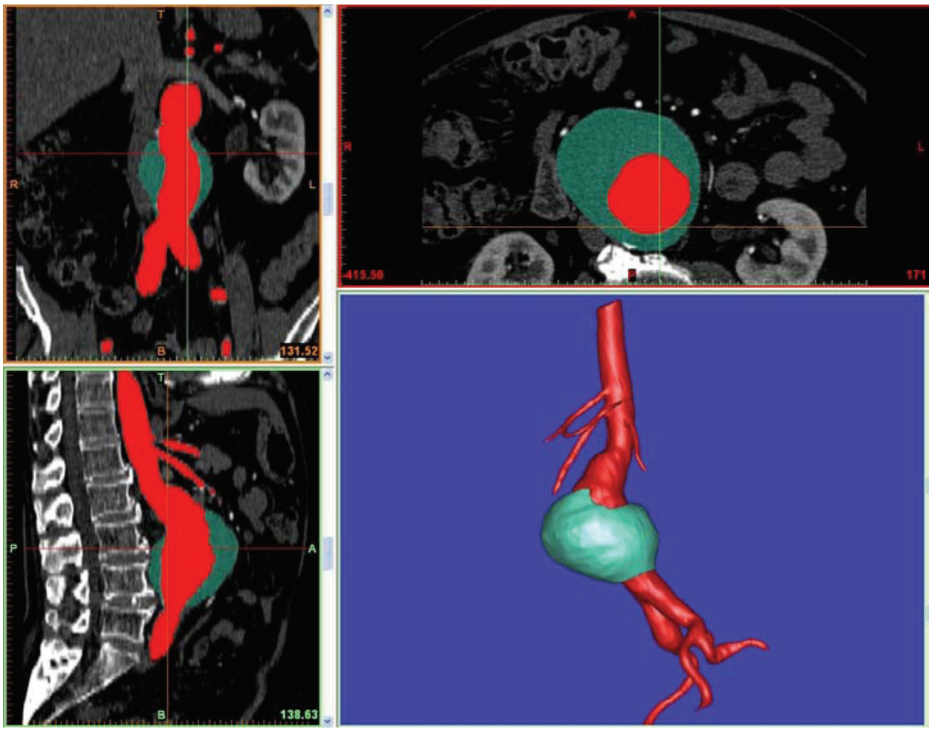
T
R
L
B
131.52
A
R
L
-415.50
171
T
P
A
B
138.63

Figure 3.7: CT-AAA: Patient CT-based Abdominal Aortic Aneurysm.

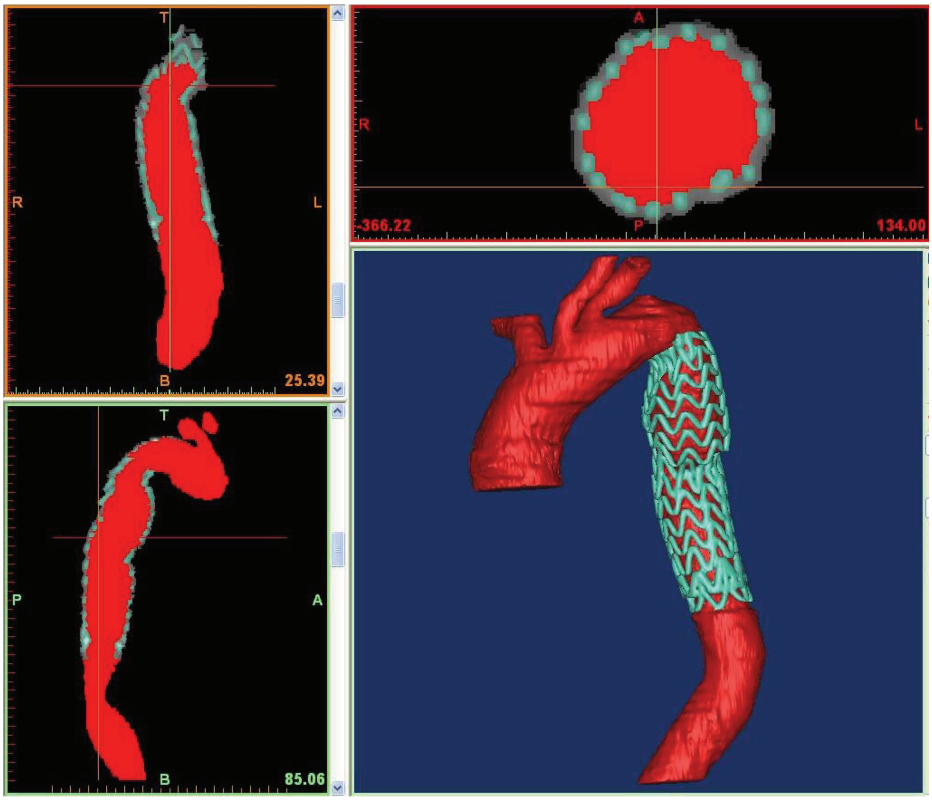
T
R
L
B
25.39
A
R
L
-366.22
P
134.00
T
P
A
B
85.06

Figure 3.8: CT-TAA: Patient CT-based Thoracic Aortic Aneurysm.

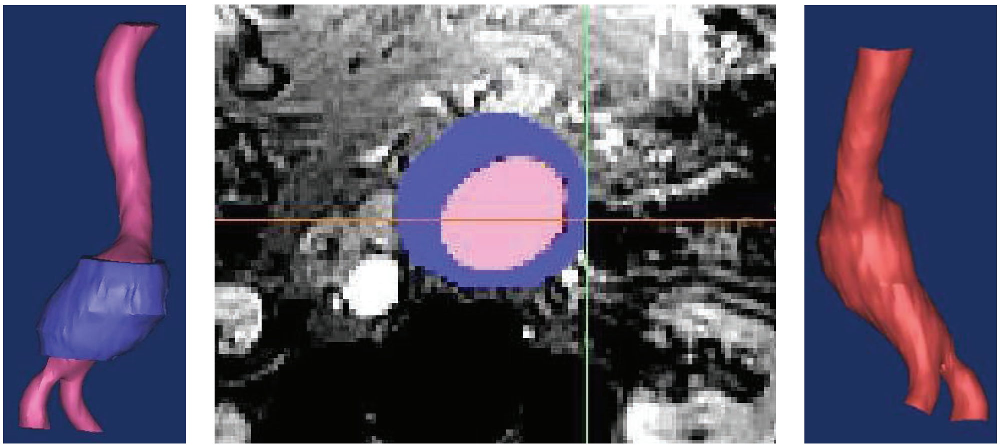

Figure 3.9: MR-AAA: Patient MR-based Abdominal Aortic Aneurysm.

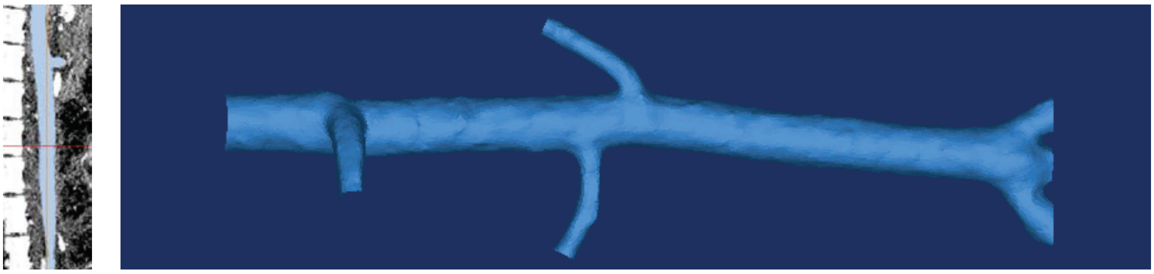

Figure 3.10: 4D-CT-P1: Porcine1 4D-CT-based Abdominal Aorta.

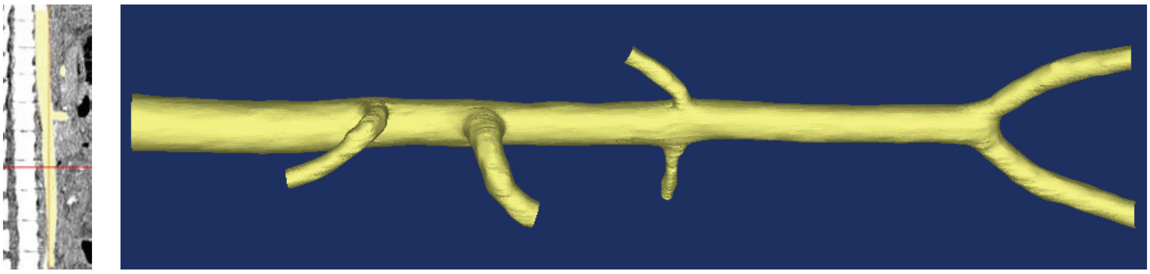

Figure 3.11: 4D-CT-P2: Porcine2 4D-CT-based Abdominal Aorta.

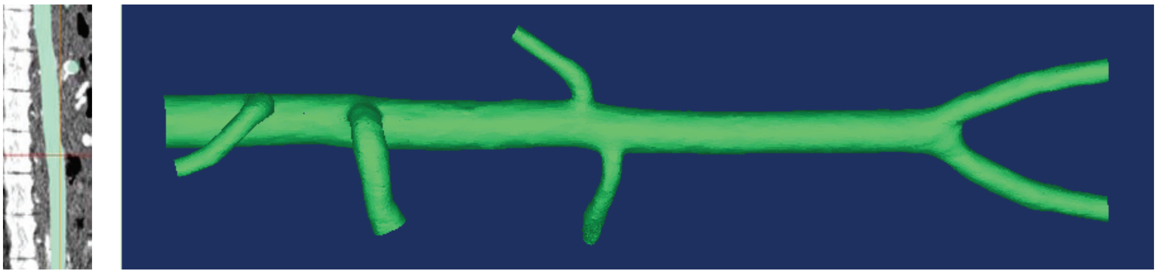

Figure 3.12: 4D-CT-P3: Porcine3 4D-CT-based Abdominal Aorta.

3.6 Summary

The aim of this chapter was to present the simulation process developed in this work for patient-specific and image-based blood flow and vessel wall modeling in the aorta. First, the procedural approach and the modeling requirements were illustrated. Then, the building of the process chain required for the computations was briefly described. The workflow consists of fine segmentation of the patient data, extraction and processing of the 3D geometrical model, generation of high-quality controlled surface and volume meshes, definition of appropriate physical models, setting of realistic boundary conditions, numerical computations using accurate mathematical solvers and finally evaluation of the simulations. Then, aspects involving the numerical stability essential for reliable computations were presented. Further, the integration of the individual steps into MoDiSim including automation of the process, expandability of the system, optimization and the individualization of the simulations, indispensable for a clinical implementation of such a patient-specific system, were described. The five components of the MoDiSim system were also briefly presented and a more detailed description will proceed in the next four chapters. Chap.4 will include the mesh generation and processing steps. While Chap.5, Chap.6 and Chap.7 will include the CSM, CFD and FSI modeling parts, respectively. Finally, the patient-specific aortic models processed in this work were presented at the end of this chapter.

Chapter 4

Mesh Generation & Processing

4.1 Introduction: Meshing Requirements

Numerical simulations of the vessel wall, the blood flow and the blood-wall interaction require exact patient-specific mesh models to be generated. Further, depending on the application, different processing techniques of the meshes have to be provided. The obtained boundary surfaces of all models presented in Sec.3.5 do not yet guarantee the stability of the simulations. Generating high-quality meshes that lead to stable patient-specific simulations is essential and must be therefore included within the mesh generation process. A poor quality mesh can lead to unstable and inaccurate solutions. Also, since timesteps generally depend on the mesh element type, size and quality, a bad mesh may slow down or even freeze convergence. Hence, while generating mesh models to meet the requisite of the simulations, it is important to keep the following in mind:

$$\textbf{High-Quality Meshes} \Longleftrightarrow \textbf{Stability} \Longleftrightarrow \textbf{Accuracy and Convergence}$$

Assigning and checking mesh quality metrics, integrating mesh control functions, investigating mesh independency, formulating appropriate mesh generation approaches, obtaining good mesh results as well as automating the mesh generation process including processing of individual FE models represent the core of patient-specific meshing requirements and were therefore conducted in this work. Based on these issues, the demands for reliable and stable individual blood flow and vessel wall simulations can be fullfilled. These essential aspects will be described in details in the next sections of this chapter.

4.2 Mesh Quality

Small local variations in mesh size between adjacent cells and gradual growth in mesh size or direction are, amongst others, characteristics of a good mesh. While smoothing may improve the overall quality by adjusting the node locations within the mesh, it should be handled with caution when applied to patient-specific models. Considering the fact that smoothing may indeed become an extensive process when dealing with complex geometries.

4.2.1 Quality Checking

A high-quality three-dimensional grid must be free of high-skewed elements. The quality of surface and volume mesh models required for stable simulations may be checked based on mesh quality metrics. To verify the quality of a mesh model, the quality range of each generated mesh element should be examined. High-quality surface and volume meshes required for the simulations must be generated so that tolerant spacing attributes are obtained and the quality ranges of the metric parameters (see below Q_{EAS} and Q_{ESS}) do not exceed certain critical average values. Otherwise, high-skewed elements must be optimized and large spacing variations between adjacent cells minimized. This is achieved through an improved remeshing of the domain and readjustment of the mesh parameters. There exist several methods to assign and check the mesh quality [Gam06]: size-based such as the *Size Change* parameter, ratio-based such as the *Aspect Ratio*, the *Diagonal Ratio* and the *Edge Ratio*, or skew-based such as the *EquiAngle Skew*, the *EquiSize Skew* and the *MidAngle Skew* metrics.

4.2.2 Quality Metrics

The most important three metrics used in this work for the specification of the mesh quality are based on the EquiAngle Skew Q_{EAS}, on the EquiSize Skew Q_{ESS} and on the Size Change parameters. These metrics are shortly discussed in the following:

- **Size Change:**
  The Size Change metric parameter specifies the maximum ratio of the size of an element relative to its neighbors. It only applies to three-dimensional elements and may be described by:

$$\boldsymbol{Q}_{SC} = \max\left[\boldsymbol{r}_1, \boldsymbol{r}_2, ...\boldsymbol{r}_n\right] \tag{4.1}$$

where $\boldsymbol{r}_i$ being the individual ratios of area or volume of an element i relative to its neighboring elements and n is the total number of elements present in the mesh. In order to compute $\boldsymbol{Q}_{SC}$, $\boldsymbol{r}_i$ is determined individually for all elements as:

$$\boldsymbol{r}_i = \frac{\boldsymbol{S}_i}{\boldsymbol{S}_j} \tag{4.2}$$

where $\boldsymbol{S}_i$ and $\boldsymbol{S}_j$ are the area or volume of the element i and its neighbor element j, respectively. $\boldsymbol{Q}_{SC}$= 1 describes an element surrounded by neighbors for which the areas or volumes have exactly the same dimensions, as found for instance in a uniform mesh.

- **EquiAngle Skew:**
  The EquiAngle Skew parameter is a normalized measure of skewness. It may be expressed as:

  $$\boldsymbol{Q}_{EAS} = \max\left[\frac{\boldsymbol{\theta}_{max} - \boldsymbol{\theta}_e}{180 - \boldsymbol{\theta}_e}, \frac{\boldsymbol{\theta}_e - \boldsymbol{\theta}_{min}}{\boldsymbol{\theta}_e}\right] \tag{4.3}$$

  where $\boldsymbol{\theta}_{min}$ and $\boldsymbol{\theta}_{max}$ being the smallest and largest angles in the cell respectively, and $\boldsymbol{\theta}_e$ being the angle for an equiangular element that corresponds to a similar form. $\boldsymbol{\theta}_e$ equals 60° for triangular and tetrahedral cells and 90° for quadratic and hexahedral cells. $\boldsymbol{Q}_{EAS}$= 0 describes a perfectly orthogonal mesh element, while $\boldsymbol{Q}_{EAS}$= 1 describes a rather degenerate, poorly shaped element. Per definition, a high-quality 3D mesh is related to average Q_{EAS} values of 0.4. All meshes generated in this work do not exceed this average value and thus conform to the definition of the high-quality mesh range.

- **EquiSize Skew:**
  The EquiSize Skew parameter is another measure of skewness based on the size of the element. It is defined by:

  $$\boldsymbol{Q}_{ESS} = \frac{\boldsymbol{S}_e - \boldsymbol{S}}{\boldsymbol{S}_e} \tag{4.4}$$

  where $\boldsymbol{S}$ is the area in 2D or the volume in 3D of the element of interest and $\boldsymbol{S}_e$ is the maximum (2D) area or (3D) volume of an equilateral cell which circumscribing radius is identical to that of the meshed element [Gam06]. Similar to the EquiAngle Skew parameter, $\boldsymbol{Q}_{ESS}$= 0 describes a perfectly equilateral element, $\boldsymbol{Q}_{ESS}$= 1 describes a rather degenerate mesh, while average $\boldsymbol{Q}_{ESS}$= 0.4 defines a high-quality 3D mesh. Also the Q_{ESS} values of all meshes generated in this work conform to the definition of high-quality meshes with average values less than 0.4.

4.3 Mesh Control Functions

Enhanced quality may be obtained by controlling and optimizing the surface and the volume meshing. Mesh optimization is included by integrating mesh control functions into the mesh generation process. Mesh control functions allow to control the properties and the configuration of the mesh in specific regions and proximal to objects to which they are attached. Three control functions adapted from Gambit are included in this work: *curvature size*, *meshed size* and *boundary layers* functions. Size functions prescribe the characteristics of the mesh elements in terms of minimum or maximum size, adjacent angles and total number. Boundary layers affect the size and type of mesh elements as well as the spacing between mesh nodes within specific defined mesh patterns.

4.3.1 Boundary Layers

Of particular importance are boundary layers, used to control the topology of the mesh in specific locations. Thanks to their geometrical topology of mapped prisms, boundary layers prevent tetrahedrons from standing with one tip on the wall, which badly affects the computation of wall fluxes. Further, by defining row sections directly attached to a particular face and by prescribing the spacing of the mesh nodes between these rows, the accuracy of information to be computed around this face can be controlled. Boundary layers can be for instance attached to the boundary surface of the vessel wall to allow for an accurate computations of parameters near the wall. Shear stresses, derived from the gradients of the velocity vectors, are characterized to be larger in the region immediately adjacent to the vessel wall than in the lumen domain. By generating small cells at locations close to the wall and decreasing the mesh density in direction toward the inside of the lumen mesh, these velocity gradients can be better resolved.

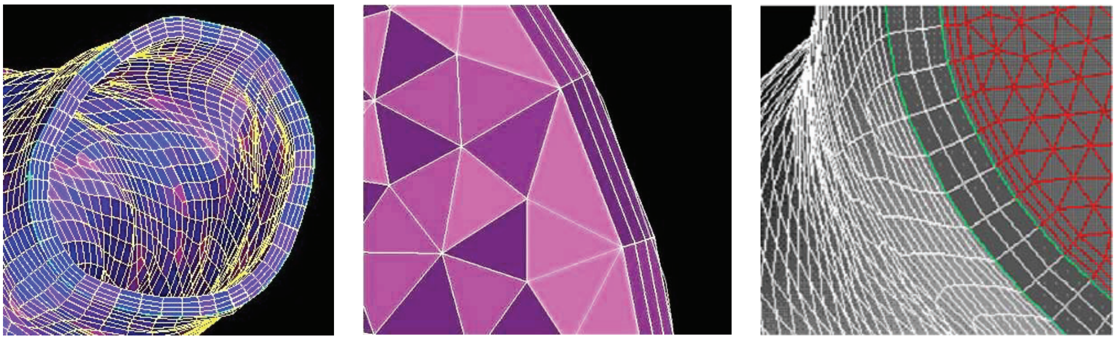
(a) Wall BL (b) Blood BL (c) Wall and blood BL

Figure 4.1: Applied boundary layers (BL).

Boundary layers are characterized by the attachment elements defining their location, by the type of the algorithm determining their shape and by the dimension of the parameters defining their characteristics. Attachment elements include the edge or face to which the boundary layer is attached. Further, if multiple directions are possible, for instance when the boundary layer is attached to a face shared by more than one volume, the corresponding volume defining the boundary layer direction must be also specified. The algorithm type determines the approach describing the general behavior of the boundary layer. The defined type of the algorithm together with the specified dimension of the parameters are applied along the boundaries of the specified attachment element in order to create the boundary layers. The dimensions of the boundary layer are determined through parameters that define its characteristics. These include the number of boundary layer rows, the height of the first row of mesh elements, the growth factor and the total number of rows. The growth factor specifies the height of each succeeding row of elements, while the total number of rows determines the depth of the boundary layer. The parameters to be specified vary according to the algorithm type used.

Boundary Layers Algorithms

Three boundary layers algorithms are provided in Gambit to define the height of the first row elements and to compute the size of the succeeding rows. In the *uniform algorithm* (Fig.4.2.a) each row within the boundary layer domain exhibits a uniform height. Thereby, the elements in the first row are first assigned a uniform size $\boldsymbol{a}$ across the attachment element. The first row size of the boundary layer is defined by the distance between its attachment element and the first row of mesh nodes within the boundary layer, so that the prism height equals the cell height. Then, a constant growth factor $\boldsymbol{G}$ representing the ratio between the heights of two successive rows is used to compute the size of the next row elements. As a result, since the growth factor is constant, all succeeding rows will also be assigned a uniform height. The uniform algorithm is simply defined by $\boldsymbol{G} = \boldsymbol{b}/\boldsymbol{a}$ [Gam06], where $\boldsymbol{b}$ is the distance between the first and second rows. Based on this algorithm, the height of any row may be computed as the product of the growth factor with the size of the previous row in the boundary layer. Further, based on the first row $\boldsymbol{a}$, on the growth factor $\boldsymbol{G}$ and on the row value $\boldsymbol{r}$ specifying the total number of rows to be included in the boundary layer, the total depth $\boldsymbol{D}$ of the boundary layer may be computed as:

$$\boldsymbol{D} = \boldsymbol{a}\left(1 + \boldsymbol{G} + \cdots + \boldsymbol{G}^{r-1}\right) = \boldsymbol{a}.\sum_{j=0}^{r-1} \boldsymbol{G}^{j} \tag{4.5}$$

The uniform algorithm has been implemented in this work through *journal* files and may be automatically executed by specifying the related parameters.

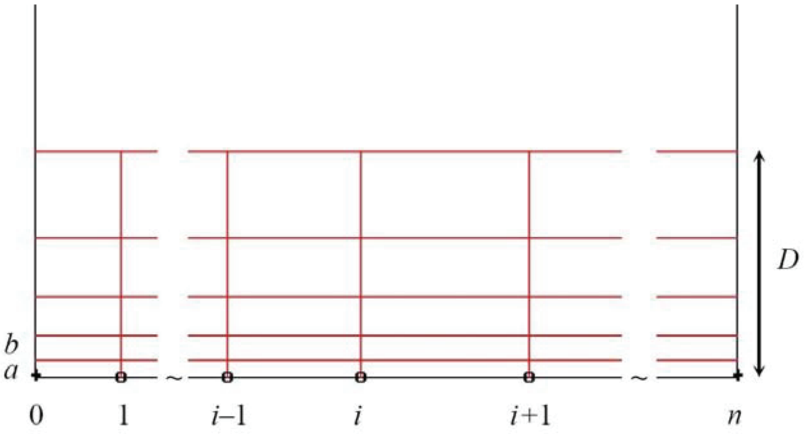

Figure 4.2: Boundary layers uniform algorithm [Gam06].

Alternatively, the *aspect ratio first* and the *aspect ratio last* algorithms may also be used to compute the shape of the boundary layer. In the aspect ratio first algorithm, the first row size varies in proportion to the edge mesh interval lengths. For the aspect ratio last algorithm, a uniform height is first assigned to all first-row elements, while individual growth factors $\boldsymbol{G}_i$ are used. $\boldsymbol{G}_i$ vary across the boundary layer in proportion to the edge mesh interval widths. A detailed description of the algorithms may be found in [Gam06].

4.3.2 Surface Size Function

Surface size functions are used to control the growth of mesh intervals and the size of elements on a 2D surface. Curvature size functions implemented in this work are surface size functions used to control the mesh size while accounting for the curvature of the wall surface. This allows, based on a curvature angle and a growth factor, to generate fine cells at sites where the curvature of the wall is high and larger ones at sites where the wall surface is rather flat. By specifying a maximum angle ϕ, a curvature size function allows to limit the angle θ between the normals in outward direction of any two adjacent mesh elements located proximal to the highly curved source surface. Thereby, the mesh characteristics of geometric configurations including highly curved surfaces can be directly influenced. The size is computed such that:

$$size = 2\mathbf{r}_c \sin\left(\phi/2\right) \tag{4.6}$$

with

$$\mathbf{r}_c = \frac{\mathrm{h}/2}{\sqrt{\left(1-\cos(\theta)\right)/2}} \quad \text{and} \quad \cos(\theta) = \frac{\mathrm{N}_A \bullet \mathrm{N}_B}{\|\mathrm{N}_A\| \bullet \|\mathrm{N}_B\|} \tag{4.7}$$

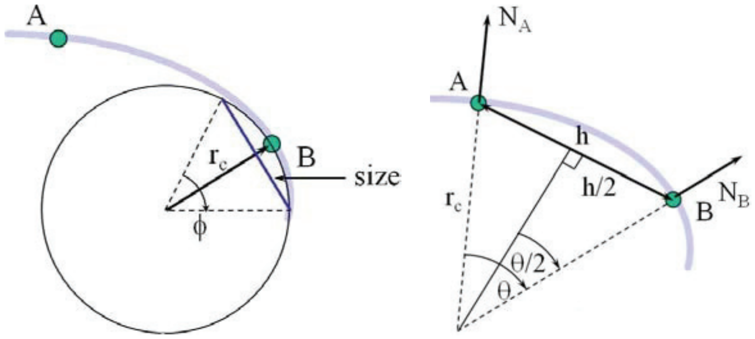

Figure 4.3: Curvature size function definition.

Patient-specific geometries include uneven curved surfaces. If meshed using a specified fixed mesh element size, the resulting mesh would represent only a coarse approximation of the geometry shape. As a result, numerical simulations based on the coarse mesh cannot provide detailed information for computed parameters at specific locations. While uniformly reducing the specified mesh size would allow to create finer elements, it would also significantly increase the overall number of mesh elements in the entire configuration. Creating a curvature size function allows better approximating the geometry without reducing the overall mesh size. Thereby, mesh refinement is applied only in locations of high curvatures such that the mesh sizes satisfy to the requirements of the curvature size function.

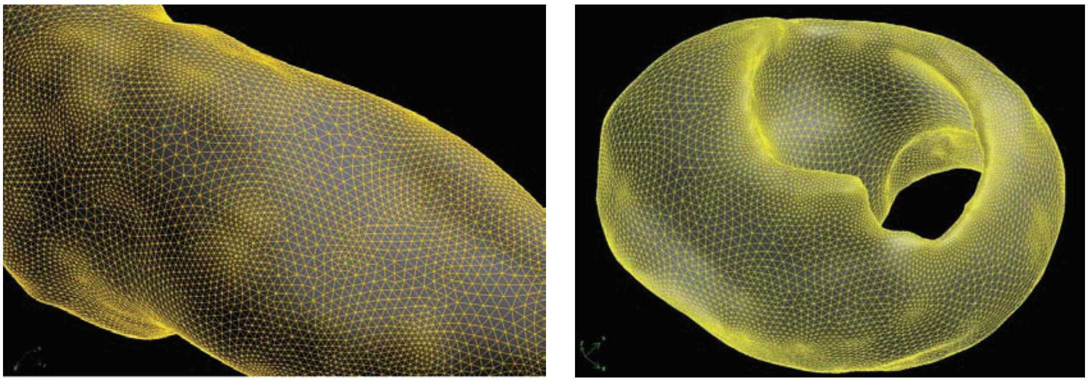

Figure 4.4: Curvature size function effects on the wall and thrombus.

Curvature size functions are characterized by the source and attachment elements defining the geometry and by the dimension of the parameters specifying the exact characteristics. The curvature size function parameters are the maximum allowable angle between the normals of adjacent mesh elements, the growth rate specifying the increasing in the edge size of the next elements and the maximum and minimum sizes of the elements specifying the maximum and minimum allowable edge lengths for the attachments, respectively.

4.3.3 Volume Size Function

An unsettled fine mesh may quickly increase the overall mesh size resulting in unnecessary expensive computational cost. Meshed size functions are 3D volume size function which allow to control the mesh distribution by confining smaller cells only to locations where they are needed. Hence, they allow to limit the mesh size over particular regions. The mesh growth is controlled from meshed sources into attachment regions. In order to reduce the overall mesh size inside the blood region, a meshed size function can be applied to control the propagation of the mesh from the meshed wall surfaces into the lumen volume. Meshed size functions control the maximum mesh size as a function of distance from a given source region [Gam06]. Thereby, non-constant start sizes are defined as to vary with location on the source according to the sizes of its existing mesh elements. Obviously, in order to apply a meshed size function, the source elements must be meshed prior to meshing the attachment region. As a result, smaller first row mesh cells are obtained at locations adjacent to fine source mesh elements. This in turn affects the growth of the mesh as well as the total number of elements created in the volume attachment region.

Similar to curvature size functions, meshed size functions require the specification of a premeshed source and attachment elements defining the shape and location of the application regions as well as the specification of the dimension of the parameters defining the mesh characteristics. The meshed size function parameters are the growth rate specifying the increase in mesh size rising from the source region and the maximum size defining the maximum allowable mesh edge length within the attachment region.

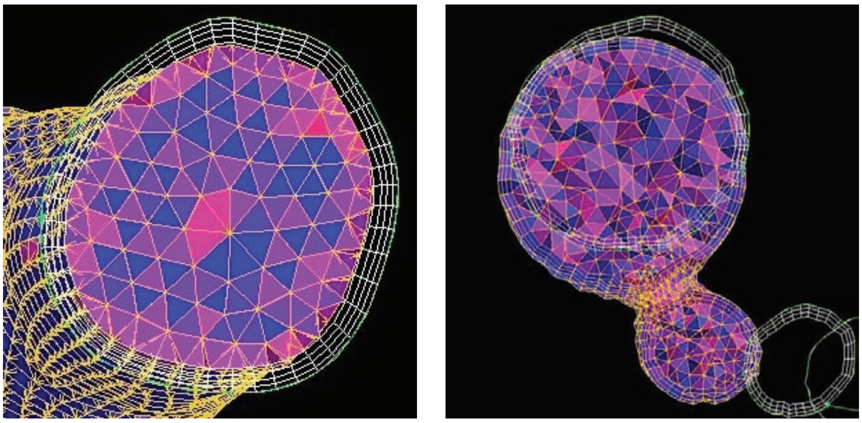
(a) At the inlet (b) Along a z-slice

Figure 4.5: Meshed size function effects within the blood.

4.4 Mesh Independency

While the stability of the simulations in terms of convergence is influenced by the type and the form of the mesh elements, the approximation and thus the stability in terms of accuracy is significantly affected by the size of the meshes. Accuracy is ensured by generating results that are independent on the mesh configuration of the model. A computational grid analysis was therefore performed in order to:

- Investigate the effects of different mesh configurations on the hemodynamics parameters of the blood flow
- Determine the mesh properties that result in accurate stable simulations
- Acquire *universal* optimized mesh parameters for the control functions that lead to mesh-independent results for individual aortic geometries.

4.4.1 Methods

Iterative simulating based on several resolution refinements is performed until mesh-independent computations are reached. The blood flow is simulated using two kinds of geometries: an idealized cylindrical and a CT-based patient-specific aortic aneurysm geometry. The velocity and the WSS distributions are computed by solving the system of partial differential equations corresponding to the continuity and momentum equations in the luminal region. Finally, the effects of the different mesh configurations on the velocity and WSS distributions within the geometries are analyzed and evaluated. The CFD simulations are based on the finite volume method in Fluent. Details on the CFD simulations and on the FVM approach are described in Chap.6.

Idealized Geometry

In order to get a rough approximation of the desired mesh parameters, an idealized geometry was first considered. The resulting parameters are then used as a first estimation for the real geometry. The idealized geometry consists of a cylinder of radius 1 cm and a height of 30 cm (Fig.4.7).
Seven mesh configurations are generated varying the size of the first layer from 0.10 % to 2.00 % of the diameter. Four layers are defined for each mesh configuration with a growth factor of 1.2. The wall surface and the rest of the volume are meshed with equally sized (0.1 cm) triangular and tetrahedral elements, respectively. The CFD simulations are carried out considering a steady laminar blood flow with a constant inlet velocity of 0.5 ms^{-1}.

Patient-Specific Geometry

For the individual blood flow computations, the simulation workflow described in Chap.3 and developed for CFD simulations is applied. The patient-specific geometry is based on a CT scan of an abdominal aortic aneurysm (CT-AAA model), consisting of the lumen region and the arterial wall.
Four different mesh configurations are used. The wall surface of all models is the same, meshed using triangular elements. The surface is thereby based on a size function accounting for the curvature at the wall, defined with a curvature angle equal 5°. This was defined as a first approximation based on mesh independency in terms of wall stresses from CSM simulations. On the other hand, varying volume meshes between the four models have been used. The propagation of the mesh from the wall surface into the volume is controlled using a meshed size function. The distribution of the fluid cell size near the wall is controlled using a boundary layers (BL) control function. The BL are defined such that the fluid domain contains small cells at locations close to the wall, and which increase in direction toward the inside of the fluid. The meshes in the boundary domain consist of three layers of wedge shaped finite elements. The size of the first BL used for the four configurations is 0.50, 0.75, 1.00 and 1.50 % of the inlet diameter (2 cm), and the growth factor is defined as 1.2. Finally, a whole cardiac cycle of period T= 0.85 s was modelled and the timestep size was successively reduced until timestep-independent computations were obtained.

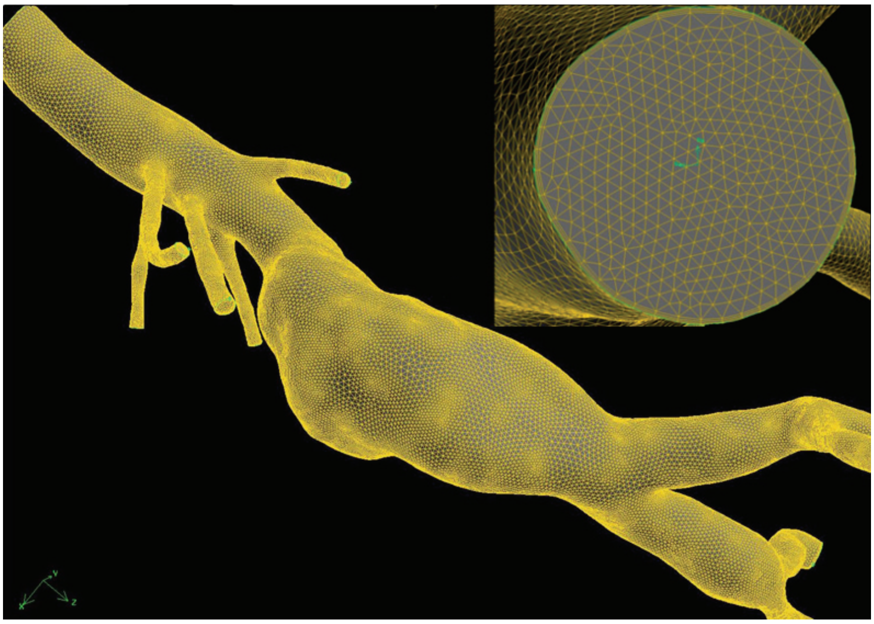

Figure 4.6: The finest AAA wall surface mesh model based on the curvature size function, and the inlet of the AAA with the finite boundary layers and volume mesh elements.

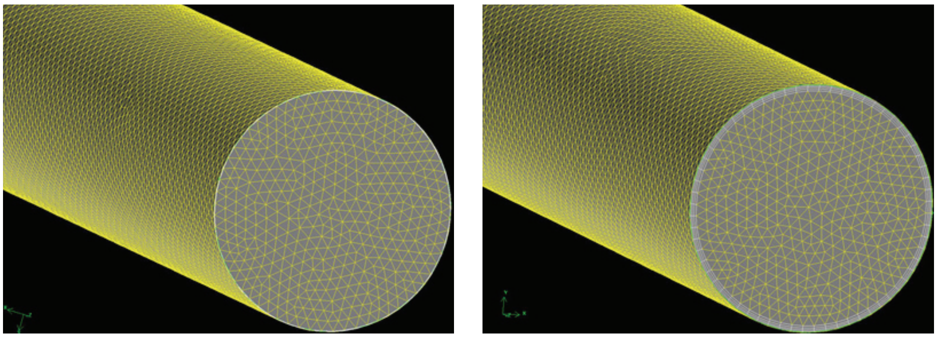

(a) 0.1 % first layer size (b) 0.5 % first layer size

Figure 4.7: Idealized mesh models with four BL of various first layer size.

4.4.2 Results

Numerical results on the effects of the different mesh resolution on the flow patterns within the idealized cylindrical and the patient-specific aortic aneurysm geometries are presented, and the stability of the CFD simulations is evaluated. Provided that the primary physical variables of interest for arterial modeling are flow-based quantities, results on the effects of the boundary layers configurations are therefore examined in terms of velocity and WSS distributions. Mesh-independency is then assessed by comparing and evaluating both the computed velocities and the computed wall shear stresses. Based on the results, automatic generation of patient-specific meshes that lead to stable simulations could be made possible (Sec.4.8).

Idealized Geometry

The velocity distribution within the plane z= 29 cm and the WSS distributions between z= 20 cm and z= 30 cm along the cylinder are evaluated for all seven mesh configurations. The relative error of the mean velocity in a portion (-1.0 cm < x < -0.7 cm) within the plane z= 29 cm decreased with mesh-refinement from 6.3 % at transition of the BL configuration from 0.10 to 2.00 % of the inlet diameter, to 2.1 % at transition from 0.10 to 0.25 %. In this domain, the distribution of the tangential velocity points near the wall is homogeneous and presents the best interpolation scheme. As a result, the error by the derivation of the gradients (WSS) is minimized. The relative error of the mean-average WSS decreased from 49.3 % at transition from 0.10 to 2.00 %, to 7.7 % at transition from 0.10 to 0.25 %. The obtained parameters for the boundary layers function of an idealized geometry with an inlet diameter and a length equal to 2 cm and 30 cm respectively, are presented in Tab.4.1.

Table 4.1: Results of the velocity (V) and WSS computations and the corresponding relative errors (%) obtained at transitions between the different mesh configurations within the idealized models.

% of diameter size of first BL	**WSS (Pa)** 29.0<z<30.0	**WSS (Pa)** 20.0<z<30.0	**V (m/s)** z=29.0	**V* (m/s)** z=29.0
0.10	1.68803	1.72217	0.49931	0.31900
0.25	1.54509	1.58993	0.49931	0.32581
0.50	1.34474	1.37504	0.49912	0.33419
0.75	1.19247	1.21731	0.49923	0.33665
1.00	1.10429	1.07663	0.49919	0.32941
1.50	0.92911	0.96452	0.49907	0.33716
2.00	0.91686	0.87322	0.49917	0.29884
Transition from	**Rel. Error**	**Rel. Error**	**Rel. Error**	**Rel. Error**
0.10 to 0.25	8.468	7.679	0.001	2.135
0.10 to 0.50	20.337	20.156	0.039	4.761
0.10 to 0.75	29.357	29.315	0.017	5.532
0.10 to 1.00	34.581	37.484	0.025	3.263
0.10 to 1.50	44.959	43.994	0.048	5.693
0.10 to 2.00	45.684	49.296	0.028	6.320

V*: Velocity at z= 29 cm for the portion -1.0 cm < x < -0.7 cm

Patient-Specific Geometry

The computations for the patient-specific aortic model are carried out along the whole cardiac cycle. Timestep independent simulations are reached using 1000 equally spaced timesteps. The velocity distribution in the lumen region within a portion -3.2 cm < x < -2.7 cm of the plane z= 16.5 cm orthogonal to the flow direction, and the WSS distributions in the aneurismal region between z= 12.5 cm and z= 21.0 cm are evaluated at peak systole (t= 0.15 s) and diastole (t= 0.34 s) for all four mesh configurations. The relative error of the mean average velocity showed its minimum, 0.1 % in the systole and 2.6 % in the diastole, for the finest BL mesh configuration at transition from 0.50 to 0.75 % of the inlet diameter. As for the WSS, the minimum was also obtained for the finest mesh configuration and the relative error of the mean-average decreased from 9.7 % to 2.5 % at systole and from 17.4 % to 7.6 % in the diastole. The parameters for the boundary layers function obtained for an aortic geometry having the approximate dimensions of an inlet diameter and a length equal to 2 cm and 30 cm, respectively are presented in Tab.4.2.

Table 4.2: Results of the velocity (V), WSS computations and the corresponding relative errors obtained at transitions between the different configurations, at systole (S) and diastole (D).

% of diameter size of first BL	**WSS - S** 12.5<z<21.0	**V^+ - S** z=16.5 //	**WSS - D** -3.2<z<-2.7	**V^+ - D** z=16.5 //
0.50 (0.10 mm)	0.23596	0.04007	0.10160	0.00691
0.75 (0.15 mm)	0.24183	0.04010	0.10933	0.00709
1.00 (0.20 mm)	0.25038	0.04012	0.11437	0.00732
1.50 (0.30 mm)	0.25874	0.04058	0.11931	0.00756
Transition from	**Rel. Error**	**Rel. Error**	**Rel. Error**	**Rel. Error**
0.50 to 0.75	2.490	0.070	7.605	2.551
0.50 to 1.00	6.110	0.120	12.564	5.916
0.50 to 1.50	9.655	1.268	17.431	9.342

V^+: Velocity at z= 16.5 cm for the portion -3.2 cm < x < -2.7 cm

The results presented in Tab.4.1 and Tab.4.2 show that mesh-independency as assessed based on computed velocities is insufficient to state mesh-independency for computed wall shear stresses. This is an indication that WSS computation is much sensitive to mesh configuration than flow velocity computation. Therewith, the present grid investigation confirms a previous study of [PE01].

As for the curvature size function (cSF) and the meshed size function (mSF) parameters, they are determined such that the mesh is optimized in the sense that it does not contain high-skewed elements for all BL configurations. Therefore, the skewness parameters defined in Sec.4.2 are assigned to all mesh configurations and checked for their quality range. The parameters of the cSF and the mSF obtained from the present analysis and used later for the automation process of individual aortic geometries, are summarized in Tab.4.3.

Table 4.3: Parameters for the curvature and the meshed size functions obtained from all boundary layers mesh configurations described above within the patient-specific CT-AAA model.

	angle (°)	**growth**	**min (mm)**	**max (mm)**
cSF	5	1.2	0.3	3
mSF	-	1.1	-	3

4.5 Mesh Generation Approaches

Various mesh generation approaches have been developed allowing the generation of high-quality meshes for CSM, CFD and FSI applications. Thereby, unstructured meshes are adopted, allowing a high flexibility for the adaptation of the grid at the boundaries of the domain. Further, hybrid meshes consisting of hexahedrons, wedges, pyramids and tetrahedrons are used providing a better control for complex geometries. The mesh generation is carried out using the mesh generators Gambit and TGrid. The mesh generation processes for surface wall and interface wall meshing, for volume blood meshing and for volume wall meshing, developed and implemented in this work are described in the following sections.

4.5.1 Surface and Interface Meshing

Biomechanical simulations of the vessel wall as well as fully coupled simulations between blood and wall require the generation of surface meshes for the definition of the boundary vessel and the common interface, respectively. The process of generating individual 3D patient-specific boundary surfaces of vessel wall models is implemented into the *MeshSurface* algorithm and can be described by the following steps:

1. First, the .stl created from the segmentation step is imported and the old mesh is reset.
2. In order to describe the wall curvature, a homogeneous fine mesh that better represents the real surface of the wall is then generated and exported as a mesh file.
3. Within a new session, the created fine mesh is read, removed and a control function accounting for the curvature of the wall surface (cSF) is created. As mentioned before, the cSF allows to control the distribution of the cell size taking into account the curvature of the wall at that location.
4. Based on appropriate parameters for the defined cSF, the wall is meshed with *triangular* elements for the decoupled wall simulations and with *quadratic* elements for the interface in the fully coupled FSI simulations.
5. Rotation and translation are then applied to align the geometry with zero-coordinates at the center of the inlet of the model.
6. Finally, the resulting mesh is saved as a .dbs file and exported into a .msh surface mesh.

4.5.2 Volume Blood Meshing

Decoupled simulations of the blood flow as well as fully coupled simulations require the generation of volume meshes to represent the blood elements. The meshing process developed for the generation of 3D finite blood volume meshes is implemented into the *MeshBloodVolume* algorithm and can be described by the following steps:

1. The geometrical volume model represented by the closed surface of the fluid domain is first created by stitching the inlet, outlets and the wall faces together. The surfaces in turn are created from the edges defining their boundaries.
2. In order to control the distribution of the fluid cell size near the wall, a BL control function is defined to generate small cells proximal to the wall surface. They consist of hex-shaped or wedge-shaped finite elements, depending on the original wall surface boundary mesh type.
3. Further, to control the propagation of the mesh from the surfaces into the volume, a mSF function is defined from the wall into the fluid domain.
4. Then appropriate parameters are associated to these control functions and the volume mesh model is generated with tetrahedrons.
5. Finally, various zones are specified based on the boundary and the continuum types. The specifications include the definition of the physical characteristics of the model at its boundaries and within its domain.

4.5.3 Volume Wall Meshing

While the vessel domain for the *decoupled* wall simulations in Abaqus may be represented by 3D shell elements, hyperelastic modeling in Adina requires the generation of 3D solid elements to represent the vessel wall. Thus, for the *fully coupled* simulations, the outer wall boundary must be additionally defined beside the inner wall to create a 3D volume of the wall model. As mentioned in Sec.3.2, detection of the outer wall border is not directly possible from the CT or MRI patient images. Instead, the generation of the volume wall domain with a homogeneous thickness is achieved in two alternative ways:

- The dilated lumen from the segmentation step is used to create the volume model represented by the closed surface of the wall domain. Then, a meshed size function is defined from the inner wall into the wall volume. Finally, the 3D volume mesh model of the defined geometry is generated using tetrahedrons.

- A volume mesh model is directly generated by mapping the inner wall mesh outwards by a certain number of boundary layers of defined size. In this way, eight-node brick elements are used for the wall volume mesh domain. This approach has two advantages: First, no information about the outer wall is necessary, that is, the dilation step in the segmentation can be skiped, saving time and effort. And second, hexahedrons are more stable for nonlinear material modeling than tetrahedral elements.

The second approach was therefore implemented into the *MeshWallVolume* algorithm as the standard method for the generation of 3D volume wall mesh models.

4.6 Meshing Results

The developed meshing processes are applied to all seven subject-specific 3D models obtained from the segmentation step and summarized in Tab.4.4. This demonstrates that the implemented meshing approaches can be applied to any shape geometry independent on its origin, thus ensuring individualization. The geometrical models originating from CT- and MRI- scans of abdominal and thoracic, healthy and diseased, humans and porcine aortas were shown in Fig.3.6 to Fig.3.12. A summary of all corresponding mesh results generated in this work including the types of the applied simulation and the associated mesh is presented in Tab.4.4.

Table 4.4: Summary of all generated mesh models.

Model	Simulation Type	Mesh Type
CT-AA	CFD	Surface, Volume Blood
CT-AAA	CSM, CFD	Surface, Volume Blood
CT-TAA(+Stent)	CSM, CFD	Surface, Volume Blood
MR-AAA	CSM, FSI	Surface, Volume Blood, Volume Wall
4D-CT-P1	CSM	Surface
4D-CT-P2	FSI	Surface, Volume Blood, Volume Wall
4D-CT-P3	FSI	Surface, Volume Blood, Volume Wall

All resulting meshes showed high quality cells required for the simulations. The quality ranges of the metric parameters Q_{EAS} and Q_{ESS} for the individual cells do not exceed 0.4 for the surface meshes and 0.97 for the volume meshes. The next sections include details on the meshing results for each mesh type.

4.6.1 Surface and Interface Meshing

Obviously, for all simulation types, the first step in creating the mesh starts by generating the boundary surface of the model. Therefore, surface meshes for all the seven models had to be generated. They are defined by the wall boundary, the lumen boundary and the interface for the CSM, the CFD and the FSI applications, respectively. The surface meshes contain triangular cells when used for CSM or CFD simulations and quadratic cells if used for FSI simulations. In both cases the mesh generation is based on curvature size functions. In total, eight surface mesh models used for ten applications are generated from the seven geometrical models. A summary of these meshes including the mesh element type and size is presented in Tab.4.5. The corresponding results are shown in Fig.4.8 to Fig.4.11 and Fig.4.13.a, Fig.4.14.a and Fig.4.15.a.

Table 4.5: Summary of the generated surface mesh models.

Model	Application	Type	Size
CT-AA-SMesh	CFD	Tri	24272
CT-AAA-SMesh	CSM, CFD	Tri	99820
CT-TAA-SMesh	CSM, CFD	Tri	26106
MR-AAA-SMesh	CSM	Tri	56656
MR-AAA-IMesh	FSI	Quad	11423
4D-CT-P1-SMesh	CSM	Tri	29094
4D-CT-P2-IMesh	FSI	Quad	23953
4D-CT-P3-IMesh	FSI	Quad	21276

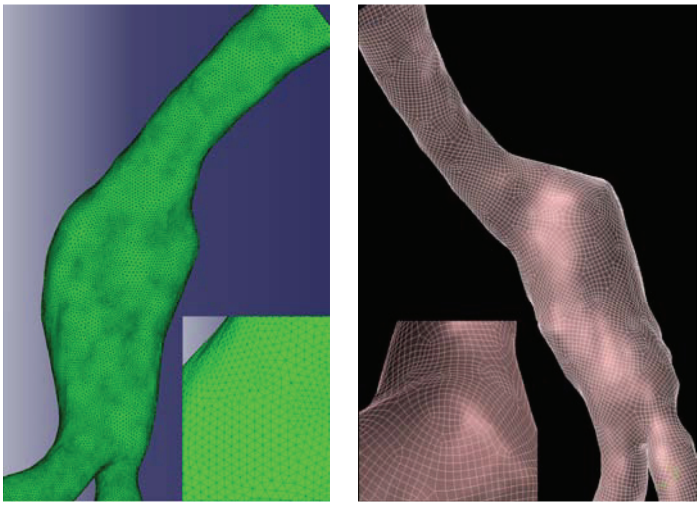
(a) MR-AAA-SMesh (b) MR-AAA-IMesh

Figure 4.8: MR-AAA: Boundary surface and interface mesh models.

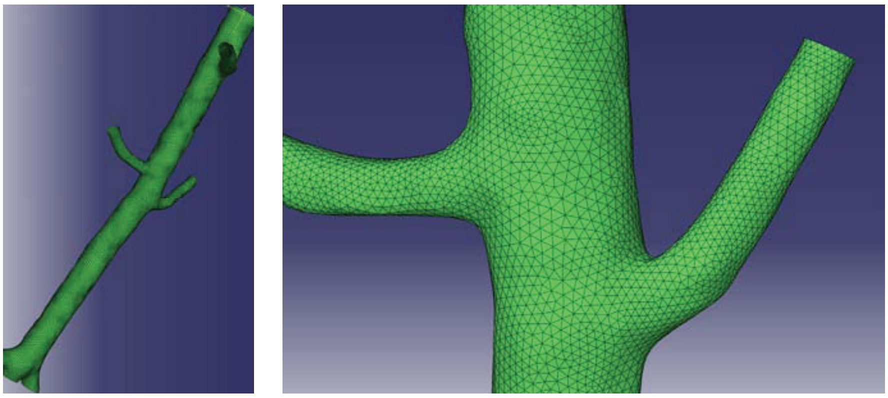

Figure 4.9: 4D-CT-P1: Wall surface mesh model (4D-CT-P1-SMesh).

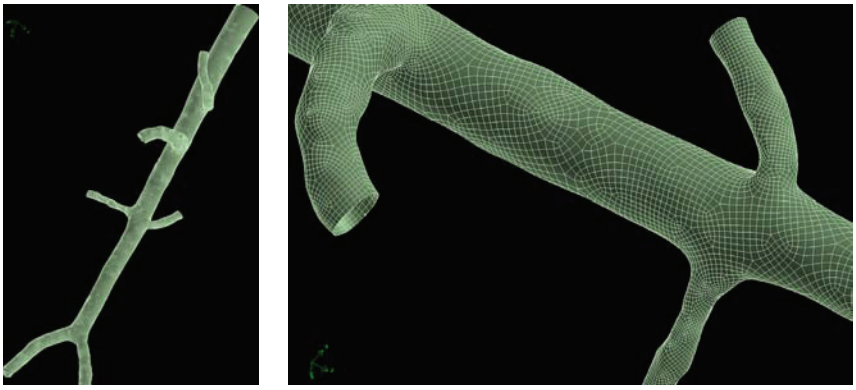

Figure 4.10: 4D-CT-P2: Interface mesh model (4D-CT-P2-IMesh).

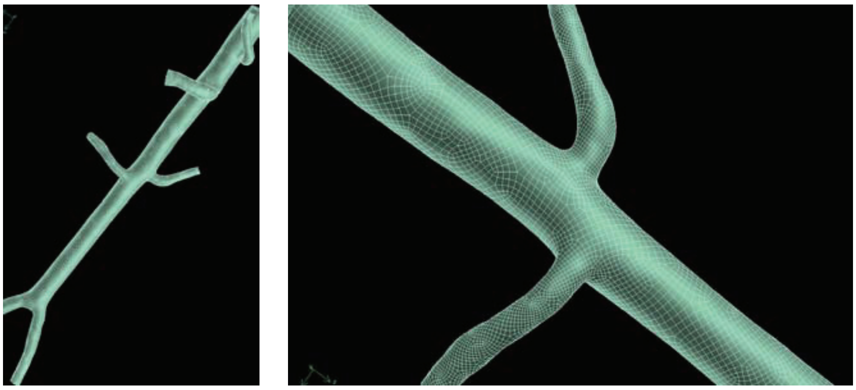

Figure 4.11: 4D-CT-P3: Interface mesh model (4D-CT-P3-IMesh).

The cSF parameters are defined with a 5° or 10° curvature angle, a 20 % growth factor and with cell sizes varying between 0.1 mm and 0.3 mm for the minimum and between 1 mm and 3 mm for the maximum parameters.

4.6.2 Volume Blood Meshing

Volume mesh models are generated to represent the blood elements for CFD and FSI applications. In total six blood volume meshes corresponding to four patients and two porcine models were generated. The volume meshing results are based on the BL and the mSF functions. The resulting element types depend on whether the available surface mesh contains triangular cells (CFD) or quadratic cells (FSI). In both cases, 4-node tetraedric elements are used for the inside of the lumen. The difference remains in the volume part enclosing the boundary layers domain. The tetrahedrons are mixed with 6-node wedge elements for the CFD meshes, and with 5-node pyramids and 8-node hexaedric flow-condition-based-interpolation (FCBI) elements for the FSI meshes (Fig.4.12). Note that model CT-AA also includes hexahedrons resulting from two extra volumes appended at two of the outlets to reduce backflow effects. A summary of the blood volume mesh models including mesh element type and size is presented in Tab.4.6. The corresponding meshing results are shown in Fig.4.13.b, Fig.4.14.b, Fig.4.15.b and Fig.4.17.a, Fig.4.18.a, Fig.4.19.a.

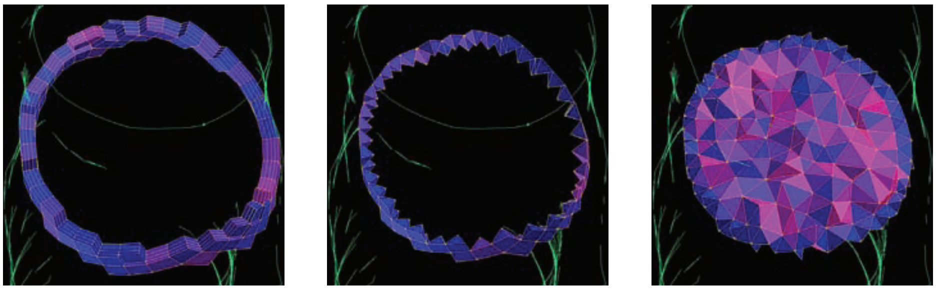

(a) 8-node Hex (b) 5-node Pyramids (c) 4-node Tet

Figure 4.12: Blood mesh cross-section showing the resulting FSI elements.

Table 4.6: Summary of the generated mesh models for the blood domain.

Model	Application	Type	Size
CT-AA-VBMesh	CFD	Wedges, Tet, Hex	209425
CT-AAA-VBMesh	CFD	Wedges, Tet	1054721
CT-TAA-VBMesh	CFD	Wedges, Tet	278089
MR-AAA-VBMesh	FSI	Hex, Pyramids, Tet	230597
4D-CT-P2-VBMesh	FSI	Hex, Pyramids, Tet	390310
4D-CT-P3-VBMesh	FSI	Hex, Pyramids, Tet	365573

The parameters used to define the BL function are: number of layers = 3 or 4, first row size varying between 0.1 mm and 0.3 mm and growth rate = 1.2. As for the mSF, it is defined by a maximum size varying between 1 mm and 3 mm and a growth factor of 10 % toward the inside of the fluid domain.

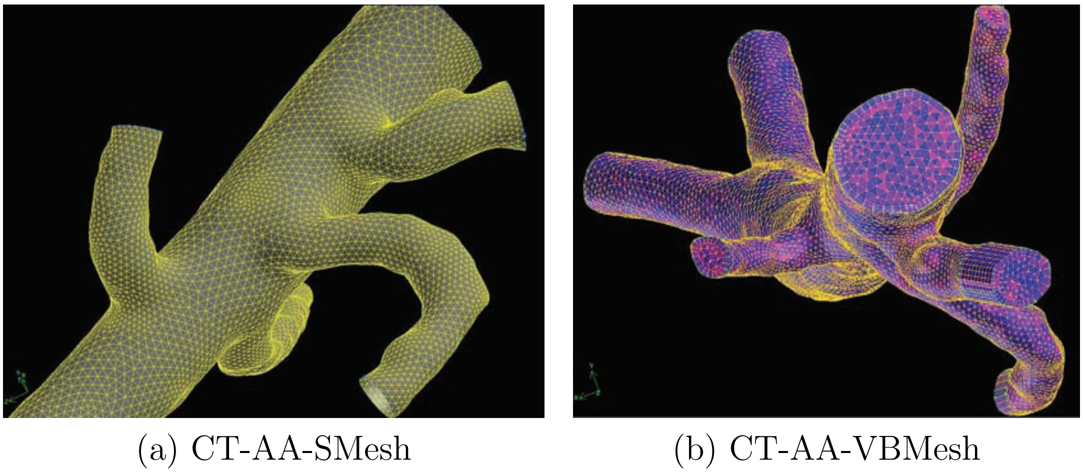

(a) CT-AA-SMesh (b) CT-AA-VBMesh

Figure 4.13: CT-AA: Boundary surface and blood volume mesh models.

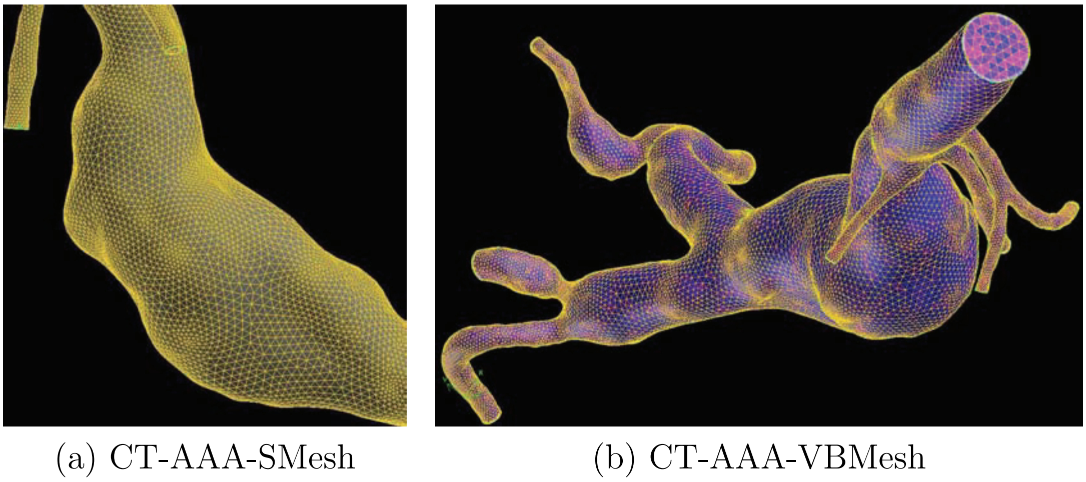

(a) CT-AAA-SMesh (b) CT-AAA-VBMesh

Figure 4.14: CT-AAA: Boundary surface and blood volume mesh models.

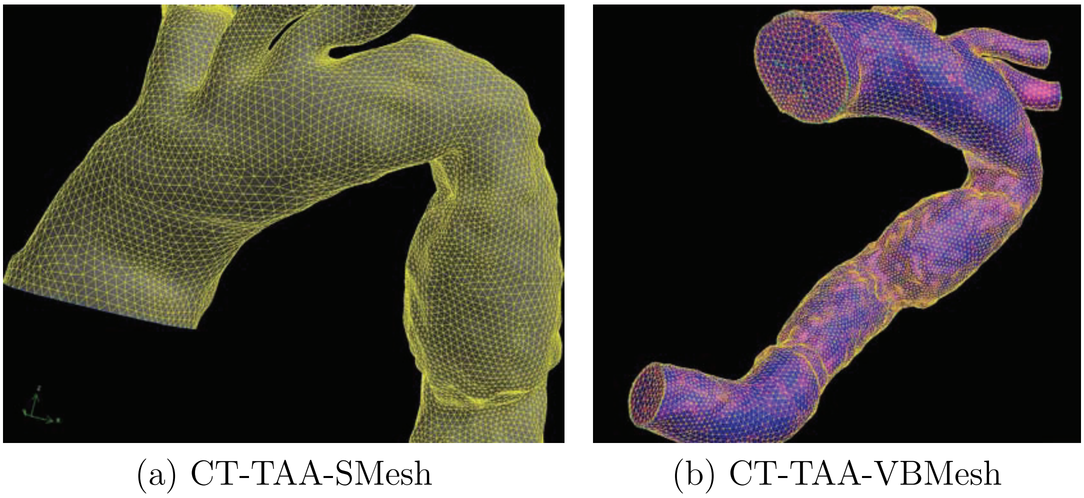

(a) CT-TAA-SMesh (b) CT-TAA-VBMesh

Figure 4.15: CT-TAA: Boundary surface and blood volume mesh models.

4.6.3 Volume Wall Meshing

Beside the blood elements, volume mesh models are generated to represent the wall elements for FSI applications. One MRI-based patient and two CT-based porcine wall mesh models are generated. The wall meshing results are obtained by extending the surface wall to include layers with a predefined homogeneous thickness as described in Sec.4.5 and shown in Fig.4.16. Eight-node brick elements are used for the wall domain, provided that the surface mesh for the FSI applications consists of quadratic cells. A summary of the volume mesh models for the wall including mesh element type and size is presented in Tab.4.7. The meshing results of the wall domain are shown in Fig.4.17.b, Fig.4.18.b and Fig.4.19.b for models MR-AAA, 4D-CT-P2 and 4D-CT-P3, respectively.

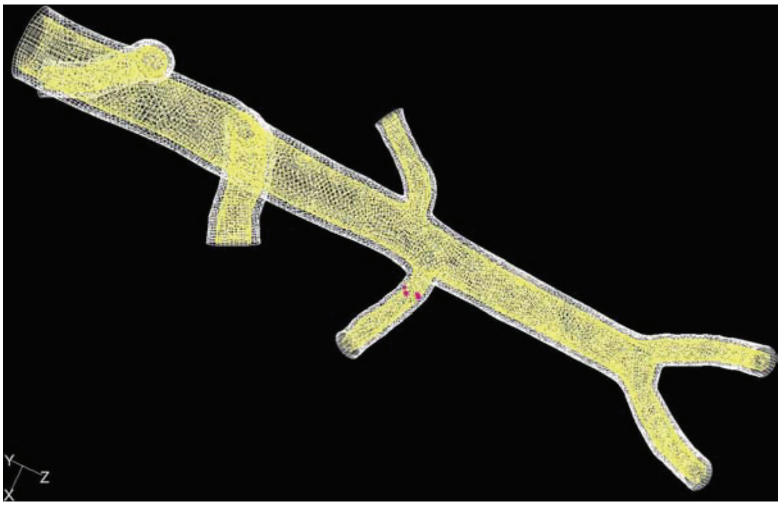

Figure 4.16: Outer wall generation from the inner boundary surface.

Table 4.7: Summary of the generated mesh models for the wall domain.

Model	Application	Type	Size
MR-AAA-VWMesh	FSI	Hex	34269
4D-CT-P2-VWMesh	FSI	Hex	95812
4D-CT-P3-VWMesh	FSI	Hex	85104

To define the wall domain the number of layers used is 3 for MR-AAA and 4 for 4D-CT-P2 and 4D-CT-P3. The surface normal is defined to point outwards as emerging from the wall. The uniform algorithm is used with a growth factor equals 1, that is generating equally sized elements of 0.5 mm. This resulted in a wall thickness of 1.5 mm for the patient and 2.0 mm for the porcine models.

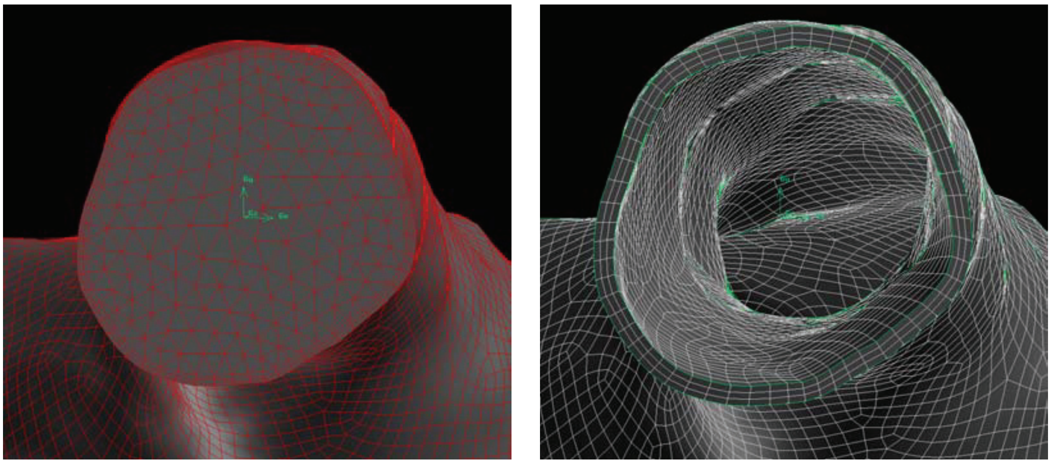

(a) MR-AAA-VBMesh (b) MR-AAA-VWMesh

Figure 4.17: MR-AAA: Blood and wall volume mesh models.

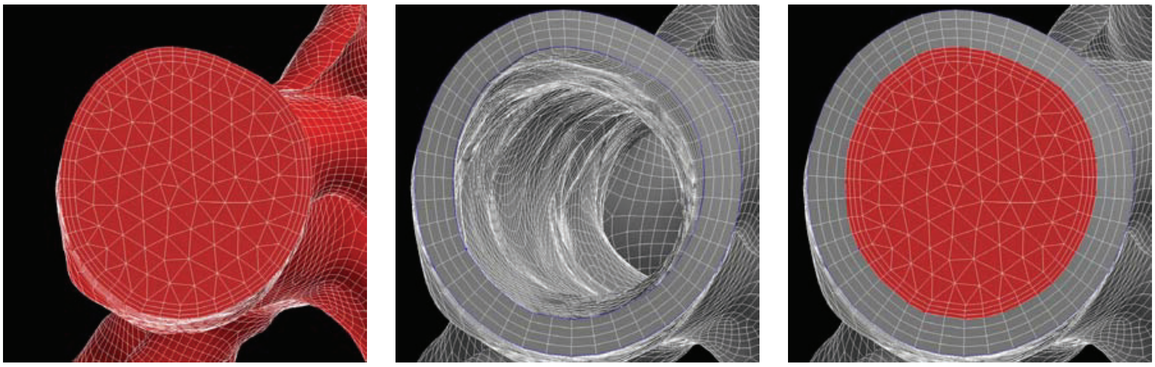

(a) 4D-CT-P2-VBMesh (b) 4D-CT-P2-VWMesh (c) 4D-CT-P2-VMesh

Figure 4.18: 4D-CT-P2: Blood, wall and combined volume mesh models.

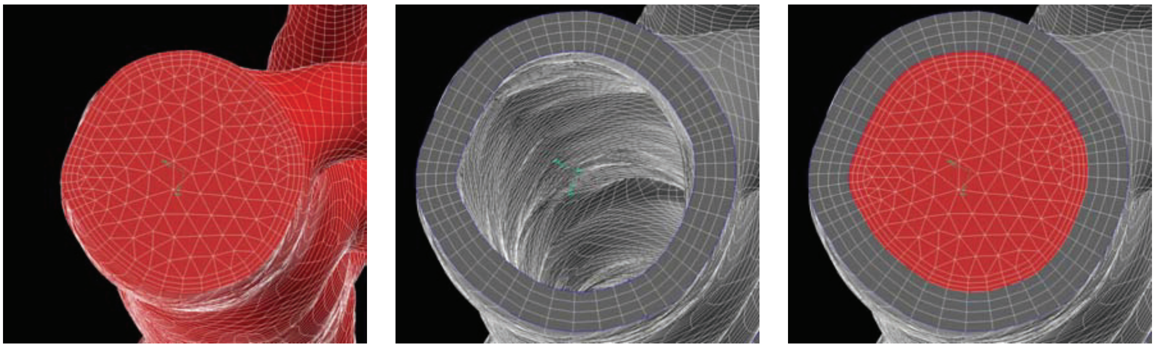

(a) 4D-CT-P3-VBMesh (b) 4D-CT-P3-VWMesh (c) 4D-CT-P3-VMesh

Figure 4.19: 4D-CT-P3: Blood, wall and combined volume mesh models.

4.7 Mesh Processing

For the application of different simulations, different mesh input files are needed to define the geometry, the physical properties and the boundary conditions. While the mesh geometry is defined by the coordinates of the nodes and by the configuration of the node-based elements, the FEM-based computations also require special sets of finite elements (FE) to be generated for the definition of various boundary and initial conditions. The mesh generation was therefore extended to further process the created meshes, by converting them and by generating appropriate predefined FE sets. The further processing strongly depends on the simulation application and on the software package to be used. Once processed, the resulting meshes can be directly used for the CFD, CSM and FSI simulations.

4.7.1 Conversion

A conversion library was first developed and integrated into MoDiSim, allowing to toggle between different mesh types. Thereby, the supported formats include .vtk, .stl, .msh, .neu, .inp and .in files. The .vtk and the .stl files consist of non-optimized surfaces with arbitrary distributed nodes generated from the marching cubes triangulation algorithm. They contain the first approximation of the model geometry resulting from the extraction of the 3D boundary surface of the segmented images. The .msh and the .neu files are Gambit and TGrid formats. The .msh file is also the Fluent input geometry file. High-quality meshes are first generated into the .msh format and can be used for blood flow (CFD) simulations in Fluent. The .inp and the .in files represent the Abaqus and the Adina formats. They are compiled in an FE language and can be used for vessel wall (CSM) and coupled blood-vessel (FSI) simulations, respectively. Depending on the application, surface and/or volume meshes are involved with each mesh type (Tab.4.8).

Table 4.8: Conversion library: Various surface (S) and volume (V) meshes.

from \ to	**.stl**	**.inp**	**.in**	**.txt**
.vtk	S	-	-	-
.stl	-	S	-	-
.msh	S	S,V	V	-
.neu	-	-	V	-
.inp	-	-	S	-
.in	-	-	S	*nodes*

4.7.2 FE-sets

Predefined sets of nodes, elements and faces, necessary for the definition of individual velocity, pressure and constraint boundary conditions for CFD, CSM and FSI applications are then generated. CFD simulations require pressure-based and/or flow-based boundary conditions, while CSM simulations require pressure-load and constraint boundary conditions. FSI simulations require beside the flow-, pressure- and constraint-based conditions, an interface boundary for the definition of the interaction conditions. Depending on the application and on the boundary condition type, various required sets at the inlet, outlets and boundary faces are extracted and defined from the meshes. Further, any contact problem if present would also require specific sets to be available for the definition of contact boundary conditions. A summary of the most important provided FE sets is presented in Tab.4.9.

Sim \ BC	**Inlet**	**Outlets**	**Wall**
CFD(Fluent)	Faces	Faces	Faces
CSM(Abaqus)	Nodes	Nodes	Elements
FSI-Blood(Adina)	Nodes	ElFaces	Nodes
FSI-Wall(Adina)	Nodes	Nodes	ElFaces

Table 4.9: Overview: FE-sets generation.

4.8 System Integration in *Mesh-Gen* and *Mesh-Pro*

Due to the specific characteristics and the complexity of patient-specific data, most of the investigations in this field manually create and process the mesh models. Further, in order not to even more increase the time effort associated with the manual processing, mesh optimization algorithms are rarely included in the generation process. Manual mesh generation generally requires more than half of the analysis time excluding the simulation time. Strategies for dealing with complex geometries depend on time available, desired quality and accuracy. Automatic mesh generation with individual awareness in terms of geometry and conditions is a prerequisite for performing fast and accurate computations of hemodynamics and biomechanics within patient-specific vessels. It represents an essential aspect for efficient evaluation of clinical procedures individually for each patient. A numerical tool was therefore developed to automatically generate and process complex patient-specific finite element mesh models from image-based vessel geometries. The automatic approach represents a compromise between computational cost, mesh quality and physics.

The automatic generation tool is evaluated using different image-based subject-specific aortic models. It is compiled in two steps providing meshing and processing with minimal interaction effort. These are integrated into the *Mesh-Gen* and the *Mesh-Pro* components of the MoDiSim system. The corresponding user interfaces provided for loading and interacting with the different mesh data are shown in Fig.4.20 and Fig.4.21, respectively.

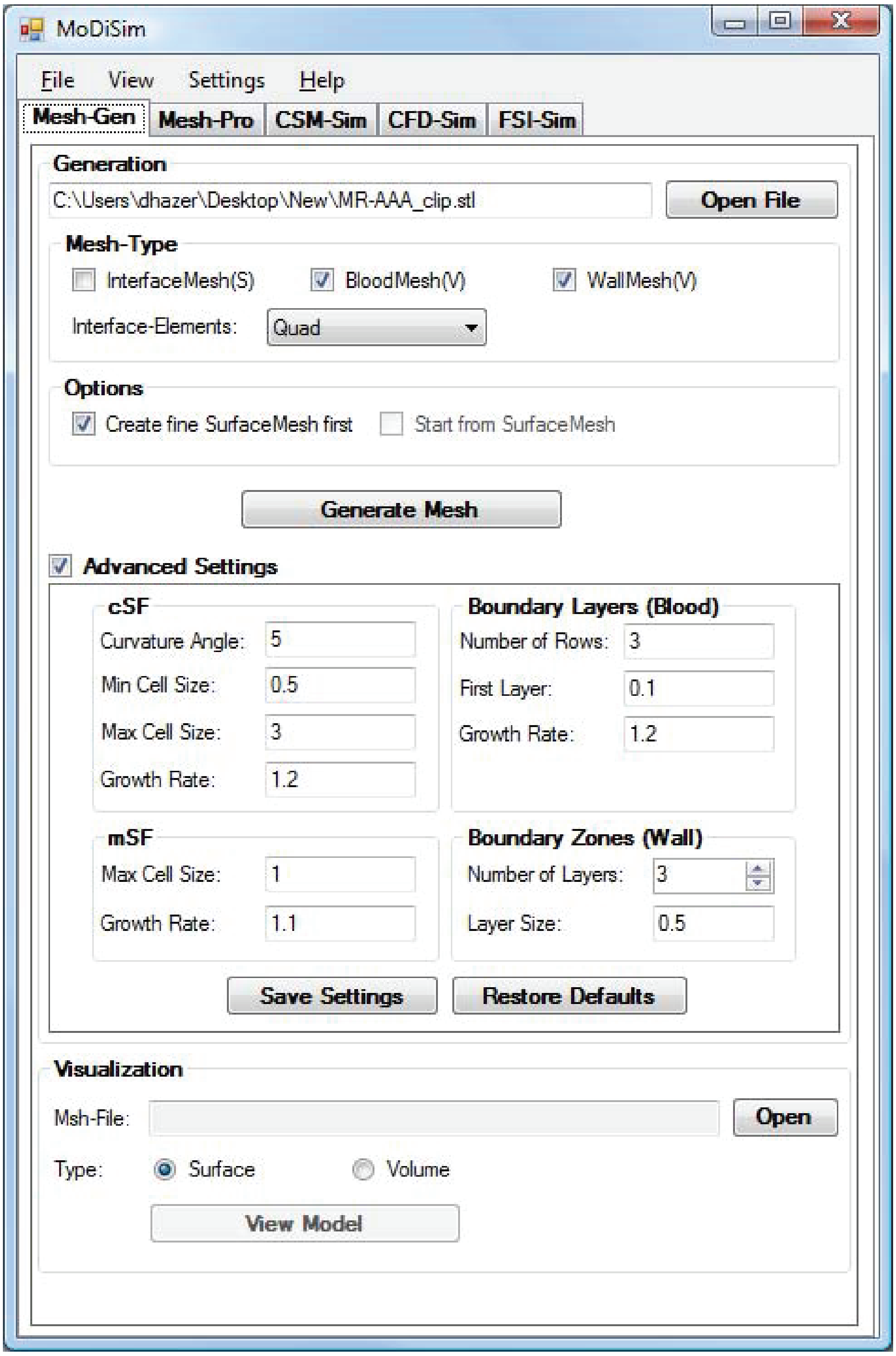
MoDiSim
File
View
Settings
Help
Mesh-Gen
Mesh-Pro
CSM-Sim
CFD-Sim
FSI-Sim
Generation
Open File
Mesh-Type
Options
Generate Mesh
cSF
Boundary Layers (Blood)
mSF
Boundary Zones (Wall)
Save Settings
Restore Defaults
Visualization
Open
View Model

C:\Users\dhazer\Desktop\New\MR-AAA_clip.stl

☐ InterfaceMesh(S) ☑ BloodMesh(V) ☑ WallMesh(V)

Interface-Elements: Quad

☑ Create fine SurfaceMesh first ☐ Start from SurfaceMesh

☑ Advanced Settings

Curvature Angle: 5
Min Cell Size: 0.5
Max Cell Size: 3
Growth Rate: 1.2

Number of Rows: 3
First Layer: 0.1
Growth Rate: 1.2

Max Cell Size: 1
Growth Rate: 1.1

Number of Layers: 3
Layer Size: 0.5

Msh-File:

Type: ● Surface ○ Volume

Figure 4.20: User-Interface of the mesh generation component *Mesh-Gen*.

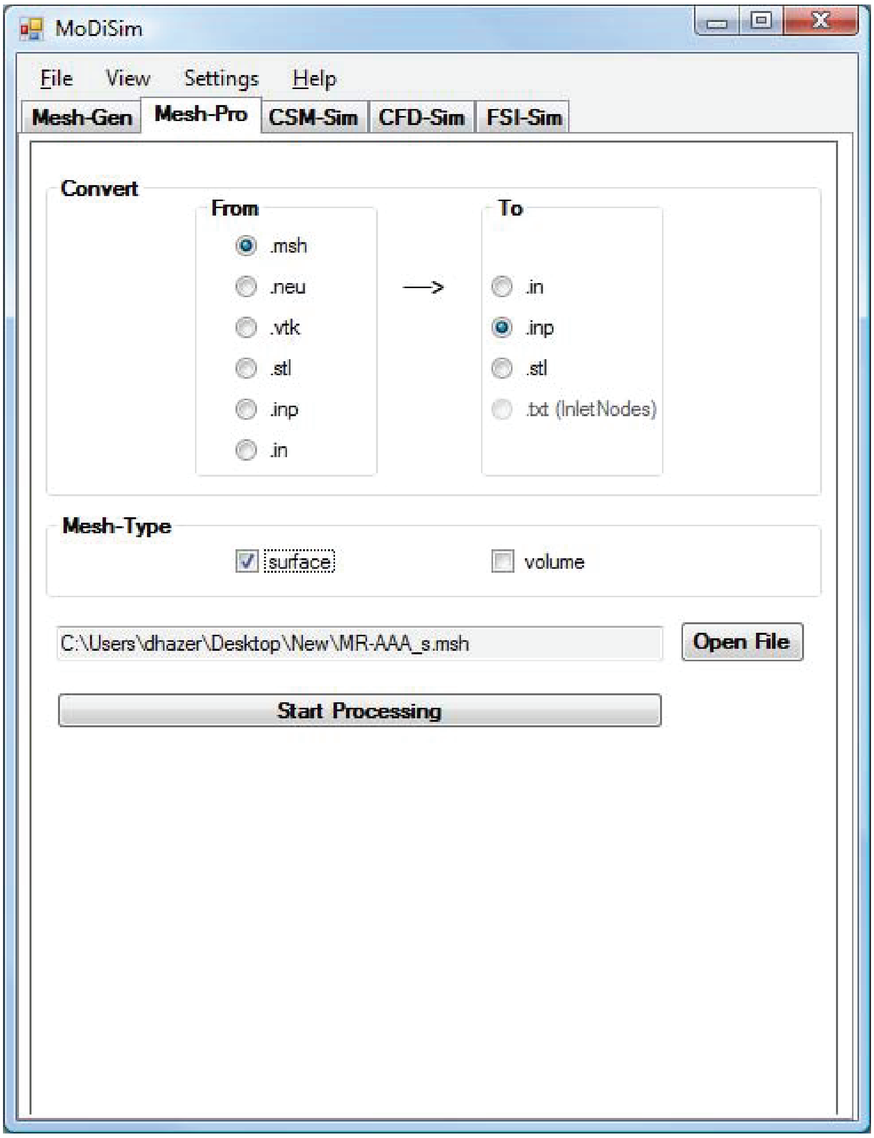

Convert

From
● .msh
○ .neu
○ .vtk
○ .stl
○ .inp
○ .in

—>

To
○ .in
● .inp
○ .stl
○ .txt (InletNodes)

Mesh-Type
☑ surface
☐ volume

C:\Users\dhazer\Desktop\New\MR-AAA_s.msh

Figure 4.21: User-Interface of the mesh processing component *Mesh-Pro*.

4.8.1 Automation of Mesh Generation

The first component *Mesh-Gen* includes the automatic generation of accurate patient-specific mesh models of healthy and diseased vessels. The automatic generation includes mesh optimization based on the integration of various control functions and thus satisfies the requirements for stable simulations. Therefore, based on the user interaction with the *Mesh-Gen* represented in Fig.4.20, various journals are created to automatically generate high-quality controlled and optimized surface and volume mesh models for various computational domains. The activity diagram of *Mesh-Gen* is illustrated in Fig.4.22. The journals consists of the individual steps of the mesh generation processes represented by the three developed algorithms described in Sec.4.5:

- The automation of the surface meshing approach for the wall and the interface is accomplished via implementation of the *MeshSurface* algorithm representing the surface wall and interface meshing process into *Mesh-Gen* for CSM and FSI applications, respectively.

- The volume mesh generation for the blood models is automated via integration of the volume blood meshing process through the *MeshBloodVolume* algorithm into *Mesh-Gen* for both CFD and FSI applications.

- As for the volume mesh generation of the wall models, it is automated by implementing the *MeshWallVolume* algorithm for the volume wall meshing process into *Mesh-Gen* for FSI applications.

Thereby, the mesh parameters needed for the automatic application of the mesh control functions are acquired from the previously performed computational grid analysis described in Sec.4.4, in which the numerical stability of the simulations in terms of mesh independency was investigated. The obtained parameters have been presented in Tab.4.2 and Tab.4.3.

4.8.2 Automation of Mesh Processing

The automatic mesh generation tool has been then extended to automatically further process the generated patient-specific mesh models as described in Sec.4.7. The second component *Mesh-Pro* includes the automatic conversion of the mesh models to specific mesh files and the generation of predefined FE sets required for the definition of appropriate boundary conditions. This occurs depending on the application, that is depending on the type of the simulation (CSM, CFD and FSI) and on the software to be applied. Therefore, based on the user interaction with *Mesh-Pro* represented in Fig.4.21, the processing tool provides access to various surface and volume mesh configurations and performs connections between the finite nodes and elements using different mesh definition types (.vtk, .stl, .msh, .neu, .inp, .in). The processing of the mesh models functions fully automatically based on various implemented algorithms as illustrated in the activity diagram in Fig.4.23. The processing is based on the zone specifications defined in the generated .msh mesh model using the boundary and the continuum types as previously described. The predefined settings are automatically created and saved into the mesh files and can be used for the application of physical properties and boundary conditions for the fluid and solid domains as well as their contact-interface where they interact together.

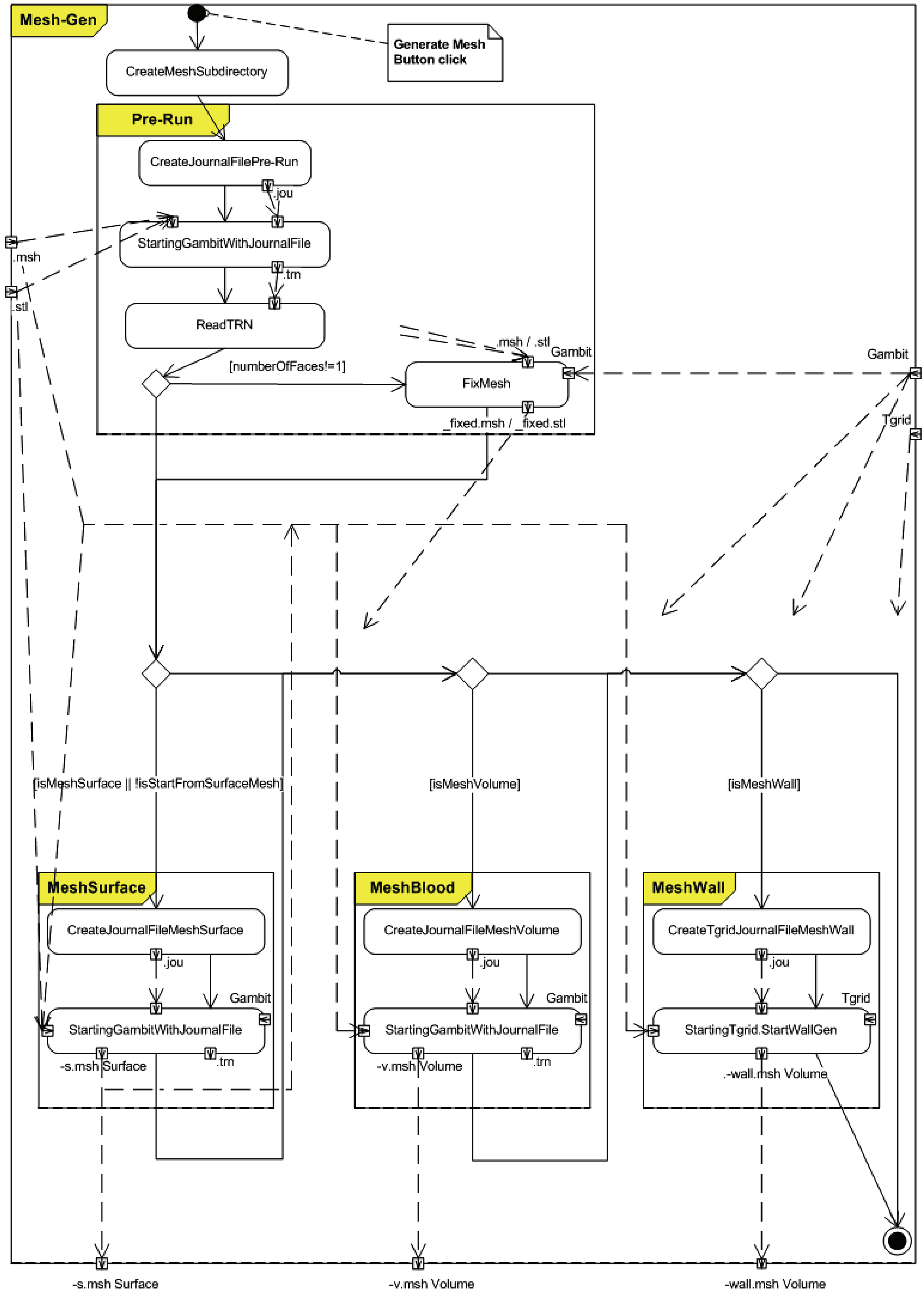
Mesh-Gen
Generate Mesh Button click
CreateMeshSubdirectory
Pre-Run
CreateJournalFilePre-Run
.jou
.msh
StartingGambitWithJournalFile
.stl
.trn
ReadTRN
.msh / .stl
Gambit
[numberOfFaces!=1]
FixMesh
_fixed.msh / _fixed.stl
Gambit
Tgrid
[isMeshSurface || !isStartFromSurfaceMesh]
[isMeshVolume]
[isMeshWall]
MeshSurface
CreateJournalFileMeshSurface
.jou
Gambit
StartingGambitWithJournalFile
-s.msh Surface
.trn
MeshBlood
CreateJournalFileMeshVolume
.jou
Gambit
StartingGambitWithJournalFile
-v.msh Volume
.trn
MeshWall
CreateTgridJournalFileMeshWall
.jou
Tgrid
StartingTgrid.StartWallGen
.-wall.msh Volume
-s.msh Surface
-v.msh Volume
-wall.msh Volume

Figure 4.22: Activity diagram of the mesh generation component *Mesh-Gen*.

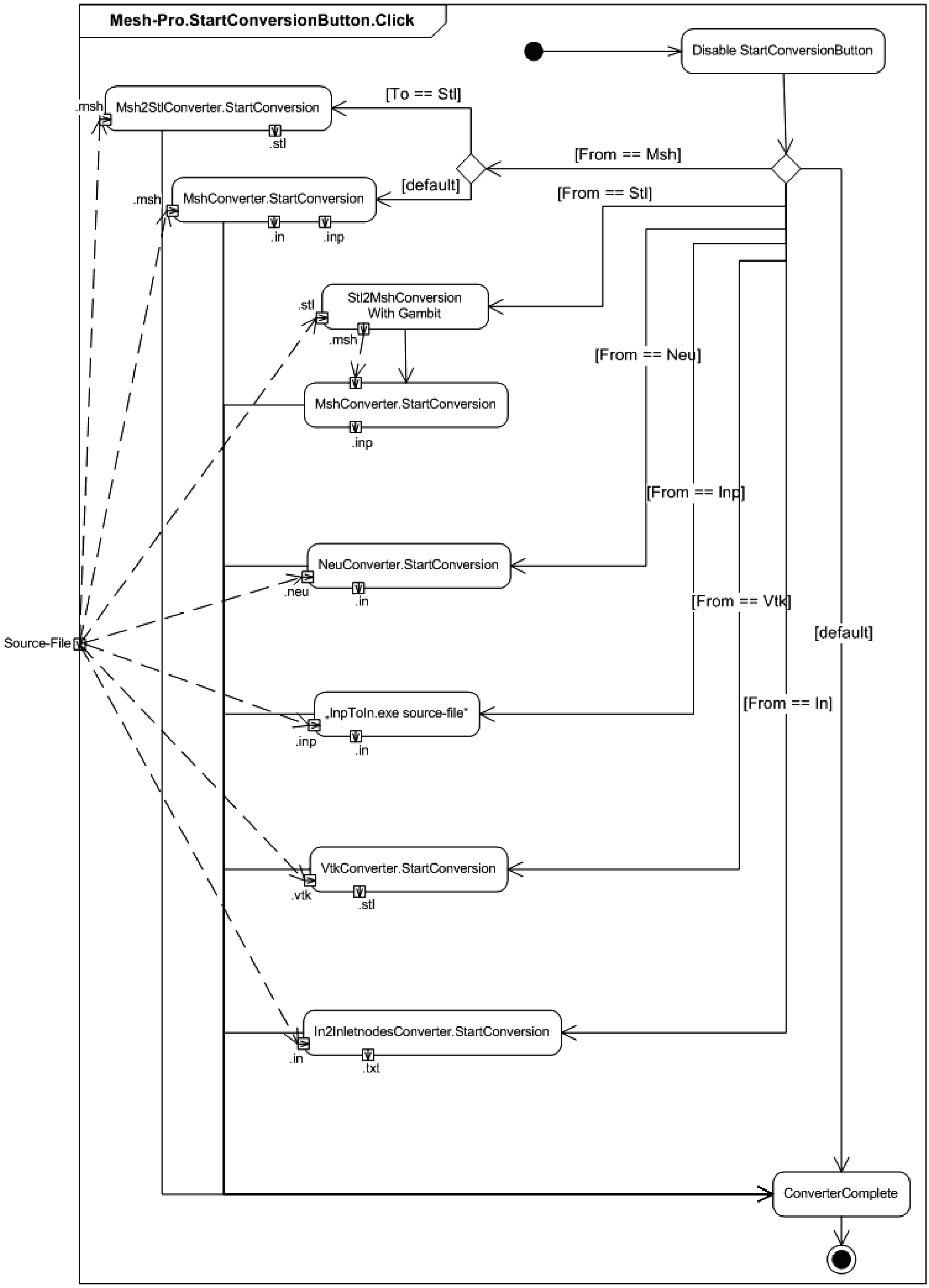
Mesh-Pro.StartConversionButton.Click
Disable StartConversionButton
[To == Stl]
[From == Msh]
[default]
[From == Stl]
Msh2StlConverter.StartConversion
.msh
.stl
MshConverter.StartConversion
.msh
.in
.inp
Stl2MshConversion With Gambit
.stl
.msh
MshConverter.StartConversion
.inp
[From == Neu]
[From == Inp]
NeuConverter.StartConversion
.neu
.in
[From == Vtk]
[default]
Source-File
„InpToIn.exe source-file"
.inp
.in
[From == In]
VtkConverter.StartConversion
.vtk
.stl
In2InletnodesConverter.StartConversion
.in
.txt
ConverterComplete

Figure 4.23: Activity diagram of the mesh processing component *Mesh-Pro*.

4.9 Summary

In this chapter the mesh generation process developed in this work and required for patient-specific and image-based blood flow and vessel wall modeling in the aorta, was presented. First, a short introduction including the meshing requirements for accurate simulations was described. Then, the metrics for assigning and checking the quality of a given mesh model were introduced. Further, mesh optimization based on the integration of mesh control functions for curvature size and mesh size as well as boundary layers and designed to enhance the mesh quality was presented. Next, mesh independency based on a computational grid analysis in which iterative mesh refinement was performed to investigate and achieve numerical stability was described. Then, the meshing approaches including three processes required for the generation of high-quality surface and volume meshes from the segmented patient data were presented. Following the meshing approaches, meshing results from the three processes were illustrated. Then, the processing of the 3D meshes and the creation of the FE-Models including appropriate FE-sets necessary for the definition of individual boundary conditions required to solve the governing system of partial differential equations is presented. Finally, the automation of the mesh generation process via the *Mesh-Gen* and the *Mesh-Pro* components integrated into the MoDiSim system, indispensible for medical applications and clinical implementation was described at the end of this chapter.

Chapter 5

Vessel Wall Modeling

5.1 Introduction

Pathological conditions of the elastomechanical functioning of the vessel weaken the wall and may lead to its rupture. Structural modeling of the vessel wall provides an insight into its mechanical behavior. It allows to identify individual parameters such as weak spots associated with high stresses and sites of excessive mechanical strain. This may enable accurate predictive simulations of development, growth, fatigue and failure of cardiovascular disease.

Physical modeling based on individual model characteristics is indispensable for realistic simulations. The approach consists of applying the concepts of physics together with constitutive modeling to simulate the dynamic behavior of objects. Image-based Computational Structural Mechanics (CSM) based on the Finite Element Method (FEM) as a numerical approach, has become an efficient tool in simulating the individual biomechanics in deformable human arteries.

The purpose of this chapter is to describe the theoretical and applied aspects behind the modeling of the vessel wall. In order to understand the fundamentals of the modeling, theoretical background on the physics of structure mechanics, followed by the biomechanical constitutive relations and the numerical approach of the FEM are first presented. Next, the CSM simulations performed by applying the modeling steps to the vessel wall are described. The integration of the modeling steps into the MoDiSim system follows the generation of the process chain. Finally, some of the results applied to various individual models will be illustrated.

5.2 Continuum Structure Mechanics

While bodies consist of atoms, continuum mechanics is the study of physics based on a simplified approach dealing with the objects as a continuum. It involves a macroscopic physical approximation, ignoring the heterogeneous material microstructures. So, notions of spins or the uncertainty principle such as present in quantenphysics, are not available here. As a result, the classical conservation equations for energy and momentum remain valid at the infinitesimale level. Continuum structure mechanics is the area of the physics dealing with the mechanics of continuum solids. It involves the study of the kinematics and mechanical behavior of bodies with defined shape. Thus, the main concept in structure mechanics deals with the notion of forces and deformation, or action and motion. In particular, the state of a system may be described in terms of stress and strain variables, and in terms of the equations of motion derived from the conservation laws. From a biomechanical point of view, soft tissue modeling consists of analyzing the mechanical properties relating the tension in the material to the deformation it undergoes.

In this section, the theoretical concepts of kinematics configurations, deformation and displacements, strain and stress as well as the equations of motion are presented. The section is concluded with the virtual work principle required for the numerical solutions. For a better understanding, particular attention is given to the physical meaning of these theoretical relations.

5.2.1 Lagrangian and Eulerian Configurations

When moving, a continuum object occupies different configurations in space at various times. In order to describe the kinematics of a continuous solid, it is therefore convenient to define the evolution of motion in terms of two configurations: a reference configuration describing the initial undeformed state of the particle and a current configuration describing its deformed status at any subsequent time. The reference or *Lagrangian* configuration is usually used in solid mechanics, while the current, *Eulerian* configuration is rather used in fluid mechanics. From an observer point of view, the Lagrangian configuration involves the description seen by an observer moving with the moving objet and observing the changes in time as the body moves in space. The results obtained are independent of the choice of initial time and reference configuration. The Eulerian configuration rather involves the description of what is currently happening at a fixed point in space as time progresses. It is based on the description seen by an observer standing in a fixed frame and observing the changes through time that are taking place at a certain position as different material points pass through it.

Consider Ω to be a finite body moving between a reference configuration Ω_0 defined at time $t_0 = 0$, and any following configuration Ω_t defined at the current time t. Let $\boldsymbol{X}$ and $\boldsymbol{x}$ be the continuous coordinate vectors of any point P in Ω, defined with respect to the Lagrangian and the Eulerian configurations, respectively Fig.5.1. As the solid evolves in time, its motion can be made either in terms of the referential Lagrangian coordinates X_i or in terms of the current Eulerian x_i coordinates.

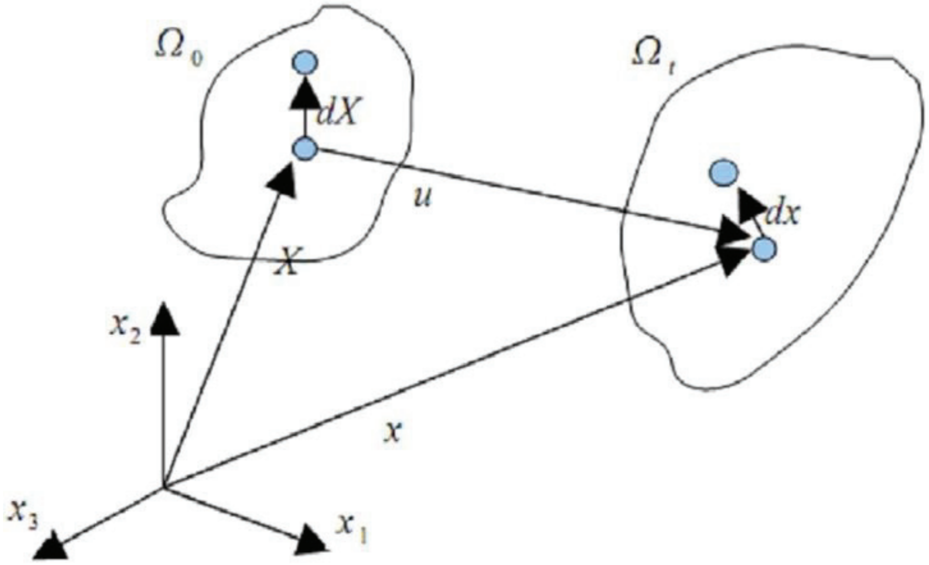

Figure 5.1: Lagrangian and Eulerian configurations.

5.2.2 Deformation and Displacement

The kinematics of a continuum body when changing its configuration can be described by a displacement. The displacement of a body consists of a simultaneous translation and rotation and of a deformation.

Deformation and Deformation Gradient Tensors

Deformation of a continuum solid specifies the change in its shape or size when it moves from the reference configuration Ω_0 to the current configuration Ω_t. In the Lagrangian configuration, it can be described by a continuous mapping of the coordinates of any point P belonging to Ω from the reference configuration onto the current configuration:

$$\boldsymbol{x} = \boldsymbol{x}(\boldsymbol{X}, t) \qquad \text{or} \qquad x_i = x_i(\boldsymbol{X}, t) \tag{5.1}$$

The deformation gradient tensor $\boldsymbol{F}$ allows mapping any elementary segment $d\boldsymbol{X}$ of Ω defined in Ω_0 into an elementary segment $d\boldsymbol{x}$ defined in the current Ω_t. It is defined as the Jacobian matrix of the function $\boldsymbol{x}$ and can be obtained by differentiating Eq.5.1 with respect to the Lagrangian coordinates:

$$d\boldsymbol{x} = \boldsymbol{F} d\boldsymbol{X} \qquad or \qquad dx_i = \sum_j \frac{\partial x_i \left(\boldsymbol{X}, t\right)}{\partial X_j} dX_j \tag{5.2}$$

with

$$\boldsymbol{F} = \left[\frac{\partial x_i}{\partial X_j}\right] = \begin{bmatrix} \frac{\partial x_1}{\partial X_1} & \frac{\partial x_1}{\partial X_2} & \frac{\partial x_1}{\partial X_3} \\ \frac{\partial x_2}{\partial X_1} & \frac{\partial x_2}{\partial X_2} & \frac{\partial x_2}{\partial X_3} \\ \frac{\partial x_3}{\partial X_1} & \frac{\partial x_3}{\partial X_2} & \frac{\partial x_3}{\partial X_3} \end{bmatrix} \tag{5.3}$$

Similarly, the reversed deformation can be described in the Eulerian configuration by mapping the coordinates of any point P in Ω from the current configuration back onto the original coordinates. It is defined by:

$$\boldsymbol{X} = \boldsymbol{X}\left(\boldsymbol{x}, t\right) \qquad \text{or} \qquad X_i = X_i\left(\boldsymbol{x}, t\right) \tag{5.4}$$

And the reversed deformation gradient tensor $\boldsymbol{G}$, defined as the Jacobian matrix of the function $\boldsymbol{X}$, can be obtained by differentiating Eq.5.4 with respect to the Eulerian coordinates:

$$\boldsymbol{G} = \left[\frac{\partial X_i}{\partial x_j}\right] = \begin{bmatrix} \frac{\partial X_1}{\partial x_1} & \frac{\partial X_1}{\partial x_2} & \frac{\partial X_1}{\partial x_3} \\ \frac{\partial X_2}{\partial x_1} & \frac{\partial X_2}{\partial x_2} & \frac{\partial X_2}{\partial x_3} \\ \frac{\partial X_3}{\partial x_1} & \frac{\partial X_3}{\partial x_2} & \frac{\partial X_3}{\partial x_3} \end{bmatrix} = \boldsymbol{F}^{-1} \tag{5.5}$$

A necessary and sufficient condition for this inverse function to exist is that the determinant of the Jacobian matrices $\boldsymbol{F}$ and $\boldsymbol{G}$ is different from zero:

$$det\left(\boldsymbol{F}\right) = \left|\frac{\partial x_i}{\partial X_j}\right| = \left|\frac{\partial X_i}{\partial x_j}\right| = det\left(\boldsymbol{G}\right) \neq 0 \tag{5.6}$$

Volume and Surface Changes

Further, the elementary *volume change* dv in the current configuration Ω_t can be obtained by mapping the elementary volume dV in the original configuration using the Jacobian J of the deformation gradient tensor $\boldsymbol{F}$:

$$dv = JdV \qquad \text{with} \qquad J = det\left(\boldsymbol{F}\right) \tag{5.7}$$

As for the elementary *surface change ds* in the current configuration Ω_t, it can be obtained from the elementary surface dS in the original configuration Ω_0 based on the Jacobian J and on the transpose of the reverse deformation gradient tensor $\boldsymbol{G}$ as follows:

$$\boldsymbol{n} ds = J \boldsymbol{G}^T \boldsymbol{N} dS \tag{5.8}$$

where $\boldsymbol{n}$ and $\boldsymbol{N}$ are the normals to ds and dS in Ω_t and Ω_0, respectively.

Displacement and Displacement Gradient Tensor

The trajectory $\boldsymbol{x}(\boldsymbol{X}, t)$ of any point in space is usually an unknown function. The notion of displacement is therefore preferably used than that of the deformation. Displacement in continuum mechanics is a vector that describes the change in position of a point P in Ω between the reference Ω_0 and the current Ω_t configurations. In the Lagrangian configuration Ω_0 it is defined as:

$$\boldsymbol{u}(\boldsymbol{X}, t) = \boldsymbol{x}(\boldsymbol{X}, t) - \boldsymbol{X} \tag{5.9}$$

An assignment of the displacement vectors for all points P in Ω when moved from Ω_0 to Ω_t is known as the displacement field. Using the definitions of $\boldsymbol{F}$ and $\boldsymbol{G}$ in Eq.5.3 and Eq.5.5 respectively, the elementary displacement variation $d\boldsymbol{u}$ in the Lagrangian configuration Ω_0 may be defined as:

$$d\boldsymbol{u}(\boldsymbol{X}, t) = d\boldsymbol{x}(\boldsymbol{X}, t) - d\boldsymbol{X} = (\boldsymbol{F} - \boldsymbol{I})\, d\boldsymbol{X} \tag{5.10}$$

The displacement gradient tensor $\nabla \boldsymbol{u}$ may be obtained by differentiating the displacement vector with respect to the Lagrangian coordinates in Ω_0. The definition of $\nabla \boldsymbol{u}$ follows then from Eq.5.10 and may be expressed as:

$$\nabla \boldsymbol{u} = \boldsymbol{F} - \boldsymbol{I} \qquad \text{with} \qquad du_i = \sum_j \frac{\partial u_i(\boldsymbol{X}, t)}{\partial X_j} dX_j \tag{5.11}$$

Similarly, defined in the Eulerian configuration Ω_t, the displacement vector $\boldsymbol{U}$, the displacement variation $d\boldsymbol{U}$ and the displacement gradient tensor $\nabla \boldsymbol{U}$ can be respectively described by:

$$\boldsymbol{U}(\boldsymbol{x}, t) = \boldsymbol{x} - \boldsymbol{X}(\boldsymbol{x}, t) \tag{5.12}$$

$$d\boldsymbol{U}(\boldsymbol{x}, t) = d\boldsymbol{x} - d\boldsymbol{X}(\boldsymbol{x}, t) = (\boldsymbol{I} - \boldsymbol{G})\, d\boldsymbol{x} \tag{5.13}$$

$$\nabla \boldsymbol{U} = \boldsymbol{I} - \boldsymbol{G} \qquad \text{with} \qquad dU_i = \sum_j \frac{\partial U_i(\boldsymbol{x}, t)}{\partial x_j} dx_j \tag{5.14}$$

5.2.3 Strain Analysis

In structure mechanics, strain is a measure of the distortion of a deformed continuum body. A body is said to be distorted if the distance between at least two of its points changes after it has moved. Strains represent the amount of change of the relative displacement between particles of a material. They are produced by forces or stresses acting on the material body. Within a deforming body, they can be represented by the normal strain and the shear strain components. Normal strains are defined by the change in length that occurs along the material lines. They are therefore associated with the amount of stretch or compression and called tensile strains and compressive strains, respectively. On the other side, shear strains are defined by the change in the angle between initially perpendicular pairs of lines. They describe the amount of distortion related with the sliding of the material planes. Thus, in order to describe the state of strain of a continuum body Ω, it is necessary to quantify the normal and shear components of the strain tensor for all points P in Ω.

Lagrangian Strain Tensors

The squared lengths of the elementary segment $d\boldsymbol{x}$ in the Lagrangian configuration may be derived using Eq.5.3:

$$d\boldsymbol{x}^2 = d\boldsymbol{x}^T d\boldsymbol{x} = d\boldsymbol{X}^T \boldsymbol{F}^T \boldsymbol{F} d\boldsymbol{X} \tag{5.15}$$

with the tensorial product defined as the *right Cauchy-Green dilation* tensor:

$$\boldsymbol{C} = \boldsymbol{F}^T \boldsymbol{F} \tag{5.16}$$

The *left Cauchy-Green dilation* tensor may be also introduced as:

$$\boldsymbol{B} = \boldsymbol{F} \boldsymbol{F}^T \tag{5.17}$$

Now using Eq.5.15 and Eq.5.16, the squared length variation in the Lagrangian configuration may be expressed as:

$$d\boldsymbol{x}^2 - d\boldsymbol{X}^2 = d\boldsymbol{X}^T \left(\boldsymbol{C} - \boldsymbol{I}\right) d\boldsymbol{X} = d\boldsymbol{X}^T 2\boldsymbol{E} d\boldsymbol{X} \tag{5.18}$$

where $\boldsymbol{E}$ represents the *Green-Lagrange* or the *Lagrangian strain* tensor:

$$\boldsymbol{E} = \frac{1}{2}\left(\boldsymbol{C} - \boldsymbol{I}\right) \tag{5.19}$$

$\boldsymbol{C}$, $\boldsymbol{B}$ and $\boldsymbol{E}$ are second-order symmetric tensors allowing the calculation of the length variation of any segment $d\boldsymbol{X}$ known in the reference configuration.

Eulerian Strain Tensors

Now using Eq.5.5, the squared lengths of the elementary segment $d\boldsymbol{X}$ in the Eulerian configuration may be derived as:

$$d\boldsymbol{X}^2 = d\boldsymbol{X}^T d\boldsymbol{X} = d\boldsymbol{x}^T \boldsymbol{G}^T \boldsymbol{G} d\boldsymbol{x} \tag{5.20}$$

The tensorial product in Eq.5.20 is defined as the *Cauchy strain* tensor:

$$\boldsymbol{c} = \boldsymbol{G}^T \boldsymbol{G} \tag{5.21}$$

Obviously, the *Cauchy strain* tensor is also the inverse of the *left Cauchy-Green dilation* tensor, $\boldsymbol{B}^{-1} = \boldsymbol{c}$. Using Eq.5.20 and Eq.5.21, the squared length variation in the Eulerian configuration may be then expressed as:

$$d\boldsymbol{x}^2 - d\boldsymbol{X}^2 = d\boldsymbol{x}^T \left(\boldsymbol{I} - \boldsymbol{c}\right) d\boldsymbol{x} = d\boldsymbol{x}^T 2\boldsymbol{e} d\boldsymbol{x} \tag{5.22}$$

where $\boldsymbol{e}$ is defined as the *Euler-Almansi* or the *Eulerian strain* tensor:

$$\boldsymbol{e} = \frac{1}{2}\left(\boldsymbol{I} - \boldsymbol{c}\right) \tag{5.23}$$

$\boldsymbol{c}$ and $\boldsymbol{e}$ are also second-order symmetric strain tensors allowing the calculation of the length variation of any segment $d\boldsymbol{x}$ known in the current configuration.

Extension Ratios and Invariants

The *extension ratios* are strain parameters appropriate for purpose of experimental evaluation. They are defined by the diagonal elements of the deformation gradient tensor $\boldsymbol{F}$:

$$\lambda_i = F_{ii} = \frac{\partial x_i}{\partial X_i} \qquad i = 1{,}2{,}3 \tag{5.24}$$

In terms of the principal strain components C_{ii} and E_{ii}, they become:

$$C_{ii} = \lambda_i^2 \qquad \text{and} \qquad E_{ii} = \frac{1}{2}\left(\lambda_i^2 - 1\right) \tag{5.25}$$

Further, the *invariants* $I_{\boldsymbol{H}}$, $II_{\boldsymbol{H}}$ and $III_{\boldsymbol{H}}$ of any second order tensor $\boldsymbol{H}$ may be defined in terms of its eigenvalues h_1, h_2 and h_3 as follows:

$$\begin{cases} I_{\boldsymbol{H}} &= tr\left(\boldsymbol{H}\right) &= h_1 + h_2 + h_3 \\ II_{\boldsymbol{H}} &= \frac{1}{2}\left[tr\left(\boldsymbol{H}\right)^2 - tr\left(\boldsymbol{H}^2\right)\right] &= h_1 h_2 + h_1 h_3 + h_2 h_3 \\ III_{\boldsymbol{H}} &= det\left(\boldsymbol{H}\right) &= h_1 h_2 h_3 \end{cases} \tag{5.26}$$

Based on this definition and using Eq.5.19 and Eq.5.25, the invariants $I_{\boldsymbol{C}}$, $II_{\boldsymbol{C}}$ and $III_{\boldsymbol{C}}$ of $\boldsymbol{C}$ may be defined for use in experiments in terms of the extension ratios rather than in terms of the principal strains E_{ii} as:

$$\left\{\begin{array}{lll} I_{\boldsymbol{C}} & = 3 + 2I_{\boldsymbol{E}} & = \lambda_1^2 + \lambda_2^2 + \lambda_3^2 \\ II_{\boldsymbol{C}} & = 3 + 4I_{\boldsymbol{E}} + 4II_{\boldsymbol{E}} & = \lambda_1^2\lambda_2^2 + \lambda_1^2\lambda_3^2 + \lambda_2^2\lambda_3^2 \\ III_{\boldsymbol{C}} & = 1 + 2I_{\boldsymbol{E}} + 4II_{\boldsymbol{E}} + 8III_{\boldsymbol{E}} & = \lambda_1^2\lambda_2^2\lambda_3^2 \end{array}\right. \tag{5.27}$$

Strain-Displacement Relationship

In the equations describing $\boldsymbol{C}$, $\boldsymbol{E}$, $\boldsymbol{c}$ and $\boldsymbol{e}$, the strain tensors are represented in terms of the deformation gradients $\boldsymbol{F}$ and $\boldsymbol{G}$. It is however important to describe the strains as a function of the displacement. Using the relationship between the displacement and the deformation in Eq.5.11, the right Cauchy-Green strain tensor $\boldsymbol{C}$ can be reexpressed as:

$$\boldsymbol{C} = \boldsymbol{F}^T\boldsymbol{F} = \boldsymbol{I} + \nabla u + \nabla u^T + \nabla u^T \nabla u \tag{5.28}$$

And from Eq.5.19, the Green-Lagrange strain tensor $\boldsymbol{E}$ can be written as:

$$\boldsymbol{E} = \frac{1}{2}\left(\nabla u + \nabla u^T + \nabla u^T \nabla u\right) \tag{5.29}$$

Thus, knowing the displacement vector $\boldsymbol{u}$, the state of a deformed body can be described in terms of the Lagrangian strain tensor $\boldsymbol{E}$ as a function of $\boldsymbol{u}$ and independently of the chosen coordinate system:

$$\boldsymbol{E} = \begin{bmatrix} \epsilon_{11} & \frac{1}{2}\epsilon_{12} & \frac{1}{2}\epsilon_{13} \\ \frac{1}{2}\epsilon_{21} & \epsilon_{22} & \frac{1}{2}\epsilon_{23} \\ \frac{1}{2}\epsilon_{31} & \frac{1}{2}\epsilon_{32} & \epsilon_{33} \end{bmatrix} \tag{5.30}$$

with

$$\left\{\begin{array}{ll} \epsilon_{11} = \frac{\partial u_1}{\partial X_1} + \frac{1}{2}\sum_k \left(\frac{\partial u_k}{\partial X_1}\right)^2; & \epsilon_{12} = \frac{\partial u_1}{\partial X_2} + \frac{\partial u_2}{\partial X_1} + \sum_k \left(\frac{\partial u_k}{\partial X_1}\frac{\partial u_k}{\partial X_2}\right) = \epsilon_{21} \\ \epsilon_{22} = \frac{\partial u_2}{\partial X_2} + \frac{1}{2}\sum_k \left(\frac{\partial u_k}{\partial X_2}\right)^2; & \epsilon_{13} = \frac{\partial u_1}{\partial X_3} + \frac{\partial u_3}{\partial X_1} + \sum_k \left(\frac{\partial u_k}{\partial X_1}\frac{\partial u_k}{\partial X_3}\right) = \epsilon_{31} \\ \epsilon_{33} = \frac{\partial u_3}{\partial X_3} + \frac{1}{2}\sum_k \left(\frac{\partial u_k}{\partial X_1}\right)^2; & \epsilon_{23} = \frac{\partial u_2}{\partial X_3} + \frac{\partial u_3}{\partial X_2} + \sum_k \left(\frac{\partial u_k}{\partial X_2}\frac{\partial u_k}{\partial X_3}\right) = \epsilon_{32} \end{array}\right.$$

5.2.4 Forces and Euler-Cauchy Principle

Consider a finite body Ω moving between an initial configuration Ω_0 and a current configuration Ω_t. Ω occupies a deformed state in Ω_t as a result of being subject to applied forces acting on it and causing its deformation. Applied forces represent the action of the outside exerted on the solid. As a reaction to the external applied forces, internal forces arise inside the material to keep it in equilibrium. The amount of forces within a continuum body can be expressed in terms of stresses based on the principle of Euler and Cauchy.

Applied Forces

In the Eulerian configuration Ω_t associated with an arbitrary deformation $\boldsymbol{x}(\boldsymbol{X}, t)$, Ω is subject to two kinds of applied forces: volume and surface forces. Volume or body forces are forces exerted on the volume, that is on the interior of a body, such as gravitational forces. If ω is a volume domain of Ω, then the volume forces may be expressed by a function f that represents the force density per unit volume of the applied volume forces: $f := \omega \longrightarrow \mathbb{R}^3$. As for surface forces, such as contact forces, they represent forces acting on the surface, that is on the boundary of the body. They may be expressed by a function g that represents the force density per unit surface of the applied surface forces: $g := \partial\omega \longrightarrow \mathbb{R}^3$. With g being applied on a finite portion of the boundary surface $\partial\omega$ of Ω.

Stress Principle of Euler and Cauchy

So far, surface and volume forces acting on a continuum body were introduced. However, the way they are related together was omitted. The Euler and Cauchy stress principle consists of formulating axioms relating these forces together. The fundamental principle is considered as the basis of continuum mechanics and indicates that: *For a deformed body Ω in the current configuration Ω_t which is subject to volume and surface forces represented by the density functions $f(\boldsymbol{x})$ and $g(\boldsymbol{x})$ respectively, there exists a vector $\boldsymbol{t}^s$ such that:*

(a) *Current stress vector:* The surface forces $g(\boldsymbol{x})$ can also be described in terms of $\boldsymbol{t}^s$ as a function of the surface normals $\boldsymbol{n}$. Thus, if $\boldsymbol{L}^s$ is the external load applied on a boundary surface element ds of Ω, then there exists a current internal stress vector $\boldsymbol{t}^s(\boldsymbol{x}, \boldsymbol{n})$ in Ω_t along the unit outer surface normal $\boldsymbol{n}$ at ds of Ω, such as:

$$\boldsymbol{t}^s(\boldsymbol{x}, \boldsymbol{n}) = g(\boldsymbol{x}) = \lim_{ds \to \infty} \frac{d\boldsymbol{L}^s}{ds} \tag{5.31}$$

(b) *Force balance:* For the continuum body Ω to be in equilibrium in Ω_t, the motion equilibrium equations with respect to an arbitrary point P in the body must be satisfied:

$$\int_v \rho \mathbf{\Gamma}^v dv = \int_v \boldsymbol{f}^v dv + \int_s \boldsymbol{t}^s ds \tag{5.32}$$

(c) *Momentum balance:* At the same time, the momentum equilibrium equations must also be satisfied in every point in the body such that:

$$\int_v \rho \mathbf{\Gamma}^v \wedge \boldsymbol{x} dv = \int_v \boldsymbol{f}^v \wedge \boldsymbol{x} dv + \int_s \boldsymbol{t}^s \wedge \boldsymbol{x} ds \tag{5.33}$$

where ρ is the mass density, Γ^v is the acceleration at point P, and $\boldsymbol{f}^v$ and $\boldsymbol{t}^s$ are the external forces. Thus, the fundamental principle of Euler and Cauchy first indicates the existence of an elementary surface vector $\boldsymbol{t}^s(\boldsymbol{x},\boldsymbol{n})\, ds$ along the surface boundaries of the deformed configuration. Then, the stress principle shows that $\boldsymbol{t}^s(\boldsymbol{x},\boldsymbol{n})\, ds$ at a point P is characterized by its geometrical dependency on *only* the surface normal vector $\boldsymbol{n}$ of ds at P. Finally, if the body is in static equilibrium, then the equilibrium equations of motion and momentum must be satisfied for zero acceleration. Thus, the principle asserts that in static equilibrium the resultant forces vector vanishes and that its resulting momentum with respect to the origin, and thus with respect to any arbitrary point (classical property of torsors) also vanishes.

5.2.5 Stress Analysis

In structure mechanics, stress is the measure of the amount of applied forces on a continuum object per unit area. Based on the continuum concept, there are internal forces distributed within the body and produced as reaction to the external applied forces. Stress is therefore a measure of the intensity of these internal forces governing the material particles of the body. Like strains, stresses may also be described by normal stress and shear stress components. Normal stresses are exerted perpendicular to the surface area on which the forces act. They are associated with a stretching or compression of the body and are called tensile and compressive stresses respectively. Further, normal stresses causing both stretching and compression are known as bending stresses. As for shear stresses, they are exerted parallel to the surface. In practice, shear stresses cause twisting of the body or sliding of the material layers over each other and are known as torsional stresses.

Cauchy Stress and Eulerian Equations of Motion

Based on the Euler and Cauchy principle, Cauchy derived one of the most important theorems in continuum mechanics. The Cauchy theorem asserts the existence of an internal second order tensor $\boldsymbol{\sigma}(\boldsymbol{x})$, corresponding to the physically true stress in the material, that is related to the stress vector $\boldsymbol{t}^s(\boldsymbol{x},\boldsymbol{n})$. Further, according to Cauchy's theorem, $\boldsymbol{\sigma}(\boldsymbol{x})$, named the Cauchy's stress tensor, is linear with respect to its second argument $\boldsymbol{n}$. Thus, the theorem states that: *For each point $\boldsymbol{x}$ of Ω in Ω_t and for all normals $\boldsymbol{n}$ at the boundary of Ω, there exists a second order tensor $\boldsymbol{\sigma}(\boldsymbol{x})$ such that*:

$$\boldsymbol{t}^s(\boldsymbol{x},\boldsymbol{n}) = \boldsymbol{\sigma}^T(\boldsymbol{x})\,\boldsymbol{n} \tag{5.34}$$

In matrix form, the relationship between the components of the Cauchy stress vector $\boldsymbol{t}^s_j$ acting on a plane with normal vector $\boldsymbol{n}$ and the components of the Cauchy stress tensor $\boldsymbol{\sigma}_{ij}$ describing the state of stress in the Eulerian configuration can be expressed by:

$$\boldsymbol{t}^s = \begin{bmatrix} t^s_1 \\ t^s_2 \\ t^s_3 \end{bmatrix} = \begin{bmatrix} \sigma_{11} & \sigma_{12} & \sigma_{13} \\ \sigma_{21} & \sigma_{22} & \sigma_{23} \\ \sigma_{31} & \sigma_{32} & \sigma_{33} \end{bmatrix}^T \cdot \begin{bmatrix} n_1 \\ n_2 \\ n_3 \end{bmatrix} = \boldsymbol{\sigma}^T\boldsymbol{n} \tag{5.35}$$

Applying the divergence theorem for tensor fields on $\boldsymbol{\sigma}$ in Eq.5.34 allows transforming the surface integral appearing in the axiom of force balance Eq.5.32 into a volume integral. As a result, the Eulerian equation of motion in Eq.5.32 becomes:

$$\rho\boldsymbol{\Gamma}^v = \boldsymbol{f}^v + div\left(\boldsymbol{\sigma}^T\right) \tag{5.36}$$

Eq.5.36 vanishes in static equilibrium when the acceleration $\boldsymbol{\Gamma}^v$ becomes zero. Further, applying the Green's formula on $\boldsymbol{\sigma}$ in Eq.5.34 allows transforming the surface integral appearing in the axiom of momentum balance Eq.5.33 into a volume integral. Using in addition Eq.5.36, the symmetry property of the Cauchy stress tensor may be derived such as:

$$\boldsymbol{\sigma}^T = \boldsymbol{\sigma} \tag{5.37}$$

Using Eq.5.37 and Eq.5.36, the equations of motion in the current configuration Ω_t may be also expressed in the form:

$$\rho\frac{\partial^2 u_i}{\partial t^2} = f^v_i + \sum_j \frac{\partial \sigma_{ij}}{\partial x_j} \tag{5.38}$$

The Cauchy theorem and its consequences may be summarized in three points. First, it indicates the existence of the Cauchy stress tensor, related to the Cauchy stress vector and proportional to the normal vector $\boldsymbol{n}$ (Eq.5.34). Second, it asserts that at each point $\boldsymbol{x}$ of $\boldsymbol{\Omega}$ the stress tensor is symmetric (Eq.5.37). This consequence leads to the Voigt notation which allows expressing $\boldsymbol{\sigma}$ in terms of only six independent stress components instead of nine and thus increasing the numerical efficiency of computational structural mechanics. Third, the theorem indicates that the tensor field $\boldsymbol{\sigma}$ and the vector fields f and g are related by partial differential equations in v and by a boundary condition on s, respectively.

Kirchhoff Stresses and Lagrangian Equations of Motion

The Cauchy stress tensor $\boldsymbol{\sigma}$ describes the state of the stress in the current configuration. However, variables defined with respect to the Eulerian configuration are usually unknown. Therefore, these variables as well as the equations of motion must be expressed in the known reference Lagrangian configuration. The equation of motion in the initial configuration is obtained using equations Eq.5.7, Eq.5.8 and Eq.5.36 and by applying the mass conservation principle (Eq.5.69):

$$\int_V \rho_0 \boldsymbol{\Gamma}^V dV = \int_V \boldsymbol{f}^V J dV + \int_S \boldsymbol{T}^T \boldsymbol{N} dS \tag{5.39}$$

where $\boldsymbol{T}$ is obtained from $\boldsymbol{\sigma}$ and represents the first Piola-Kirchhoff stress tensor:

$$\boldsymbol{T} = J\boldsymbol{G}\boldsymbol{\sigma} \tag{5.40}$$

$\boldsymbol{T}$, also known as the Lagrange tensor, describes the forces in the present configuration related to areas in the reference configuration. It therefore corresponds to the internal stress tensor that would be obtained by applying the current external load onto the initial undeformed configuration. In general, the components of the 1st Piola-Kirchhoff stress tensor depend on the orientation of the body with $\boldsymbol{T}^T \neq \boldsymbol{T}$. The first Kirchhoff stress tensor is thus not symmetric. However, the constitutive equations in the reference configuration take usually a simpler form when related to a symmetric stress tensor. The second Kirchhoff stress tensor $\boldsymbol{S}$ is therefore introduced. $\boldsymbol{S}$ may be obtained from the first tensor $\boldsymbol{T}$ such as:

$$\boldsymbol{S} = \boldsymbol{T}\boldsymbol{G}^T = J\boldsymbol{G}\boldsymbol{\sigma}\boldsymbol{G}^T \tag{5.41}$$

The second Kirchhoff stress tensor is symmetric and its components are independent on the orientation of the body. It relates forces and areas defined in the initial configuration. $\boldsymbol{S}$ corresponds to the internal stress tensor defined in the initial configuration and equivalent to the current stress tensor. It preserves and takes into account all geometrical changes between both configurations [MS91]. Based on $\boldsymbol{S}$, the current equation of motion in the Lagrangian configuration then becomes:

$$\int_V \rho_0 \boldsymbol{\Gamma}^V dV = \int_V \boldsymbol{f}^V J dV + \int_S \boldsymbol{F}\boldsymbol{S}^T \boldsymbol{N} dS \tag{5.42}$$

5.2.6 Virtual Work Principle

In absence of analytical resolution approaches for the equations of motion described in Eq.5.36 and Eq.5.38, the kinematics of the system must be resolved using another principle. The finite element representation is usually formulated in terms of a (weak) variational form of the dynamics differential equations. In structural mechanics, the weak variational formulation is achieved using the principle of virtual work.
If $\partial\hat{\boldsymbol{u}}$ denotes an arbitrary virtual displacement in the current configuration of the body Ω, and $\boldsymbol{r}$ is a residual force applied on Ω, then the virtual mechanical work $\partial\hat{W}$ applied to Ω by $\boldsymbol{r}$ during $\partial\hat{\boldsymbol{u}}$ per unit volume and time is:

$$\partial\hat{W} = \boldsymbol{r}\partial\hat{\boldsymbol{u}} \tag{5.43}$$

In static equilibrium, the virtual work $\partial\hat{W}$ vanishes implying that equation Eq.5.43 becomes zero.

Variational Formulation in the Eulerian Configuration

The local equation of virtual work in the current configuration is obtained by applying the principle of virtual work to (Eq.5.36). The inner product of a vector field $\partial\hat{\boldsymbol{u}}^T$ that vanishes on a part s' of the boundary surface s, where the essential boundary conditions are prescribed, gives:

$$\partial\hat{\boldsymbol{u}}^T \rho \boldsymbol{\Gamma}^v = \partial\hat{\boldsymbol{u}}^T \boldsymbol{f}^v + \partial\hat{\boldsymbol{u}}^T div\left(\boldsymbol{\sigma}^T\right) \tag{5.44}$$

Integrating (Eq.5.44) over v and applying a divergence transformation leads to the variational weak form:

$$\int_v \partial\hat{\boldsymbol{u}}^T \rho \boldsymbol{\Gamma}^v dv = \int_v \partial\hat{\boldsymbol{u}}^T \boldsymbol{f}^v dv + \int_s \partial\hat{\boldsymbol{u}}^T \boldsymbol{t}^s \boldsymbol{n} ds - \int_v tr\left(\partial\hat{\boldsymbol{e}}^T \boldsymbol{\sigma}\right) dv \tag{5.45}$$

Transformation to the Lagrangian Configuration

The description of the state variables in the Lagrangian configuration in terms of the Eulerian stress and strain tensors $\boldsymbol{\sigma}$ and $\boldsymbol{e}$ may be obtained from Eq.5.5, Eq.5.19, Eq.5.23 and Eq.5.41:

$$\partial \boldsymbol{e} = \boldsymbol{G}^T \partial \boldsymbol{E} \boldsymbol{G} \quad and \quad \boldsymbol{\sigma} = J^{-1} \boldsymbol{F} \boldsymbol{S} \boldsymbol{F}^T \tag{5.46}$$

The variational weak form described in Eq.5.45 may be then derived in the reference configuration using Eq.5.46 such as:

$$\int_V \partial \hat{\boldsymbol{u}}^T \rho_0 \boldsymbol{\Gamma}^V dV = \int_V \partial \hat{\boldsymbol{u}}^T \boldsymbol{f}^V dV + \int_S \partial \hat{\boldsymbol{u}}^T \boldsymbol{t}^S \boldsymbol{N} dS - \int_V tr\left(\partial \hat{\boldsymbol{E}}^T \boldsymbol{S}\right) dV \tag{5.47}$$

where $\boldsymbol{\Gamma}^V$, $\boldsymbol{f}^V$ and $\boldsymbol{t}^S$ are the reference acceleration and external actions equivalent to $\boldsymbol{\Gamma}^v$, $\boldsymbol{f}^v$ and $\boldsymbol{t}^s$ used in the current configuration.

5.3 Physical Constitutive Laws

A boundary value problem consists of equilibrium, kinematical and constitutive equations together with prescribed and natural boundary conditions. Constitutive laws label all that we do not know about the boundary value problem. In the previous section stresses and strains were described as state variables reflecting force and deformation measurements. Thereby, the deformation was written in terms of the strains while the equilibrium equations were expressed in terms of the internal stresses. The way these variables depend on each other was omitted. The present section consists of formulating constitutive equations relating the stresses in the material to the strains it undergoes. Constitutive relationships are material specific functions describing the deformation response of a material when a force acts on it. They represent a relation between physical variables which do not follow directly from a physical law. Combined with the equilibrium equations that do represent physical laws, a physical problem can be solved.

Constitutive relationships are obviously influenced by the type of material under consideration. Common material descriptions are hereby hyperelastic, elastoplastic, viscoplastic and viscoelastic models. Furthermore, constitutive equations may be time-independent as in the case of small strain linear elastic models, or strain-rate dependent as in the case of viscous materials. They also depend on further physical properties such as compressibility or anisotropy.

5.3.1 Elasticity Theory

In general, a material for which the internal stress at any point P is a function of the current strain associated with that point is known as elastic. Further, the *theory of elasticity* states that *the stress at any time t depends only upon the local deformation at that time, and not upon the history of the deformation* [OS89]. The constitutive behavior of elastic materials may be described as a function relating the deformation gradient tensor $\boldsymbol{F}$ and the Piola-Kirchhoff second stress tensor $\boldsymbol{S}$. Thereby, the objectivity principle must be satisfied, stating that the internal state of the material must be invariant when the current configuration undergoes a rigid body deformation. Thus, decomposing $\boldsymbol{F}$ into an orthogonal rotation $\boldsymbol{R}$ and a right $\boldsymbol{U}$ or left $\boldsymbol{V}$ stretch tensors gives:

$$\boldsymbol{F} = \boldsymbol{R}\boldsymbol{U} = \boldsymbol{R}\boldsymbol{C}^{-1} \quad \textit{and} \quad \boldsymbol{F} = \boldsymbol{V}\boldsymbol{R} = \boldsymbol{B}^{-1}\boldsymbol{R} \tag{5.48}$$

$\boldsymbol{S}$ should not depend on the rotation component but rather on $\boldsymbol{F}$ only through the stretch component, for instance through the right Cauchy-Green dilation tensor $\boldsymbol{C} = \boldsymbol{U}^2 = \boldsymbol{F}^T\boldsymbol{F}$. The formulation of elasticity thus becomes:

$$\boldsymbol{S} = \boldsymbol{S}(\boldsymbol{F}) = \boldsymbol{S}(\boldsymbol{C}) \tag{5.49}$$

Nonlinear Elasticity

Nonlinear elasticity includes physical and geometrical nonlinearities. Physical nonlinearities may be described by the nonlinear function between stress and strain, for instance between $\boldsymbol{S}$ and $\boldsymbol{C}$. As for geometrical nonlinearities, they are described by the nonlinear relationship between the strain and the deformation, for instance between $\boldsymbol{C}$ and $\boldsymbol{F}$. Considering an isotropic material, the general constitutive Eq.5.49 may be developed as follows:

$$\boldsymbol{S}(\boldsymbol{C}) = a_0\boldsymbol{I} + a_1\boldsymbol{C} + \cdots + a_n\boldsymbol{C}^n \tag{5.50}$$

Further, based on the Cayley-Hamilton theorem, the tensor $\boldsymbol{C}$ must satisfy its own characteristic equation:

$$\boldsymbol{C}^3 - I_C\boldsymbol{C}^2 + II_C\boldsymbol{C} - III_C\boldsymbol{I} = \boldsymbol{0} \tag{5.51}$$

As a result, the formulation of nonlinear elasticity in Eq.5.50 may be expressed in terms of $\boldsymbol{C}$ or $\boldsymbol{E}$ as :

$$\boldsymbol{S}(\boldsymbol{C}) = a_0\boldsymbol{I} + a_1\boldsymbol{C} + a_2\boldsymbol{C}^2 \qquad \text{or} \qquad \boldsymbol{S}(\boldsymbol{E}) = \alpha_0\boldsymbol{I} + \alpha_1\boldsymbol{E} + \alpha_2\boldsymbol{E}^2 \tag{5.52}$$

where a_0, a_1, a_2 and $\alpha_0, \alpha_1, \alpha_2$ are fucntions of the invariants I_C, II_C, III_C and I_E, II_E, III_E, respectively.

Linear Elasticity

A continuous material is said to be linear elastic if both geometrical and physical linearities apply [Lei74]. Geometrical linearity may be assumed if the Eulerian and Lagrangian configurations are very close and approximately the same. In case of small deformations, the geometrical linear relation derived from Eq.5.52 and expressed in terms of the infinitesimal strain ϵ becomes:

$$\boldsymbol{\sigma}\left(\boldsymbol{\epsilon}\right) \approx \alpha_0 \boldsymbol{I} + \alpha_1 \boldsymbol{\epsilon} + \alpha_2 \boldsymbol{\epsilon}^2 \tag{5.53}$$

Physical linearity may be assumed if the stress and the strain tensors, $\boldsymbol{S}$ and $\boldsymbol{E}$, are related by a linear law. This may be obtained by developing the tensor $\boldsymbol{C}$ and its invariants in terms of the tensor $\boldsymbol{E}$ and its invariants and by omitting all existent quadratic terms. In this case, the physical linear relation derived from equations Eq.5.52 becomes:

$$\boldsymbol{S} = \boldsymbol{S}^0 + \lambda I_E \boldsymbol{I} + 2\mu \boldsymbol{E} \tag{5.54}$$

with $\boldsymbol{S}^0 = [0]$ since the initial undeformed state of the material is also unstressed. λ and μ are known as the *Lamé constants*. Combining both linearities together, the constitutive relationship for linear elastic materials may be described in terms of the *Hooke law* as:

$$\boldsymbol{\sigma} = \boldsymbol{K}^E \boldsymbol{\epsilon} = \lambda tr(\boldsymbol{\epsilon}) \boldsymbol{I} + 2\mu \boldsymbol{\epsilon} \tag{5.55}$$

For purpose of rheological experimentation, other forms of the Hooke law have been developed by introducing the *Young modulus* E and the *Poisson coefficient* ν defined by:

$$E = \frac{\mu\left(3\lambda + 2\mu\right)}{\lambda + \mu} \quad \text{and} \quad \nu = \frac{\lambda}{2\lambda + \mu} \tag{5.56}$$

And the vectorial form of the Hooke's law in terms of E and ν becomes:

$$\begin{bmatrix} \sigma_{11} \\ \sigma_{22} \\ \sigma_{33} \\ \sigma_{i<j} \end{bmatrix} = \frac{E}{\left(1+\nu\right)\left(1-2\nu\right)} \begin{bmatrix} 1-\nu & \nu & \nu & 0 \\ \nu & 1-\nu & \nu & 0 \\ \nu & \nu & 1-\nu & 0 \\ 0 & 0 & 0 & \frac{(1-2\nu)}{2} \end{bmatrix} \begin{bmatrix} \epsilon_{11} \\ \epsilon_{22} \\ \epsilon_{33} \\ 2\epsilon_{i<j} \end{bmatrix}$$

Nonlinear Hyperelasticity

Hyperelasticity describes nonlinear elastic materials which behavior is indeed path-independent. Thereby, during a deformation process, the work done by the stresses only depends on the initial and final configurations at times t_0 and t. While linear elasticity is characterized by its mathematical simplicity, most biological soft tissue are hyperelastic materials. Therefore, hyperelastic constitutive behavior is particularly convenient in biomechanical modeling. It indeed constitutes the basis for more complex material models derivation.

Hyperelastic constitutive equations may be described by a stored strain energy function W relating the first Piola-Kirchhoff stress tensor $\boldsymbol{T}$ to the deformation gradient tensor $\boldsymbol{F}$:

$$\boldsymbol{T} = \frac{\partial W(\boldsymbol{F})}{\partial \boldsymbol{F}} \tag{5.57}$$

W describes the internal elastic potential stored in the material per unit undeformed volume resulting from the work done by the stresses from the initial to the current position, as a function of the strain at that point in the material. Introducing again $\boldsymbol{F}$ through $\boldsymbol{C}$ to account for the objectivity principle and using Eq.5.41 for the second Piola-Kirchhoff stress tensor $\boldsymbol{S}$, the hyperelasticity equation becomes:

$$\boldsymbol{S} = 2\frac{\partial W(\boldsymbol{C})}{\partial \boldsymbol{C}} \tag{5.58}$$

Considering an isotropic material, the strain energy function $W(\boldsymbol{C})$ may be written in terms of the three invariants of $\boldsymbol{C}$ as $W(I_C, II_C, III_C)$. As a result, $\boldsymbol{S}$ in Eq.5.58 may be developed as follows:

$$\boldsymbol{S} = 2\left[W_I \frac{\partial I_C}{\partial \boldsymbol{C}} + W_{II} \frac{\partial II_C}{\partial \boldsymbol{C}} + W_{III} \frac{\partial III_C}{\partial \boldsymbol{C}}\right] \tag{5.59}$$

The derivatives of the invariants may be obtained from the characteristic Eq.5.51 such as:

$$\frac{\partial I_C}{\partial \boldsymbol{C}} = \boldsymbol{I}; \quad \frac{\partial II_C}{\partial \boldsymbol{C}} = I_C\boldsymbol{I} - \boldsymbol{C}; \quad \frac{\partial III_C}{\partial \boldsymbol{C}} = II_C\boldsymbol{I} - I_C\boldsymbol{C} + \boldsymbol{C}^2 \tag{5.60}$$

Inserting Eq.5.60 into Eq.5.59, the general forms of elasticity obtained in Eq.5.52 may be found again. Thereby, the specific hyperelasticity coefficients are:

$$\begin{gathered} a_0 = 2\left(W_I + I_C W_{II} + II_C W_{III}\right), \\ a_1 = -2\left(W_{II} + I_C W_{III}\right) \qquad \text{and} \qquad a_2 = 2W_{III} \end{gathered} \tag{5.61}$$

5.3.2 Anisotropy

Anisotropy is a mechanical property that describes the direction-dependent constitutive behavior of the material. In soft tissue, it results from material degeneration leading to an increase in mechanical anisotropy with the circumferential stiffening direction. Planar biaxial mechanical evaluation allows for 3D constitutive modeling as well as investigation of the nature of mechanical anisotropic behavior. The general form of the strain energy function for an anisotropic hyperelastic material may be decomposed into two parts: an isotropic component related to the matrix material and an anisotropic component characterizing the orientation of the material fibers.

$$W = W\left(\boldsymbol{C}, \theta\right) = W_{isotropic}\left(\boldsymbol{C}\right) + W_{anisotropic}\left(\boldsymbol{C}, \theta\right) \tag{5.62}$$

where θ denotes the angle between the fiber reinforcement vectors and the circumferential stiffening direction of the wall. The isotropic part includes the isochoric and the volumetric elastic responses of the material and must be written in terms of the three invariants of $\boldsymbol{C}$ only. As for the anisotropic part, it can be expressed as scalar-valued functions in terms of the invariants I_i, $i = 4, \cdots, 8$:

$$W = W_{isotropic}\left(I_1, I_2, I_3\right) + W_{anisotropic}\left(I_4, I_5, I_6, I_7, I_8\right) \tag{5.63}$$

Where the isotropic invariants are:

$$\begin{cases} I_1 = I_{\boldsymbol{C}} & = tr\left(\boldsymbol{C}\right) \\ I_2 = II_{\boldsymbol{C}} & = \frac{1}{2}\left[tr\left(\boldsymbol{C}\right)^2 - tr\left(\boldsymbol{C}^2\right)\right] \\ I_3 = III_{\boldsymbol{C}} & = det\left(\boldsymbol{C}\right) \end{cases} \tag{5.64}$$

And the anisotropic invariants are expressed in terms of $\boldsymbol{C}$, $\boldsymbol{a}_0$, and $\boldsymbol{b}_0$ as:

$$\begin{cases} I_4 = \boldsymbol{a}_0.\boldsymbol{C}.\boldsymbol{a}_0 & & I_5 = \boldsymbol{a}_0.\boldsymbol{C}^2.\boldsymbol{a}_0 \\ & I_6 = \boldsymbol{a}_0.\boldsymbol{C}.\boldsymbol{b}_0 & \\ I_7 = \boldsymbol{b}_0.\boldsymbol{C}.\boldsymbol{b}_0 & & I_8 = \boldsymbol{b}_0.\boldsymbol{C}^2.\boldsymbol{b}_0 \end{cases} \tag{5.65}$$

with $\boldsymbol{a}_0$ and $\boldsymbol{b}_0$ represent the directions of the collagen fibers:

$$[\boldsymbol{a}_0] = [\cos\theta \quad \sin\theta \quad 0] \qquad \text{and} \qquad [\boldsymbol{b}_0] = [\cos\theta \quad -\sin\theta \quad 0] \tag{5.66}$$

The material parameters of W used to model the anisotropic behavior may be obtained by means of nonlinear regression analysis fitting the model to biaxial representative stress-stretch experimental data.

A material is said to be isotropic, if its constitutive behavior can be assumed to be identical in any chosen material direction/axes. For a hyperelastic material, this requires that the strain energy function relationship W must be independent on the fiber orientation angle θ. Thus, the anisotropic contribution $W_{anisotropic}$ in Eq.5.63 vanishes and the strain energy function W expressed only as a function of the invariants of $\boldsymbol{C}$ becomes for an isotropic material:

$$W = W\left(\boldsymbol{C}\right) = W_{isotropic}\left(I_C, II_C, III_C\right) \tag{5.67}$$

5.3.3 Compressibility

Compressibility is related to the change in volume of a material once subjected to a force or pressure. Its relative magnitude is usually measured in terms of the compressibility modulus κ, defined as the relative volume decrease caused by an applied increase in pressure. For an isothermal process, κ is given by:

$$\kappa = -\frac{1}{V}\frac{\partial V}{\partial p} = \frac{1}{K} \tag{5.68}$$

where K is the bulk modulus, defined as the inverse of the compressibility and measures the resistance of a material to an applied compression. Using the mass conservation principle and Eq.5.7, and to account for both configurations, compressibility may also be expressed by the Jacobian J of the deformation gradient tensor $\boldsymbol{F}$:

$$J = det\left(\boldsymbol{F}\right) = \frac{dv}{dV} = \frac{\rho_0}{\rho} \tag{5.69}$$

If at large deformations, the change in volume is negligible compared to the change in shape, then $J = 1$ and the material is said to be incompressible [OS89]. In practice however, large strain processes in soft-tissue applications take place under nearly incompressible conditions. Nearly incompressible materials denote truly incompressible materials which still include a small volumetric deformation in their numerical treatment. Thus, although J may be replaced by 1 in the case of incompressibility, retaining J in the upcoming equations is necessary to describe the nearly incompressible case. This has the advantage that the finite element analysis is not strictly constrained, and hence numerical stability is enforced. For an isotropic incompressible material subjected to a hydrostatic pressure p, it is physically appropriate to separate the p component from the true deviatoric component of the stress tensor. For applications in biomechanics, the true Cauchy stress tensor may be decomposed into an elastic and a pressure stress components:

$$\boldsymbol{\sigma} = \boldsymbol{\sigma}'\left(\boldsymbol{C}\right) - p\boldsymbol{I} \tag{5.70}$$

Substituting Eq.5.70 into Eq.5.40 and Eq.5.41, similar decomposition can be established in terms of the Lagrangian stress tensors. The equivalent second Piola-Kirchhoff stress tensor may be expressed as:

$$\boldsymbol{S} = \boldsymbol{S}'\left(\boldsymbol{C}\right) - pJ\boldsymbol{C}^{-1} \tag{5.71}$$

The above equation is important as it enables the hydrostatic pressure p to be directly evaluated from S:

$$p = \frac{1}{3} tr\left(\boldsymbol{\sigma}\right) = \frac{1}{3} J^{-1} tr\left(\boldsymbol{SC}\right) \tag{5.72}$$

Further, from Eq.5.3, Eq.5.16, Eq.5.51 and Eq.5.60 we have:

$$III_C = J^2 \qquad \text{and} \qquad \frac{\partial III_C}{\partial \boldsymbol{C}} = III_C \boldsymbol{C}^{-1} \tag{5.73}$$

Thus, assuming a hyperelastic material and using Eq.5.73, the second Piola-Kirchhoff stress tensor becomes:

$$\boldsymbol{S} = \boldsymbol{S}'\left(\boldsymbol{C}\right) - \frac{p}{J}\frac{\partial III_C}{\partial \boldsymbol{C}} \tag{5.74}$$

Furthermore, it is useful to isolate the third determinant III_C governing the compressibility in the strain energy function. W may be therefore expressed as a sum of two differentiable functions by decomposing it into a distortional energy component W_1 and a dilatational energy component W_2 involving the volume properties such that:

$$W\left(I_C, II_C, III_C\right) = W_1\left(I_C, II_C\right) + W_2\left(III_C\right) \tag{5.75}$$

Using Eq.5.75, and writing W_2 as a function of the *Lagrange multiplier* L, the second Piola-Kirchhoff stress tensor $\boldsymbol{S}$ in Eq.5.58 becomes:

$$\boldsymbol{S} = \frac{\partial W_1\left(I_c, II_c\right)}{\partial \boldsymbol{E}} + \frac{\partial W_2\left(III_c\right)}{\partial \boldsymbol{E}} = \boldsymbol{S}'\left(\boldsymbol{C}\right) + L\frac{\partial III_c}{\partial \boldsymbol{E}} \tag{5.76}$$

Alternatively, the dilatational component W_2 in the strain energy function may be expressed in terms of $U\left(J\right)$ as a function of the *bulk modulus* K, so that the incompressibility constraint is generally enforced by L or K being related to the hydrostatic pressure p as follow:

$$L = -\frac{p}{2J} \qquad \text{or} \qquad K = \frac{p}{J-1} \tag{5.77}$$

5.3.4 Hyperelastic Models

As mentioned, the constitutive behavior of materials may be described using 3D stress-strain relationships. For most soft tissue, the mechanical properties follow hyperelastic material laws. Their constitutive response can be therefore modeled using a strain energy function, from which stress-strain equations may be derived. The aim of experimentation is to predict the mechanical behavior of the materials by describing their constitutive properties. While for linear elastic materials this is trivial, quantifying the mechanical response of nonlinear materials remains a challenging task due to lack in measurement methods. Formulating general mathematical models to predict the constitutive response of a material under well-defined conditions is therefore very helpful. In the following, various available forms of strain energy functions for hyperlastic models useful for use in soft-tissue modeling are presented. The general form of the strain energy function W for an isotropic material may be written as a function of the three invariants. In an undeformed state, $I_C = I_1 = 3$, $II_C = I_2 = 3$ and $III_C = I_3 = 1$. Thus, W per unit of reference volume may be expressed as a Taylor series in power of $(I_1 - 3)$, $(I_2 - 3)$ and $(I_3 - 1)$ [Ogd84]:

$$W = \sum_{p,q,r=0}^{\infty} c_{p,q,r} \left(I_1 - 3\right)^p \left(I_2 - 3\right)^q \left(I_3 - 1\right)^r \tag{5.78}$$

The constitutive law parameters are quantified via experimentation. For application in experiments, it is more appropriate to express the strain energy function in terms of the extension ratios λ_1, λ_2 and λ_3. Thus, using Eq.5.27, W described in Eq.5.78 may be written as [Ogd84]:

$$W = \sum_{p,q,r=0}^{\infty} a_{p,q,r} \left\{\left[\lambda_1^p \left(\lambda_2^q + \lambda_3^q\right) + \lambda_2^p \left(\lambda_3^q + \lambda_1^q\right) + \lambda_3^p \left(\lambda_2^q + \lambda_1^q\right)\right] \left(\lambda_1\lambda_2\lambda_3\right)^r - 6\right\} \tag{5.79}$$

with $c_{000} = a_{000} = 0$ and (p, q, r) are integer numbers.

- **Polynomial Forms:**
  Based on the distortional and dilatational energy components W_1 and W_2 the general polynomial form of W may be written as:

  $$W\left(I_1, I_2, I_3\right) = \sum_{p+q=1}^{N} c_{p,q,0} \left(I_1 - 3\right)^p \left(I_2 - 3\right)^q + \sum_{r=1}^{M} c_{0,0,r} \left(I_3 - 1\right)^r \tag{5.80}$$

  where the first terms give the initial shear modulus $\mu_0 = 2\left(c_{1,0,0} + c_{0,1,0}\right)$. A particular case of the polynomial form is the second-order *Mooney-Rivlin* model obtained for N = M = 2.

- **Reduced Polynomial Forms:**
  If additionally all terms related to the second invariant I_2 can be disregarded, Eq.5.80 leads to the general reduced polynomial form:

$$W\left(I_1, I_3\right) = \sum_{p=1}^{N} c_{p,0,0}\left(I_1 - 3\right)^p + \sum_{r=1}^{M} c_{0,0,r}\left(I_3 - 1\right)^r \tag{5.81}$$

  Particular cases of the reduced polynomial model are for instance the first-order *Neo-Hookean* and the third-order *Yeoh* potentials obtained for N = M equal 1 and 3, respectively.

- **Ogden Form:**
  In the Ogden model, W is formulated in terms of the extension ratios described in Eq.5.79. It is derived by expressing the distortional and dilatational energy components W_1 and W_2 in terms of λ_i such that:

$$W = \sum_{p=1}^{N} 2a_{p,0,0}\left(\lambda_1^p + \lambda_2^p + \lambda_3^p - 3\right) + \sum_{r=1}^{M} 6a_{0,0,r}\left[\left(\lambda_1\lambda_2\lambda_3\right)^r - 1\right] \tag{5.82}$$

  The Ogden forms are generally more accurate in fitting experimental results, require however multiple uni- and biaxial test data to be available.

- **Exponential Form:**
  In some applications, it is convenient to express W as an exponential relation. The form was derived on the basis of the uniaxial exponential relation first developed by Fung. In terms of the invariants it integrated in the form [Sny72]:

$$W\left(I_1, I_2, I_3\right) = \sum_{p+q=1}^{N} c_{p,q,0}\; e^{\alpha(I_1-3)^p + \beta(I_2-3)^q} + W_2\left(I_3\right) \tag{5.83}$$

- **Saint Venant-Kirchhoff Model:**
  Finally, it is worth to mention that the simplest form of a hyperelastic material is the St. Venant-Kirchhoff model, being an extension of the linear elasticity to the nonlinear regime. It is obtained analog to the Hooke's law defined in Eq.5.55 by replacing the infinite strain ϵ by the Lagrangian Green strain $\boldsymbol{E}$. It has the form:

$$\boldsymbol{W} = \frac{\lambda}{2}\left[tr(\boldsymbol{E})\right]^2 + \mu tr(\boldsymbol{E}^2) \tag{5.84}$$

  Through few manipulations, W may be expressed in terms of the invariants. In practice however, the St. Venant-Kirchhoff model has been found to be inaccurate beyond the small strain regime.

5.4 Finite Element Method

The basics of continuum mechanics and constitutive laws provide the differential equations necessary to describe the physical behavior of the material system under consideration. Mathematical resolution approaches are needed to obtain temporal and spacial solutions of the unknown state variables. Numerical solutions are obtained by defining necessary transformations of the system of partial differential equations to a discrete formulation of the problem. The Finite Element Method (FEM) is a numerical technique appropriate to solve complex systems of nonlinear partial differential equations which can not be solved via analytical approaches.

Soft-tissue modeling includes in general physical and geometrical nonlinearities. Thus, for realistic simulation of nonlinear processes, resolution methods must take this aspect into account. The nonlinear FEM allows approximating a solution using incremental techniques applied on spatial and temporal finite discretized domains, combined with explicit or implicit integration approaches and updated via appropriate iterative schemes.

5.4.1 Galerkin's Formulations

The general continuous equations of motion in the deformed and the reference coordinates have been derived in terms of the variational forms in Eq.5.45 and Eq.5.47. The Galerkin formulation represents the basis of the FEM in which the basic equations are approximated with appropriate discrete weighting functions and then integrated over the region of interest [Zie89]. It is equivalent to the weak variational equations written in the form of the virtual work principle, such as:

$$\partial \hat{\boldsymbol{W}}^{tot} = \partial \hat{\boldsymbol{W}}^{ext} + \partial \hat{\boldsymbol{W}}^{int} \tag{5.85}$$

In the Eulerian configuration, the Galerkin formulation follows from Eq.5.45 and can be written as:

$$\begin{cases} \partial \hat{\boldsymbol{W}}^{tot} = \int_v \partial \hat{\boldsymbol{u}}^T \rho \boldsymbol{\Gamma}^v dv & \textit{inertial virtual work} \\ \partial \hat{\boldsymbol{W}}^{ext} = \int_v \partial \hat{\boldsymbol{u}}^T \boldsymbol{f}^v dv + \int_s \partial \hat{\boldsymbol{u}}^T \boldsymbol{t}^s \boldsymbol{n} ds & \textit{external virtual work} \\ \partial \hat{\boldsymbol{W}}^{int} = -\int_v \partial \hat{\mathrm{e}}^T \boldsymbol{\sigma}' dv & \textit{internal virtual work} \end{cases} \tag{5.86}$$

where $\boldsymbol{\sigma}'$ and $\mathbf{e}$ are the vectorial forms of the original $\boldsymbol{\sigma}$ and $\boldsymbol{e}$ tensors.

Similarly, in the form of the virtual work principle, the Galerkin formulation in the Lagrangian configuration is equivalent to the variational equations derived in Eq.5.47 and written as:

$$\begin{cases} \partial\hat{\boldsymbol{W}}^{tot} = \int_V \partial\hat{\boldsymbol{u}}^T \rho_0 \boldsymbol{\Gamma}^V dV & \textit{inertial virtual work} \\ \partial\hat{\boldsymbol{W}}^{ext} = \int_V \partial\hat{\boldsymbol{u}}^T \boldsymbol{f}^V dV + \int_S \partial\hat{\boldsymbol{u}}^T \mathbf{t}^S \boldsymbol{N} dS & \textit{external virtual work} \\ \partial\hat{\boldsymbol{W}}^{int} = -\int_V \partial\hat{\mathbf{E}}^T \mathbf{S} dV & \textit{internal virtual work} \end{cases} \tag{5.87}$$

where $\mathbf{S}$ and $\mathbf{E}$ are the vectorial forms of the original $\boldsymbol{S}$ and $\boldsymbol{E}$ tensors.

5.4.2 Geometric Discretization

The FEM is based on the geometrical discretization of the continuous domain Ω by approximating the space to a discrete domain of finite element meshes with regular shapes. As a result, any continuous function $g(P)$ applied to a point P in Ω may be expressed as an interpolated function of the discrete mesh by a finite system of equations $g(N_i)$ in terms of the node coordinates.

Shape Functions

Shape functions H_i provide a mean for interpolation between the discrete node variables N_i within a finite mesh element. They are defined in a local system (ξ, η, ζ) resulting from an element transformation from the global to the local coordinates. The general interpolation form for approximating an unknown continuous function by a discrete expression may be written as:

$$g(P) = \sum_i^n H_i(\xi_i, \eta_i, \zeta_i) g(N_i) \tag{5.88}$$

with the functions $H_i(\xi_l, \eta_l, \zeta_l) = \delta_{il}$ and δ_{il} is the *Kronecker delta*, reflecting the one-to-one correspondence between the nodes of the parent element in the local and the distorted element in the global coordinate system. In general, any finite element shape compatible with the space dimension to discretize can be used for defining the shape functions. However, the use of functions arising from regular shaped elements with symmetric properties are more convenient to specify the relation between the global and local coordinate systems. Such functions are known as basic shape functions and may be approximated in terms of reduced parameters based on the same polynomial functions for all mesh elements [ZT06]. Their associated interpolation procedures and corresponding elements are known as *isoparametric*.

Further, interpolating a constant function over the simulation domain, that is specifying a constant value of $g(N_i)$ for all N_i, must result in a constant value of $g(P)$. This leads to the characteristic property for standard shape functions stating that $\sum_{i=1}^{n} H_i = 1$ for all nodes n of Ω. In terms of coordinate vectors $\boldsymbol{X}$ and $\boldsymbol{N}$ for an arbitrary point and its corresponding elementary nodes respectively, shape functions may be defined as:

$$\boldsymbol{X} = \sum_{i}^{n} H_i N_i = \boldsymbol{H}\boldsymbol{N} \tag{5.89}$$

Different interpolation schemes for standard shape functions in one, two and three dimensions may be derived from isoparametric procedures for lines, triangles, quadrilaterals, tetrahedrons and hexahedrons. Linear interpolations may be obtained using first-order polynomial functions:

$$\begin{cases} \boldsymbol{X}_{1D-Line} = \frac{1-\xi}{2}\boldsymbol{N}_1 + \frac{1+\xi}{2}\boldsymbol{N}_2 \\ \boldsymbol{X}_{2D-Tri} = \xi\boldsymbol{N}_1 + \eta\boldsymbol{N}_2 + (1-\xi-\eta)\,\boldsymbol{N}_3 \\ \boldsymbol{X}_{2D-Quad} = \frac{(1-\xi)(1-\eta)}{4}\boldsymbol{N}_1 + \frac{(1+\xi)(1-\eta)}{4}\boldsymbol{N}_2 + \frac{(1+\xi)(1+\eta)}{4}\boldsymbol{N}_3 + \frac{(1-\xi)(1-\eta)}{4}\boldsymbol{N}_4 \\ \boldsymbol{X}_{3D-Tet} = (1-\xi-\eta-\zeta)\,\boldsymbol{N}_1 + \xi\boldsymbol{N}_2 + \eta\boldsymbol{N}_3 + \zeta\boldsymbol{N}_4 \\ \boldsymbol{X}_{3D-Hex} = \sum_{i=1}^{8} h_i\boldsymbol{N}_i \quad \text{with} \quad h_i = \frac{1}{8}(1\pm\xi)(1\pm\eta)(1\pm\zeta) \end{cases}$$

Similarly, different orders of interpolating shape functions can be applied to enhance the accuracy of the mesh element. For higher orders of interpolation, derivatives are additionally needed for the calculation of the coefficients of the polynomials. Nonlinear quadratic interpolations may be obtained using second-order polynomial functions, like for instance the six-node interpolation of a quadratic 2D triangular element described by its shape function:

$$\boldsymbol{H} = [\alpha\,(2\alpha-1) \quad \xi\,(2\xi-1) \quad \eta\,(2\eta-1) \quad 4\xi\alpha \;\; 4\xi\eta \quad 4\eta\alpha] \tag{5.90}$$

with $\alpha = 1 - \xi - \eta$. Extensions of the standard shape functions for finite element programs are well described in relevant literature [Sch91].

Discretized Equations of Motion

In order to apply the geometrical discretization to the continuous equations of motion, the displacement functions $\boldsymbol{u}$ of the application points P of $\boldsymbol{f}_n^V$ and $\boldsymbol{t}_n^S$ as well as their derivatives $\dot{\boldsymbol{u}}$ and $\ddot{\boldsymbol{u}}$ are expressed based on Eq.5.89 in terms of the nodal displacement vectors $\boldsymbol{U}$ such as:

$$\begin{aligned} \boldsymbol{u}^f &= \boldsymbol{H}^f\boldsymbol{U} & \dot{\boldsymbol{u}}^f &= \boldsymbol{H}^f\dot{\boldsymbol{U}} & \ddot{\boldsymbol{u}}^f &= \boldsymbol{H}^f\ddot{\boldsymbol{U}} \\ \boldsymbol{u}^t &= \boldsymbol{H}^t\boldsymbol{U} & \dot{\boldsymbol{u}}^t &= \boldsymbol{H}^t\dot{\boldsymbol{U}} & \ddot{\boldsymbol{u}}^t &= \boldsymbol{H}^t\ddot{\boldsymbol{U}} \end{aligned} \tag{5.91}$$

In addition, the strain-displacement relationship defined in Eq.5.19 may be written in terms of $\boldsymbol{U}$ and the nonlinear differential operator $\boldsymbol{B}$ as $\boldsymbol{E} = \boldsymbol{B}(\boldsymbol{U})\,\boldsymbol{U}$. Consequently, the Galerkin's formulation in Eq.5.87 for the general nonlinear constitutive relationship where $\boldsymbol{S}(\boldsymbol{E}, \dot{\boldsymbol{E}})$ transforms in the weak form of the virtual work as:

$$\partial\hat{\boldsymbol{W}}^{tot} = \partial\hat{\boldsymbol{W}}^{ext} + \partial\hat{\boldsymbol{W}}^{int} \tag{5.92}$$

with

$$\begin{cases} \partial\hat{\boldsymbol{W}}^{tot} = \partial\hat{\boldsymbol{U}}^T \left(\int_V \rho_0 \boldsymbol{H}^T\boldsymbol{H}dV\right)\ddot{\boldsymbol{U}} \\ \partial\hat{\boldsymbol{W}}^{ext} = \partial\hat{\boldsymbol{U}}^T \left(\int_V \boldsymbol{H}^{f^T}\boldsymbol{f}^V dV + \int_S \boldsymbol{H}^{t^T}\boldsymbol{t}^S\boldsymbol{N}dS\right) \\ \partial\hat{\boldsymbol{W}}^{int} = -\partial\hat{\boldsymbol{U}}^T \left[\int_V \mathbf{B}^T\mathbf{S}(\boldsymbol{U}, \dot{\boldsymbol{U}})dV\right] \end{cases} \tag{5.93}$$

where $\mathbf{B}$ and $\mathbf{S}$ are the vectorial forms of the original $\boldsymbol{B}$ and $\boldsymbol{S}$ tensors. The general elementary finite tensorial equation representing the dynamic response of the system is obtained after removing the virtual nodal displacement $\partial\hat{\boldsymbol{U}}$:

$$\boldsymbol{M}\ddot{\boldsymbol{U}} + \boldsymbol{\Pi}\left(\boldsymbol{U}, \dot{\boldsymbol{U}}\right) = \boldsymbol{L} \tag{5.94}$$

with

$$\begin{cases} \boldsymbol{M} = \int_V \rho_0 \boldsymbol{H}^T\boldsymbol{H}dV & \textit{mass matrix} \\ \boldsymbol{\Pi} = \int_V \mathbf{B}^T\mathbf{S}(\boldsymbol{U}, \dot{\boldsymbol{U}})dV & \textit{int. force vector} \\ \boldsymbol{L} = \int_V \boldsymbol{H}^{f^T}\boldsymbol{f}^V dV + \int_S \boldsymbol{H}^{t^T}\boldsymbol{t}^S\boldsymbol{N}dS & \textit{nodal ext. force vector} \end{cases} \tag{5.95}$$

Similar forms for the global tensorial equations may then be derived by combining all the elementary equations. Furthermore, when the stress tensor $\boldsymbol{S}$ may be decomposed in terms of independent viscous and elastic components, such the case of the *Kelvin Voigt* constitutive material, the internal force vector $\boldsymbol{\Pi}$ may be expressed in terms of uncoupled damping $\boldsymbol{D}$ and stiffness $\boldsymbol{K}$ matrices [Hug00], so that the dynamic response defined in Eq.5.94 becomes:

$$\boldsymbol{M}\ddot{\boldsymbol{U}} + \boldsymbol{D}\dot{\boldsymbol{U}} + \boldsymbol{K}\boldsymbol{U} = \boldsymbol{L} \tag{5.96}$$

5.4.3 Incremental Approach

In order to describe the dynamic mesh response to the applied forces, the discretized differential system defined in Eq.5.94 for the global vector $\boldsymbol{U}$ must be solved. In general, solutions for the second-order dynamic equations cannot be obtained in their common nonlinear form. Instead, the nonlinear time-dependent system must be discretized into piecewise finite temporal domains allowing and replaced with linear incremental relations. Iterative step-by-step approximation of the solution may then be applied using linear integration algorithms allowing an incremental update of the variables at each iteration step. Applying incremental approaches requires that all relations are expressed in their incremental forms. The Eulerian incremental approach in which all the variables refer to the deformed state is inconvenient, since the current configuration is the problem unknown to be solved [Kle89]. While in the *Total Lagrangian* approach the variables are described in the original undeformed configuration, the *Updated Lagrangian*, also known as the *Approximate Eulerian*, is more general and has proven to be computationally efficient referring to the recently computed configuration. Thus, referred to any previous configuration, the increments in the Piola-Kirchhoff stress $\boldsymbol{S}_n \equiv \boldsymbol{S}(t_n)$ and the Green-Lagrange strain $\boldsymbol{E}_n \equiv \boldsymbol{E}(t_n)$ variables may be defined as:

$$\Delta \boldsymbol{S} = \boldsymbol{S}_{n+1} - \boldsymbol{S}_n \qquad \text{and} \qquad \Delta \boldsymbol{E} = \boldsymbol{E}_{n+1} - \boldsymbol{E}_n \tag{5.97}$$

Further, writing the increments in strain as a sum of a linear and a nonlinear components using Eq.5.29 gives:

$$\Delta \boldsymbol{E} = \Delta \boldsymbol{E}^L + \Delta \boldsymbol{E}^{NL} \quad \text{with} \tag{5.98}$$

$$\begin{cases} \Delta \boldsymbol{E}^L = \frac{1}{2}\left[\Delta\left(\nabla \boldsymbol{u}_n\right) + \Delta\left(\nabla \boldsymbol{u}_n^T\right) + \Delta\left(\nabla \boldsymbol{u}_n^T\right)\nabla \boldsymbol{u}_n + \nabla \boldsymbol{u}_n^T \Delta\left(\nabla \boldsymbol{u}_n\right)\right] \\ \Delta \boldsymbol{E}^{NL} = \frac{1}{2}\left[\Delta\left(\nabla \boldsymbol{u}_n^T\right)\Delta\left(\nabla \boldsymbol{u}_n\right)\right] \end{cases}$$

Incremental Equations

The elementary Galerkin's equation in the Eulerian configuration at step $n+1$ may be concluded from the known variables at step n using Eq.5.86 such as:

$$\partial \hat{\boldsymbol{W}}_{n+1}^{tot} = \partial \hat{\boldsymbol{W}}_{n+1}^{ext} + \partial \hat{\boldsymbol{W}}_{n+1}^{int} \tag{5.99}$$

With regard to the Lagrangian incremental approach, these Eulerian equations of motion must be moved into the previous configuration where all variables are assumed to be known at step n. The Galerkin's formulation in the Lagrangian configuration may be described as:

$$\begin{cases} \partial\hat{\boldsymbol{W}}^{tot}_{n+1} = \int_V \partial\hat{\boldsymbol{u}}^T_{n+1}\rho_n\boldsymbol{\Gamma}^V_{n+1}dV & \textit{inertial} \\ \partial\hat{\boldsymbol{W}}^{ext}_{n+1} = \int_V \partial\hat{\boldsymbol{u}}^T_{n+1}\boldsymbol{f}^V_{n+1}dV + \int_S \partial\hat{\boldsymbol{u}}^T_{n+1}\boldsymbol{t}^S_{n+1}\boldsymbol{N}dS & \textit{external} \\ \partial\hat{\boldsymbol{W}}^{int}_{n+1} = -\int_V \partial\hat{\mathbf{E}}^T_{n+1}\mathbf{S}_{n+1}dV & \textit{internal} \end{cases} \tag{5.100}$$

where the volume, surface and local normal to the external surface are defined at step n. In contrast to the internal work, the external forces applied on the current -unknown- configuration at step $n+1$ can not be defined in the previous configuration at step n. The work arising from the external forces was therefore expressed by assuming that their description in the previous and current configurations is equal. Using Eq.5.97 and Eq.5.98 and writing $\partial\boldsymbol{E}_{n+1} = \partial(\Delta\boldsymbol{E})$, the internal virtual work defined in Eq.5.100 may be divided into:

$$\partial\hat{\boldsymbol{W}}^{int}_{n+1} = \partial\hat{\boldsymbol{W}}^{LS}_{n+1} + \partial\hat{\boldsymbol{W}}^{L\Delta}_{n+1} + \partial\hat{\boldsymbol{W}}^{NS}_{n+1} + \partial\hat{\boldsymbol{W}}^{N\Delta}_{n+1} \tag{5.101}$$

By defining $\boldsymbol{K}^M_n$ and $\boldsymbol{S}^R_n$ as the tangent material stiffness matrix and the residual constitutive stress respectively, the incremental strain-stress constitutive relationship may be written as:

$$\Delta\boldsymbol{S} = \boldsymbol{K}^M_n\Delta\boldsymbol{E} + \boldsymbol{S}^R_n \tag{5.102}$$

Further, by assuming that $\partial\hat{\boldsymbol{W}}^{N\Delta}_{n+1} = 0$ and $\Delta\boldsymbol{S} \approx \Delta\boldsymbol{S}(\Delta\boldsymbol{E}^L)$ which allow linearizing $\partial\hat{\boldsymbol{W}}^{int}_{n+1}$ in Eq.5.101, the virtual incremental equation of motion defined in Eq.5.99 becomes:

$$\partial\hat{\boldsymbol{W}}^{tot}_{n+1} = \partial\hat{\boldsymbol{W}}^{1}_{n+1} + \partial\hat{\boldsymbol{W}}^{2}_{n+1} + \partial\hat{\boldsymbol{W}}^{3}_{n+1} + \partial\hat{\boldsymbol{W}}^{ext}_{n+1} \tag{5.103}$$

with the first term reflecting the inertial effects, and

$$\begin{cases} \partial\hat{\boldsymbol{W}}^{tot}_{n+1} = \int_V \partial\hat{\boldsymbol{u}}^T_{n+1}\rho_n\boldsymbol{\Gamma}^V_{n+1}dV & \textit{inertial} \\ \partial\hat{\boldsymbol{W}}^{1}_{n+1} = -\int_V \partial\left(\Delta\hat{\mathbf{E}}^L\right)^T\left[\mathbf{S}_n + \mathbf{S}^R_n\right]dV & \textit{internal force} \\ \partial\hat{\boldsymbol{W}}^{2}_{n+1} = -\int_V \partial\left(\Delta\hat{\mathbf{E}}^L\right)^T\mathbf{K}^M_n\Delta\mathbf{E}^L dV & \textit{linear strain} \\ \partial\hat{\boldsymbol{W}}^{3}_{n+1} = -\int_V \partial\left(\Delta\hat{\mathbf{E}}^{NL}\right)^T\left[\mathbf{S}_n + \mathbf{S}^R_n\right]dV & \textit{geometric} \\ \partial\hat{\boldsymbol{W}}^{ext}_{n+1} = \int_V \partial\hat{\boldsymbol{u}}^T_{n+1}\boldsymbol{f}^V_{n+1}dV + \int_S \partial\hat{\boldsymbol{u}}^T_{n+1}\boldsymbol{t}^S_{n+1}\boldsymbol{N}dS & \textit{external} \end{cases} \tag{5.104}$$

Finite Incremental Equations

In order to convert the incremental virtual work defined in Eq.5.104 into a finite element formulation, a discretization as defined in Eq.5.91 is considered, allowing indeed using $\boldsymbol{E} = \boldsymbol{B}\boldsymbol{U}$ to express the linear and nonlinear components of the strain-displacement relations in the form:

$$\Delta\boldsymbol{E}^{L} = \boldsymbol{B}_{n}^{L}\Delta\boldsymbol{U} \qquad \text{and} \qquad \psi\Delta\boldsymbol{E}^{NL} = \Delta\boldsymbol{U}^{T}\boldsymbol{B}_{n}^{NL^{T}}\Psi\boldsymbol{B}_{n}^{NL^{T}}\Delta\boldsymbol{U} \tag{5.105}$$

where, for any matrix ψ, Ψ is a matrix composed of ψ matrices on its diagonal and zeros elsewhere. Thereby, $\Delta\boldsymbol{U}$ represents the incremental nodal displacement at step n. Inserting these into Eq.5.103, the incremental finite virtual formulation for real work ($\Delta\hat{\boldsymbol{U}} \equiv \Delta\boldsymbol{U}$) becomes:

$$\boldsymbol{M}_{n}\ddot{\boldsymbol{U}}_{n+1} + \left(\boldsymbol{K}_{n}^{L} + \boldsymbol{K}_{n}^{NL}\right)\Delta\boldsymbol{U} = \boldsymbol{L}_{n+1} - \boldsymbol{R}_{n} \tag{5.106}$$

with

$$\begin{cases} \boldsymbol{M}_{n} \;= \int_{V}\rho_{n}\boldsymbol{H}^{T}\boldsymbol{H}dV & \textit{tangent mass matrix} \\ \boldsymbol{K}_{n}^{L} \;= \int_{V}\mathbf{B}_{n}^{L^{T}}\mathbf{K}_{n}^{M}\mathbf{B}_{n}^{L}dV & \textit{linear tangent stiffness matrix} \\ \boldsymbol{K}_{n}^{NL} = \int_{V}\mathbf{B}_{n}^{NL^{T}}\left[\mathbf{S}_{n} + \mathbf{S}_{n}^{R}\right]\mathbf{S}_{n}^{NL}dV & \textit{geometric stiffness matrix} \\ \boldsymbol{R}_{n} \;= \int_{V}\mathbf{B}_{n}^{L^{T}}\left[\mathbf{S}_{n} + \mathbf{S}_{n}^{R}\right]dV & \textit{int. force vector} \\ \boldsymbol{L}_{n+1} = \int_{V}\boldsymbol{H}^{f^{T}}\boldsymbol{f}_{n+1}^{V}dV + \int_{S}\boldsymbol{H}^{t^{T}}\boldsymbol{t}_{n+1}^{S}\boldsymbol{N}dS & \textit{nodal ext. force vector} \end{cases} \tag{5.107}$$

In the general case where $\boldsymbol{S} = \boldsymbol{S}(\boldsymbol{E}, \dot{\boldsymbol{E}})$, Eq.5.102 is replaced by:

$$\Delta\boldsymbol{S} = \boldsymbol{K}_{n}^{M}\Delta\boldsymbol{E} + \boldsymbol{D}_{n}^{M}\Delta\dot{\boldsymbol{E}} + \boldsymbol{S}_{n}^{R} \tag{5.108}$$

And the general incremental finite virtual work formulation in Eq.5.106 may be developed from Eq.5.96, after including the tangent damping matrix $\boldsymbol{D}_{n}$ and combining the linear and the nonlinear stiffness terms into the tangent stiffness matrix $\boldsymbol{K}_{n}$, as:

$$\boldsymbol{M}_{n}\ddot{\boldsymbol{U}}_{n+1} + \boldsymbol{D}_{n}\dot{\boldsymbol{U}}_{n+1} + \boldsymbol{K}_{n}\Delta\boldsymbol{U} = \boldsymbol{L}_{n+1} - \boldsymbol{R}_{n} \tag{5.109}$$

with

$$\boldsymbol{R}_{n} = \boldsymbol{L}_{n} - \boldsymbol{M}_{n}\ddot{\boldsymbol{U}}_{n} - \boldsymbol{D}_{n}\dot{\boldsymbol{U}}_{n} \qquad \text{and} \qquad \boldsymbol{R}_{n+1} = \boldsymbol{R}_{n} + \boldsymbol{K}_{n}\Delta\boldsymbol{U} \tag{5.110}$$

5.4.4 Time Integration

Solving for the unknown $\Delta\boldsymbol{U}$, explicit or implicit time integration methods for approximating the acceleration, the velocity and the displacement are provided allowing temporal incremental solutions of the problem.

Explicit Integration Approach

In the explicit time integration, the governing equilibrium is assumed to be known at step n to obtain a solution for the unknown $\Delta\boldsymbol{U}$ at step $n+1$. An explicit formulation based on *central difference* approximations is given by:

$$\ddot{\boldsymbol{U}}_n = \frac{1}{\Delta t^2}\left(\boldsymbol{U}_{n+1} - 2\boldsymbol{U}_n + \boldsymbol{U}_{n-1}\right) = \frac{1}{\Delta t^2}\left[\Delta\boldsymbol{U} - \left(\boldsymbol{U}_n - \boldsymbol{U}_{n-1}\right)\right] \quad (5.111)$$

$$\dot{\boldsymbol{U}}_n = \frac{1}{2\Delta t}\left(\boldsymbol{U}_{n+1} - \boldsymbol{U}_{n-1}\right) = \frac{1}{2\Delta t}\left[\Delta\boldsymbol{U} + \left(\boldsymbol{U}_n - \boldsymbol{U}_{n-1}\right)\right] \quad (5.112)$$

Incremental equations may be then obtained by inserting Eq.5.111 and Eq.5.112 into Eq.5.109 written for $n-1$ to give:

$$\underbrace{\left[\frac{1}{\Delta t^2}\boldsymbol{M}_n + \frac{1}{2\Delta t}\boldsymbol{D}_n\right]}_{\boldsymbol{A}_n}\Delta\boldsymbol{U} = \boldsymbol{L}_n - \underbrace{\left[\boldsymbol{R}_n - \left(\frac{1}{\Delta t^2}\boldsymbol{M}_n - \frac{1}{2\Delta t}\boldsymbol{D}_n\right)\left(\boldsymbol{U}_n - \boldsymbol{U}_{n-1}\right)\right]}_{\boldsymbol{Y}_n}$$

with $\boldsymbol{A}_n$, $\boldsymbol{L}_n$ and $\boldsymbol{Y}_n$ being the effective stiffness matrix, the nodal external force vector and the effective internal force vector respectively, defined at n. The central difference approach is effective if the mass and damping matrices are diagonal, since then no effective stiffness matrix needs to be factorized [Bat96]. Also, it is more effective when used with low-order elements, avoiding the use of quadratic elements. No zero-mass degree of freedom may be employed, otherwise singularities in the displacements will be obtained. Indeed, the explicit approach does not reduce to the static case when the inertial and viscous effects are neglected.

Implicit Integration Approach

The implicit method assumes the equilibrium at $t + \Delta t$ to obtain solution at $t + \Delta t$. The implicit formulations for the finite approximation at step $n+1$ based on the *Newmark method* are written in terms of two parameters:

$$\begin{aligned}
\boldsymbol{U}_{n+1} &= \boldsymbol{U}_n + \dot{\boldsymbol{U}}_n \Delta t + \left[\left(\frac{1}{2} - \alpha \right) \ddot{\boldsymbol{U}}_n + \alpha \ddot{\boldsymbol{U}}_{n+1} \right] \Delta t^2 && (5.113) \\
\dot{\boldsymbol{U}}_{n+1} &= \dot{\boldsymbol{U}}_n + \left[(1-\beta) \ddot{\boldsymbol{U}}_n + \beta \ddot{\boldsymbol{U}}_{n+1} \right] \Delta t && (5.114)
\end{aligned}$$

By deriving $\ddot{\boldsymbol{U}}_{n+1}$ and $\dot{\boldsymbol{U}}_{n+1}$ from these equations and inserting them into Eq.5.109, the incremental dynamics formulation becomes:

$$\boldsymbol{A}_n \Delta \boldsymbol{U} = \boldsymbol{L}_{n+1} - \boldsymbol{Y}_n \tag{5.115}$$

with

$$\begin{cases}
\boldsymbol{A}_n = \frac{1}{\alpha \Delta t^2} \boldsymbol{M}_n + \frac{\beta}{\alpha \Delta t} \boldsymbol{D}_n + \boldsymbol{K}_n \qquad \text{and} \\
\boldsymbol{Y}_n = \boldsymbol{R}_n - \boldsymbol{M}_n \left[\frac{1}{\alpha \Delta t} \dot{\boldsymbol{U}}_n + \left(\frac{1}{2\alpha} - 1 \right) \ddot{\boldsymbol{U}}_n \right] - \boldsymbol{D}_n \left[\left(\frac{\beta}{\alpha} - 1 \right) \dot{\boldsymbol{U}}_n + \frac{\Delta t}{2} \left(\frac{\beta}{\alpha} - 2 \right) \ddot{\boldsymbol{U}}_n \right]
\end{cases}$$

where α and β being the Newmark control parameters enhancing stability and accuracy of the time integration. For $(\alpha; \beta)$ equal $(0.5; 0.25)$ and $(1; 0.5)$, the method reduces to the trapezoil rule and the implicit Euler, respectively. Since the Newmark method assumes the equilibrium at the unknown time $t+\Delta t$, the tangent matrix $\boldsymbol{K}_n$ appears as factor of the required $\Delta \boldsymbol{U}$. A factorization of the effective stiffness matrix is always required, whether the mass and damping matrices are diagonal or banded. The method is more effective when employed with higher-order elements and consistent mass discretization. Furthermore, it can be used for static analysis by neglecting the inertial and viscous effects.

5.4.5 Implicit Iteration Methods

As a result of the incremental formulation, the nonlinear equations must be replaced by finite linear incremental relations. The dynamic equilibrium in the explicit solution is established at the known configuration at time t. Thus, the explicit finite element solution is consistent with the dynamic conditions. On the other hand, the solution in the implicit approach does not satisfy in general the nodal equilibrium accurately. Therefore, improving the implicit solution is necessary, where the equilibrium equations are considered at an unknown $t+\Delta t$ configuration. An effective solution may be obtained by performing additional iterations within each time step based on the *Newton-Raphson* schemes to ensure that nodal point equilibrium is sufficiently satisfied [Kle89].

Full Newton-Raphson

The iterative algorithm used in the full Newton-Raphson scheme to solve the dynamics equations can be described as follow:

$$\boldsymbol{M}_n\ddot{\boldsymbol{U}}^i_{n+1} + \boldsymbol{D}_n\dot{\boldsymbol{U}}^i_{n+1} + \boldsymbol{K}^i_{n+1}\Delta\boldsymbol{U}^i = \boldsymbol{L}_{n+1} - \boldsymbol{R}^{i-1}_{n+1} \qquad \text{with} \tag{5.116}$$

$$\boldsymbol{K}^0_{n+1} = \boldsymbol{K}_n \qquad \boldsymbol{R}^0_{n+1} = \boldsymbol{R}_n \qquad \boldsymbol{U}^0_{n+1} = \boldsymbol{U}_n \qquad \text{as initial conditions}$$

with $i \equiv (1,2,3,\ldots)$ and $\ddot{\boldsymbol{U}}^i_{n+1}$, $\dot{\boldsymbol{U}}^i_{n+1}$ and $\boldsymbol{U}^{i-1}_{n+1} + \Delta\boldsymbol{U}^i$ are the approximations of the nodal acceleration, velocity and displacement vectors obtained at the i-th iteration, respectively. As for the vector of internal nodal force $\boldsymbol{R}^{i-1}_{n+1}$, it is equivalent to the state of element stresses corresponding to the displacements configuration $\boldsymbol{U}^{i-1}_{n+1}$, with $\boldsymbol{U}^{(i)}_{n+1} = \boldsymbol{U}^{(i-1)}_{n+1} + \Delta\boldsymbol{U}^{(i)}$ and where $\Delta\boldsymbol{U}^i$ is the i-th correction to the incremental displacement vector. The full Newton-Raphson iteration algorithm imposes that the effective stiffness matrix is updated and factorized at the beginning of each new iteration load step Fig.5.2 (left).

Modified Newton-Raphson

The use of solution techniques that are less expensive and more efficient in accounting for nonlinear responses where the full scheme does not must be considered. The iterative algorithm may be formulated as:

$$\boldsymbol{M}_n\ddot{\boldsymbol{U}}^i_{n+1} + \boldsymbol{D}_n\dot{\boldsymbol{U}}^i_{n+1} + \boldsymbol{K}_n\Delta\boldsymbol{U}^i = \boldsymbol{L}_{n+1} - \boldsymbol{R}^{i-1}_{n+1} \tag{5.117}$$

In the modified Newton-Raphson iteration scheme the tangent stiffness matrix $\boldsymbol{K}_n$ is not updated at each iteration and the effective stiffness matrix is factorized only once at each time step Fig.5.2 (right). In this case, all nonlinearities are included in the evaluation of the internal nodal force vector $\boldsymbol{R}^{i-1}_{n+1}$.

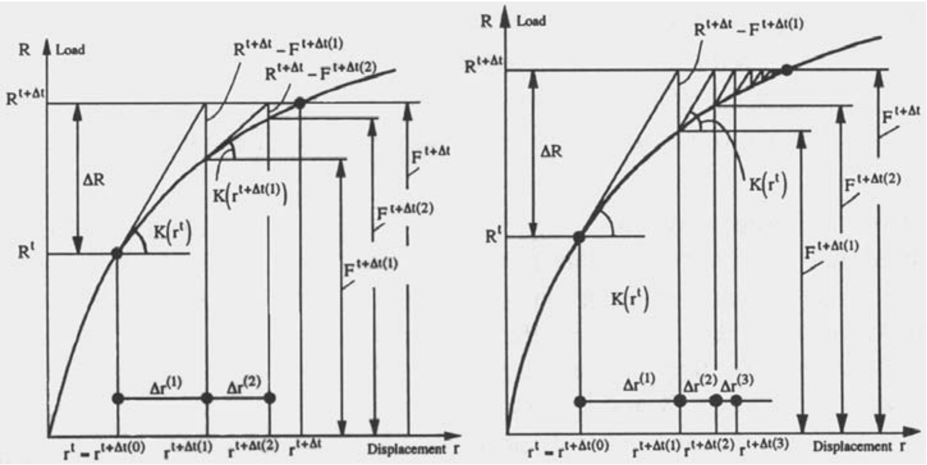
R
Load
$R^{t+\Delta t} - F^{t+\Delta t(1)}$
$R^{t+\Delta t} - F^{t+\Delta t(2)}$
$R^{t+\Delta t}$
ΔR
$F^{t+\Delta t}$
$K(r^{t+\Delta t(1)})$
$F^{t+\Delta t(2)}$
R^t
$K(r^t)$
$F^{t+\Delta t(1)}$
$\Delta r^{(1)}$
$\Delta r^{(2)}$
$r^t = r^{t+\Delta t(0)}$
$r^{t+\Delta t(1)}$
$r^{t+\Delta t(2)}$
$r^{t+\Delta t}$
Displacement r
R
Load
$R^{t+\Delta t} - F^{t+\Delta t(1)}$
$R^{t+\Delta t}$
$F^{t+\Delta t}$
ΔR
$K(r^t)$
$F^{t+\Delta t(2)}$
R^t
$F^{t+\Delta t(1)}$
$K(r^t)$
$\Delta r^{(1)}$
$\Delta r^{(2)}$
$\Delta r^{(3)}$
$r^t = r^{t+\Delta t(0)}$
$r^{t+\Delta t(1)}$
$r^{t+\Delta t(2)}$
$r^{t+\Delta t(3)}$
Displacement r

Figure 5.2: Full and modified Newton-Raphson iterations [Kle89].

5.5 CSM Simulation Models

The theoretical principles described above are applied to simulate the vessel wall as a structure. Three-dimensional computations have been carried out to numerically describe the elastomechanics of the vessel wall domain at any time. The generation of image-based biomechanical models is based on the developed workflow described in Chap.3 and applied to Computational Structure Mechanics (CSM). Based on patient-specific geometries and meshes, static and dynamic physical models, arterial wall material properties, realistic boundary and initial conditions, mathematical solution methods and finally stability analysis are needed and discussed in detail in the following sections. The CSM simulations are based on the FEM approach to compute and evaluate the wall stress distribution (Fig.5.3), vessel deformation (Fig.5.3) and material parameters (Fig.5.5). The numerical solvers of the FEM-based program Abaqus are used to solve the fundamental equations governing the vessel wall domain.

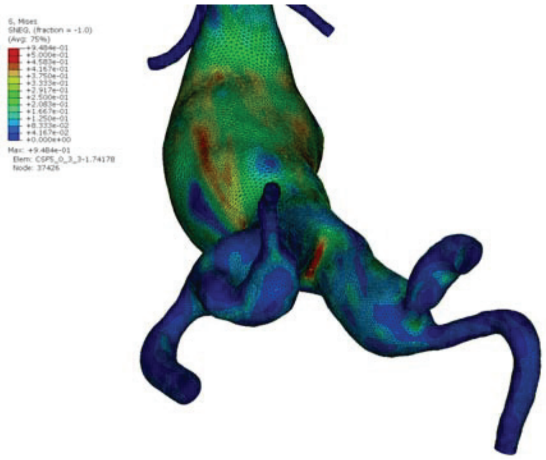
S, Mises
SNEG, (fraction = -1.0)
(Avg: 75%)
+9.484e-01
+5.000e-01
+4.583e-01
+4.167e-01
+3.750e-01
+3.333e-01
+2.917e-01
+2.500e-01
+2.083e-01
+1.667e-01
+1.250e-01
+8.333e-02
+4.167e-02
+0.000e+00
Max: +9.484e-01
Elem: CSPS_0_3_3-1.74178
Node: 37426

Figure 5.3: Stress distribution.

Figure 5.4: Strain analysis.

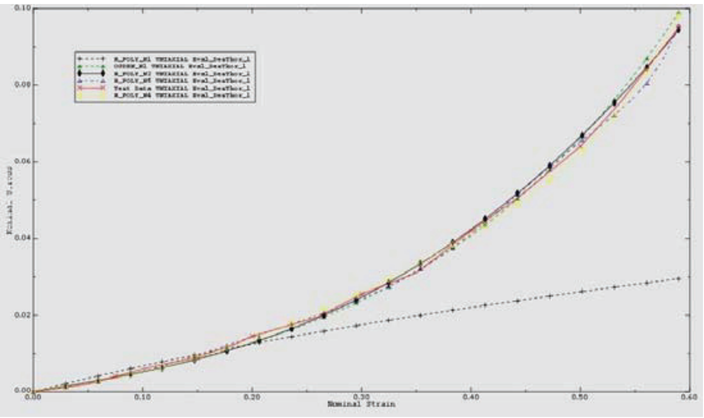

Figure 5.5: Constitutive evaluation of material parameters.

5.5.1 Physical and Constitutive Modeling

Physical modeling is a two-stages process involving two aspects: First the dynamic behavior of the vessel wall is described through the fundamental equations, and second the vessel material properties are described through their constitutive equations.

Wall Governing Equations

The three-dimensional fundamental equations governing the vessel wall domain are described based on the Euler-Cauchy principle. They are represented by the dynamics equations and the symmetry of the Cauchy stress tensor derived from the force and momentum balance equations, respectively. Solving the vessel wall domain is therefore equivalent to solving the boundary value problem represented by the time-dependent equations given by:

$$\rho_w \ddot{\boldsymbol{u}}_w = \boldsymbol{f}_w^v + \nabla \left(\boldsymbol{\sigma}_w^T \right) \tag{5.118}$$

and

$$\boldsymbol{\sigma}_w^T = \boldsymbol{\sigma}_w \tag{5.119}$$

where ρ_w is the wall density, $\ddot{\boldsymbol{u}}_w$ the wall acceleration, $\boldsymbol{\sigma}_w^T$ the current wall stress tensor and $\boldsymbol{f}_w^v$ the wall forces per unit volume.

Wall material properties

A reliable biomechanical analysis of the arterial wall requires not only a precise three-dimensional description of the governing equations, but also appropriate constitutive modeling of the elastomechanical material behavior of the vessel. Structural constitutive models describe the elasticity, the anisotropy and the compressibility of the wall. The arterial wall is assumed to be a homogeneous, isotropic material with the energy strain function W expressed in terms of the three invariants of the Cauchy-Green dilation tensor:

$$W = W_{isotropic}\left(C\right) = W\left(I_1, I_2, I_3\right) \tag{5.120}$$

Many structural studies have used aortic models based on the theory of linearized elasticity. However, ex-vivo experiments show that the vascular tissue is a complex structure, materially nonlinear and that the constitutive behavior of the aortic wall is highly affected by the presence of a pathology, such as an aneurysm or a stenosis, compared to a healthy aorta [RWV96].

Eight vascular models are implemented in this work. Besides a simplified linear elastic model, the vascular tissue is considered as a nonlinear hyperelastic material based on a finite strain constitutive theory assuming that the wall undergoes large displacements prior to rupture.

- **Abdominal Aneurysmal Vascular Model:**
  The constitutive behavior of abdominal aneurysms is based on equations derived from the abdominal aneurysmal arterial tissue. It is mathematically described by a second-order ($n = 2$) reduced polynomial model:

  $$W = c_{100} \left(I_1 - 3\right) + c_{200} \left(I_1 - 3\right)^2 \tag{5.121}$$

  The material parameters of this constitutive model are adapted from realistic measurements obtained from ex-vivo uniaxial testing and analysis of 69 AAAs and estimated to the population mean values [RV00], with:

  $$c_{100} = 0.174 \text{ Nmm}^{-2} \quad \text{and} \quad c_{200} = 1.881 \text{ Nmm}^{-2}$$

- **Thoracic Aneurysmal Vascular Model:**
  The behavior of thoracic aneurysms is based on constitutive equations derived for the thoracic aneurysmal tissue. It is also described by the second-order reduced polynomial model presented in Eq.5.121. Its material parameters are adapted from realistic biaxial tensile data derived from ex-vivo analysis of patients with TAAs [VSE+03]:

  $$c_{100} = 0.11 \text{ Nmm}^{-2} \quad \text{and} \quad c_{200} = 0.53 \text{ Nmm}^{-2}$$

- **Abdominal Healthy Vascular Model:**
  The constitutive modeling of healthy abdominal aortas is derived from measurements performed on healthy human abdominal aortic tissue. It is described by the third-order reduced polynomial model:

  $$W = c_{100} \left(I_1 - 3\right) + c_{200} \left(I_1 - 3\right)^2 + c_{300} \left(I_1 - 3\right)^3 \tag{5.122}$$

  The corresponding material parameters are obtained from biaxial tensile data derived by [VGSV04]:

  $$c_{100} = 0.01296 \text{ Nmm}^{-2}; \; c_{200} = 0.00114 \text{ Nmm}^{-2}; \; c_{300} = 0.00591 \text{ Nmm}^{-2}$$

- **Thoracic Healthy Vascular Model:**
  The mechanical behavior of healthy thoracic aortas is based on measurements performed on healthy human thoracic aortic tissue. It is described by the second-order reduced polynomial model with parameters derived from biaxial tensile data obtained by [VSE+03]:

  $$c_{100} = 0.110 \text{ Nmm}^{-2} \quad \text{and} \quad c_{200} = 0.090 \text{ Nmm}^{-2}$$

- **Porcine Abdominal Vascular Model:**
  Further, the constitutive mechanical behavior of porcine abdominal aortas is based on a third-order polynomial hyperelastic model given by:

  $$W = c_{010}\left(I_2 - 3\right) + c_{110}\left(I_1 - 3\right)\left(I_2 - 3\right) + c_{300}\left(I_1 - 3\right)^3 \qquad (5.123)$$

  The parameters are derived from ex-vivo experiments performed by [PLD$^+$03] on the abdominal aortic tissue, with:

  $c_{010} = 0.01536 \text{ Nmm}^{-2}$; $c_{110} = 0.01634 \text{ Nmm}^{-2}$; $c_{300} = 0.003407 \text{ Nmm}^{-2}$

- **Porcine Thoracic Vascular Model:**
  As for the porcine thoracic aorta, it is described based on Eq.5.121. The material parameters are derived by means of evaluation, performed in this work, of stress-strain data obtained from [Sok07] (Fig.5.6):

  $$c_{100} = 0.00838 \text{ Nmm}^{-2} \quad \text{and} \quad c_{200} = 0.0198 \text{ Nmm}^{-2}$$

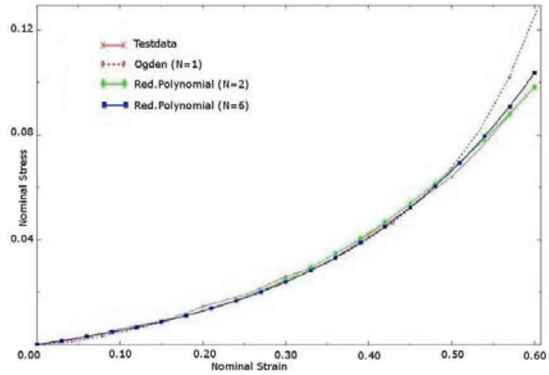

Figure 5.6: Evaluation of the thoracic porcine model from testdata.

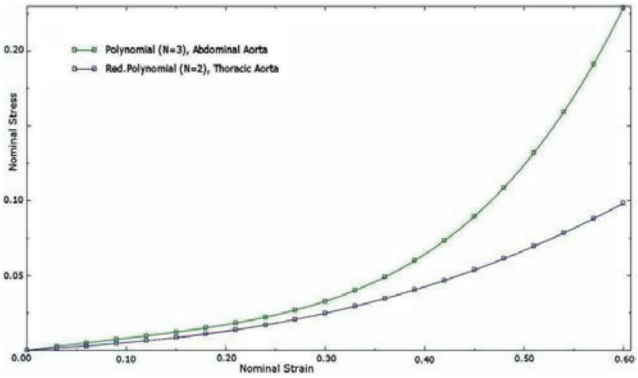

Figure 5.7: Stress-Strain curves for both porcine material models.

- **Thrombus Hyperelastic Model:**
  Also, the constitutive behavior of the surrounding intraluminal thrombus material is implemented based on equations derived from a second-order ($n = 2$) polynomial model:

  $$W = c_{010}\,(I_2 - 3) + c_{020}\,(I_2 - 3)^2 \tag{5.124}$$

  with material parameters obtained from uniaxial tensile measurements performed by [DMV03] and given by:

  $$c_{010} = 0.028 \text{ Nmm}^{-2} \quad \text{and} \quad c_{020} = 0.0286 \text{ Nmm}^{-2}$$

- **Linear Elastic Model:**
  Finally, for comparison and to examine the influence of the hyperelastic material properties on the elastomechanics, a linear elastic wall model is considered with a Youngs modulus of elasticity $E = 2.7$ MPa.

Furthermore, the arterial wall is considered as a nearly incompressible material with a density $\rho_w = 1200$ Kgm^{-3} and a Poisson ratio $\nu = 0.499$. The incompressibility constraint is modeled by the expression of the second Piola-Kirchhoff stress tensor $\boldsymbol{S}$ in terms of its deviatoric component $\boldsymbol{S}'$ and the Lagrangian strain tensor $\boldsymbol{E}$, given by Eq.5.76 and Eq.5.77.

5.5.2 Initial and Boundary Conditions

Biomechanical simulations of the vessel require the knowledge of the load distribution on the wall and of a set of prescribed displacement constraints. The Neumann and Dirichlet conditions, describing the load and the constraint conditions, respectively, are needed to solve and initialize the system of differential equations governing the structural model. Both static and dynamic computations have been carried out on the patient geometries. For the dynamic simulations, the transient load distribution on the inner aortic wall is based on real time-dependent pressure profiles obtained either from previous blood flow (CFD) simulations for the same patient as shown in Fig.5.8 [HKU$^+$07] or from direct in-vivo or ex-vivo measurements. Fig.5.8 shows the relative total pressure distribution on the aortic wall at peak systole. In order to get rid of undesirable oscillations and instabilities in the simulations, the pressure profile is slightly idealized by smoothing the curve (Fig.5.9.b). Indeed, the pressure profile is considered as homogeneous in space assuming that the local blood pressure variation within the aorta is relatively small [SF07]. A stabilization phase of 1s is applied prior to both simulations to increase the pressure from 0 to its initial value p_{ini}. For the static simulations, only diastolic p_d and peak systolic p_s pressures are considered (Fig.5.9.a).

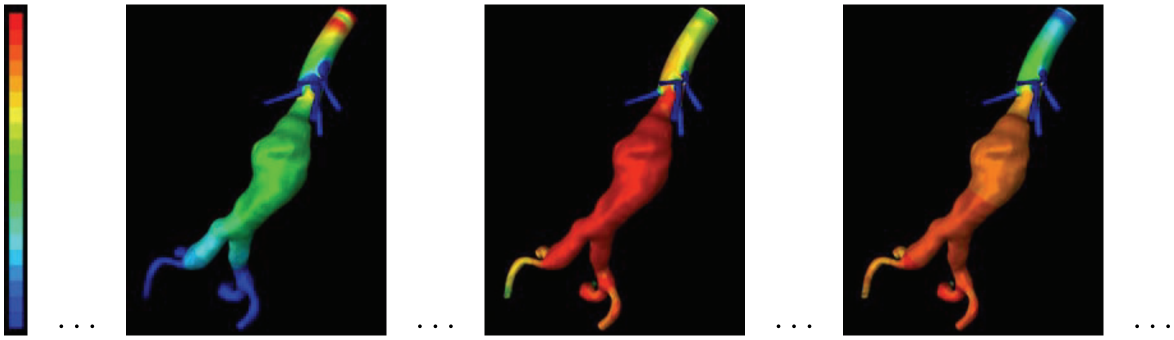

Figure 5.8: CFD simulations: Wall pressure distribution at various times.

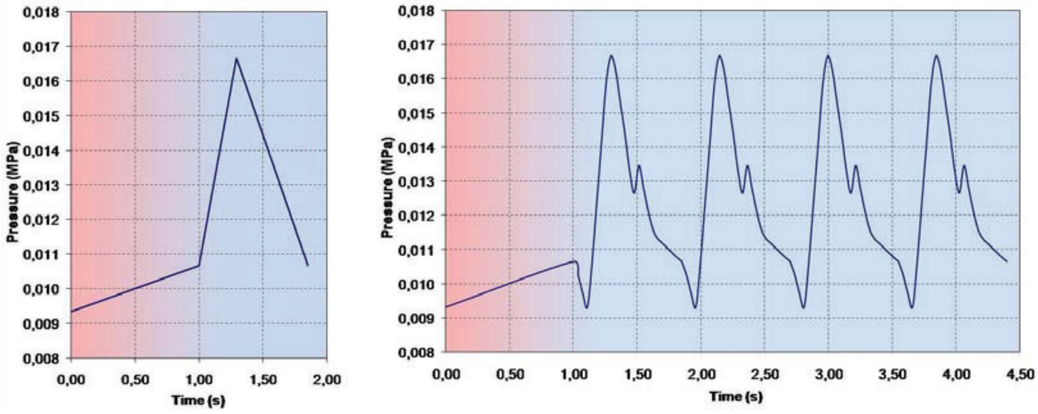

(a) Static (b) Dynamic

Figure 5.9: Load boundary conditions: Static and dynamic pressure profiles.

As for the boundary of the vessel wall defined by the inlet and the outlets, the displacement constraint condition is implemented for all degrees of freedom. Thereby, zero translation is imposed on the nodes ends. This allows fixing the aorta, reflecting the real situation being hold by the surrounding organs.

5.5.3 Mathematical and Numerical Modeling

The resulting three-dimensional equations governing the vessel wall domain consist of a complex nonlinear system of partial differential equations. The numerical discretization of the simulation domain is based on the finite element approach. The CSM simulations are carried out using the FEM-program Abaqus. Thereby, the computational domain is discretized into three-node finite shell elements. The interpolation scheme between the discrete node variables within the finite elements is based on a linear polynomial function. The interpolating shape function is hereby expressed by:

$$\boldsymbol{H}_{shell} = [\xi \quad \eta \quad (1 - \xi - \eta)] \tag{5.125}$$

The coordinate vectors of an arbitrary point $\boldsymbol{X}$ and of its elementary nodes $\boldsymbol{N}$ are related through $\boldsymbol{H}$ by $\boldsymbol{X} = \sum_i^n H_i N_i$. The conservation equations are integrated over the individual cells in their weak form generating a set of differential equations. The field variables are then approximated at the centre of the cells so that dynamic equilibrium, represented by the error function $\Psi(u)$:

$$\Psi(u) = \boldsymbol{E}(u) - \boldsymbol{F} = 0 \tag{5.126}$$

is achieved. $\boldsymbol{E}(u)$ is the internal energy expressed as a function of the displacement u, produced by the structure as a reaction to the external forces $\boldsymbol{F}$ applied on it. The nonlinear second-order discretized equations are replaced with incremental equations by applying the *Updated Lagrangian* approach. The time-dependent incremental equations for the finite displacements are obtained using an implicit time integration. The implicit formulation is based on the *Newmark method* assuming equilibrium at time $t+\Delta t$ to obtain solution at $t + \Delta t$. The Newton-Raphson iteration method is used to solve the nonlinear system of governing equations. As a result, the analysis can be assumed as linear and $\boldsymbol{E}(u)$ can be represented as a linear function of the stiffness matrix $\boldsymbol{K}$:

$$\boldsymbol{E}(u) = \boldsymbol{K}u \tag{5.127}$$

Nodal equilibrium of the resulting linearized system of equations is solved using an iterative approach based on the Gauss-Seidel algorithm, described in Sec.7.2.8. Finally the local solution is integrated into the whole domain. Consequently, the stress distributions and the vessel deformation are computed and evaluated at any instant of time within the computational domain.

5.5.4 Numerical Stability - Discussion

Explicit integration is conditionally stable, requiring that the time step size Δt is smaller than a critical step size calculated from the smallest period in the finite element mesh. Δt is related to the element properties and is given by:

$$\Delta t \leq \Delta t_{cr} = \frac{T_{Nmin}}{\pi} = \frac{2}{w_{Nmax}}$$

In order to overcome the stability limitation of explicit methods, the implicit time integration is used to achieve more accurate solutions and faster convergence. The implicit formulation is unconditionally stable, meaning that the choice of the time step increment Δt is rather based on accuracy issues and that much larger sizes Δt can be used. Thereby, in order to obtain fast convergence, an appropriate selection of the Newmark control parameters α and β is of great importance. The method is in general stable for:

$$\beta \geq 0.5 \qquad \text{and} \qquad \alpha \geq 0.25\ (\beta + 0.5)^2$$

The trapezoil rule is obtained for $\beta = 0.5$ and $\alpha = 0.25$. With T_{low} being the lowest period of interest, the step size Δt recommended for dynamic analysis with the trapezoil rule is given by:

$$\frac{\Delta t}{T_{low}} = w_{low}\Delta t \leq 0.20$$

Further, the use of the Newton-Method allows improving the implicit solution, where the equilibrium equations are considered at an unknwon time configuration. The full Newton-Raphson iteration scheme combined with a reasonable load incrementation method is usually sufficient to ensure an accurate solution of the dynamic response of the model. However, since the algorithm imposes that the effective stiffness matrix is updated and factorized at the beginning of each new load step and in each iteration as shown in Fig.5.2, this method may be computationally expensive per iteration. Still with the advantage that the more expensive per iteration the method is, the less iterations are needed to achieve convergence. Alternatively, the modified Newton-Raphson may be also used in order to achieve convergence. The method does not impose the recomputation of the tangent of the stiffness matrix after every iteration. Instead, the same initially computed matrix is used for the whole course of iterations. As a result, the modified Newton-Raphson scheme may be computationally less expensive than the full Newton, however at the cost of the total number of iterations required to reach time convergence. Therefore, the *Quasi Newton-Raphson* method is used as another alternative choice, combining the advantages of both methods. The algorithm imposes the recomputation of the tangent of the stiffness matrix only after a certain interval n of iteration steps.

Finally, mathematical stability is ensured by generating time-step independent computations, characterized by a few numbers of iterations and small residuals, while compromising between accuracy and computational cost. Furthermore, all dynamic results represented below are evaluated at the fourth cardiac cycle, ensuring convergence and providing indeed periodicity. As for the physical stability, it is ensured by using mesh configurations based on the previous stability study [HBK$^+$07] carried out on individual aortic models. Exact solutions are guaranteed by the large number of finite elements present in the computational domain.

5.6 System Integration in *CSM-Sim*

The vessel wall modeling steps are integrated in MoDiSim into the component *CSM-Sim*. As described in Sec.3.4, *CSM-Sim* was developed to automatically generate, perform and quantify computational vessel wall simulations in patient-specific aortic models at any time. The user interface of *CSM-Sim* is shown in Fig.5.10. The system integration includes the process automation, the physical optimization as well as individualization and expandability.

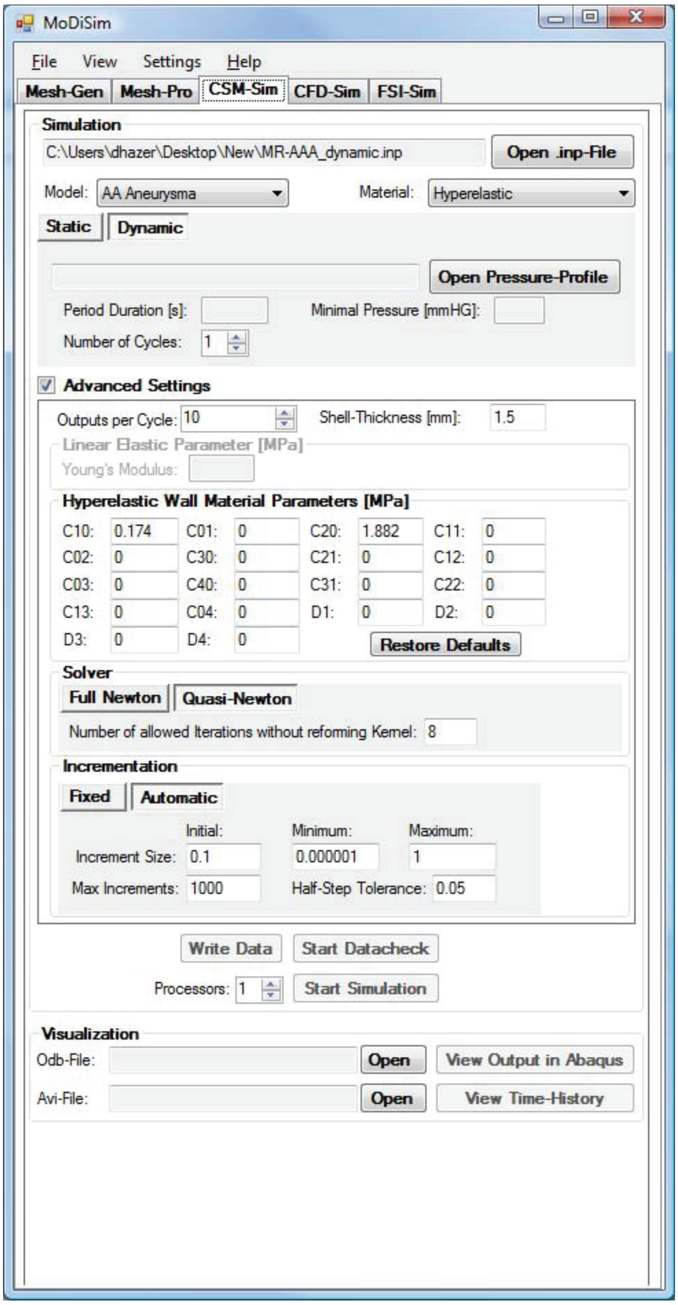
MoDiSim
File
View
Settings
Help
Mesh-Gen
Mesh-Pro
CSM-Sim
CFD-Sim
FSI-Sim
Open .inp-File
Static
Dynamic
Open Pressure-Profile
Restore Defaults
Full Newton
Quasi-Newton
Fixed
Automatic
Write Data
Start Datacheck
Start Simulation
Open
View Output in Abaqus
Open
View Time-History

Simulation

C:\Users\dhazer\Desktop\New\MR-AAA_dynamic.inp

Model: AA Aneurysma
Material: Hyperelastic

Period Duration [s]:
Minimal Pressure [mmHG]:
Number of Cycles: 1

☑ Advanced Settings

Outputs per Cycle: 10
Shell-Thickness [mm]: 1.5

Linear Elastic Parameter [MPa]
Young's Modulus:

Hyperelastic Wall Material Parameters [MPa]

C10:	0.174	C01:	0	C20:	1.882	C11:	0
C02:	0	C30:	0	C21:	0	C12:	0
C03:	0	C40:	0	C31:	0	C22:	0
C13:	0	C04:	0	D1:	0	D2:	0
D3:	0	D4:	0				

Solver

Number of allowed Iterations without reforming Kernel: 8

Incrementation

	Initial:	Minimum:	Maximum:
Increment Size:	0.1	0.000001	1

Max Increments: 1000
Half-Step Tolerance: 0.05

Processors: 1

Visualization

Odb-File:
Avi-File:

Figure 5.10: User-Interface of the CSM simulation component *CSM-Sim*.

5.6.1 Automation

The process automation of the vessel wall simulations is achieved via integration of the CSM modeling steps into the component *CSM-Sim*. These are processed by the program automatically based on a minimal user interaction. Once the vessel wall model is defined and the computations are performed, the simulation results can be also visualized and analyzed, providing a physical insight into the elastomechanical vessel parameters. The most important actions in the *CSM-Sim* component sketched in Fig.5.11 are described below:

- **Write Data:**
  The *WriteInp* method first checks the data in the .inp input surface mesh of the aorta for any existing simulation settings by looking for predefined Abaqus command keywords. Then, a new simulation subdirectory is created to which the .inp file is copied. All simulation settings will be written into this new .inp file.

- **Adjust Physical Settings:**
  The *StoreAndAdjustExistingSettings* method replaces the thickness of all shell sections with the thickness of the aortic wall. *WriteMaterial* adds a material model into the .inp file describing the aortic wall and associates appropriate material parameters. The selection of the material models and their parameters is user-defined. Therefore, the input .inp has to include at least one section definition for the aortic wall material.

- **Define Boundary Conditions:**
  WriteAmplitude adjusts the values in the pressure profile to the minimum pressure before writing these into the .inp file as amplitude *RAMP*. *WriteBoundaryCondition* defines a DOF constraint condition at all ending nodes. Therefore, a nodeset including all nodes of the inlet and outlets must be predefined in the input .inp file as described in Sec.4.7.

- **Define Simulation Steps and Solvers:**
  WriteLiftUpStep defines a static step to lift the pressure to its initial value. *WriteDynamicStep* writes a dynamic cardiac cycle using the defined amplitude. *WriteStaticStep* writes a static simulation step related to the systolic pressure. All pressure loads are applied on the inner side of the aortic surface, which has to be predefined in the input surface mesh file. The output requests are subsequently written into the .inp file after every n steps using *WriteOutputRequests*. The frequency of the output requests per step may be defined by the user. Finally, the desired solver and timestep settings are applied to each defined step in the cycles.

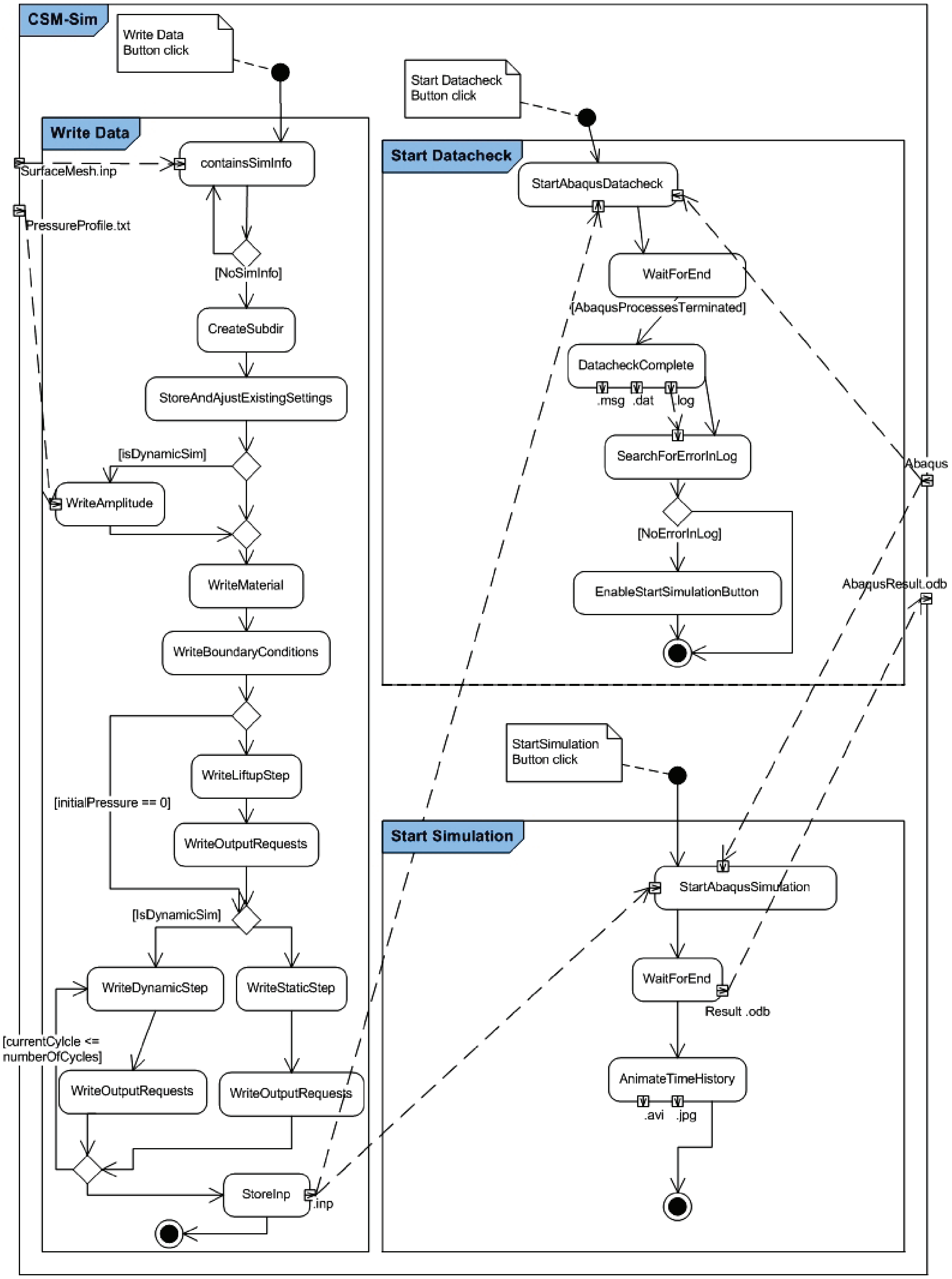
CSM-Sim
Write Data
Button click
Write Data
SurfaceMesh.inp
containsSimInfo
PressureProfile.txt
[NoSimInfo]
CreateSubdir
StoreAndAjustExistingSettings
[isDynamicSim]
WriteAmplitude
WriteMaterial
WriteBoundaryConditions
WriteLiftupStep
[initialPressure == 0]
WriteOutputRequests
[IsDynamicSim]
WriteDynamicStep
WriteStaticStep
[currentCylcle <=
numberOfCycles]
WriteOutputRequests
WriteOutputRequests
StoreInp
.inp
Start Datacheck
Button click
Start Datacheck
StartAbaqusDatacheck
WaitForEnd
[AbaqusProcessesTerminated]
DatacheckComplete
.msg
.dat
.log
SearchForErrorInLog
[NoErrorInLog]
EnableStartSimulationButton
Abaqus
AbaqusResult.odb
StartSimulation
Button click
Start Simulation
StartAbaqusSimulation
WaitForEnd
Result .odb
AnimateTimeHistory
.avi
.jpg

Figure 5.11: Activity diagram of the CSM simulation component *CSM-Sim*.

- **Start the Datacheck:**
  StartAbaqusDatacheck starts an Abaqus datacheck on the stored .inp file, which includes the simulation settings. *WaitForEnd* waits for all Abaqus processes to terminate. *SearchForErrorInLog* searches for errors in the resulting job.log file and outputs them.

- **Start the Simulation:**
  StartAbaqusSimulation starts Abaqus with the parameter ‘continue’. *WaitForEnd* waits again for all Abaqus processes to terminate. Finally, the simulation status will be printed in the .log, as soon as the .sta file is created in the simulation subdirectory.

- **Visualize the Results:**
  Finally, automatic quantification of the results is performed. Using a predefined python script, *AnimateTimeHistory* starts Abaqus again and creates pictures and videos, animating the results of the wall stress distribution and deformation sequences along the simulated aortic model.

5.6.2 Optimization

A step by step approach was adopted while integrating the individual models of *CSM-Sim* into MoDiSim. Thereby, simpler properties were integrated first, while in the next step these were optimized and improved by extending them to more complex models. At the end, various modeling options are implemented. Static and dynamic realistic computations of the wall mechanics are now possible. Linear elastic and nonlinear hyperelastic material models are implemented for the constitutive modeling of the vessel wall. Further, both polynomial and reduced polynomial material models are integrated for hyperelastic modeling. Various homogeneous wall thicknesses can also be modeled. Both the Newton-Raphson and the Quasi-Newton-Raphson iteration techniques are integrated and may be employed for the computation of the stiffness matrices. For the solution of the linear system of equations, the AMG iterative FEM-based implicit solver is mainly adopted, but the direct solution method may be also alternatively used. Both fixed and automatic time advancement are implemented in the advanced settings allowing a flexible control of the time stepping and thus the convergence behavior of the simulations. As for the representation of the results, *CSM-Sim* also includes automatic quantification of the wall *von Mises* stress and deformation sequences for the whole modeled aorta. Furthermore, the effects of these various models have been evaluated for their physical effects and some of them are presented in the results section.

5.6.3 Individualization

Individual strain energy functions with appropriate material parameters for healthy and aneurysmal, for human and porcine, and for thoracic and abdominal models are integrated allowing the simulation of various and individual aortas. Also, the implementation of a flexible controlling of the wall thickness is an essential factor for simulating different models. Further, the wall boundary conditions, defined based on individual pressure data that are obtained from direct in-vivo measurements or from subject-specific CFD-based simulations, enhances the individuality of the modeling. The individualization is also expressed by the system independency in terms of the imaging source and in terms of the shape of the geometry or of the pathology. In total, four subject-specific aortic wall models have been processed and simulated using *CSM-Sim*. These are shown in overview in Fig.5.12 and originate from the CT-based human abdominal aortic aneurysm (Fig.3.7), the CT-based thoracic aortic aneurysm (Fig.3.8) with and without stent-graft, the MRI-based human abdominal aortic aneurysm (Fig.3.9) and the 4D-CT based porcine abdominal aorta (Fig.3.10). Details on the results will be presented in the next section.

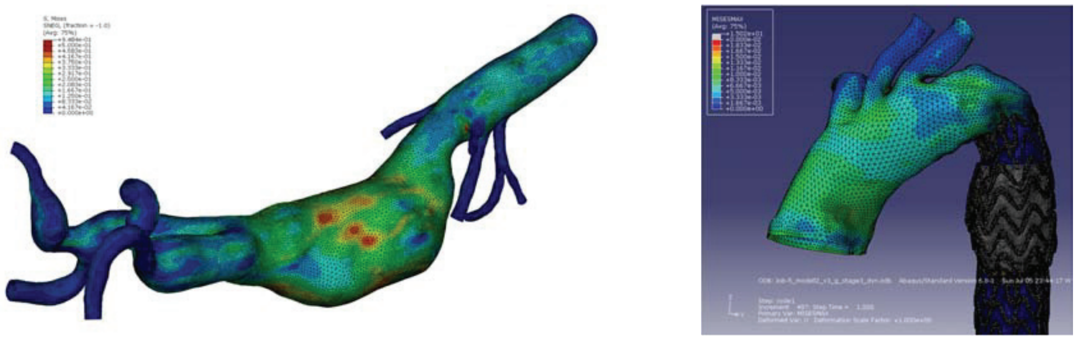

(a) CT-AAA (b) CT-TAA

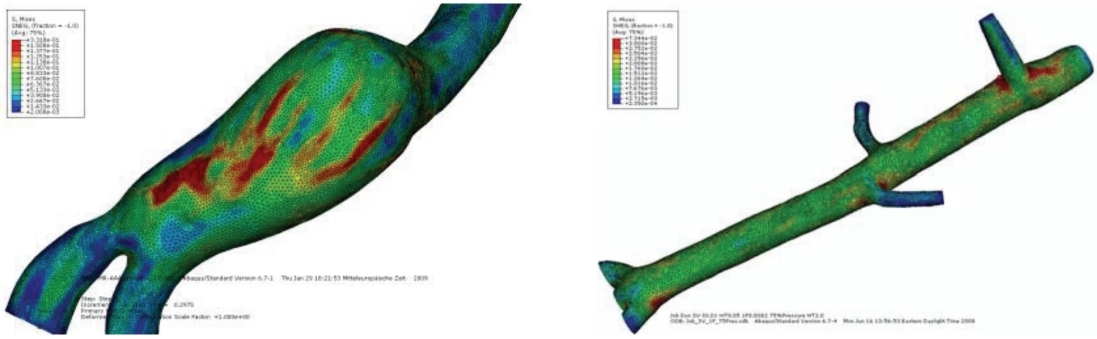

(c) MR-AAA (d) 4D-CT-P1

Figure 5.12: CSM simulations with four individual vessel wall aortic models.

5.7 CSM Simulation Results

Simulation results of the vessel wall mechanics within the four individual models are presented in terms of strains for the quantification of the wall deformation and in terms of von Mises stresses for the analysis of the wall material failure. The von Mises stress index is a function of the invariants of the stress tensor. It is based on the von Mises shear distortion failure criterion and is therefore an adequate indicator of the wall strength state. Furthermore, all dynamic simulation results represented below are evaluated at the fourth cardiac cycle, ensuring convergence and periodicity.

5.7.1 Effects of transient pressure and material nonlinearity using CT-AAA

Within the patient-specific CT-based AAA model individual biomechanical simulations are presented as a transient indirect coupled approach of fluid and structure based on the finite element method. The vessel wall stress and deformation can be accurately evaluated as being based on dynamic and realistic pressure patient-specific simulations from CFD (Sec.6.7.3). The effects of the transient pressure distribution and of the material nonlinearity are evaluated by performing static/dynamic and elastic/hyperelastic simulations respectively. The effects on the diseased geometry are also evaluated by analyzing the simulations within and distal to the aneurysmal bulge model. In all simulations, high wall stresses are found near points where the surface curvature changes its orientation from convex to concave within the aneurysmal bulge. Whereas, low stress values are always located at healthy regions distal to the aneurysmal bulge. All maximum wall stresses occur at the peak systolic stage and are always found at the same node location where the aorta splits into the iliac arteries. Tab.5.1 represents the maximum, minimum and mean von Mises values at peak systole within the whole AAA geometry for the elastic static, hyperelastic static, elastic dynamic and hyperelastic dynamic models.

Table 5.1: Maximum, minimum and mean von Mises values at peak systole for the various simulations.

	Max (MPa)	Min (MPa)	Mean (MPa)
Elastic Static	0.648	0.00150	0.116
Hyperelastic Static	0.952	0.00216	0.121
Elastic Dynamic	0.641	0.00153	0.115
Hyperelastic Dynamic	0.948	0.00220	0.121

Effect of Transient Pressure Distribution

To evaluate the effect of the time-dependent pressure distribution on the biomechanics, static and dynamic simulations have been performed on the AAA geometry. The dynamic simulations utilize the time-dependent pressure profile shown in Fig.5.9.b to simulate the effect of blood pressure on the wall stresses and deformation along four cardiac cycles. The cycle period was 0.85 s, with peak pressure occurring at t= 0.30 s. The static simulations compute only the diastolic p (t= 0.10 s) and peak systolic p (t= 0.30 s) pressures. A stabilization phase of 1 s is applied prior to both simulations to increase the pressure to its initial value. The results were analyzed at the peak systolic phase. For both the elastic (Fig.5.13) and the hyperelastic (Fig.5.14) models, maximum, minimum and mean values of the strain and the von Mises stress are found to be similar with slightly lower strains and higher stress distribution for the static model. The difference observed is less than 2 %.

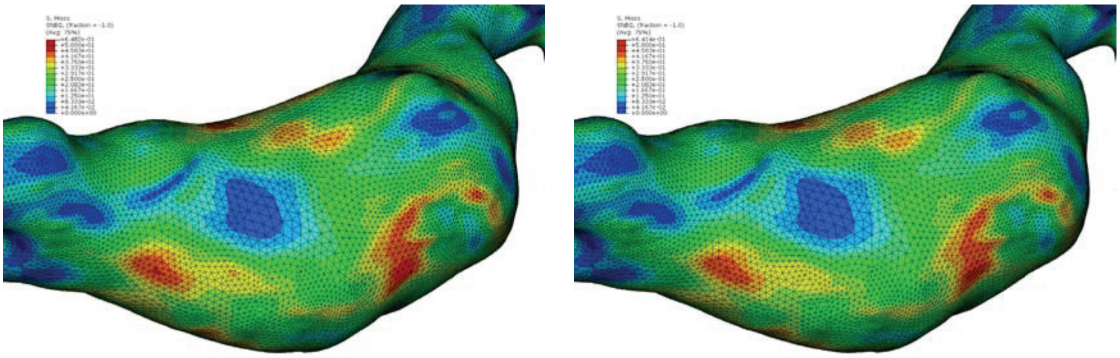

Figure 5.13: Static (left) and dynamic (right) von Mises wall stress computations at peak systole for the elastic model.

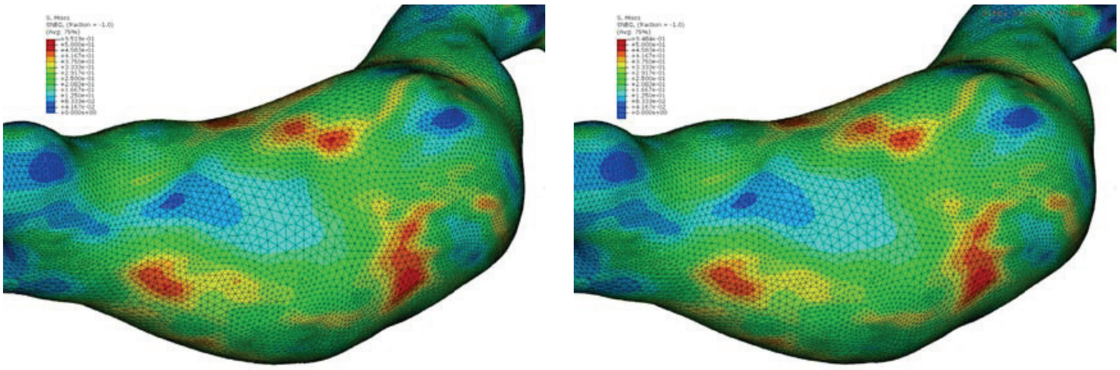

Figure 5.14: Static (left) and dynamic (right) von Mises wall stress computations at peak systole for the hyperelastic model.

Effect of Material Nonlinear Elasticity

Dynamic computations have been performed on the elastic and hyperelastic models to evaluate the effect of the material constitutive nonlinearity on the strain and stress distributions. Fig.5.15 shows the stress results on the deformed AAA geometry at early systole, peak systole and peak diastole. During systolic ascension, similar stress distribution is observed in both models with most of the values lying between 0.2 and 0.3 Nmm^{-2}. Strains and stresses reached their maximum at peak systole (t= 0.30 s) with significantly larger values found in the nonlinear model. Thereby, the stress increased by a factor of 4.4 in the hyperelastic model and only 2.6 in the elastic model. At the third diastolic time represented by the second pressure peak (t= 0.52 s), the strains and stresses decelerated again with slower deceleration found in the hyperelastic model. In general, the stress distribution and the stress change rate are found to be always higher in the hyperelastic material.

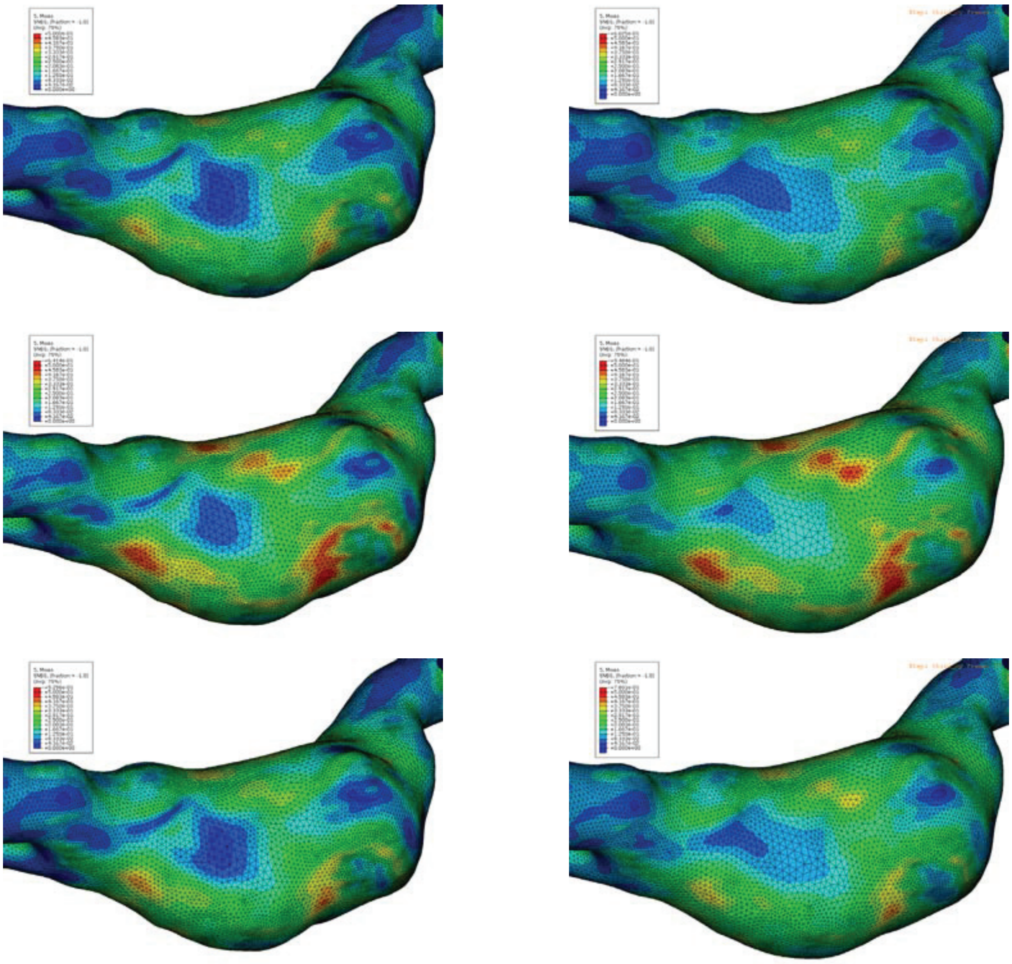

Figure 5.15: Elastic (left) and hyperelastic (right) von Mises stresses at t= 0.17 s (top), t= 0.30 s (middle) and t= 0.52 s (bottom).

5.7.2 Effects of Wall Thickness using MR-AAA

CSM simulations within the patient-specific MR-based AAA model have been performed with various wall thicknesses. With an average thickness of 1.5 mm found for patients with AAA, diseased walls with calcification become thicker while aneurysms without thrombus have much thinner walls.

To quantify the significance of wall thickness variation on the simulations, five models with 1.0 mm, 1.2 mm, 1.5 mm, 1.8 mm and 2.0 mm homogeneous thicknesses were simulated. The simulations were conducted using the hyperelastic material model for the abdominal aneurysmal aortic tissue as given in Sec.5.5.1. For all five models, the local maximum stress within the aneurysm was found at the same location, represented by element 30668 shown in Fig.5.17. The von Mises stress over time for this element is illustrated in Fig.5.16.a. Tab.5.2 summarizes the maximum, mean and minimum stress values for this element.

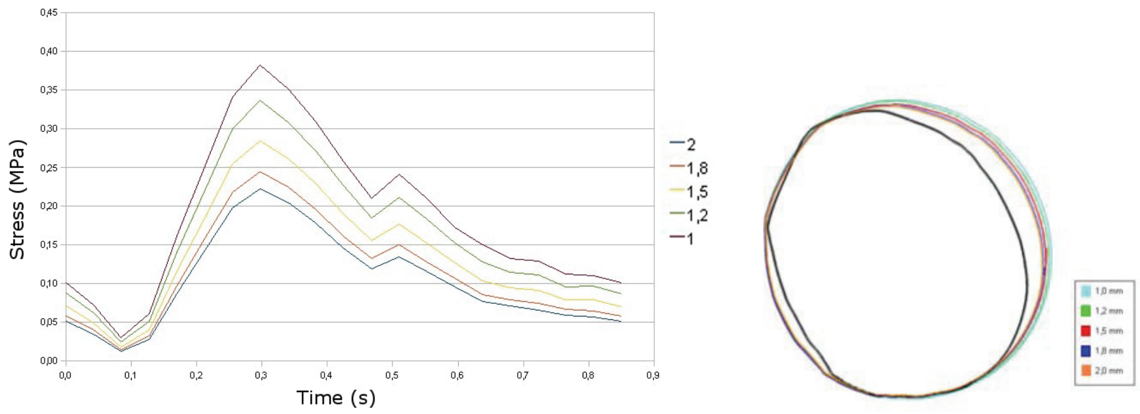

(a) Max von Mises stress (b) Peak axial deformation

Figure 5.16: Maximum stress profile over time and peak cross-sectional deformation in the aneurysm for all thicknesses.

For all five thicknesses, the maximum stresses are found at the peak systolic time t= 0.30 s. The stress increase between the thicker and the thinner models is equal 80.6 %, equivalent to 0.083 MPa relative to the time-averaged von Mises stress. Further, compared to the average thickness 1.5 mm, the maximum stress change is larger when decreasing the thickness to 1.2 mm i.e. 1.0 mm than when increasing it to 1.8 mm i.e 2.0 mm. A 0.3 mm thickness decrease i.e increase results in +0.0399 MPa = +21.829 % i.e -0.062 MPa = -14.031 % stress change, respectively. Similarly, a 0.5 mm thickness decrease i.e increase results in +0.098 MPa = +34.484 % i.e -0.062 MPa = -21.809 %. This demonstrates that the stress distribution is much more affected by a thinning than by a thickening of the wall.

Fig.5.16.b shows the deformation profiles at peak systolic time for all five thicknesses along an axial cross-section in the middle of the aneurysmal bulge. The black contour represents the initial undeformed state of the cross-section at zero-pressure. Obviously, the thinner wall deforms at most and the maximum deformation takes place in direction of the bulge.

Table 5.2: Maximum, mean and minimum stresses over the cardiac cycle.

Wall Thickness (mm)	2.0	1.8	1.5	1.2	1.0
Max Stress (MPa)	0.222098	0.244189	0.284044	0.346049	0.381995
Mean Stress (MPa)	0.102570	0.114025	0.134847	0.161831	0.185243
Min Stress (MPa)	0.012397	0.014492	0.018741	0.024885	0.030444

Additionally, the stress variation at five different elements for all wall thicknesses is shown in Fig.5.17. As expected, the stress profiles for the thicknesses 1.8 mm and 2.0 mm are closer to each other than the other curves. Further, while the profiles of 1.5 mm, 1.8 mm and 2.0 mm show similar courses, those of 1.0 mm and 1.2 mm are quite different. This demonstrates that thinner walls are much more sensitive to the stress distribution.

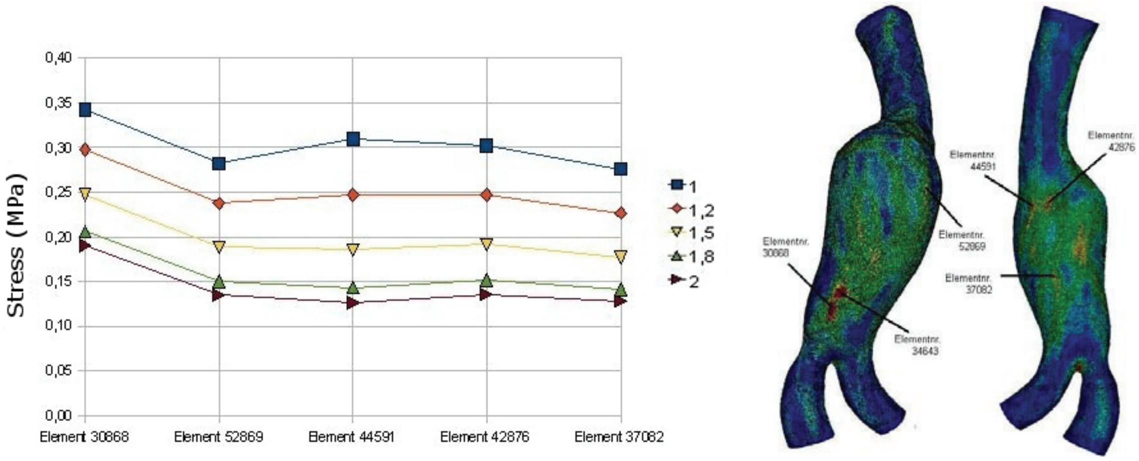

(a) Stress variation (b) Elements overview

Figure 5.17: Stresses at five different elements at peak pressure time with elements overview.

Fig.5.18 illustrates the static and dynamic stress distributions at the peak systolic time for all wall thicknesses. The stresses decrease continuously from the thinner to the thicker model. However, as mentioned above, the decrease is not linear. Also here, similar strain and stress distributions were found for the static and the dynamic computations with slightly lower strains and higher stress distribution for the static model.

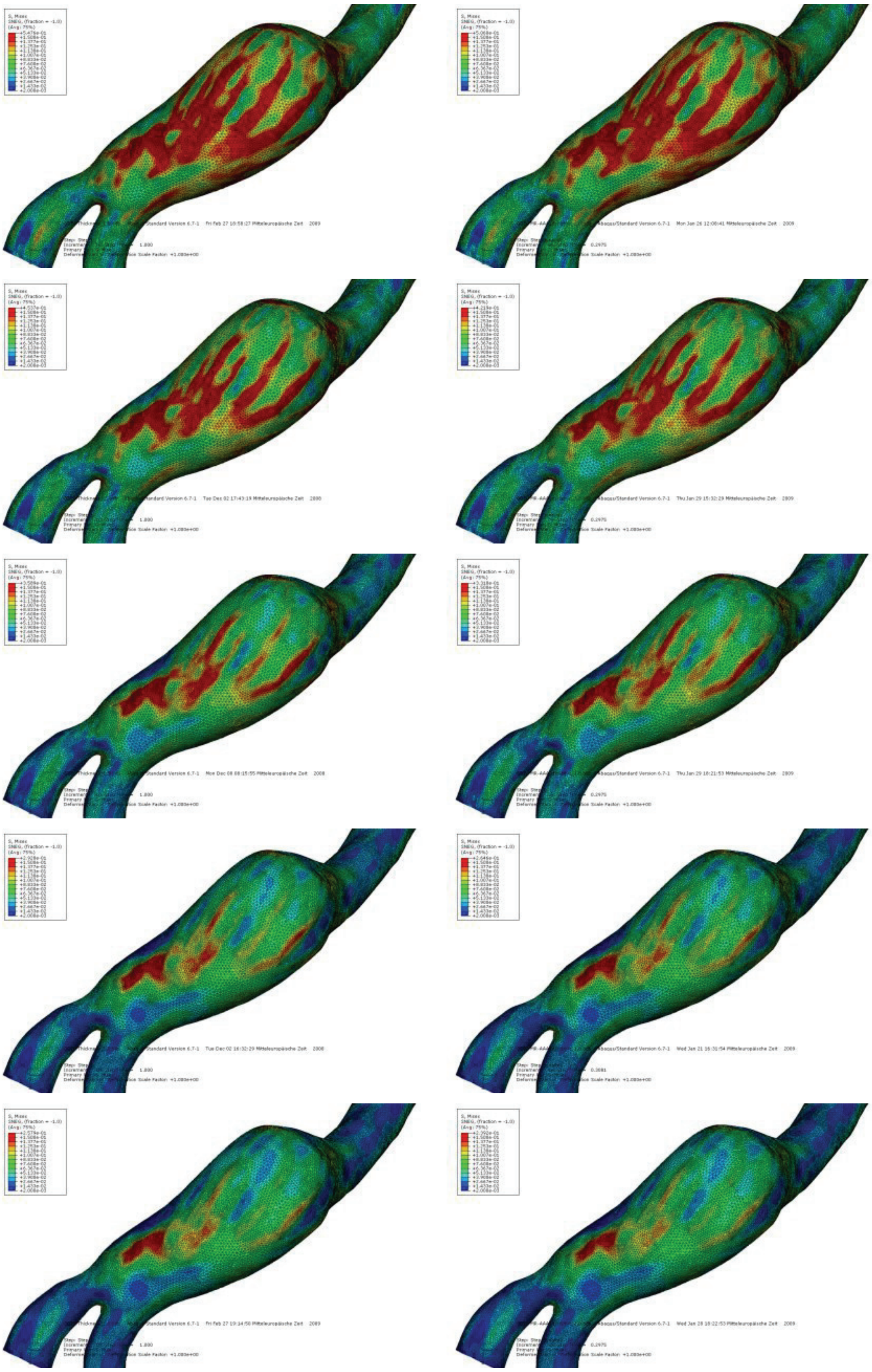

Figure 5.18: Static (left) and dynamic (right) von Mises stresses for the 1.0, 1.2, 1.5, 1.8 and 2.0 mm wall thicknesses shown from the top to the bottom, respectively.

5.7.3 Effects of Stent and Stent-Graft using CT-TAA

The design of endovascular devices affects the vessel morphology which in turn influences the strain and stress distribution at the wall. In this section, patient-specific vessel wall modeling in the CT-based thoracic aorta CT-TAA (Fig.3.8) after endovascular treatment is presented. Post-endovascular modeling enables accurate predictive simulations of material failure and potential complications by evaluating the state of the patient vessel based on the quantification of its elastomechanics. Various simulations of the interaction between the structural models - aorta, stent and stent-graft - are presented below.

CT-TAA without Stent-Graft

In order to evaluate the effects of the endovascular device on the elastomechanics, a simulation of the thoracic aorta *without stent-graft* was first performed. The wall constitutive material is based on the hyperelastic thoracic aortic model presented in Sec.5.5.1. For the boundary conditions, the time-dependent pressure profile shown in Fig.5.9 was applied at the inner wall, while the DOF constraint was used for the inlet and the outlets. The pressure curve was scaled such that the diastolic minimum pressure found at t= 0.1 s corresponds to 0 mmHg, while the maximum of 41.25 mmHg occurred at t= 0.287 s. The simulation is conducted in two steps: a static step in which the pressure is increased to its initial value at 6 mmHg and a dynamic step using the pressure profile with a period T= 0.8 s. Fig.5.19 illustrates the von Mises stress distribution at the systolic time with peak values found in the descending part where the stent-graft has been implanted and around the inlet.

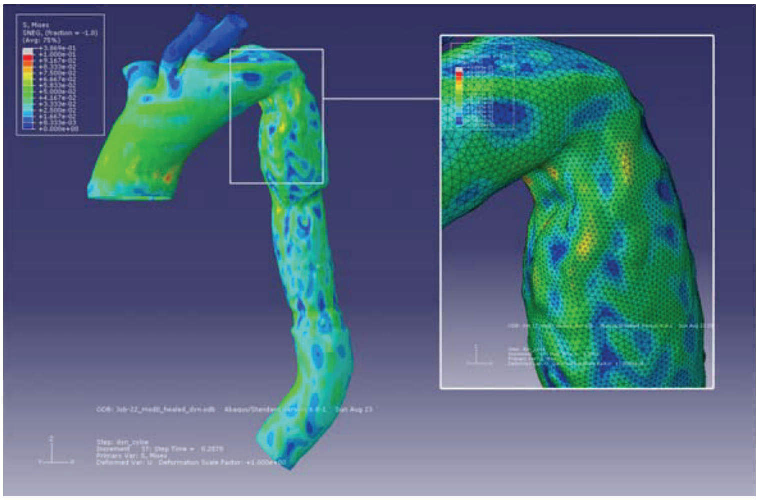

Figure 5.19: Wall stress distribution *without stent-graft* at t= 0.287 s.

CT-TAA with Stent

The aorta *with stent* was next simulated with a *tied linear contact* modeled between the inner surface of the aorta and the surface of the stent volume. For the definition of the contact interaction, the aorta was chosen as the *slave surface* while the stent as the *master surface*. The stent material model of nitinol is used as a linear elastic model with an elasticity modulus E= 75 GPa [AAL+04], a poisson number ν= 0.33 and a density ρ= 6450 Kgm^{-3} [Meda]. Compared to the simulation without stent, the von Mises stresses presented in Fig.5.20 are clearly lower in the aortic part carried by the stent. This is due to the circular aortic strains being constrained by the stent.

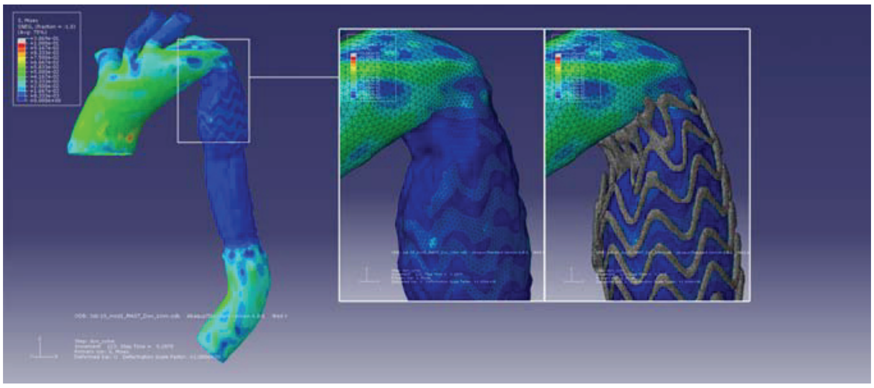

Figure 5.20: Stress distribution in the aorta of the simulation *with stent* at t= 0.287 s (scale: 0 Nmm^{-2} in blue, 0.1 Nmm^{-2} in red).

The contact of the stent with the aorta also results in much higher stresses in the stent as shown in Fig.5.21. This is due to the stent being less elastic, which also results in much smaller stent strains, compared to the aortic strains in the area outside the stent. The largest stent stresses are found at the curved locations, associated with the zig-zag stent geometry.

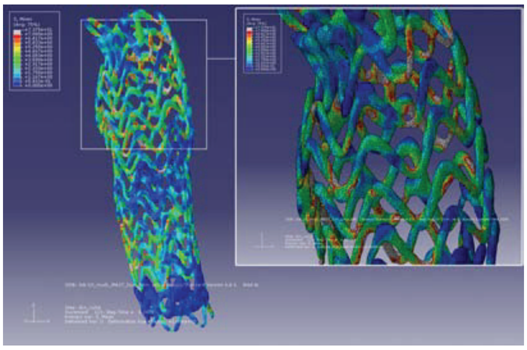

Figure 5.21: Stress distribution in the stent of the simulation *with stent* at t= 0.287 s (scale: 0 Nmm^{-2} in blue, 7 Nmm^{-2} in red).

CT-TAA with Stent-Graft

A geometrical model of the graft was additionally generated and included in the simulations. The stent-graft type could be identified from the shape of the stent and consists of nitinol and PET materials [Medb]. The PET material is modeled as a linear elastic model with E= 3 GPa, ν= 0.4 and ρ= 0.133 Kgm^{-3} [PMW+09]. Based on the simulations of the aorta, two *tied linear contacts* with the *surface-to-surface* approach are modeled: between aorta and graft and between graft and stent. Through the adaptation to the stent, the graft surface is less regular than that of the aorta and therefore the aortic surface was chosen as the *slave surface* for the aorta-graft contact. As for the graft-stent contact, the stent surface was chosen as the slave surface, since it has clearly a much finer mesh.

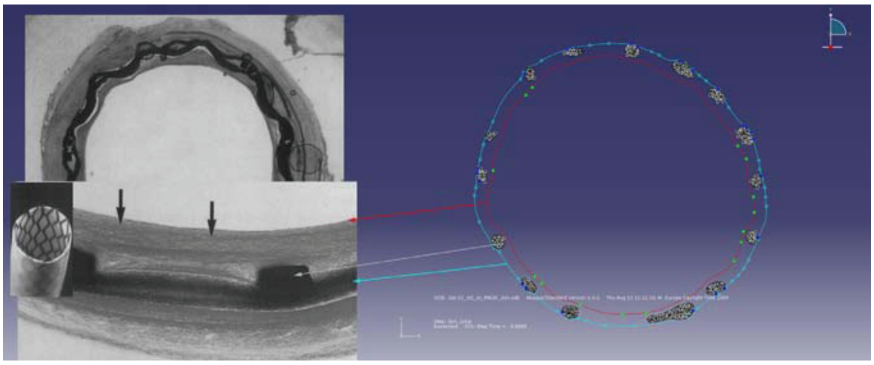

Figure 5.22: Histological cross-section from [DB00] compared to the generated aorta (red), stent (grey) and graft (blue).

Compared to the simulation with *only* the stent, the aortic von Mises stresses in the area of the stent-graft are much smaller as shown in Fig.5.23. This is due to the aortic strains being constrained through the graft.

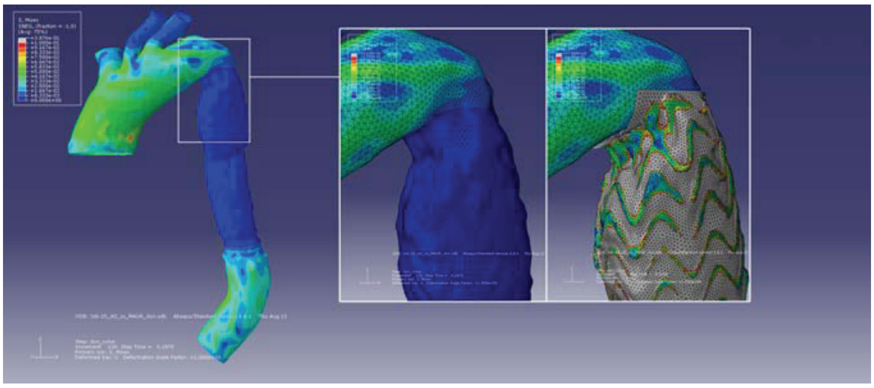

Figure 5.23: Stress distribution in the aorta of the simulation *with stent-graft* at t= 0.287 s (scale: 0 Nmm^{-2} in blue, 0.1 Nmm^{-2} in red).

The stress generated in the graft is much higher than the aortic stress and is therefore shown in Fig.5.24.a using a different scale. The largest graft stresses are found at the upper and lower ends, since at these ends, the graft is not *supported* by the stent and the graft displacements are not constrained. The smallest stresses are found in the areas in contact with the stent.

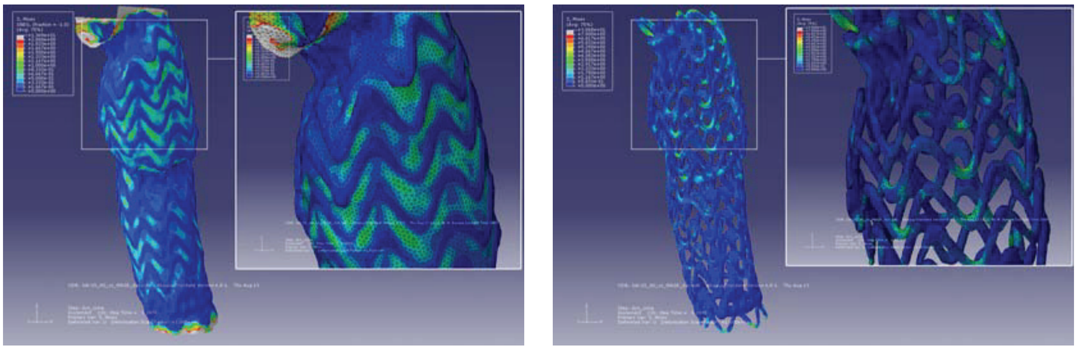
(a) Stress in the graft (b) Stress in the stent

Figure 5.24: Stress distribution in the graft (a) and stent (b) of the simulation *with stent-graft* at t= 0.287 s (scale (a): 0 Nmm^{-2} in blue, 2 Nmm^{-2} in red; scale (b): 0 Nmm^{-2} in blue, 7 Nmm^{-2} in red).

The stress in the stent generated through the contact with the graft and shown in Fig.5.24.b is clearly smaller than that of the simulation with *only* the stent, since the aorta with stent-graft is additionally supported by the graft.

Aorta with Stent-Graft-*Equivalent*

Instead of considering individual material models for the stent and the graft, it is possible to generate one material model that reproduces the elasticity of the connected stent-graft structure. This is denoted as the stent-graft-*equivalent* and has the advantage that only one contact between the aorta and the stent-graft needs to be modeled. For the simulation, a *tied linear contact* is used in the same way as done in Sec.5.7.3.

- **Stent-Graft-*Equivalent* from measurements:**
  [LK05c] generated a stent-graft-equivalent material based on measurements on self-made stent-grafts conducted by [SIK$^+$01] and analyzed under steady and dynamic pressure variations. The elasticity modulus, the poisson number and the shell thickness are E= 10 MPa, ν= 0.27 and d= 0.2 mm, respectively. The corresponding von Mises stresses on the aortic part that is hold by the stent are clearly higher than the previous simulation with the stent-graft. This is obviously due to the smaller elasticity modulus of the stent-graft-*equivalent* material model.

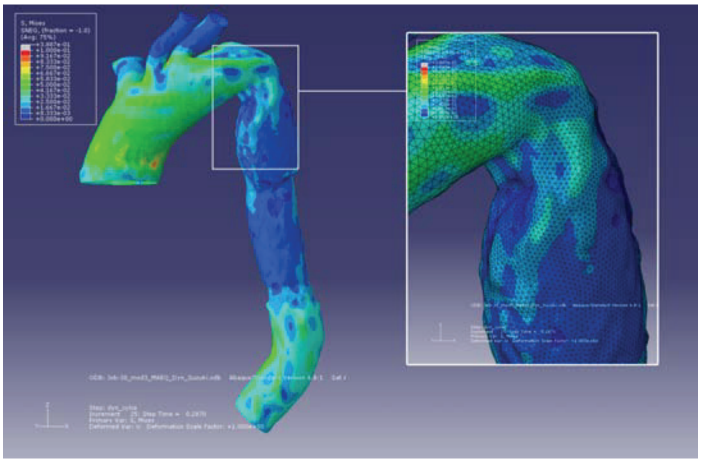

Figure 5.25: Stress distribution in the aorta of the simulation *with stent-graft-equivalent* from measurements at t= 0.287 s (scale: 0 Nmm^{-2} in blue, 2 Nmm^{-2} in red).

- **Stent-Graft-*Equivalent* from manufacturer's data:**

From manufacturer's data of an industrial stent-graft [Coo03] with a PET material for the graft and steel for the stent, [LK06a] generated a stent-graft-*equivalent* material model with E= 100 MPa, ν= 0.35 and d= 0.2 mm, respectively. Although this stent-graft is stiffer than the self-made from [SIK$^+$01], it still has a lower elasticity modulus than that of the PET graft material alone (3 GPa). Consequently, the von Mises stresses on the aortic part hold by the stent are also here higher than those of the simulation with stent-graft described in Sec.5.7.3.

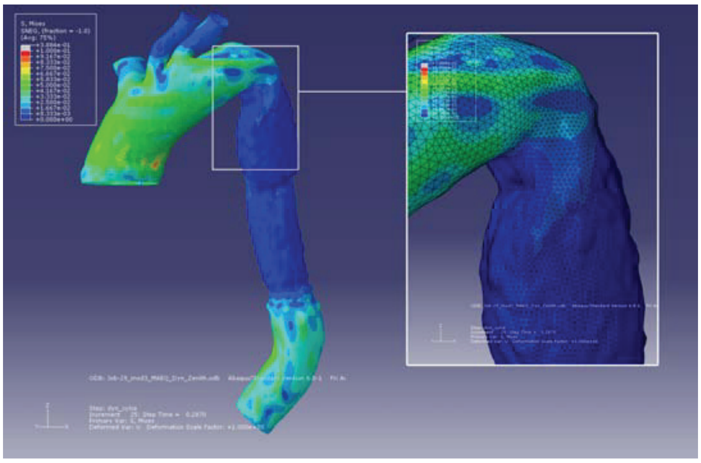

Figure 5.26: Stress distribution in the aorta of the simulation *with stent-graft-equivalent* from manufacturer's data at t= 0.287 s (scale: 0 Nmm^{-2} in blue, 2 Nmm^{-2} in red).

5.7.4 Cross-sectional Strain Analysis using 4D-CT-AA

The 4D-CT-P1 porcine model, obtained from a dynamic CT scan was simulated to quantify the stress distribution and the deformation along 20 phases of the cardiac cycle. The quantification of the deformation is used for the validation of the structural simulations and will be described in detail in Chap.8.

A cross-sectional strain analysis is performed for the quantification of the deformation within the porcine model. The deformation over the cardiac cycle is analyzed along various cross-sections of the aorta obtained from lateral cuts. Strain computations showed that the nodes located along the cross-sectional rings are not the same at the different times. This demonstrates that the deformation of the vessel is subject to distortion, that the displacement does not only occur in radial direction and that there are also rotation and translation acting in the other directions. This can be explained by the fact that subject-specific geometries are not homogeneous, resulting in distortion and forces acting inconstantly on the elements. Furthermore, the deformation computed based on a linear elastic model is found to be less valuable than that obtained from the hyperelastic model. This can be estimated by the fact that elastic models based on linear theories only apply at small loads and on the undeformed geometry and thus do not account for all cross-sectional strains. Fig.5.27 show the stress distribution along the aortic model and strain analysis across a cross-section located at mid-distance between the renal arteries and the aortic bifurcation obtained from the hyperelastic model.

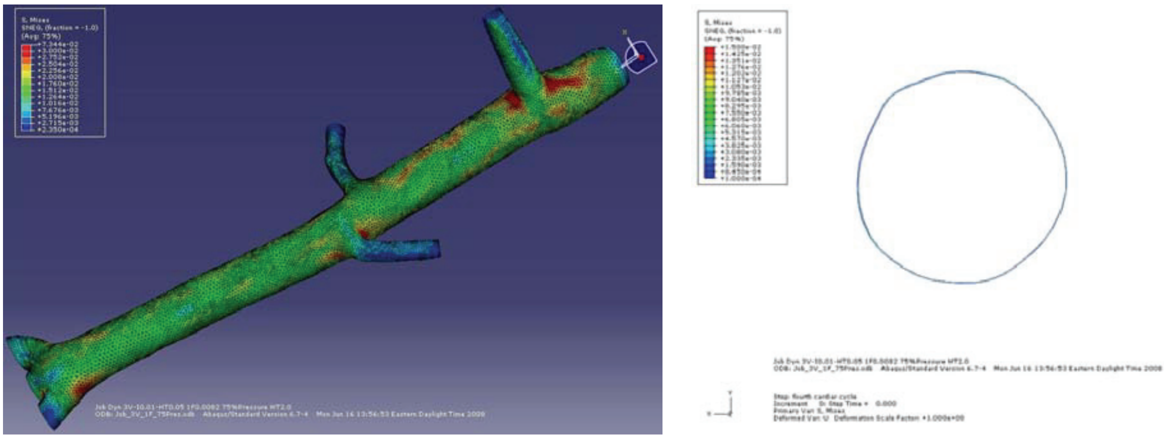

(a) Stress distribution (b) Strain analysis

Figure 5.27: Stress distribution and cross-sectional strain analysis.

The wall deformation results along five different cross-sections are presented and compared to the dynamic CT deformation obtained from the experiments in Sec.8.4.

5.8 Summary

In this chapter, computational modeling of the vessel wall to describe, simulate and analyze the mechanical behavior of the vessel wall within individual aortic models was presented. First, the physical fundamentals behind the modeling based on the concepts of continuum structural mechanics were illustrated by means of the elasticity theory and the strain-stress relationships. Then, the biomechanical constitutive laws necessary to describe the material behavior of the structure to be modeled were presented. The mathematical relations for the numerical discretization and the resolution of the governing equations based on the finite element method were then presented. Next, the theoretical aspects described in the first three sections were applied to the vessel wall in the CSM simulation section. Further, the integration of the vessel wall modeling steps into the *CSM-Sim* component of the MoDiSim simulation system was also described. Thereby, the automation of the steps, the optimization of the individual models as well as the individualization of the CSM simulations were presented. Finally, some simulation results obtained from four individual image-based models are shown at the end of this chapter. The effects of various models and aspects were thereby also presented.

Chapter 6

Blood Flow Modeling

6.1 Introduction

Cardiovascular diseases originate from complex hemodynamics conditions of the blood flow. The involved flow patterns and the associated high intraluminal pressure affect the vessel wall resulting in various forms of pathologies. Blood flow modeling provides an insight into the pathological conditions of the hemodynamics inside the vessel. It enables accurate predictive simulations of individual parameters such as sites of high pressures, velocity fields, recirculation zones or shear stress distributions.

Physically-based modeling is necessary to produce realistic blood flow simulations. Image-based Computational Fluid Dynamics (CFD) based on the Finite Volume Method (FVM) as a numerical approach, has become an efficient tool in simulating the individual hemodynamics in human arteries. The CFD approach consists of applying the physics of fluid dynamics, combined with constitutive modeling of the blood to simulate the dynamic behavior of the flow.

In this chapter the theoretical and applied aspects behind blood flow modeling will be described. The concepts of the modeling are first introduced based on the theoretical physics of fluid dynamics. Then, the constitutive laws governing the blood and the numerical approach of the finite volume method are presented. Next, the generation of the process chain and the performed simulations for the blood flow are described. Then, the integration of the CFD modeling steps into MoDiSim is presented. Finally, individual results from various patient-specific aortic models will be illustrated.

6.2 Continuum Fluid Dynamics

Continuum fluid dynamics is associated with the area of the physics dealing with the dynamics of continuous fluids. It involves the study of the mechanics of bodies with undefined shape. The basic concept of fluid dynamics is based on mathematical statements of three fundamental principles from the laws of physics. In particular, describing the motion of a fluid involves the continuity, momentum and energy equations derived from the mass, momentum and energy conservations, respectively. Thus, based on fundamental governing equations derived from *extensive* (mass, momentum and energy) properties, the state of a fluid may be described in terms of its *intensive* (flow velocity, pressure, density and temperature) variables being independent on the amount of the considered material.
The aim of the present section is to describe the theoretical concepts of fluid dynamics by discussing the fundamental conservation laws from which the basic equations of fluid motion are derived. Due to its importance for a better understanding, particular attention is given to the physical meaning of these fundamental principles in obtaining an appropriate flow model and in extracting the suitable mathematical equations that describe these physical principles.

6.2.1 Configuration Formulations

The common approach for formulating a suitable solid model, from which the conservation equations are derived, is based on the description of a given control mass. This is not a trivial approach for a fluid. While for a solid body it is easy to visualize and define a certain control mass, it is rather hard to define and trace a fixed amount of mass for a fluid in motion. In order to define a suitable model for a moving fluid, it is easier to describe it in a given space, namely a control volume, instead of tracing its control mass. Also, an accurate representation of the conservation law in an appropriate configuration is important for the numerical solution as described in Sec.6.4.

Finite and Infinitesimal Control Volumes

A volume space may be defined in terms of a *finite* or an *infinitesimal* control volume. A finite control volume is a closed volume V defined within a finite, reasonably large, region of the flow and bounded by a closed control surface S (Fig.6.1.a). The governing fluid equations derived *directly* by applying the conservation physical laws to a finite control volume are in integral form.

Processing these forms allows to *indirectly* obtain the governing partial differential equations. An infinitesimal control volume is an infinitesimal small fluid element in the flow with a differential volume dV that is enclosed by a differential surface dS (Fig.6.1.b). Despite its infinitesimal definition, the fluid element still contains enough molecules so that it can be considered as a continuous medium. Applying the fundamental physical principles to an infinitesimal fluid element leads *directly* to the fluid governing equations in partial differential equation form.

Fixed and Moving Configurations

Furthermore, the control volume may be considered as either *fixed* in space with the fluid moving through it, or *moving* with the fluid such that the same fluid particles are always inside it (Fig.6.1). For an infinitesimal moving control volume, its trajectory is indeed along a streamline with a velocity vector $\boldsymbol{v}$ equal to the velocity of the flow at each point. Based on these formulations, various forms of the governing equations may be derived. The fluid equations obtained, directly or indirectly, from a control volume fixed in space represent the *conservation form* of the governing equations. While the equations obtained from a control volume moving with the fluid, represent the *non-conservation* form of the governing equations. In general, through simple manipulation it is possible to toggle from one form to the other. While for analytical fluid dynamics it is irrelevant which form is used, the numerical stability in CFD applications strongly depends on the choice of the equations form and therefore it is necessary to distinguish between the use of these various forms.

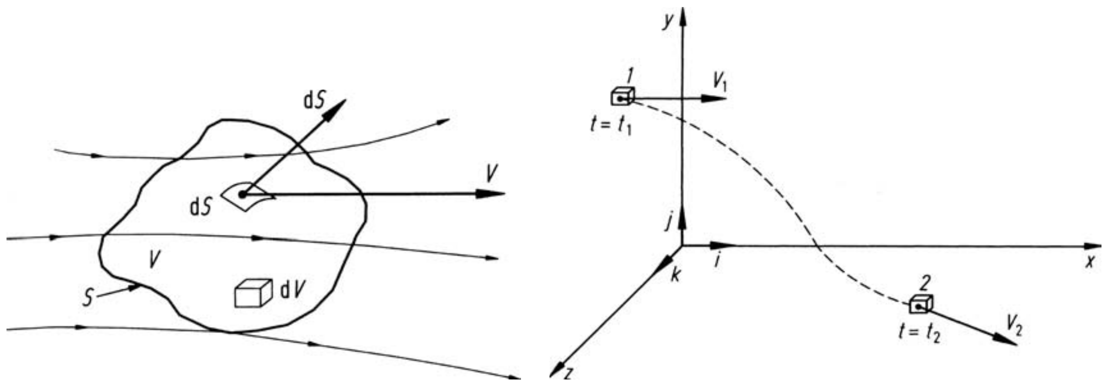

(a) Finite control volume fixed in space

(b) Infinitesimal fluid element moving with the flow

Figure 6.1: Finite and infinitesimal control volumes within fixed and moving configurations [WA09].

6.2.2 Substantial Derivative

A common term used in fluid dynamics which physical meaning is of vital importance for the derivation and the understanding of the governing equations is the substantial derivative. Considering the infinitesimal flow model with a small fluid element of volume dV moving with the flow through a cartesian space with unit vectors $\mathbf{i}_i = (\mathbf{i}_1, \mathbf{i}_2, \mathbf{i}_3)$, the motion of the fluid from point 1 at $t = t_1$ to point 2 at $t = t_2$ is illustrated in Fig.6.1.b. For a general unsteady flow, the velocity field vectors in this space expressed in terms of the position vectors $\mathbf{x} = (x_1, x_2, x_3)$ are given by:

$$\mathbf{v} = v_1(\mathbf{x}, t)\mathbf{i}_1 + v_2(\mathbf{x}, t)\mathbf{i}_2 + v_3(\mathbf{x}, t)\mathbf{i}_3 = \sum_{i=1}^{3} v_i(\mathbf{x}, t)\mathbf{i}_i \tag{6.1}$$

Taking the scalar density as field variable for the derivation of the substantial derivative, written as a function of both space and time $\rho = \rho(\mathbf{x}, t)$, then the density ρ_2 of the fluid element dV at point 2 and time t_2 may be expressed as a Taylor series about point 1 at t_1 where the density of dV is ρ_1 as follow:

$$\rho_2 = \rho_1 + \left(\frac{\partial \rho}{\partial x_1}\right)_1 \Delta x_1 + \left(\frac{\partial \rho}{\partial x_2}\right)_1 \Delta x_2 + \left(\frac{\partial \rho}{\partial x_3}\right)_1 \Delta x_3 + \left(\frac{\partial \rho}{\partial t}\right)_1 \Delta t \tag{6.2}$$

+ higher order terms, with $\Delta x_i = x_i(2) - x_i(1)$ and $\Delta t = t_2 - t_1$. Dividing Eq.6.2 by Δt and taking the limit as t_2 approaches t_1 while ignoring higher order terms, the instantaneous time rate of change of density of the fluid element as it moves through point 1 may be defined as:

$$\frac{D\rho}{Dt} \equiv \lim_{t_2 \to t_1} \left(\frac{\rho_2 - \rho_1}{t_2 - t_1}\right) = \sum_{i=1}^{3} v_i \frac{\partial \rho}{\partial x_i} + \frac{\partial \rho}{\partial t} \tag{6.3}$$

From Eq.6.3 and using the vector operator ∇, the expression of the *substantial derivative* operator becomes:

$$\frac{D}{Dt} \equiv \frac{\partial}{\partial t} + (\mathbf{v}.\nabla) \tag{6.4}$$

$\frac{D}{Dt}$ and $\frac{\partial}{\partial t}$ have different physical and numerical implications: while $\frac{D\rho}{Dt}$ is the time rate of change corresponding to the moving configuration as the fluid element sweeps through the space, $\frac{\partial \rho}{\partial t}$ represents the *local derivative* corresponding to the fixed configuration and is physically the time rate of change at stationary point due to transient fluctuations in the flow field.

As for $(\mathbf{v}.\nabla)$, it represents the *convective derivative* and is physically the time rate of change due to the movement of the fluid element from one location to another in the flow field where the flow properties are spatially different.

The substantial derivative may be applied to any flow field variable and its vectorial expression in Eq.6.4 is valid for any coordinate system. Mathematically, it is equivalent to the total differential $\frac{\mathrm{d}}{\mathrm{d}t}$ in calculus notation, defined by applying the chain rule to a variable and writing $\frac{\mathrm{d}x_i}{\mathrm{d}t}$ in terms of the i-th velocity v_i after differentiating with respect to time such as:

$$\frac{\mathrm{d}}{\mathrm{d}t} = \frac{\partial}{\partial t} + \sum_{i=1}^{3} v_i \frac{\partial}{\partial x_i} \tag{6.5}$$

6.2.3 Mass Conservation

The physical statement of the mass conservation principle applied to an appropriate fluid model leads to the continuity equation which reflects the first fundamental law of fluid dynamics. As mentioned above, the governing equations may be derived in various forms having different physical meanings depending on the definition of the control volume and the configuration used. Due to its physical relevance when applied to CFD problems, the distinction in using either the conservation or the non-conservation forms of the governing equations is derived below.

Continuity Equation from a Finite Fixed Configuration

Applying the mass conservation principle to a finite control volume fixed in space leads to *indirectly* obtain the conservation form of the partial differential equations. The physical formulation of this approach states that *the net mass flow out of the control volume V through its surface S is equal to the time rate of mass decrease inside the control volume*, that is:

$$\frac{\partial}{\partial t} \int_V \rho dV + \int_S \rho \mathbf{v} \mathrm{d}\mathbf{S} = 0 \tag{6.6}$$

which is the integral conservation form of the continuity equation. The differential form of these equations may be obtained by placing the time derivative inside the integral, which is possible since the limits of integration of a fixed control volume are constant, and by applying the divergence theorem to transform the surface integral into a volume integral:

$$\int_V \frac{\partial \rho}{\partial t} dV + \int_V \nabla(\rho \mathbf{v}) \mathrm{d}V = 0 \tag{6.7}$$

The integral in Eq.6.7 must vanish for an arbitrary choice of the finite control volume within the fluid domain. Thus, at every point within the control volume the integrand must be zero, so that the partial conservation form of the continuity equation becomes:

$$\frac{\partial\rho}{\partial t} + \nabla(\rho\mathbf{v}) = 0 \tag{6.8}$$

Continuity Equation from an Infinitesimal Moving Configuration

On the other hand, considering the model of an infinitesimal fluid element moving with the flow leads to *directly* obtain the non-conservation form of the partial differential equations. Manipulating these equations allow indeed to obtain their conservation form. Based on this approach, the physical statement of the mass conservation principle may be formulated as *the time rate of change of the mass of the fluid element is zero as the element moves along with the flow*. Denoting the fixed mass of the element by ∂m and its volume by ∂V, and using the physical meaning of the substantial derivative invoking the time rate of change, we have:

$$\frac{D(\partial m)}{\partial t} = 0 \qquad \text{or} \qquad \frac{D\rho}{\partial t} + \rho\left[\frac{1}{\partial V}\frac{D(\partial V)}{Dt}\right] = 0 \tag{6.9}$$

The term in brackets is defined as the divergence of the velocity given by $\nabla\mathbf{v}$. Physically, $\nabla\mathbf{v}$ reflects the time rate of change of the volume of a moving fluid element with constant mass, per unit volume. From this definition Eq.6.9 becomes:

$$\frac{D\rho}{\partial t} + \rho\nabla\mathbf{v} = 0 \tag{6.10}$$

which is the non-conservation form of the continuity equation from which the conservation form may be further obtained. Substituting the expressions resulting from the definitions of $\nabla(\rho\mathbf{v})$ and $\frac{D\rho}{\partial t}$ into Eq.6.10, gives:

$$\left(\frac{\partial\rho}{\partial t} + \mathbf{v}\nabla\rho\right) + (\nabla(\rho\mathbf{v}) - \mathbf{v}\nabla\rho) = 0 \tag{6.11}$$

which is, after simplification, the same conservation form of continuity equation obtained in Eq.6.8.

6.2.4 Momentum Conservation

Applying the momentum conservation principle to an appropriate fluid model leads to the momentum equations, also known as the Navier-Stokes equations named in honor of the physicists C. Navier and G. Stokes who independently derived these equations in the first half of the nineteenth century. The general Navier-Stokes equations arise from applying the fundamental physical principle of Newton's second law of motion to fluid dynamics. Physically, Newton's second law applied to the infinitesimal moving fluid element model with constant mass states that *the net force vector applied on the fluid element is equal to the product of its mass with its acceleration*, or for the x_i direction:

$$F_i = ma_i \tag{6.12}$$

Applied Forces

As already discussed in the last chapter, a moving object is subject to two kinds of forces: volume forces acting directly on its volumetric mass and surface forces acting directly on its surface. Volume forces usually act *at distance* such as gravitation or electro-magnetic forces. Denoting f_i as the volume force per unit mass acting on the fluid element in the x_i direction, then the volume force on the fluid element in this direction can be written as:

$$f_i^v = \rho f_i dV \tag{6.13}$$

Surface forces in the fluid originate from the pressure and from the shear and normal stress distributions, both exerted by the outside flow surrounding the fluid element. The fluid shear and normal stresses are imposed by means of friction and depend on the velocity gradients in the flow. They are related to the time rate of deformation change of the fluid element, specifically, to the time rate of change of the shearing deformation and the time rate of change of the volume, respectively. Fig.6.2 illustrates the surface forces acting on a fluid element in the x_1 direction, with τ_{ij} denoting the stress in the x_j direction applied on a plane perpendicular to the x_i axis. Thereby, the force directions on opposite faces are consistent with the convention that positive increases in all velocity components v_i occur in the positive axes directions. Thus, on the faces adhe i.e. bcgf perpendicular to the x_1 axis, the pressure forces pdx_2dx_3 i.e. $[p + (\partial p/\partial x_1)dx_1]dx_2dx_3$ always press inward on the fluid element. As for the viscous actions of the normal stresses $\tau_{11}dx_2dx_3$ i.e. $\tau_{11} + [(\partial\tau_{11}/\partial x_1)dx_1]dx_2dx_3$, they try to pull the element in the negative i.e. positive x_1 direction, keeping the value of v_1 just to the left i.e. right of face adhe i.e. bcgf smaller i.e. larger than its value on that face.

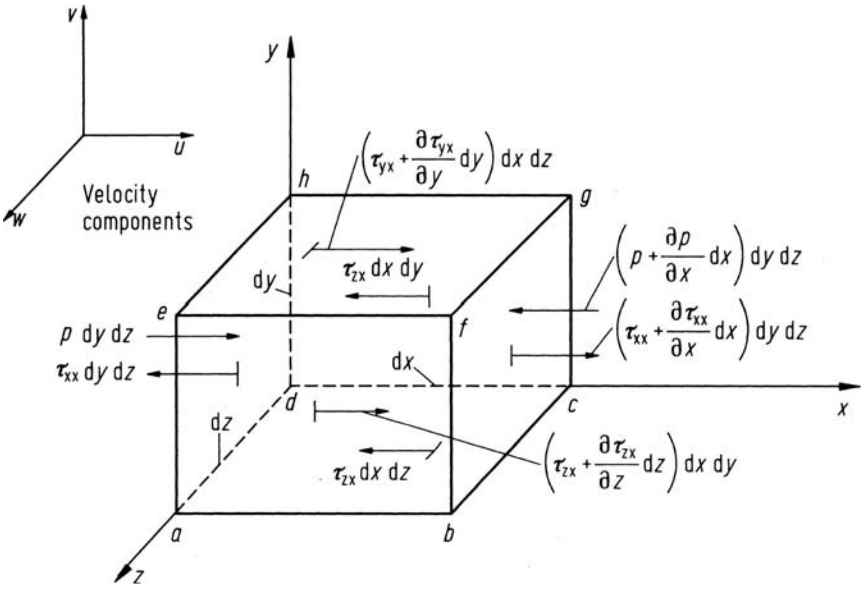
v
u
w
Velocity components
y
h
g
e
f
a
b
c
d
x
z
dy
dx
dz
$\left(\tau_{yx}+\frac{\partial\tau_{yx}}{\partial y}dy\right)dx\,dz$
$\tau_{zx}\,dx\,dy$
$\left(p+\frac{\partial p}{\partial x}dx\right)dy\,dz$
$\left(\tau_{xx}+\frac{\partial\tau_{xx}}{\partial x}dx\right)dy\,dz$
$p\,dy\,dz$
$\tau_{xx}\,dy\,dz$
$\tau_{zx}\,dx\,dz$
$\left(\tau_{zx}+\frac{\partial\tau_{zx}}{\partial z}dz\right)dx\,dy$

$(x,y,z)\equiv(x_1,x_2,x_3)$ *and* $(u,v,w)\equiv(v_1,v_2,v_3)$

Figure 6.2: Surface forces acting on a fluid element [WA09].

Considering all force components exerted on the fluid element, the total surface force t_i^s in an x_i direction may be simplified as:

$$t_i^s = \left(-\frac{\partial p}{\partial x_i} + \frac{\partial \tau_{1i}}{\partial x_1} + \frac{\partial \tau_{2i}}{\partial x_2} + \frac{\partial \tau_{3i}}{\partial x_3}\right) dV = \nabla t_i dV \tag{6.14}$$

where t_i is the stress tensor representing the molecular transport rate of the impulse in the x_i direction, composed of a viscous and a pressure term:

$$t_i = -p\mathbf{i}_i + \sum_{j=1}^{3} \tau_{ji}\mathbf{i}_j \tag{6.15}$$

Navier-Stokes Equations

The total force vector F_i applied in the x_i direction on a moving fluid element may be obtained by adding f_i^v and t_i^s. F_i represents the left-hand side of the momentum conservation equation. The right-hand side can be obtained by expressing the fixed mass of the moving fluid element as $m = \rho dV$ and its acceleration a_i as the time rate of change of its velocity, namely by its substantial derivative. Inserting these into Eq.6.12, the x_i component of the momentum equation for a viscous flow takes after simplification the form:

$$\rho\frac{Dv_i}{Dt} = -\frac{\partial p}{\partial x_i} + \frac{\partial \tau_{1i}}{\partial x_1} + \frac{\partial \tau_{2i}}{\partial x_2} + \frac{\partial \tau_{3i}}{\partial x_3} + \rho f_i \tag{6.16}$$

The governing momentum equations derived based on this approach are directly obtained as partial differential equations in the non-conservation form. Processing these equations allows indeed to obtain the conservation form of the Navier-Stokes equations. By using the definition of the substantial derivative and applying the product divergence theorem, the left-hand side of Eq.6.16 becomes:

$$\rho \frac{Dv_i}{Dt} = \frac{\partial \rho v_i}{\partial t} - v_i \frac{\partial \rho}{\partial t} - v_i \nabla \left(\rho \mathbf{v}\right) + \nabla \left(\rho v_i \mathbf{v}\right) \tag{6.17}$$

The second and third terms of this equation include the left-hand side of the continuity equation given in Eq.6.8 which indeed equals zero. Consequently, substituting the simplified Eq.6.17 into Eq.6.16 leads to the general Navier-Stokes equations in conservation form given in the x_i direction by:

$$\frac{\partial \rho v_i}{\partial t} + \nabla(\rho v_i \mathbf{v}) = \nabla \left(-p\mathbf{i}_i + \sum_{j=1}^{3} \tau_{ji} \mathbf{i}_j \right) + \rho f_i \tag{6.18}$$

6.2.5 Energy Conservation

The physical statement of the fundamental principle of energy conservation represents the first law of thermodynamics translated in terms of the energy equations. Applied again to the infinitesimal moving control volume model, the energy conservation states that *the rate of change of energy inside the fluid element = the net flux of heat into the element + the rate of work done on the element due to volume and surface forces.*

Rate of Work: The expression for the rate of work done by a force applied on a moving fluid element is equivalent to that force multiplied with the velocity component in the force direction. Thereby, forces in the positive i.e. negative x_i direction do positive i.e. negative work. Considering body forces $\mathbf{f}$ exerted on the fluid element moving at a velocity $\mathbf{v}$, the rate of work done by these forces is $W^v = \rho \mathbf{f} \mathbf{v} dV$. Further, the rate of work W_i^s done by the surface forces illustrated in Fig.6.2 and acting in the x_i direction on the moving fluid element is simply the product of the v_i component of the velocity with these forces. In total, the net rate of work W^{net} done on the moving fluid element due to the surface force contributions in the x_1, x_2 and x_3 directions, as well as the body force contribution may be obtained as the total sum:

$$W^{net} = \left[\sum_{i=1}^{3} \left(-\frac{\partial(v_i p)}{\partial x_i} + \frac{\partial(v_i \tau_{1i})}{\partial x_1} + \frac{\partial(v_i \tau_{2i})}{\partial x_2} + \frac{\partial(v_i \tau_{3i})}{\partial x_3} \right) + \rho \mathbf{f} \mathbf{v} \right] dV \tag{6.19}$$

Eq.6.19 includes indeed the divergence $\nabla(p\mathbf{v})$ represented by the sum of the three terms including the pressure.

Net Flux of Heat: The heat flux into the element originates from volumetric heating due to absorption or emission of radiation and from heat transfer across the surface due to thermal conduction. If $\dot{q}$ denotes the positive rate of volumetric heat change per unit mass, then the volumetric heating H^{vh} may be defined by:

$$H^{vh} = \rho \dot{q} dV \tag{6.20}$$

Further, defining $\dot{q}_i$ as the heat transfer in the x_i direction per unit time and area due to temperature gradients, the heat transferred across all faces into the fluid element by thermal conduction becomes:

$$H^{ht} = -\left(\frac{\partial \dot{q}_1}{\partial x_1} + \frac{\partial \dot{q}_2}{\partial x_2} + \frac{\partial \dot{q}_3}{\partial x_3}\right) dV \tag{6.21}$$

Taking into account that the heat transfer by thermal conduction $\dot{q}_i$ is proportional to the local temperature gradient $\partial T/\partial x_i$ via the thermal conductivity coefficient k, the net heat flux into the element H^{net} expressed as the sum of H^{vh} and the total H^{ht} becomes:

$$H^{net} = \left[\sum_{i=1}^{3} \frac{\partial}{\partial x_i}\left(k \frac{\partial T}{\partial x_i}\right) + \rho \dot{q}\right] dV \tag{6.22}$$

Rate of Change of Energy: At last, the time rate of change of energy per unit mass inside a moving fluid element may be expressed in terms of the substantial derivative. With the total energy of a moving fluid per unit mass defined as the sum of its internal energy e and its kinetic energy $v^2/2$ and with the mass of the fluid element being again ρdV, the rate of change of energy E^{net} becomes:

$$E^{net} = \rho \frac{D}{Dt}\left(e + \frac{v^2}{2}\right) dV \tag{6.23}$$

Energy Equations

Finally, the energy equation in non-conservation form derived from the application of the energy physical principle to an infinitesimal moving control volume is obtained by setting $E^{net} = H^{net} + W^{net}$. The energy equation in conservation form may be derived in a similar way as for the momentum equations by using the definition of the substantial derivative and applying the divergence theorem such as:

$$\rho \frac{D}{Dt}\left(e + \frac{v^2}{2}\right) = \frac{\partial}{\partial t}\left[\rho\left(e + \frac{v^2}{2}\right)\right] + \nabla\left[\rho\left(e + \frac{v^2}{2}\right)\mathbf{v}\right] \tag{6.24}$$

The final energy equation in conservation form written in terms of the total energy may be obtained by substituting the E^{net} term in the non-conservation form by the right-hand side of Eq.6.24 so that:

$$\begin{aligned}\frac{\partial}{\partial t}\left[\rho\left(e+\frac{v^2}{2}\right)\right]+\nabla\left[\rho\left(e+\frac{v^2}{2}\right)\mathbf{v}\right]=\left[\sum_{i=1}^{3}\frac{\partial}{\partial x_i}\left(k\frac{\partial T}{\partial x_i}\right)+\rho\dot{q}\right]\\+\left[\sum_{i=1}^{3}\left(-\frac{\partial(v_i p)}{\partial x_i}+\frac{\partial(v_i\tau_{1i})}{\partial x_1}+\frac{\partial(v_i\tau_{2i})}{\partial x_2}+\frac{\partial(v_i\tau_{3i})}{\partial x_3}\right)+\rho\mathbf{f}\mathbf{v}\right]\end{aligned} \tag{6.25}$$

6.2.6 Numerical Equations Form

All above equations derived from the fundamental principles include the divergence of some physical flux on the left-hand side of their conservation form; the divergence of the mass flux $\rho\mathbf{v}$ is involved in Eq.6.8, the x_i component of the momentum flux $\rho v_i\mathbf{v}$ in Eq.6.18 and the (total) energy flux $\rho\left(e+\frac{v^2}{2}\right)\mathbf{v}$ in Eq.6.25. These conservation forms are the direct result of applying the physical laws on a control volume that is fixed in space. For such a configuration, the concerned quantities are the mass, momentum and energy fluxes into and out of the volume. They become therefore the dependent variables rather than the primitive variables for pressure, velocity, density and temperature. Further, the conservation forms of these equations take all the same generic form and the entire system of the conservation equations may be therefore represented in terms of column vectors **U**, **F**, **G**, **H** and **J** in the form [WA09]:

$$\frac{\partial\mathbf{U}}{\partial t}+\frac{\partial\mathbf{F}}{\partial x_1}+\frac{\partial\mathbf{G}}{\partial x_2}+\frac{\partial\mathbf{H}}{\partial x_3}=\mathbf{J} \tag{6.26}$$

As a result, the obtained solution variables based on this approach invoke the elements in **U** (ρ, ρv_i and $\rho(e+\frac{v^2}{2})$) as the dependent variables rather than the primitive variables v_i and e. These are usually solved numerically in steps of time, from which the primitive variables may be further derived. Also, the terms in Eq.6.26 include all flow variables and thus all flow information within the single x_i and t derivatives. Compared to Eq.6.18 and Eq.6.25 containing x_i derivatives explicitly appearing in their right-hand side, the flow equations in the form of Eq.6.26 are said to be in strong conservation form. Another form of the conservation equations is the general transport equation for a scalar quantity ϕ. In the continuity equation ϕ is equivalent to 1 while in the momentum equation ϕ represents the velocity v_i. With Γ_ϕ denoting the diffusion coefficient and f_ϕ the source of ϕ per unit volume, the general transport scalar equation may be expressed in vector form as:

$$\frac{\partial\rho\phi}{\partial t}+\nabla(\rho\phi\mathbf{v})=\nabla(\Gamma_\phi\nabla\phi)+f_\phi \tag{6.27}$$

6.3 Physical Properties and Constitutive Laws

An essential aspect while modeling the dynamics of the flow is an accurate and realistic description of the physical nature of the fluid as a material. Thus, a reliable flow analysis requires not only a description of the fundamental equations but also appropriate constitutive laws for the fluid material. In the previous section the governing equations of fluid dynamics were derived based on the fundamental conservation principles. These equations contain terms such as the density describing the compressibility or the shearing stress containing the viscous physical nature of the fluid. Furthermore, the fundamental equations are basically derived for laminar flow and do not include the effects of turbulence. Constitutive relationships allow describing these physical properties governing the general behavior of the fluid. Substituted into the governing equations, a physical problem may be accurately solved. This section deals with the description of various material properties of the fluid which influence the behavior of the flow and based on which constitutive equations may be derived for the definition of a suitable flow model. To mention that from this point on, the energy equation will be omitted and the description will be restricted to the continuity and the momentum equations.

6.3.1 Incompressibility

Compressibility was introduced in the last chapter for soft tissue modeling. Also in fluid dynamics, its relative magnitude may be measured in terms of the bulk modulus K defined in Eq.5.68. It is similarly related to the change in volume of a fluid with a fixed mass once subjected to a force or pressure. Compressible fluids are therefore fluids with variable density. Most liquids exhibit no change in volume at constant temperature. Such fluids have a constant density and are said to be incompressible. On the other hand, most gases are rather compressible fluids and their density takes variable values following the general gas equations $p = \rho RT$.
Considering a fluid element with constant mass moving along a streamline in an incompressible flow, then the density of this element is constant resulting in a constant volume. As a result, the divergence of v being the time rate of change of the volume of a fluid element per unit volume and defined as part of Eq.6.9 becomes zero. Consequently, the mass conservation principle leads to the continuity equation for an incompressible fluid in the form:

$$\nabla \mathbf{v} = 0 \tag{6.28}$$

This result complies with the continuity equation derived in Eq.6.8 for a general compressible fluid with $\frac{\partial \rho}{\partial t} = 0$.

As for the vectorial form of the momentum equation for an incompressible fluid, it may be expressed by:

$$\rho\left[\frac{\partial \mathbf{v}}{\partial t}+(\mathbf{v}\nabla)\,\mathbf{v}\right]=-\nabla p+\nabla\tau+\rho\mathbf{f} \tag{6.29}$$

6.3.2 Viscosity

An realistic modeling requires also an accurate description of the physical nature of the viscous properties of the fluid. Viscosity describes the resistance of fluid deformation due to the flow. Glenn Elert mentioned in the Physics Hypertextbook that *fluids resist the relative motion of immersed objects through them as well as to the motion of layers with differing velocities within them.* Isaac Newton defined in the late seventeenth century the fluid resistance, or the molecular viscosity μ as the ratio of the shearing stress to the fluid time rate of strain, or velocity gradients. Based on Newton's statement, Stokes derived in 1845 the following relationship for viscous fluids:

$$\tau_{ij}=2\mu D_{ij}-2/3\mu\delta_{ij}\nabla\mathbf{v} \tag{6.30}$$

where D_{ij} is the rate of deformation tensor, given by:

$$D_{ij}=\frac{1}{2}\left(\frac{\partial v_i}{\partial x_j}+\frac{\partial v_j}{\partial x_i}\right)\qquad \textit{or}\qquad \mathbf{D}=\frac{1}{2}\left[\nabla\mathbf{v}+(\nabla\mathbf{v})^T\right] \tag{6.31}$$

The stress tensor defined in Eq.6.15 takes then the form:

$$t_i=-p\mathbf{i}_i+\sum_{j=1}^{3}\mu\left(\frac{\partial v_i}{\partial x_j}+\frac{\partial v_j}{\partial x_i}\right)\mathbf{i}_j-\frac{2}{3}\frac{\partial v_j}{\partial x_j}\mu\mathbf{i}_i \tag{6.32}$$

Consequently, the resulting conservative form of the Navier-Stokes equation with viscosity terms may be obtained by replacing Eq.6.32 into Eq.6.18. Further, the fluid is assumed as *Newtonian* if its dynamic viscosity is constant. Stokes' derivation was originally defined for Newtonian fluids. However, in some fluids such as the blood, the flow behavior in areas of low shear rates cannot be neglected. Under such varying conditions, the dynamic viscosity becomes a function of the shear rate and cannot be modeled as constant. Instead, the shear stresses and the velocity gradients exhibit a nonlinear relationship. This behavior with shear-dependant viscosity is known as *non-Newtonian* behavior. Viscous equations are used to reproduce the non-Newtonian properties by describing the shear-viscosity relation within the fluid flow.

Furthermore, non-Newtonian models may describe a shear-thinning or a shear-thickening behavior where the dynamic viscosity is a decreasing or increasing function of the shear rate, respectively. In both cases, the shear rate is defined as a function of the second invariant of the rate of deformation tensor [SC05].

$$\dot{\gamma} = \sqrt{\frac{1}{2}\sum_i \sum_j D_{ij} D_{ji}} \tag{6.33}$$

6.3.3 Laminar and Turbulent Flow

Despite all advances achieved in the field of turbulent fluid dynamics by Reynolds, Prandl, Heisenberg or Landau, it is still until the date simpler to explain the black hole theory than to estimate the velocity of the water flowing out of the tap! Turbulence is still one of the most complex physical disciplines and is up to date not fully understood. A flow that exhibits a regular motion along parallel streamlines which layers do not interfere together is called laminar. A turbulent flow on the other hand, is a fluid flow in which apparent randomness, unpredictable fluctuations and irregular motions occur. It is characterized by recirculation zones, chaotic vortices and unregulated property changes. Turbulent flows contain *eddies* of different characteristic length scales, affecting in turn velocity scales and time scales. Eddies of large scales are unstable and may break up with their total kinetic energy giving rise to smaller eddies with smaller energy. The breaking process continues iteratively with the smaller eddies until a sufficiently small length scale is achieved. An exact and definite definition of turbulence in fluid dynamics is however complex and recirculation, fluctuations and eddies may also be present in laminar flows. The onset of turbulence may be described by means of the dimensionless Reynolds number Re, defined as the ratio of the inertial forces to viscous forces present in the flow. For a flow in a pipe of diameter D, the Reynolds number (1883) is defined as:

$$\mathrm{Re} = \frac{\rho \mathbf{v} D}{\mu} = \frac{\mathbf{v} D}{\nu} \tag{6.34}$$

Turbulent flow usually occurs at large values of the Reynolds number. In practice, Reynold found out that for such fluids, the flow is laminar for $Re \leq 2000$ and becomes turbulent for $Re \geq 4000$. Mathematically, there exist various approaches for modeling and prediction of turbulence effects. Three categories of methods are briefly discussed here.

Direct Numerical Simulation

The most accurate way to simulate turbulent flow behavior is to numerically solve the governing equations only by means of discretization, without any turbulence modeling approximation. This numerical technique is therefore known as the direct numerical simulation (DNS). In this way, all flow motions associated with the whole range of small eddies must be resolved in space and time. Thereby, the dimension of the numerical domain must be at least as large as the physical domain or the smallest turbulent vortex to ensure that all significant structures are enclosed. A common scale hereby is the integral scale L, which represents the length for which the velocity fluctuations still correlate. On the other hand, a valid simulation must also reflect the whole dissipation of the kinetic energy, which takes place at the smallest scales where the viscosity dominate. Thus, the numerical domain can not be larger than the scale dominated by the viscosity, called the *Kolmogorov scale*, η. Consequently, the number of mesh points in each direction must at least equal L/η, which can be proven to be proportional to $Re_L^{3/4}$ [TL90]. As a result, the number of timesteps integration and thus the total computational effort also grow proportional to Re_L^3. Even at low Reynolds numbers and for most applications the DNS effort exceeds the capacity of most modern nowadays available supercomputers.

Large Eddy Simulation

An alternative numerical approach for solving the partial differential equations governing the turbulent flow domain is the large eddy simulation (LES), first formulated in the late 1960s. In this method only the large scale motions associated with the large eddies in the flow are resolved explicitly, while the smaller eddies approximations are modeled using subgrid scale (SGS) models. This is equivalent to solving the filtered Navier-Stokes equations with an additional SGS stress term. The most used SGS models are the *Smagorinsky* model (1963) and its dynamic forms as well as the deconvolution model. By adding an extra *eddy viscosity* into the governing equations, these models compensate for the unresolved small turbulent scales. The LES technique is based on *Kolmogorov's* theory (1941) of self similarity stating that large eddies are influenced by the flow geometry, while smaller eddies have a universal shape being self similar. The computational effort associated with the LES is less than that of the DNS but still larger than that of solving the Reynolds-averaged Navier-Stokes equations.

Fig.6.3 illustrates an LES and a DNS turbulence motion and the corresponding time-dependent velocity components.

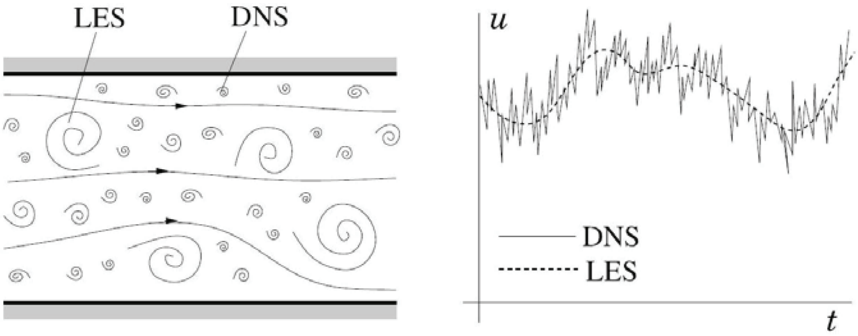

Figure 6.3: LES and DNS turbulence motions and their velocity components [FP08].

Reynolds-Averaged Navier-Stokes

As shown in the previous sections, for moderate Reynolds numbers, it is possible to describe turbulent flows by means of the DNS, however with restrictions depending on the computational resources and the algorithm efficiency. Real-life flow problems may be better solved based on the Reynolds-averaged Navier-Stokes equations (RANS) combined with turbulence modeling to simulate the effects of turbulent flows. Although the LES is able to provide an increased level of instantaneous characteristics compared to the RANS, this remains only an advantage for flow simulations involving chemical reactions or acoustic prediction. Mathematically, RANS modeling is based on the Reynolds decomposition, allowing to separate the flow into an average component and a perturbation or fluctuation component. Such a decomposition mainly leads to additional Reynolds stress terms describing additional momentum transfer and which can be used to resolve the turbulent flow besides the governing equations. The RANS approach and an overview on the turbulence models will be described in the next section.

6.3.4 RANS Equations and Turbulence Models

In the Reynolds-averaged methods, the whole unstationarity is averaged, that is, the whole time variation is considered as a part of the turbulence. Through the averaging, nonlinearities in the governing equations lead to extra terms which have to be additionally modeled. The complexity of the turbulence makes it almost impossible to find a unique RANS-based model able to describe the whole turbulence in an enough accurate way. That is why turbulence models are more engineering approximations rather than physical laws [FP08].

RANS Equations

As mentioned above, RANS modeling is based on the Reynolds decomposition separating the flow into an average part and a perturbation part. Thus, a variable ϕ may be written as a sum of its time averaged value and a perturbation around this average such as:

$$\phi(x_i,t)=\bar{\phi}(x_i,t)+\phi'(x_i,t) \tag{6.35}$$

For quasi-steady flows, $\bar{\phi}(x_i)$ is constant in time and may be indeed written within a large enough time interval T as:

$$\bar{\phi}(x_i)=\lim_{T\to\infty}\frac{1}{T}\int_0^T\phi(x_i,t)dt \tag{6.36}$$

While for unsteady flows $\bar{\phi}(x_i,t)$ denotes the *Reynolds-average* and its mean value along N *Ensemble* members is:

$$\bar{\phi}(x_i,t)=\lim_{N\to\infty}\frac{1}{N}\sum_{n=1}^{N}\phi_n(x_i,t) \tag{6.37}$$

Eq.6.36 shows indeed that the fluctuations are defined such that their time average equals zero, $\bar{\phi}'=0$. Physically, this means that the average of a linear term is identical to the value of that term itself. On the other hand, two nonlinear uncorrelated variables ϕ and φ lead to additional *covariance* terms $\overline{\phi'\varphi'}$ describing the correlation of the fluctuations, such as:

$$\overline{\phi\varphi}=\overline{(\bar{\phi}+\phi')(\bar{\varphi}+\varphi')}=\bar{\phi}\bar{\varphi}+\overline{\phi'\varphi'} \tag{6.38}$$

Applying the above equations to the governing equations leads to the RANS equations for turbulent flow. These contain the additional nonlinear *Reynolds stresses* term that introduces additional momentum transfer to reflect the turbulence. The RANS turbulence equations in terms of the continuity and the x_i-component of the momentum equations are:

$$\frac{\partial\rho}{\partial t}+\sum_{j=1}^{3}\frac{\partial\rho\bar{v}_j}{\partial x_j}=0 \qquad \text{and} \tag{6.39}$$

$$\frac{\partial\rho\bar{v}_i}{\partial t}+\sum_{j=1}^{3}\frac{\partial\left(\rho\bar{v}_i\bar{v}_j+\rho\overline{v_i'v_j'}\right)}{\partial x_j}=-\frac{\partial\bar{p}}{\partial x_i}+\sum_{j=1}^{3}\frac{\partial\bar{\tau}_{ji}}{\partial x_j}+\rho\bar{f}_i \tag{6.40}$$

$$\text{with} \qquad \bar{\tau}_{ji}=\bar{\tau}_{ij}=\mu\left(\frac{\partial\bar{v}_i}{\partial x_j}+\frac{\partial\bar{v}_j}{\partial x_i}\right)-2/3\mu\delta_{ij}\nabla\bar{\mathbf{v}} \tag{6.41}$$

Where the fluctuations effects due to the time-averaged normal and shear stresses are relatively small and therefore neglected in the expression of $\bar{\tau}_{ji}$.

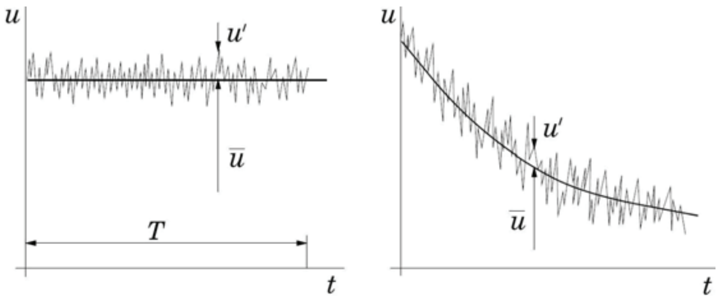

Figure 6.4: RANS: Steady and unsteady averaging processes [FP08].

Turbulence Models

With the additional turbulent stresses $\rho\overline{v_i'v_j'}$ in the RANS equations, the governing system becomes unsolvable, including more unknown than equations. The so known *closure problem* imposes that additional equations must be defined in order to solve the flow dynamics. This is achieved by adopting approximations, defined as turbulence models, that describe the additional fluctuations in the flow. In 1877 J. Boussinesq proposed to model turbulent stresses in a way similar to that of the normal and shear stresses and introduced the concept of the *eddy viscosity.* His concept is based on the formulation that the additional Reynolds stresses are given by augmenting the molecular viscosity with an eddy viscosity. Writing the RANS equations in a vectorial form gives:

$$\frac{\partial \rho \bar{\mathbf{v}}}{\partial t} + \rho \left(\bar{\mathbf{v}} \nabla \right) \bar{\mathbf{v}} = -\nabla \bar{p} + \nabla \bar{\tau} + \nabla \bar{\tau}_t + \rho \bar{\mathbf{f}} \tag{6.42}$$

with τ_t denotes the Reynolds stress tensor with $-\rho\overline{v_i'v_j'}$ turbulent stress variables. After Boussinesq, these turbulent stresses may be expressed -analog to the viscous stresses in Eq.6.41- in terms of the eddy viscosity μ_t in the form:

$$-\rho\overline{v_i'v_j'} = \mu_t \left(\frac{\partial \bar{v}_i}{\partial x_j} + \frac{\partial \bar{v}_j}{\partial x_i} \right) - 2/3 \rho \delta_{ij} k \tag{6.43}$$

where $k = 1/2\ \overline{v_i'v_i'}$ denotes the kinetic energy of the turbulence. Turbulence models that are based on the concept of Boussinesq aim to model μ_t. They are classified following the number of additional partial differential equations they include. Algebraic turbulent models are known as zero-level models, while models requiring one or two PDE are known as one-level and two-level models, respectively. Further derivation of these models based on modeling of μ_t may be found in the books of fluid dynamics such as in [OBD09] or [FP08]. The most known two-level model is the $k - \epsilon$ model, which will be integrated for the simulations in this work.

6.4 Finite Volume Method

The fundamental equations of fluid dynamics are the results of physical statements of the mass, momentum and energy conservation laws applied on a closed volume. Together with the constitutive material laws, these dynamics equations describe the complex physical behavior of the flow motion. The main complexity lies in the hybrid character of the flow leading to a mixed regions with different characteristic equations. As a result, great numerical effort as well as sophisticated mathematical resolution approaches are required to solve these equations iteratively. The purpose of the numerical techniques remain to obtain a temporal and spacial derivation of the unknown flow variables.
Furthermore, the blood flow is dominated by physical and geometrical nonlinearities, which are even more dominant as in soft-tissue modeling. These nonlinearities must also be taken into account by the resolution methods for realistic simulations. The Finite Volume Method (FVM) is an appropriate numerical technique which has shown great efficiency in solving complex systems of nonlinear time-dependent fluid dynamics problems. Similar to the FEM, the FVM solution is approximated based on spatial and temporal discretization of the fluid domain using incremental techniques and combined with numerical integration methods and suitable iterative schemes.

6.4.1 FVM versus FEM

The FVM holds the same geometric characteristic, in the sense of flexibility, as the FEM. In both methods, the continuum domain is subdivided into cells (FVM) or elements (FEM) forming a grid which may have structured or unstructured forms. The use of unstructured grids allows handling very complex geometries and represents an important advantage of these methods compared to the finite difference method (FDM) which needs a structured grid. On the other hand, while the discrete solution of the FEM problem have a prescribed form, the FVM solution is not assumed to do so. The FEM solution has to belong to a function space built by linearly or quadraticaly varying function values between values in the nodes. The nodes in turn are chosen at specific positions belonging to the elements which makes the numerical solution strongly influenced by the geometric discretization of the domain. The FVM solution does not require a definition of a function space and the choice of the nodes may be defined *in a way that does not imply an interpolation structure* [WA09]. Furthermore, in the FVM the volumes to which the conservation laws are applied may be decoupled from the cells related to geometry discretization. As a result, the freedom in determining the function definition of the discrete flow field in the FVM is enhanced and becomes larger than in the FEM.

However, in contrast to the FDM, defining derivatives in the FVM is not trivial. Since the computational grid is usually neither orthogonal nor equally spaced, a definition of a derivative based on a Taylor expansion is not possible. Furthermore, the FVM does not have a mechanism similar to the weak formulation, to convert higher order derivatives into lower ones as it is the case in the FEM. In the FVM, it is extremely important to accurately represent the conservation laws for the numerical solution. In order to achieve this, in many situations where discontinuities occur, the solution of the fundamental equations is to be interpreted in its weak form, as a solution of the equations in their integral form. Therefore, the numerical solution in the FVM is based on the discretization of the integral form of the equations rather than the differential form.

In summary, the FVM combines the freedom in the geometric representation of the grid from the FEM with the flexibility in the function representation of the discrete flow field variables from the FDM. It is this combination together with the control volume based formulation of a flow problem, reflecting a robust physical discretization, which mark the specific distinctiveness of the FVM in CFD applications.

6.4.2 Spatial Discretization

In general, the FVM-based discretization process for the solution of the governing conservation laws consists of the decomposition of the flow domain into finite control volumes based on a generated numerical grid and the integration of the governing equations over the individual control volumes. Based on the discretized nonlinear equations, algebraic equations for the discrete dependent flow variables may be derived and linearized. Finally, the resultant linearized algebraic system of equations may be solved iteratively using interpolation and coupling techniques to determine the values of the dependent variables within the flow domain. The first step in the discretization is the definition of the points in the computational domain, where the values of the unknown variables will be calculated. The distribution problem is more complex as it seems and is indeed related to the properties of the conservation equations.

Cell-Volume Formulation

A grid is first generated by decomposing the computational domain into a finite number of non-overlapping cells spaming the flow field. Complex problems usually require that the cells are elements of an unstructured grid, allowing high flexibility in the adjustment of the gid to the boundaries of the domain.

Further, control volumes must be defined for which the conservation laws are applied. The flow field variables are then determined in some discrete points of the cells, called nodes. There are many possibilities for the definition of the control volumes and the distribution of the computational points within the numerical domain. The choice of the nodes strongly depends on the intention to represent the solution by an interpolation structure or not. The *FEM-like* FVM uses cells to which an interpolation structure is associated. Thereby, the control volumes are defined to adapt the grid geometry and the computational points are defined in the cell-centres (Fig.6.5.a) for representation as piecewise constant functions or in the cell-vertices (Fig.6.5.b) for representation as piecewise linear or bilinear functions. Alternatively, since the FVM does not require a definition of a function space, nodes can be chosen without associating an interpolation structure. More flexibility in the flux definition can be obtained by using an interweaving grid with nodes at the vertices of the grid and which can be constructed by connecting the centres of the cells as shown in (Fig.6.5.c). Here, The semi-discretization is very close to the FDM and is called *conservative FDM-like* or *vertex-based* FVM. Another alternative, is to first fix the position of the computational points, and then define the control volumes such that their sides lie at mid-distance between two computational points. Advantadge of the first cell-centred formulation is that the value of the dependent variables equals the mean value over the control volume with second-order accuracy, higher than that of the vertex-based method. In the cell-vertex formulation, the control volumes can either coincide with the cells or consist of a group of cells around a node. In both cases a linear interpolation of the fluxes is possible making this formulation second order accurate in space, independent on the grid irregularity. Advantage of the last method is that the central difference approximation of the derivative at a side is more precise when the side occupies such a configuration. The discretization principle is similar for all variants, the relationship between the different points positions in the integration domain must be however adapted each time.

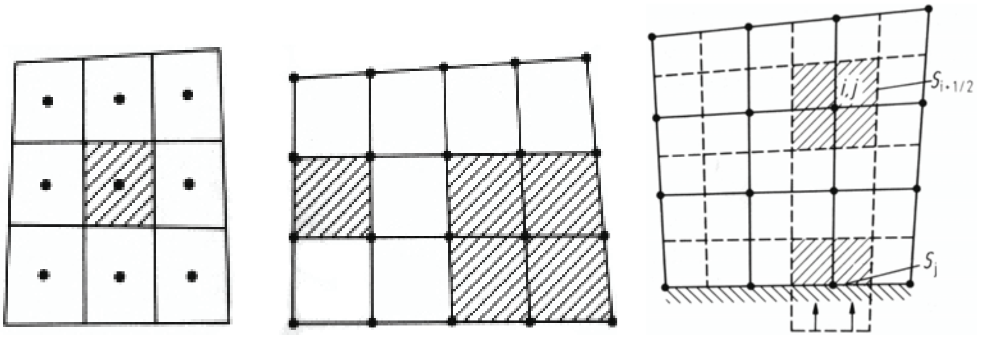

(a) Cell-centred (b) Cell-vertex (c) Vertex-based

Figure 6.5: FVM: Control volumes [WA09].

Discretized Conservation Equations

The finite control volume approach applied to a fixed configuration in space is used to convert the governing equations to an algebraic equation which can be solved numerically. For the geometric discretization, the cell-centred formulation is considered with values of the dependent variables representing the mean value over the control volume. While the FDM approximates the differential quotients in the governing equations to difference quotients, the FVM uses the integral form of the equations as a starting point.
Considering the general three-dimensional scalar transport form from Eq.6.27 and using the Gauss theorem, the expression of the integral form for an arbitrary control volume may be written as:

$$\int_V \frac{\partial \rho\phi}{\partial t} dV + \int_S \rho\phi\mathbf{v}\mathbf{n}dS = \int_S \Gamma_\phi \nabla\phi\mathbf{n}dS + \int_V \rho f_\phi dV \tag{6.44}$$

The conservation laws in their integral form are satisfied over the whole computational domain by adding these equations for all control volumes. In order to derive an algebraic equation for a specific control volume, the surface and volume integrals must be numerically approximated for each V. In this way, since the surface integrals along the inner sides of the control volumes compensate each other, the global conservation required by the physical laws is provided. For a multi-dimensional arbitrary unstructured meshes, the general form of the semi-discretization is obtained by approximating the steady-state form of the general scalar transport equation which results in:

$$\sum_f^{N_f} \rho_f\phi_f\mathbf{v}_f\mathbf{n}_f dS_f = \sum_f^{N_f} \Gamma_\phi \nabla\phi_f\mathbf{n}_f dS_f + \rho f_\phi V \tag{6.45}$$

where N_f represents the number of faces enclosing the control volume and f denotes a certain face. These discretized equations contain the unknown scalar values ϕ of a flow variable at the centre of the corresponding control volume as well as the unknown scalar values ϕ_f through the boundary faces enclosing the volume. The solution of this equation leads in general to a nonlinear form with respect to these variables. Using Newton-based approaches, a linearization of Eq.6.45 may be achieved and the result of the discretization may be expressed in the form:

$$a_c\phi = \sum_{nc} a_{nc}\phi_{nc} + b \tag{6.46}$$

Where nc denotes the neighbour cells and a_c and a_{nc} represent the linearized coefficients of the scalar values ϕ and ϕ_{nc} stored at the center c of V and its the neigbour cells. nc depends on the grid topology and except for boundary cells is in general equal the number of faces enclosing the cell.

6.4.3 Interpolation and Differentiation

In order to solve the discretized equations for a flow variable at the centers of a control volume, the unknown scalar values ϕ_f in the convection term as well as their gradient values $\nabla\phi_f$ in the diffusion term at the faces enclosing that volume must be additionally calculated. There are many approaches to interpolate the boundary surface values of a scalar from surrounding cell center values. Some of these approaches, require the evaluation of differentials, also needed for the computation of the gradients of the scalar values $\nabla\phi_f$ in the diffusion term at these faces.

Interpolation Schemes

The interpolation of the boundary surface values from surrounding cell center values may be achieved using central, upwind or weighted average combination schemes of various accuracy orders. Two schemes that are used in this work are described here [FI06]:

- **Upwind Interpolation:**
  In the upwind schemes, the cell variables located upstream, or upwind, relative to the normal velocity direction v_n in Eq.6.45 are used to derive the boundary surface scalar values ϕ_f. A first-order upwind accuracy may be obtained by assuming the values at the surface to be equal to the values in the cell they belong to, in the upwind direction. The cell values are in turn assumed as constant within the whole cell and are determined as a cell-average values calculated at the centre of the cell. While first-order accuracy may be sufficient for simple problems, it is important to adapt higher order accuracy schemes for solving complex problems where reliable results are desired. Higher order accuracy may be achieved using a multidimensional linear reconstruction approach [BJ89]. Thereby, the computation of the boundary surface scalar values is based on a Taylor series expansion of the cell-centered values ϕ in the upstream cell, about the centre of the cell. The computation of the scalar values ϕ_f based on a second-order upwind scheme may be expressed by:

  $$\phi_f = \phi + \nabla\phi.\mathbf{r} \tag{6.47}$$

  where $\mathbf{r}$ represents the displacement vector from the centre of the upstream cell centroid to the centre of the boundary face. In order to solve Eq.6.47, the scalar gradients $\nabla\phi$ in each cell need indeed to be evaluated.

- **QUICK Interpolation:**
  QUICK schemes are used to compute higher-order boundary face convected values in meshes where the grid can be assumed as aligned with the flow direction, that is, where only upstream and downstream faces and cells are found. Thereby, a boundary face variable ϕ_f is evaluated as a weighted average of second-order upwind and central interpolations [LM90]. Considering the one-dimensional control volume illustrated in Fig.6.6 and that the flow direction is from left to right, the ϕ_e through face e is computed as:

  $$\phi_e = \theta \left[\frac{S_d}{S_c + S_d} \phi_P + \frac{S_c}{S_c + S_d} \phi_E \right] + (1 - \theta) \left[\frac{S_u + 2S_c}{S_u + S_c} \phi_P - \frac{S_c}{S_u + S_c} \phi_W \right] \tag{6.48}$$

  The value of θ is determined such that new solution extrema are avoided. Choosing $\theta = 1$ results in a central second-order interpolation while $\theta = 0$ results in a second-order upwind discretization. Practically, the QUICK scheme is used with $\theta = 1/8$.

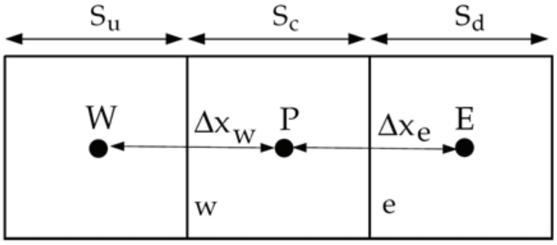

Figure 6.6: Illustration of the QUICK scheme: 1D control volume [FI06].

Differentiation Schemes

Differentiation schemes are needed for the computation of gradients and derivatives. These must be evaluated in order to solve the unknown diffusion terms in the general flow conservation equation as well as for the computation of boundary face scalars in the upwind schemes. The gradient of a scalar may be computed based on the *Green-Gauss* or the *Least Squares* approaches. Using the Green-Gauss theorem, the discrete gradient $\nabla\phi$ of a given scalar variable ϕ at the centre c of the cell may be expressed as [FI06]:

$$(\nabla\phi)_c = \frac{1}{\nu} \sum_f \bar{\phi}_f S_f \mathbf{n}_f \tag{6.49}$$

where f representing the number of faces enclosing the volume.

- **Cell-based differentiation:**
  A Green-Gauss cell-based interpolation of $\bar{\phi}_f$ at the face-centre of the cell may be obtained from the arithmetic average of the cell-centre values of the surrounding cells ci, such that:

  $$\bar{\phi}_f = \frac{\sum_i^{nc} \phi_{ci}}{nc} \tag{6.50}$$

  where nc represents the number of the neighbour cells.

- **Node-based differentiation:**
  A Green-Gauss node-based interpolation, more accurate for unstructured triangular and tetrahedral meshes, may be alternatively used. Thereby, $\bar{\phi}_f$ at the face-centres of the cell are evaluated as arithmetic average over the nodal values of the face:

  $$\bar{\phi}_f = \frac{\sum_i^{n_f} \phi_{ni}}{n_f} \tag{6.51}$$

  where n_f denotes the number of nodes belonging to the face f, and ϕ_{ni} represent the nodal values computed as weighted average from the surrounding cell-centered values, by solving a constrained minimization problem based on the approach proposed by [RBY91].

With the definition of the discrete cell-centred gradients $(\nabla\phi)_c$ and the face values $\bar{\phi}_f$, the discrete face values ϕ_f may be evaluated and thus the semi-discretization is completed.

6.4.4 Pressure-based Formulation

A pressure-based formulation, appropriate for low-speed incompressible flow problems, may be used to solve the discretized equations governing the flow for the mass and momentum conservation and, when appropriate, for energy conservation or other constitutive scalars such as for turbulence modeling.

Pressure Interpolation

Considering the integral conservation form of the momentum equations obtained from Eq.6.44 for a scalar value $\phi = \mathbf{v}$:

$$\int_V \frac{\partial \rho \mathbf{v}}{\partial t} dV + \int_S \rho \mathbf{v}\mathbf{v}\mathbf{n} dS = -\int_S p\mathbf{I}\mathbf{n} dS + \int_S \tau \mathbf{n} dS + \int_V \rho \mathbf{f} dV \tag{6.52}$$

The discretized form of the momentum conservation in the x_i-direction is obtained based on the control volume approach with $\phi = v_i$ leading to:

$$a_c v_i = \sum_{nc} a_{nc} v_{i,nc} + \sum_{f} p_f S \mathbf{i}_i + \rho f_i \tag{6.53}$$

In order to obtain a solution for the velocity field, the unknown face pressure field and face mass fluxes must be first computed. A co-located scheme is used, storing both pressure and velocity at the cell centers. Thus, for the derivation of the pressure face values p_f from the cell values, a pressure interpolation scheme is additionally required. Thereby, p_f are interpolated based on momentum equation coefficients [RC83] given by:

$$p_f = \left(\frac{p_{c0}}{a_{c,c0}} + \frac{p_{c1}}{a_{c,c1}} \right) / \left(\frac{1}{a_{c,c0}} + \frac{1}{a_{c,c1}} \right) \tag{6.54}$$

Using this scheme, a smooth and valid interpolation may be achieved as long as the pressure variation between the cell centers and thus the gradients in the momentum terms between the control volumes may be assumed as small. For flow problems including strongly curved domains or high recirculations, refining the mesh in regions of high gradient is necessary for an adequate resolution of the pressure variation. Alternatively, the PRESTO (PREssure STaggering Option) interpolation scheme, using the discrete continuity balance for a staggered control volume about the face to compute the face pressure may also be used [FI06]. The PRESTO approach is based on a similar algorithm to that of the staggered-grid schemes proposed in [Pat80].

Mass-Flux Interpolation

The continuity equation in integral conservation form may be similary obtained from Eq.6.44 for a scalar value $\phi = 1$ such as:

$$\int_V \frac{\partial \rho \mathbf{v}}{\partial t} dV + \int_S \rho \mathbf{v} \mathbf{n} dS = 0 \tag{6.55}$$

Approximating Eq.6.55 over the control volume V results in the discrete continuity equation in the form:

$$\sum_f \rho_f v_n S_f = 0 \tag{6.56}$$

where $\rho_f v_n = J_f$ denotes the face mass flux through f. Here again, a solution of the mass fluxes through the faces is needed to resolve the velocity field.

The co-located scheme requires to interpolate the face values of the velocity v_n from the stored cell-centred values. In order to prevent unphysical checkerboarding of pressure, a linear interpolation should be avoided [FI06]. Instead, a nonlinear scheme based on momentum weighted averaging as outlined in [RC83] may be performed. Finally, the velocity values at the faces are interpolated using weighting factors based on the a_c coefficient from Eq.6.53, leading to an expression of the face fluxes J_f in the form:

$$\rho_f v_n = \rho_f \frac{a_{c,c0} v_{n,c0} + a_{c,c1} v_{n,c1}}{a_{c,c0} + a_{c,c1}} + d_f \left[\left(p_{c0} + (\nabla p)_{c0} . \mathbf{r}_0 \right) - \left(p_{c1} + (\nabla p)_{c1} . \mathbf{r}_1 \right) \right] \tag{6.57}$$

where p_{c0}, p_{c1} are the pressures and $v_{n,c0}, v_{n,c1}$ the normal velocities defined at the centres of the two cells enclosing the face f (in 2D), while d_f is a function of $\bar{a}_c$, denoting the average of the momentum equation a_c coefficients for these two cells. Finally, while upwind interpolation for the density at cell faces may be performed for compressible flow computations using for instance the ideal gas law, incompressible flows are based on simple arithmetic density averaging.

Pressure-Velocity Coupling

The flow problem is solved by coupling the pressure and the velocity fields. Thereby, an additional condition for the pressure is extracted by manipulating the continuity equation using Eq.6.57. The pressure-velocity coupling is performed based on either a segregated or a coupled algorithm.

- **Segregated Algorithms:**
  In this formulation, the governing equations are solved segregated from each other. Many schemes based on the predictor-corrector approach may be used to achieved a pressure-velocity segregated coupling. Thereby, mass conservation is enforced and the pressure field is derived based on the relationship between the velocity and the pressure corrections. Using Eq.6.57, the solution of the momentum equation with a guessed pressure field p^* may be expressed in the form:

  $$J_f^* = \hat{J}_f^* + d_f \left(p_{c0}^* - p_{c1}^* \right) \tag{6.58}$$

  where J_f^* is the guessed resulting mass face flux and $\hat{J}_f^*$ contains the guessed influence of velocities from the two cells located on either side of the face f. In order to satisfy to the continuity equation, the corrected flux J_f is obtained by adding a correction flux J_f' based on a cell-centred pressure correction p' to the guessed flux J_f^* such as:

  $$J_f' = d_f \left(p_{c0}' - p_{c1}' \right) \tag{6.59}$$

Substituting the guessed flux and the correction flux equations into the continuity equation Eq.6.56 for the corrected flux term J_f leads to the discrete pressure correction p' equation in the cell given by:

$$a_c p' = \sum_{nc} a_{nc} p'_{nc} + \sum_{f} J^*_f S_f \tag{6.60}$$

where the second term corresponds to the net flow rate into the cell. Eq.6.60 may be solved using an algebraic multigrid (AMG) method (Sec.7.2.8) leading to a solution in which the corrected cell pressure, related to an under-relaxation factor α_p, and the corrected face flux, satisfying the discrete continuity equation, are given respectively as:

$$p = p^* + \alpha_p p' \qquad \text{and} \qquad J_f = J^*_f + d_f \left(p'_{c0} - p'_{c1}\right) \tag{6.61}$$

The segregated approach described above is known as the SIMPLE algorithm. Extended variants of this basic procedure with further benefits are the SIMPLE-Consistent or SIMPLEC and the PISO algorithms. In the SIMPLEC approach a modified equation is indeed used for the face flux correction to enhance convergence [FI06]. In the modified expression, the coefficients d_f used in Eq.6.59 for J'_f are redefined as a function of the linearized coefficients a_c and a_{nc} in terms of $(\overline{a_c - \sum_{nc} a_{nc}})$.

- **Coupled Algorithms:**
  Alternatively, the momentum and the pressure-based continuity equations may be solved using a coupled algorithm. Thereby, the pressure-velocity coupling is achieved by processing the momentum and the pressure-correction equations from the segregated algorithm in a single step in which the coupled system of equations is solved. Remaining scalar equations, if present, are then solved in a decoupled manner using the segregated algorithm. In general, since the discrete system of momentum and continuity equations is solved together, the convergence of the solution is significantly improved when using the coupled algorithm. However, since all momentum and pressure equations in the system need to be stored simultaneously when solving for the velocity and pressure fields, the memory requirement for the coupled algorithm is much higher compared to the segregated algorithm, where just a single equation need to be stored at once. In the end, the size of the mesh and the available time and memory represent the main issues in deciding whether a segregated or a coupled algorithm should or could be used for the pressure-velocity coupling problem.

6.4.5 Time Integration

Unsteady flow simulations require indeed the discretization of the governing equations in time. Thus, the transient terms of the governing equations discretized in space must be integrated over time steps Δt. Integrating Eq.6.44 over each control volume and taking into account that the integration domain is independent on time since the equations are derived for control volumes fixed in space, the discretization of the time-dependent equations may be written as a function f involving the spacial discretization for the variable ϕ and given in the generic form as $f(\phi) = \partial\phi/\partial t$.

A first-order discretization scheme is obtained by integrating the transient derivative using a backward difference method based on Taylor's series expansion, leading to the first-order accurate time integration in the form:

$$\frac{\phi^{n+1} - \phi^{n}}{\Delta t} = f\left(\phi\right) \tag{6.62}$$

A more accurate discretization is obtained by neglecting terms of order $(\Delta t)^3$ and higher, resulting in the second-order time discretization in the form:

$$\frac{3\phi^{n+1} - 4\phi^{n} + \phi^{n-1}}{2\Delta t} = f\left(\phi\right) \tag{6.63}$$

Methods for the integration and linearization of the governing unsteady equations with respect to the dependent variables $\phi(t)$ may be achieved in an explicit or implicit way, depending on the evaluation time level of $f(\phi)$.

Explicit Time Integration

An explicit integration is based on the evaluation of the function $f(\phi)$ at the current time such that the variable values $\phi(t + \Delta t)$ at the next time step are explicitly derived from the existing values $\phi(t)$ at the previous time:

$$\phi^{n+1} = \phi^{n} + \Delta t f\left(\phi^{n}\right) \tag{6.64}$$

This explicit approach is known as the *forward Euler* method. Alternative explicit time integration methods advancing the solution from time t to $t + \Delta t$ are the multi-stage Runge-Kutta methods [FP08]. Explicit methods were originally developed because they are easy to define and simple to implement. However, the major restriction of these methods is their stability characteristics. Furthermore, the explicit application is restrictive and should not be used for incompressible computations, which need to be iterated within each time step to achieve accurate convergence [FI06].

Implicit Time Integration

The implicit integration is based on the evaluation of the function $f(\phi)$ at the next time such that the variable values at the next time step $\phi(t+\Delta t)$ are related to the surrounding values $\phi(t+\Delta t)$ at the same time through f. The general *Euler-alpha* time implicit integration form is given for $\alpha \neq 0$ by:

$$\phi^{n+1} = \phi^n + \Delta t \left[\alpha f\left(\phi^{n+1}\right) + (1-\alpha) f\left(\phi^n\right)\right] \tag{6.65}$$

This one-step implicit equation represents in general a nonlinear system and is known as the *backward Euler* for $\alpha = 1$ and as the *trapezoidal* method for $\alpha = 1/2$, respectively. Solving such a nonlinear system, requires a high computational effort per time step which unless reduced would lead to a disadvantage with respect to explicit methods. To reduce this effort and simplify this system of equations, a linearization is performed such that:

$$f\left(\phi^{n+1}\right) = f\left(\phi^n\right) + \frac{\partial f^n}{\partial \phi}\left(\phi^{n+1} - \phi^n\right) \tag{6.66}$$

where $\frac{\partial f^n}{\partial \phi}$ represents the Jacobian matrix evaluated at time t. By introducing $\Delta\phi = \phi^{n+1} - \phi^n$, the linearized implicit time integration equation may be written as a system of unknown $\Delta\phi$ in the form:

$$\left[1 - \alpha \Delta t \frac{\partial f^n}{\partial \phi}\right] \Delta\phi = \Delta t f\left(\phi^n\right) \tag{6.67}$$

Eq.6.67 is solved iteratively at each time step to account for nonlinearities and has the advantage being unconditionally stable with respect to the size of the integration time step.

6.4.6 Iterative Algorithms

When the governing equations are discretized in space, the resulting system is in general nonlinear with respect to the variables. To account for the nonlinearity of the discretized equations being derived, it is necessary to solve the variations of these equations using incremental approaches. This is usually solved by relaxation methods (i.e. Gauss-Seidel, Jacobi) (Sec.7.2.8), representing adaptations to a nonlinear system of methods developed for linear systems.

Iterative Steady-State Algorithm

For the steady-state flows, the discretized system of equations is usually solved using iterative under-relaxation algorithms.

- **Variables Under-Relaxation:**
  The under-relaxation of variables, or *explicit relaxation*, is used for material properties to control the change of the variables ϕ by reducing their values produced during each iteration. Within each control volume, the algorithm relates the new value of ϕ with its old value ϕ_o, the computed change $\Delta\phi$, and the under-relaxation factor α such that:

$$\phi = \phi_o + \alpha \Delta \phi \tag{6.68}$$

- **Equations Under-Relaxation:**
  The under-relaxation of equations, or *implicit relaxation*, is used to stabilize the convergence behavior of the outer nonlinear iterations in the system of discretized equations. This is achieved by introducing for each control volume selective amounts of variable ϕ such that:

$$\frac{a_c \phi}{\alpha} = \sum_{nc} a_{nc} \phi_{nc} + b + \frac{1-\alpha}{\alpha} a_c \phi_o \tag{6.69}$$

Iterative Time-Advancement Algorithm

For time-dependent flows, the discretized form of the generic transport equations is solved using time-advancement algorithms. An implicit discretization of the transient derivative in Eq.6.44 is achieved by evaluating all convective, diffusive and source terms in the flow fields at time $t + \Delta t$ such that:

$$\int_V \frac{\partial \rho \phi}{\partial t} dV + \int_S \rho^{n+1} \phi^{n+1} \mathbf{v}^{n+1} \mathbf{n} dS = \int_S \Gamma_\phi^{n+1} \nabla \phi^{n+1} \mathbf{n} dS + \int_V q_\phi^{n+1} dV \tag{6.70}$$

The splitting error introduced by the segregated solution solving the equations sequentially is controlled using an iterative time-advancement scheme. Thereby, nonlinearity of the individual and coupled equations is fully accounted for by solving all equations iteratively for a given timestep until the convergence criteria are met by eliminating the splitting error. This is achieved by performing a number of outer iterations before advancing the solutions by one time-step.

6.5 CFD Simulation Models

The fundamental principles of fluid dynamics, constitutive modeling and the FVM approach described above are applied to the blood as flow and material. Three-dimensional computations have been carried out to simulate the hemodynamics within the blood domain and along the lumen boundary at any time. The blood flow simulations consist of a similar process described for the vessel wall, though here applied to Computational Fluid Dynamics (CFD). CFD simulation models are generated to compute velocity fields (Fig.6.7), pressure distributions (Fig.6.8.a) and shear stresses (Fig.6.8.b) in the aorta. For the solution of the governing equations, the numerical solvers of the CFD program Fluent are used to obtain FVM-based results of the blood hemodynamics through the vessel.

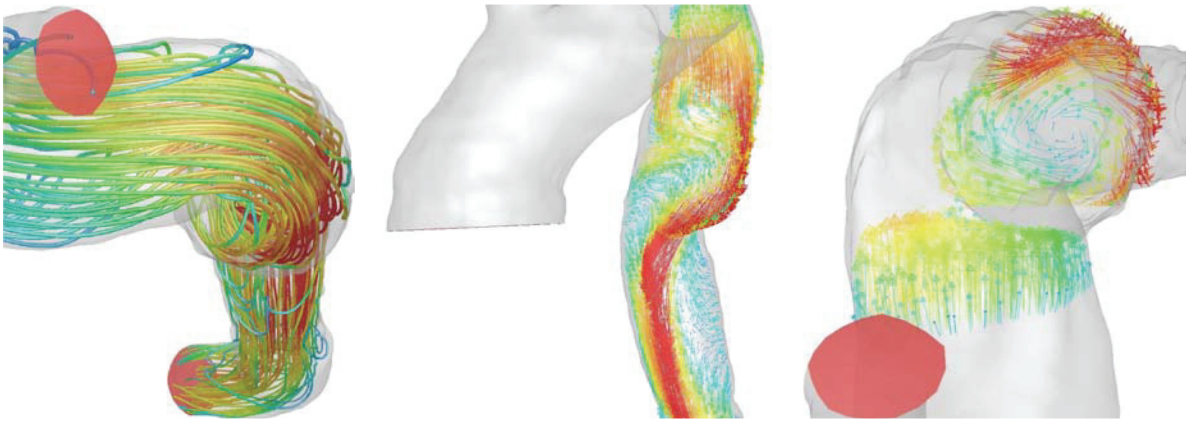

(a) Pathlines (b) Velocity vectors (c) Vortices

Figure 6.7: Velocity pathlines, vectors and vortices in the thoracic aorta.

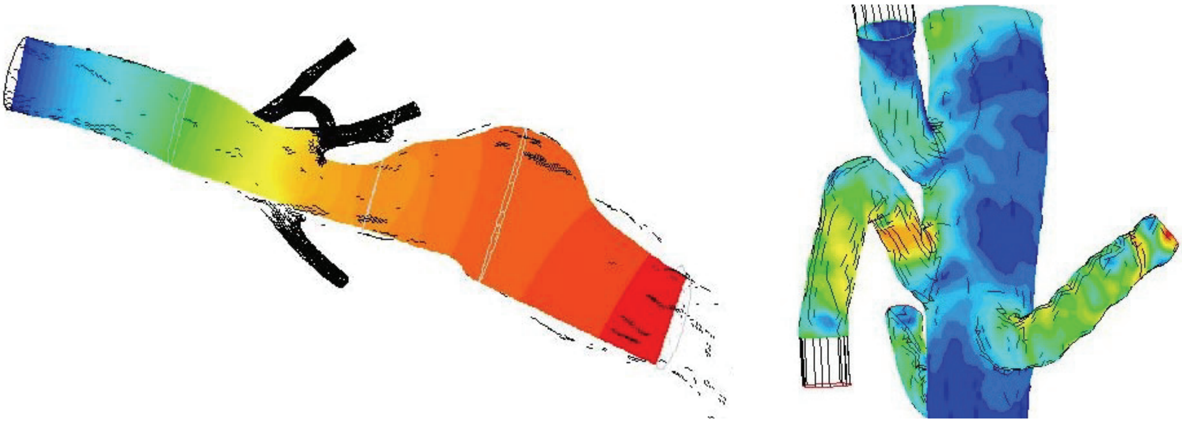

(a) Pressure (b) WSS

Figure 6.8: Pressure and wall shear stress (WSS) distributions.

6.5.1 Physical and Constitutive Modeling

As mentioned before, physical modeling involves the description of the dynamics behavior of the flow through the fundamental equations as well as the description of the fluid properties through the constitutive equations which are then included into the fundamental equations.

Blood Flow Governing Equations

Solving the blood flow is equivalent to solving the time-dependent fundamental equations including the mass, momentum and energy conservation laws. Assuming that inside the body the temperature variations along the aorta are small, the energy conservation may be neglected and the system of governing equations is described by the continuity and Navier-Stokes equations. For the blood domain, they represent a mathematical relationship between the main blood flow variables, pressure p and velocity v in the flow direction, together with the blood physical properties in the lumen region. For a laminar blood flow, the continuity and Navier-Stokes equations are respectively:

$$\frac{\partial \rho_b}{\partial t} + \nabla(\rho_b \mathbf{v}) = 0 \tag{6.71}$$

and

$$\frac{\partial \rho_b \mathbf{v}}{\partial t} + \rho_b \left(\mathbf{v}\nabla\right) \mathbf{v} = -\nabla p + \nabla \tau + \rho_b f_b \tag{6.72}$$

Blood and Blood Flow Properties

An accurate description of the physical nature of the blood as a fluid is an essential aspect in modeling the blood flow. Eq.6.71 and Eq.6.72 include the mass density ρ_b and the viscosity μ_b (in τ) of the blood and do not include turbulence effects. These must be physically defined beside the fundamental blood dynamics conservation equations. The physical behavior of the blood is described in terms of its constitutive equations based on blood rheology and in terms of turbulence models for the blood flow.

For the blood flow type, with a time-averaged calculated Reynolds number less than 2000, the flow is assumed to be laminar. In models where Re approximated from Eq.6.34 takes higher values, turbulence based on the Reynolds-averaged approach is included into the governing equations. Thereby, the RANS equations are determined based on the $k - \epsilon$ two-level model, where turbulence is solved by:

$$\frac{\partial(\rho k)}{\partial t} + \frac{\partial(\rho v_j k)}{\partial x_j} = P_k - \rho\epsilon + \frac{\partial}{\partial x_j}\left[\left(\mu + \frac{\mu_t}{\sigma_k}\right)\frac{\partial k}{\partial x_j}\right] \tag{6.73}$$

and

$$\frac{\partial(\rho\epsilon)}{\partial t} + \frac{\partial(\rho v_j \epsilon)}{\partial x_j} = C_{\epsilon 1} P_k \frac{\epsilon}{k} - \rho C_{\epsilon 2} P_k \frac{\epsilon^2}{k} + \frac{\partial}{\partial x_j}\left[\left(\mu + \frac{\mu_t}{\sigma_\epsilon}\right)\frac{\partial \epsilon}{\partial x_j}\right] \tag{6.74}$$

Details on the derivation of these equations may be found in [FP08]. $C_{\epsilon 1}= 1.44$ and $C_{\epsilon 2}= 1.92$ are model constants, $\sigma_k= 1.0$ and $\sigma_\epsilon= 1.3$ are the turbulent Prandtl numbers for k and ϵ, respectively. P_k is the production rate and with $C_\mu= 0.09$, the eddy viscosity μ_t may be expressed by:

$$\mu_t = \rho C_\mu \frac{k^2}{\epsilon} \tag{6.75}$$

As for the blood rheology, in general, the shear rate within the blood in large arteries may be assumed as greater than 100 s^{-1} [BPC06] and therefore blood may be treated as a Newtonian fluid. The Newtonian model is approximated by the high shear rate limit viscosity. Its shear independent dynamic viscosity μ is considered to be constant and equal 0.0035 Nsm^{-2}. However, a higher order of accuracy is achieved by modeling the real shear-thinning behavior of the blood. Over a cardiac cycle the shear rate varies between 0 and 1000 s^{-1} [AWWL06]. Thus, the behavior of the blood flow in areas of low shear rates should not be neglected. For shear rates lower than 100 s^{-1}, red blood cells (RBC) stack together and form rouleaux, increasing the blood viscosity. RBC aggregation degrades as the shear rate increases. Due to these blood varying conditions, the dynamic viscosity becomes a function of the shear rate and cannot be modeled as constant anymore. Instead, the shear stresses and the velocity gradients exhibit a nonlinear relationship. Therefore, the non-Newtonian shear-dependent blood viscosity is also integrated by including the viscous terms from the constitutive equations into the system of governing equations. Practically, blood constitutive equations representing the non-Newtonian viscous properties follow the Carreau, the power-law or the Casson models [BPC06] sketched in Fig.6.9.

The Carreau model is implemented in this work and is given by:

$$\mu = \mu_\infty + (\mu_0 + \mu_\infty)\left[1 + (F(T)\dot{\gamma}\lambda)^2\right]^{(n-1)/2} \tag{6.76}$$

with

$$F(T) = exp\left[\alpha\left(\frac{1}{T - T_0} - \frac{1}{T_\alpha - T_0}\right)\right] \tag{6.77}$$

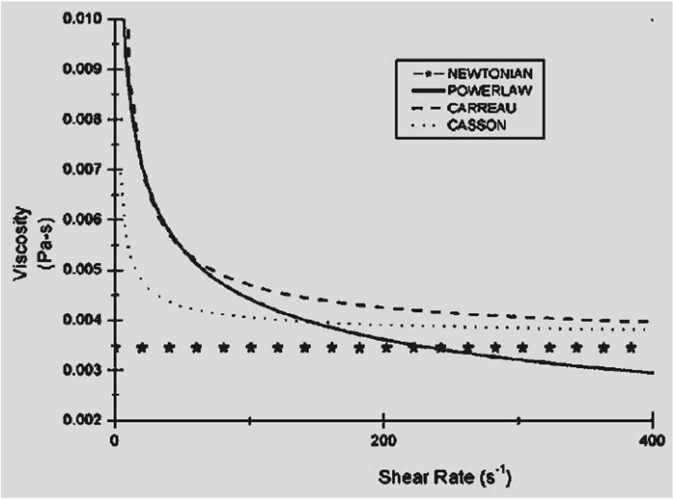

Figure 6.9: Newtonian and non-Newtonian blood viscosity models.

The Carreau model is characterized by the zero μ_0 and the infinite μ_∞ shear rate viscosities, by the relaxation time constant λ, the power law index n and by the reference temperature T_α. μ_0 and μ_∞ represent the upper and lower limiting values of the blood viscosities, respectively. λ and n describe the transition and deviation of the blood from Newtonian fluid, respectively. T_α is the reference temperature at which the viscosity is temperature-independent, that is for which $F(T) = 1$. These non-Newtonian input parameters depend on the constituents of the blood and are chosen for the viscous constitutive equations to fit experimental data from [ABK⁺05], with:

$\mu_0 = 0.056$ Nsm^{-2}; $\mu_\infty = 0.0035$ Nsm^{-2}; $\lambda = 3.313$ s; $n = 0.357$; $T_\alpha =$ 310 K

By including the viscous terms from the constitutive equations into the system of partial differential equations, the new viscosity can be evaluated and recalculated at each iterative process of the simulations.

Finally, beside its viscous and flow turbulent properties, blood is assumed as a homogeneous continuous and incompressible fluid with a constant density of 1050 Kgm^{-3}.

6.5.2 Initial and Boundary Conditions

In order to solve the system of partial differential equations governing the blood flow, a set of initial and boundary conditions needs to be defined. Using proper conditions is essential to successfully solve fluid flow problems. For patient-specific simulations, realistic and individual data based on physiological flow and pressure measurements are used to set the conditions at the boundaries of the aortic model. The needed conditions are presented below:

Initial Conditions

For the initial conditions at time t= 0 s, the whole model is initialized with the velocity v_0 at the end of the late diastole. If indeed v_0= 0 m/s, the initialization results in zero-velocity everywhere in the computational domain.

Inlet Boundary Conditions

The boundary conditions at the inlet of the aortic model are determined from individual flow measurements based on pulsatile velocity profiles.

- **Homogeneous flow-based measurements:**
  A time-dependent homogeneous velocity profile based on MR or Ultrasound flow measurements is used to set the inlet boundary conditions for unsteady simulations. The profile is idealized by smoothing the curve in order to get rid of undesirable oscillations in the simulations and then transformed to describe the mean velocity of the flow within one cardiac cycle. The unsteady profiles are measured in planes above the renal arteries and behind the cardiac valve for application at the inlet of the abdominal and thoracic aortic models, respectively. One of the MR-based velocity profiles used in this work is shown in Fig.6.10.a Thereby, the input flow shows its peak at t= 0.18 s and become zero at t= 0.44 s.
- **Spatial flow-based distribution:**
  For a more accurate description of the flow, the spacial distribution at the inlet may be considered. This spatial flow-based condition have been developed in this work primarily for applications to the simulation of the interaction between the blood and the wall. The derivation of this condition is therefore described in Sec.7.3.2. Nevertheless, it can certainly be also used at this point for the blood flow simulations.

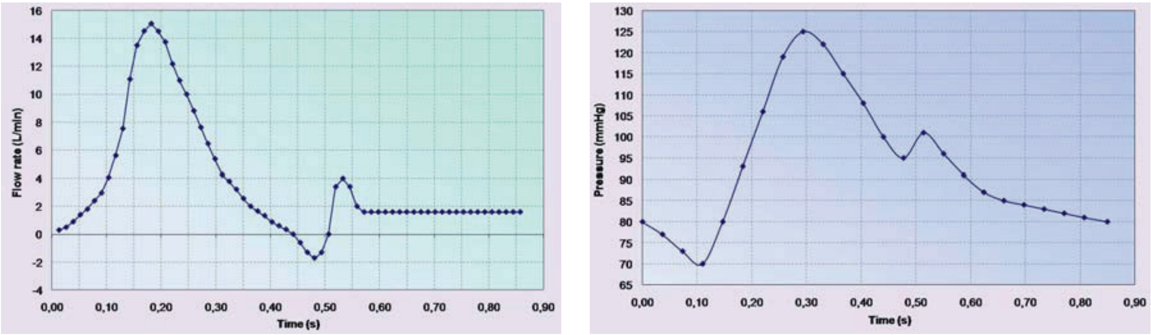

(a) Velocity-Inlet (b) Pressure-Outlet

Figure 6.10: Flow-based and pressure-based boundary conditions.

Outlet Boundary Conditions

The boundary conditions at the outlets are determined from individual pressure-based measurements or alternatively derived in terms of outflow rates.

- **Pressure-based measurements:**
  An unsteady homogeneous pressure profile based on individual measurements is used to set the boundary conditions at the outlets of the aortic model. Here also, the pressure curve within one cardiac cycle is smoothed in order to avoid undesirable oscillations in the simulations. An example of an unsteady pressure profile measured in the aorta and used as boundary conditions at the outlet of the aortic models is shown in Fig.6.10.b. The profile shows its peak at t= 0.1 s and becomes zero at t= 0.3 s, respectively.
- **Velocity-based outflow-rates:**
  Alternatively, the boundary conditions at the outlets are determined in terms of outflow-rates. Thereby, the inlet velocity profile is used to derive the flow rates at the outlets based on physiological data taken from [BKMH78]. Obviously, the calculated scaled rates depend on the geometry shape of the aorta being modeled. Therefore, a code has been developed to automatically scale and compute the rates at the outlets using input information about the available outlets in a given model as shown in Fig.6.11. Thereby, the user defines through the interface which outlets exist, for which the scaled outflow rates are automatically calculated.
- **Pressure-based outlet-specific:**
  A more accurate outlet boundary condition may be derived based on distinct pressure profiles that are computed individually for each outlet. This outlet-specific pressure-based condition has been developed in this work mainly for application to the coupled blood flow and vessel wall simulations. Though, it may be certainly applied for decoupled blood flow modeling as well. The derivation of this conditions is described in Chap.7.

Wall BC

In CFD simulations, the blood vessel is usually modeled as rigid. Assuming non-moving walls, the no-slip boundary condition is defined:

$$\mathbf{v}_b = \dot{\mathbf{u}}_w \tag{6.78}$$

resulting in a zero-velocity $\mathbf{v}_b$ of the blood at the wall.

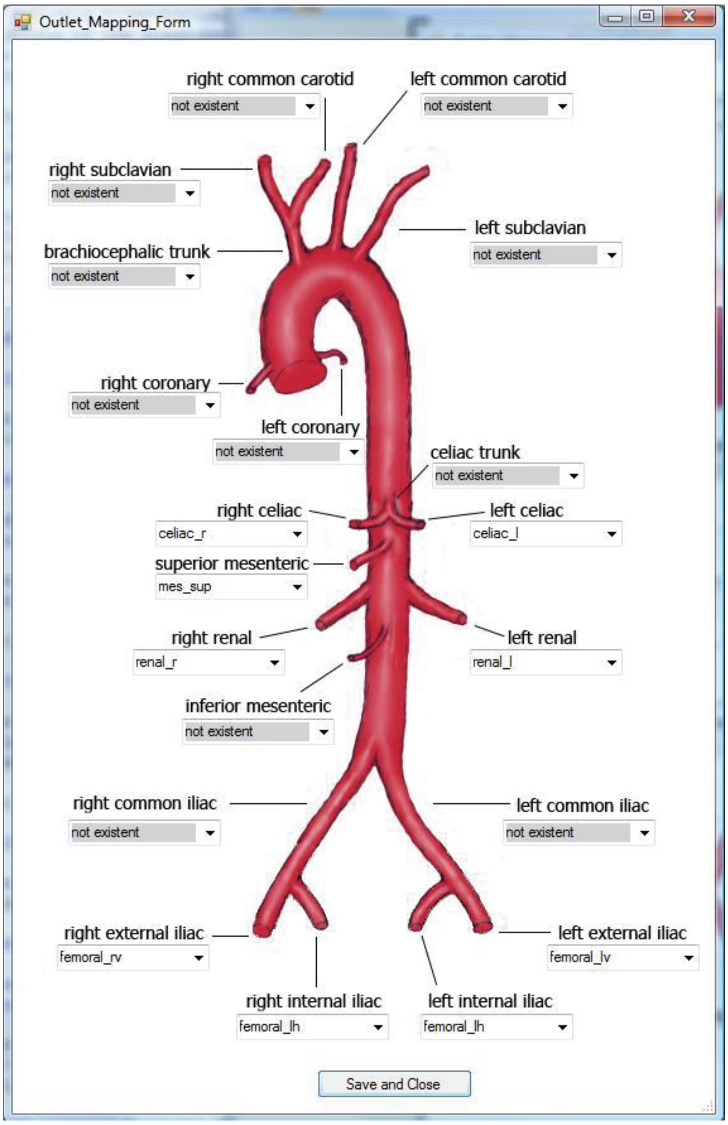

right common carotid: not existent
left common carotid: not existent
right subclavian: not existent
left subclavian: not existent
brachiocephalic trunk: not existent
right coronary: not existent
left coronary: not existent
celiac trunk: not existent
right celiac: celiac_r
left celiac: celiac_l
superior mesenteric: mes_sup
right renal: renal_r
left renal: renal_l
inferior mesenteric: not existent
right common iliac: not existent
left common iliac: not existent
right external iliac: femoral_rv
left external iliac: femoral_lv
right internal iliac: femoral_lh
left internal iliac: femoral_lh

Figure 6.11: Mapping the flow rates at the existing outlets.

6.5.3 Mathematical and Numerical Modeling

The flow domain is numerically solved based on the finite volume approach. The CFD simulations are carried out using the program Fluent. A numerical code integrated in the FVM-program based on the cell-centred formulation where the control volumes are defined to adapt to the grid geometry is chosen to spacially discretize the computational domain. Thereby, the computational points are defined in the centres of the cells where the values of the dependent variables are stored. The flow equations are solved using the second-order upwind interpolation scheme for the convection and viscous terms of each governing equation. Further, the cell-based Green-Gauss differentiation algorithm is used to compute the discrete gradients at the face-centre of the cells.

The pressure-based approach is adopted to discretize the resulting complex time-dependent system of nonlinear equations. In this formulation, the velocity fields are extracted from the momentum equations using pressure followed by velocity interpolations. While the pressure fields are derived by solving the pressure correction equations, obtained by manipulating the continuity and the momentum equations. The time-dependent differential continuity and Navier-Stokes equations are discretized in an implicit manner using the Euler integration. Hereby, the field variables are interpolated to the faces of the control volumes using a second-order time discretization scheme. For the pressure-velocity coupling, the segregated approach in which the governing equations are solved one by one is used. Thereby, the solver employed the Pressure Implicit Splitting of Operators (PISO) algorithm, a variant of the SIMPLE approach useful for unsteady problems, to solve the 3D Navier-Stokes equations. In the PISO algorithm the pressure-velocity coupling uses a higher degree of the approximate relation between the pressure and the velocity corrections. Thereby, an iterative *skewness correction* is performed in which the pressure-correction gradient is recomputed after the initial solution of the pressure-correction equation and used to update the mass flux corrections. In addition, an iterative *neighbor correction* process is performed to move the repeated calculations inside the solution of the pressure-correction equation needed to satisfy momentum balance.

Finally, the iterative steady-state and time-advancement algorithms are used to account for nonlinearities. The resulting linearized system of governing equations is solved based on the Algebraic Multigrid (AMG) relaxation Gauss-Seidel technique as described in Sec.7.2.8.

6.5.4 Numerical Stability - Discussion

The spacial discretization used based on the cell-centred formulation has the advantage being of second order accuracy, higher than that of the vertex-based method as described in Sec.6.4.2. Overall time-discretization error is determined by the choice of the time discretization and the time-advancement approaches. Truncation errors are introduced by the time discretization scheme and were reduced from $O(t)$ to $O(t)^2$ by using a second-order scheme. Further, the splitting errors introduced by the segregated solution process when solving the flow equations in sequence is controlled using an appropriate time-iteration scheme. While the non-iterative approach would reduce the splitting error to the same order as the truncation error, the iterative scheme used in this work reduces that error to zero. Thus, overall accuracy is enhanced, although the number of outer-iterations required per timestep becomes larger than one.

When explicit methods are adopted, the used integration time step is limited by the Courant-Friedrich-Lewy condition to an upper allowable bound which equals the minimum of all the local time steps in the domain. To overcome the limitation in stability characteristics of explicit methods, the implicit formulation is rather used to achieve more accurate solutions and faster convergence. In addition, the implicit discretization of the convective terms in Eq.6.70 yields to non-linear terms in the discretized equations, which solution requires a large number of iterations per time step. To reduce the nonlinear terms in the resulting equations and speed up the convergence within each time step, the *Frozen Flux Formulation* in Fluent is used for the simulation of transient problems. This iterative formulation provides an alternative discretization of the convective terms which preserves the same order of accuracy of the solution. However, the discretization is based on the mass flux at the cell faces from the previous time t.

Furthermore, with two additional skewness and neighbour corrections, PISO improves the efficiency by reducing the number of iterations required to achieve convergence, though it needs a little more time per solver iteration. Thereby, beside the neighbour correction, the *skewness correction* process significantly accelerates convergence of distorted meshes, if present. The use of a high-quality finite mesh with a large number of elements generated based on control functions result in exact accurate solutions. Further, using meshes with individual optimized parameters obtained from the grid refinement analysis described in Sec.4.4, ensured the generation of simulation results that are independent on the mesh configuration of the model.

To overcome the simulation cost in terms of computational time and effort, the tetrahedral volume elements are converted into polyhedral cells. This is adapted within Fluent when the computational capacities are passed over, reducing the number of cells by a factor of four. The computational time varied depending on the domain size and the hardware used. For instance, performed on an 6.4 GHz 8 GB Ram PC, a CFD computation required approximately 20 hours. Timestep independent results were achieved using approximately 1000 equally spaced time steps to model a whole cardiac cycle. This is equivalent to a timestep size ts= 0.8 ms for a cycle period T= 0.8 s. The computational results based on these timesteps settings showed mathematically stable solutions characterized by fast convergence, few numbers of iterations and small residuals. Further, the computations could be performed without undesired physical effects, such as backflows. The maximum number of iterations per timestep was set to 20. Near the systole, 5 to 7 iterations were required to converge the solution, whereas near the diastole up to 20 iterations were needed.

6.6 System Integration in *CFD-Sim*

The modeling steps of the blood flow simulations are integrated in MoDiSim into the component CFD-Sim. CFD-Sim has been developed to automatically perform and visualize computational blood flow simulations in patient-specific aortic models at any time. The user interface of CFD-Sim is shown in Fig.6.12. Automation of the simulation process, physical optimization and individualization within CFD-Sim are described in the next sections.

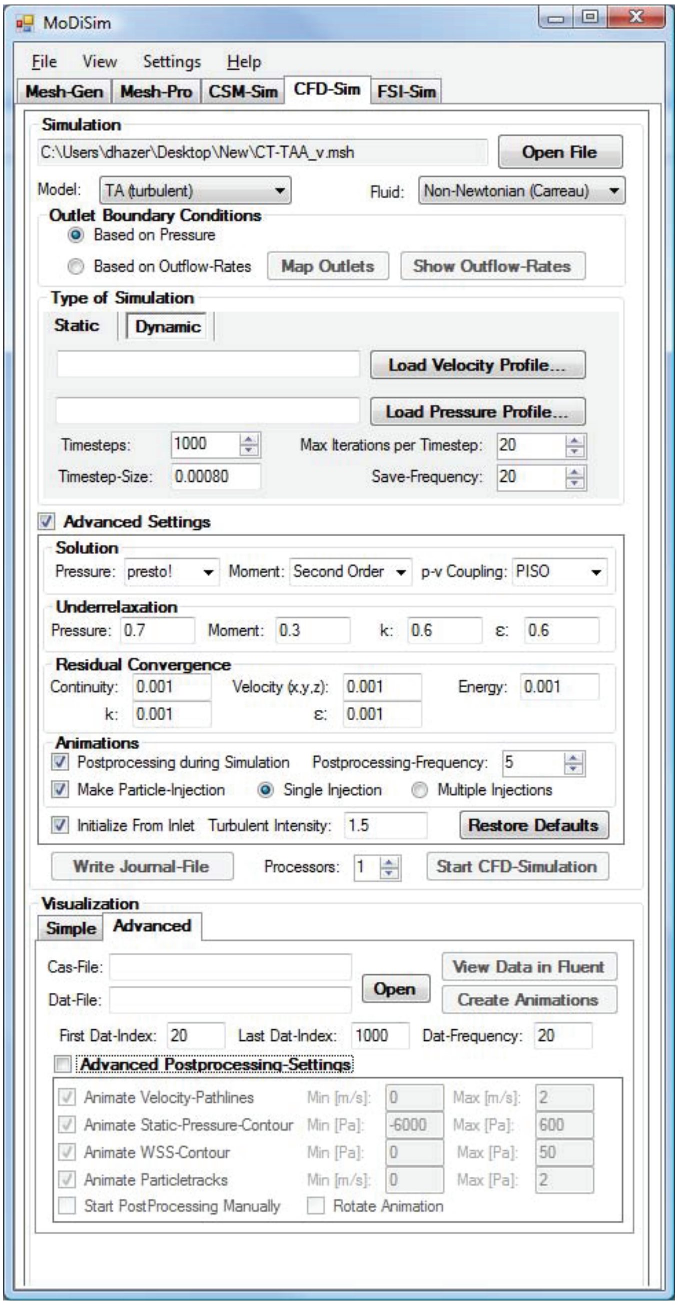
MoDiSim
File View Settings Help
Mesh-Gen
Mesh-Pro
CSM-Sim
CFD-Sim
FSI-Sim
Simulation
Open File
Outlet Boundary Conditions
Map Outlets
Show Outflow-Rates
Type of Simulation
Static
Dynamic
Load Velocity Profile...
Load Pressure Profile...
Solution
Underrelaxation
Residual Convergence
Animations
Restore Defaults
Write Journal-File
Start CFD-Simulation
Visualization
Simple
Advanced
Open
View Data in Fluent
Create Animations

C:\Users\dhazer\Desktop\New\CT-TAA_v.msh

Model: TA (turbulent)
Fluid: Non-Newtonian (Carreau)

● Based on Pressure
○ Based on Outflow-Rates

Timesteps: 1000
Max Iterations per Timestep: 20
Timestep-Size: 0.00080
Save-Frequency: 20

☑ Advanced Settings

Pressure: presto!
Moment: Second Order
p-v Coupling: PISO

Pressure: 0.7
Moment: 0.3
k: 0.6
ε: 0.6

Continuity: 0.001
Velocity (x,y,z): 0.001
Energy: 0.001
k: 0.001
ε: 0.001

☑ Postprocessing during Simulation
Postprocessing-Frequency: 5
☑ Make Particle-Injection
● Single Injection
○ Multiple Injections
☑ Initialize From Inlet
Turbulent Intensity: 1.5

Processors: 1

Cas-File:
Dat-File:
First Dat-Index: 20
Last Dat-Index: 1000
Dat-Frequency: 20

☐ Advanced Postprocessing-Settings

☑ Animate Velocity-Pathlines Min [m/s]: 0 Max [m/s]: 2
☑ Animate Static-Pressure-Contour Min [Pa]: -6000 Max [Pa]: 600
☑ Animate WSS-Contour Min [Pa]: 0 Max [Pa]: 50
☑ Animate Particletracks Min [m/s]: 0 Max [Pa]: 2
☐ Start PostProcessing Manually
☐ Rotate Animation

Figure 6.12: User-Interface of the CFD simulation component *CFD-Sim*.

6.6.1 Automation

The automation of the blood flow simulations is achieved via integration of the CFD modeling steps into the component CFD-Sim. MoDiSim executes these steps automatically based on a minimal user interaction. Further, CFD-Sim includes automatic post-processing part providing a visualization of the hemodynamics. That involves the quantification of wall pressure, shear stresses, velocity pathlines and particle trace for the whole simulated model. The most important actions in the CFD-Sim component sketched in Fig.6.13 are described below:

- **Create Directories:**
  CreateSubdirectories and *CreatePostProcessingDirectories* create first a new subdirectory for all generated files as well as subdirectories for the different plots of the simulation results and for the animation files, respectively.

- **Define Postprocessing Settings:**
  The *CreateInjectionSettings* writes journal commands for the creation of injections. Single or multiple injections are defined in MoDiSim with velocities and times relying on the given velocity profile. *CreatePostProcessingScheme* creates a scheme file which contains new custom commands that generate plots of the simulation results and animation of these plots.

- **Write First Commands:**
  WriteInitialCommands defines settings to start the transcript, load the profiles, check the grid and set the simulation type (unsteady or steady). These commands have to be written first, because they influence the available commands afterwards. *WriteFileSectionSettings* writes the commands to set the file saving-frequency and the file names.

- **Define Physical and Boundary Settings:**
  WriteDefineSectionSettings defines the commands to set the physical models including settings for laminar or turbulent flow and settings for material properties. Also, commands for setting various boundary conditions are defined here.

- **Define Solver Settings:**
  WriteSolveSectionSettings writes the commands for the numerical solution. These include defining discretization schemes, multigrid settings, convergence limits, initialization of the simulation as well as monitoring settings.

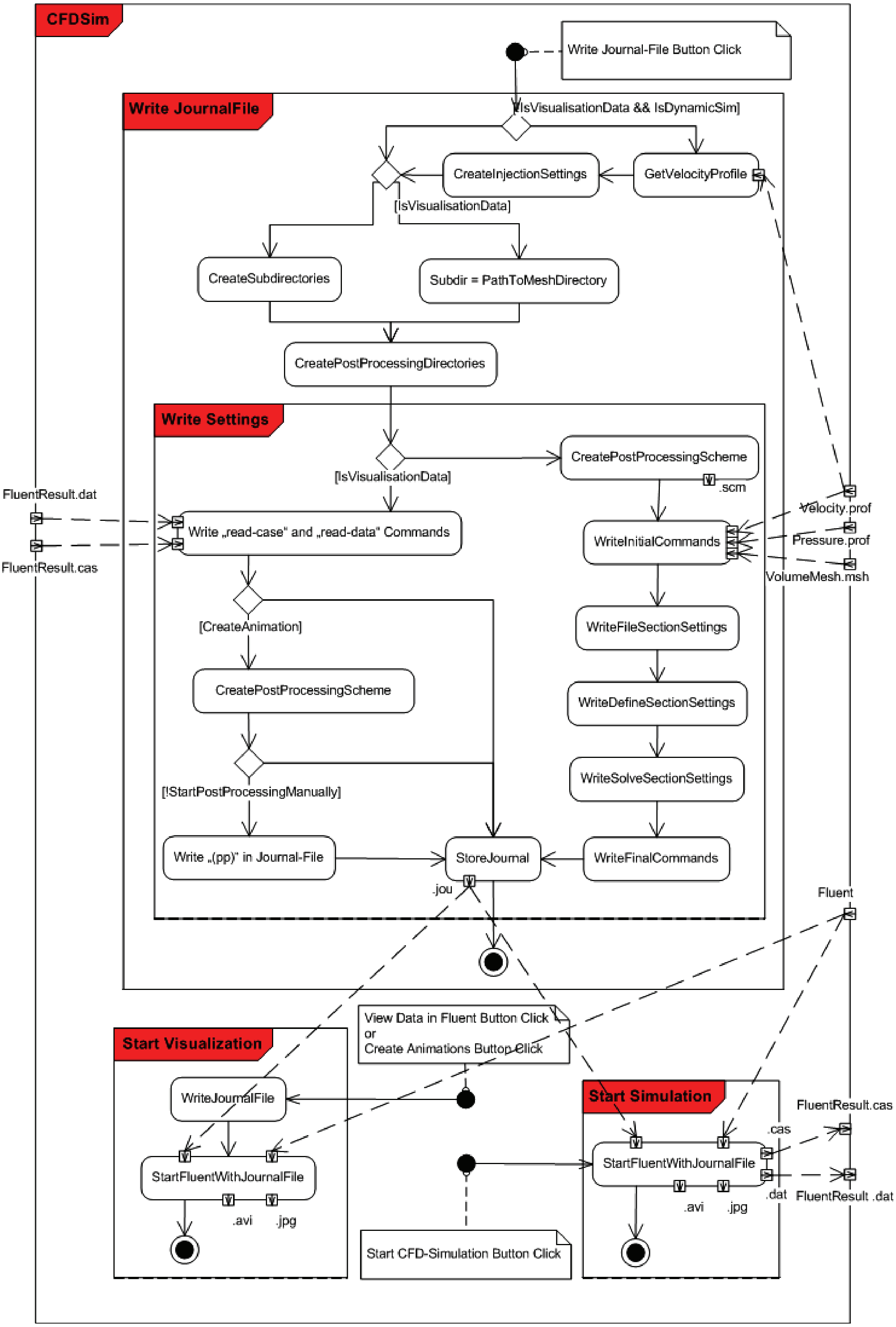
CFDSim
Write Journal-File Button Click
Write JournalFile
[IsVisualisationData && IsDynamicSim]
CreateInjectionSettings
GetVelocityProfile
[IsVisualisationData]
CreateSubdirectories
Subdir = PathToMeshDirectory
CreatePostProcessingDirectories
Write Settings
[IsVisualisationData]
CreatePostProcessingScheme
.scm
FluentResult.dat
FluentResult.cas
Write „read-case" and „read-data" Commands
WriteInitialCommands
Velocity.prof
Pressure.prof
VolumeMesh.msh
[CreateAnimation]
WriteFileSectionSettings
CreatePostProcessingScheme
WriteDefineSectionSettings
WriteSolveSectionSettings
[!StartPostProcessingManually]
Write „(pp)" in Journal-File
StoreJournal
WriteFinalCommands
.jou
Fluent
Start Visualization
View Data in Fluent Button Click
or
Create Animations Button Click
WriteJournalFile
StartFluentWithJournalFile
.avi
.jpg
Start Simulation
FluentResult.cas
.cas
StartFluentWithJournalFile
.dat
FluentResult .dat
.avi
.jpg
Start CFD-Simulation Button Click

Figure 6.13: Activity diagram of the CFD simulation component *CFD-Sim*.

- **Write Final Commands:**
  WriteFinalCommands defines the last commands to start the simulation, save the settings before and after the simulation and exit the program. Also the commands for the injections and to load and execute the scheme files during the simulation are written here.

- **Write Journal File:**
  WriteSettingsInJournalFile writes all commands in an executable journal file. For the simulations, the journal contains all commands to set the various simulation settings. For visualization, only settings for opening the results files are written. For animations, the commands for loading the scheme file are additionally defined.

- **Start Simulation and/or Visualization:**
  The *StartFluentWithJournalFile* action is finally implemented to run Fluent with different journal files in order to perform and/or visualize the simulation.

6.6.2 Optimization

The automated process in CFD-Sim was next optimized by improving and extending the integrated models. Consequently, optimized modeling is achieved in CFD-Sim, allowing a wide range of simulation options. Steady-state and unsteady-pulsatile computations of the hemodynamics are possible. Beside modeling of laminar flows, the k-ϵ turbulent model is also integrated to simulate the dynamics of the flow. Further, constitutive behavior of the blood viscosity is included by integrating both the Newtonian and the non-Newtonian Carreau viscosity models. The effects of these viscosity models have been additionally evaluated and are discussed in the results section. For the pressure-velocity coupling, the Pressure Implicit Splitting of Operators (PISO) as well as the SIMPLE and the SIMPLEC algorithms are integrated, useful for unsteady and steady solutions of the 3D Navier-Stokes equations, respectively. Various discretization and interpolation schemes are implemented for different order of accuracy. The convergence behavior of the simulations may be quasi-controlled directly in CFD-Sim by the timestep number and size inputs, the underelaxation parameters and the residual criteria. Furthermore, several options for defining the boundary conditions are integrated, allowing pressure-based and flow-based outlet conditions. This in turn allows improving the backflows behavior of the simulations. Automatic quantification of the WSS, the pressure and the velocity-based pathlines is also included and may be conducted during the simulations or/and within the extra advanced post-processing option.

6.6.3 Individualization

Individual blood flow simulations, independent on the vessel region, is made possible in MoDiSim mainly through the integration of laminar and turbulent flow models allowing to simulate both abdominal and thoracic parts of the aorta, respectively. Individualization in terms of conditions is also achieved through MoDiSim by allowing the definition of inlet and outlet boundary conditions based on individual pressure and/or flow data obtained from direct patient measurements. Shape-independent (pathology) simulations is rather achieved at the meshing level. The computation of steady-state and unsteady flows is made possible through the integration of different appropriate solvers. In total, three patient-specific aortic models have been processed and simulated using CFD-Sim. These are human-based and are shown in Fig.6.14. They originate from the CT-based abdominal aorta (Fig.3.6), the CT-based abdominal aortic aneurysm (Fig.3.7) and the CT-based thoracic aortic aneurysm after stent-graft implantation (Fig.3.8). Details on the results are presented in the next section.

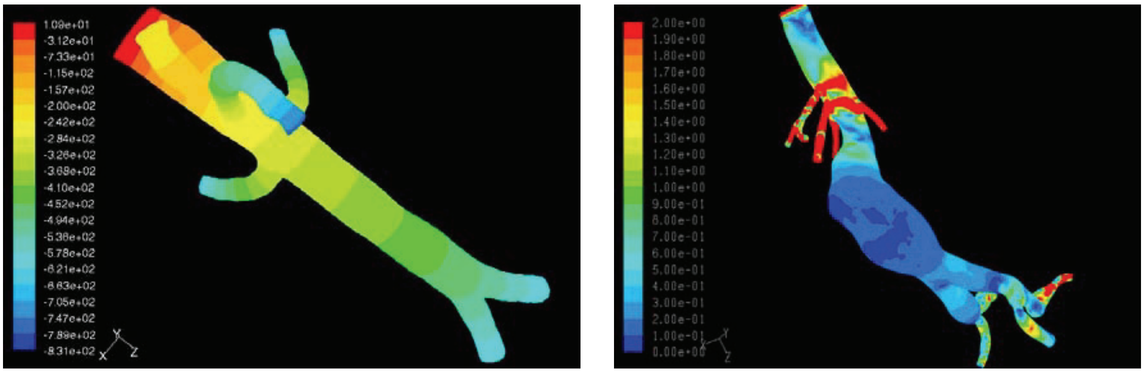

(a) CT-AA: Pressure contours (b) CT-AAA: Wall shear stress

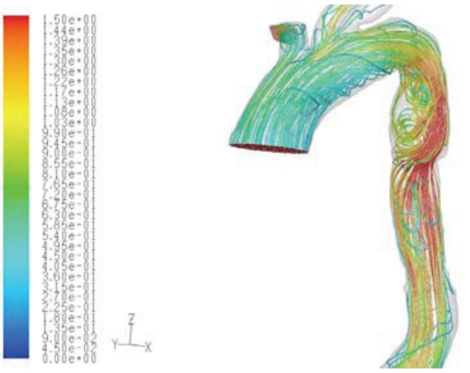

(c) CT-TAA: Velocity pathlines

Figure 6.14: CFD simulations with three individual blood flow aortic models.

6.7 CFD Simulation Results

Numerical results on the performed CFD simulations are illustrated here on the examples of the three models shown in Fig.6.14. The CFD computations were carried out to describe velocity fields, pressure and shear stress distributions along the aortic wall and within the blood domain at any time. The effects of various physical models on the simulations are also discussed.

6.7.1 Wall Shear Stresses using CT-AA

In order to evaluate the hemodynamics in a normal subject, the simulations are first applied to the model of the healthy abdominal aorta CT-AA shown in Fig.3.6. A whole cardiac cycle of period T= 0.85 s was modeled using 1000 equally spaced timesteps. The velocity profile shown in Fig.6.10.a was thereby applied at the inlet, while the outflow rates were computed for the outlet boundaries. Fig.6.15 shows the velocity vectors near the wall surface (a and c) and the corresponding wall shear stress distribution (b and d) at t= 0.31 s and t= 0.18 s, respectively.

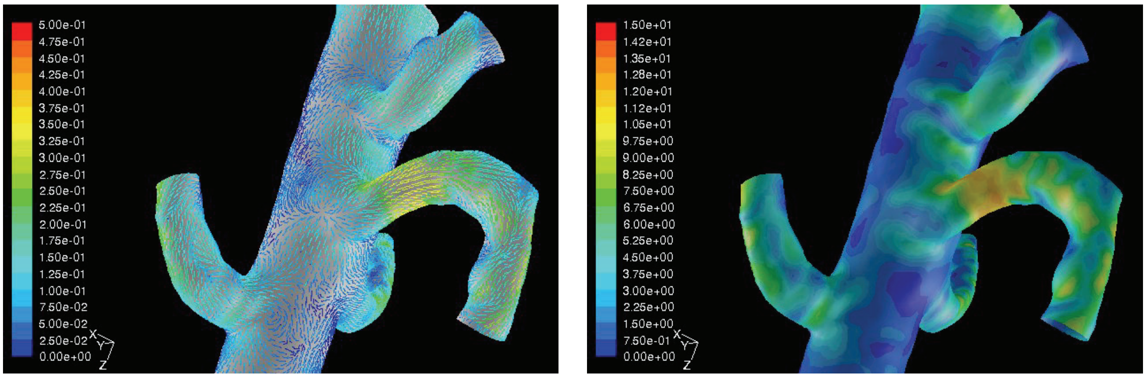
5.00e-01
4.75e-01
4.50e-01
4.25e-01
4.00e-01
3.75e-01
3.50e-01
3.25e-01
3.00e-01
2.75e-01
2.50e-01
2.25e-01
2.00e-01
1.75e-01
1.50e-01
1.25e-01
1.00e-01
7.50e-02
5.00e-02
2.50e-02
0.00e+00
X
Y
Z
1.50e+01
1.42e+01
1.35e+01
1.28e+01
1.20e+01
1.12e+01
1.05e+01
9.75e+00
9.00e+00
8.25e+00
7.50e+00
6.75e+00
6.00e+00
5.25e+00
4.50e+00
3.75e+00
3.00e+00
2.25e+00
1.50e+00
7.50e-01
0.00e+00
X
Y
Z

(a) Velocity vectors, t= 0.31 s (b) WSS, t= 0.31 s

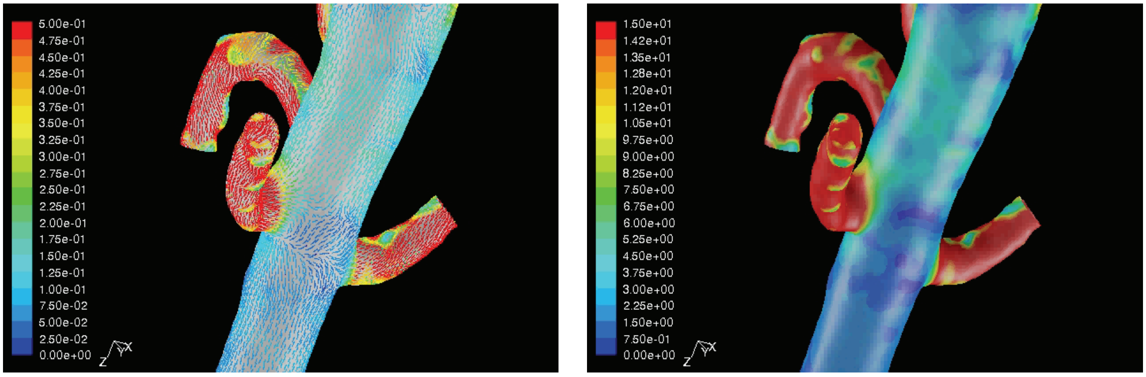
5.00e-01
4.75e-01
4.50e-01
4.25e-01
4.00e-01
3.75e-01
3.50e-01
3.25e-01
3.00e-01
2.75e-01
2.50e-01
2.25e-01
2.00e-01
1.75e-01
1.50e-01
1.25e-01
1.00e-01
7.50e-02
5.00e-02
2.50e-02
0.00e+00
Z
Y
X
1.50e+01
1.42e+01
1.35e+01
1.28e+01
1.20e+01
1.12e+01
1.05e+01
9.75e+00
9.00e+00
8.25e+00
7.50e+00
6.75e+00
6.00e+00
5.25e+00
4.50e+00
3.75e+00
3.00e+00
2.25e+00
1.50e+00
7.50e-01
0.00e+00
Z
Y
X

(c) Velocity vectors, t= 0.18 s (d) WSS, t= 0.18 s

Figure 6.15: Velocity vectors and corresponding shear stress distributions.

The WSS are computed from the resultant of the velocity gradients near the wall. Fig.6.16.a to Fig.6.16.e show the WSS distributions along the aortic model at t= 0.09 s, 0.18 s, 0.36 s, 0.50 s and 0.53 s, respectively. They nicely show how the WSS increase from the early systole to the peak systole, where they become maximal, then decrease to the late systole, until they reach a value near zero during the diastole, and increase again at the peak diastole. The figures on the left represent a colored scale of the magnitude of the WSS in Pascal, while the figures on the right represent an XY-plot of the WSS (y-axis in Pascal) along the z-position in aortic flow direction (x-axis in mm).

Regions of relative low WSS were observed below the renal arteries level (blue on left-figures and $z > 70$ mm on right-figures), while higher WSS values were found within the small arteries (red on left-figures and $z < 70$ mm on right-figures). This can be estimated, according to the definition of the WSS, by the large diameter and the low velocity fields in regions of large diameters i.e. below the renal arteries, and by the small diameters and the high velocity fields within the small arteries. This explanation can be also approximated to the Hagen-Poiseuille formulation which assumes, for parabolic blood velocity profiles in near-circular lumens, the mean shear stresses to be proportional to the volume flow and inverse proportional to the radius R^3.

The mean WSS were expressed in terms of area weighted averages (AWA) over the wall along the whole cardiac cycle. The maximum mean WSS was found at the peak systole with a relative high value of 6.85 Pa. The high systolic WSS at t= 0.18 s can be explained by the high peak velocity at that time i.e. where the velocity field exhibits its maximum. As for the lowest mean WSS, it was found to be 0.2 Pa at t= 0.50 s during the diastole, and is due to the nearly zero inlet velocity profile at that time. Further, the mean WSS at early systole (t= 0.09 s), late systole (t= 0.3 s) and peak diastole (t= 0.53 s) were 1.03 Pa, 0.86 Pa and 1.58 Pa, respectively. Note that these values are the averages along the whole model, including high values in the small arteries and that the percentage p of cells at the wall surface with WSS values less than 0.5 Pa is 91.1 % at early systole, 88.4 % at peak systole, 93.2 % at late systole, 99.5 % at diastole and 88.7 % at peak diastole.

The mean range of the computed values agrees with the range obtained by other in vivo and in vitro methods. [OKM$^+$95] and [TCE$^+$02] reported mean WSS values varying between 0 Pa and 1.04 Pa under resting conditions with an approximate blood flow of 3 litres/min. Their values however excluded the small arteries, thus only included the infrarenal and supraceliac regions. This corresponds to our results simulated at early (t= 0.09 s) and late (t= 0.36 s) systole, for z-positions larger than 70 mm. Fig.6.16.a and Fig.6.16.c show mean values of approximately 0.5 Pa in these regions.

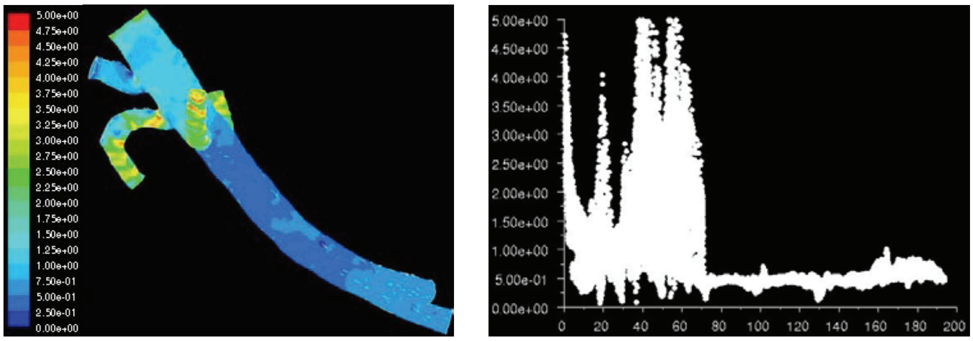

(a)
t= 0.09 s,
AWA= 1.03 Pa,
p= 91.1 % cells

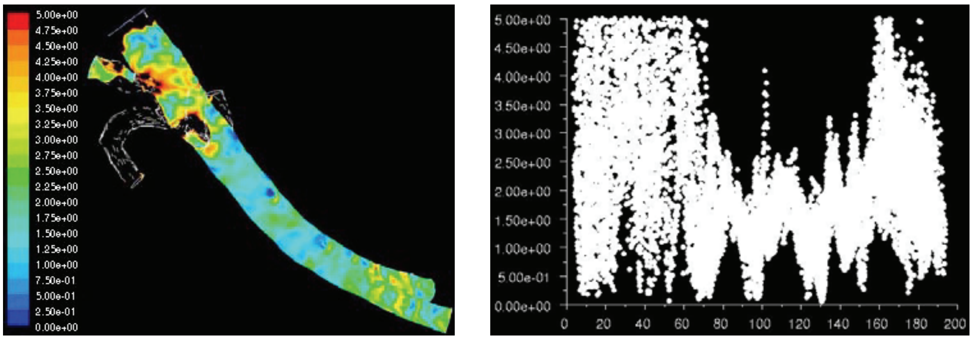

(b)
t= 0.18 s,
AWA= 6.85 Pa,
p= 88.4 % cells

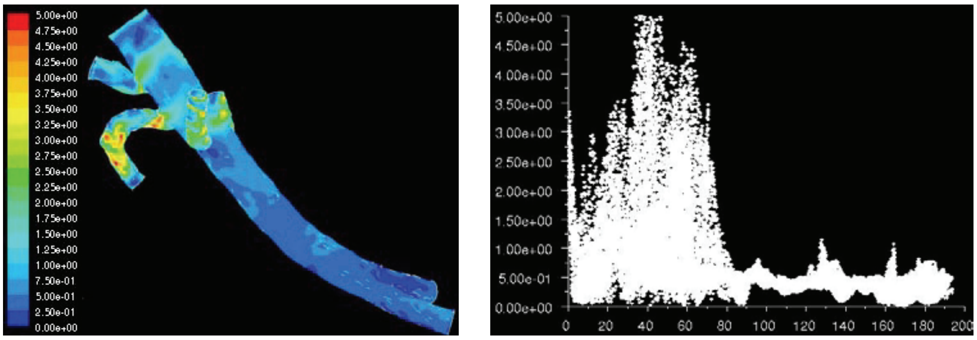

(c)
t= 0.36 s,
AWA= 0.86 Pa,
p= 93.2 % cells

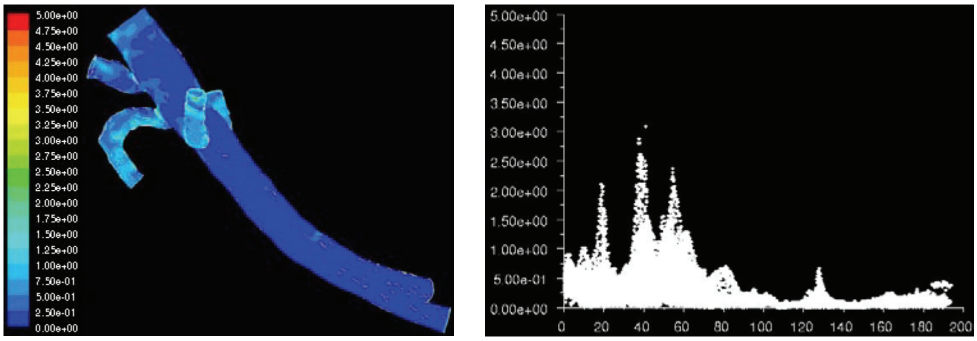

(d)
t= 0.50 s,
AWA= 0.28 Pa,
p= 99.5 % cells

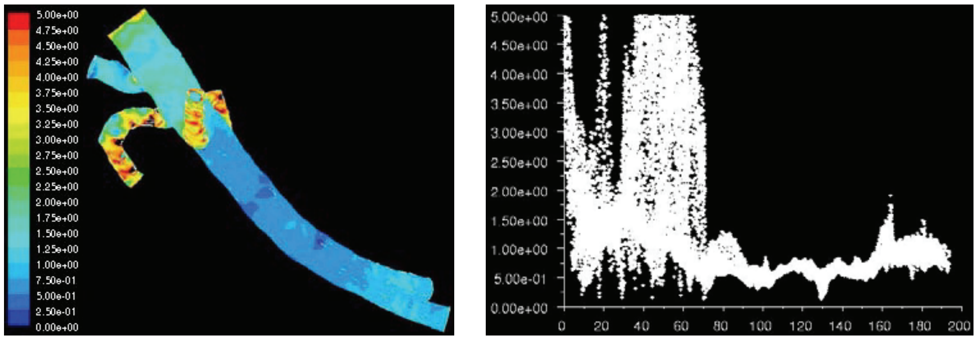

(e)
t= 0.53 s,
AWA= 1.58 Pa,
p= 88.7 % cells

Figure 6.16: Shear stress distribution on the wall (left) and in the flow z-direction (right) at five different times.

6.7.2 Pathological Aneurysm Conditions using CT-AAA

Pathological blood flow characteristics are simulated using the CT-based patient-specific geometry of the abdominal aortic aneurysm shown in Fig.3.7, consisting of the lumen region and the arterial wall. Fig.6.17 shows the dynamic and the static pressure contours along a sagittal cut in the flow direction at the diastolic time t= 0.34 s. The dynamic pressure is a function of squared the velocity, while the static pressure rather reflects the wave propagation due to the pulsatile nature of the cardiac cycle. Obviously, high intraluminal static pressure is present within the aneurysmal bulge.

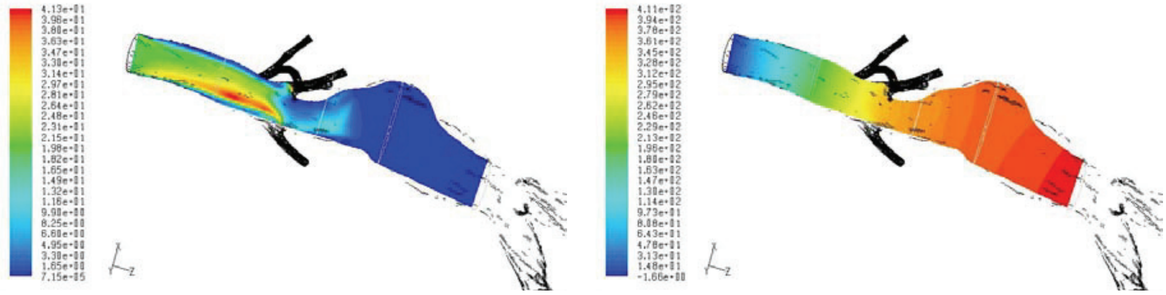

(a) Dynamic pressure (b) Static pressure

Figure 6.17: Dynamic and static pressures along a vertical plane at t= 0.34 s.

The effects of recirculation zones on the WSS distribution are illustrated in Fig.6.18. While the velocity flow at the systole represents almost laminar pathlines (a), the diastolic phase is characterized by the formation of recirculation zones associated with abnormal curved areas arising due to the aneurysm. At early systole few of the vortices start to develop, and during the diastole the recirculation zones grow to large 3D vortices with reversed flow. As a result, the diastolic velocity gradients at the inlet of the aneurysmal bulge take higher values leading to higher local WSS (d) compared to the systolic values (c).

6.7.3 Effects of non-Newtonian Blood using CT-AAA

Although blood is actually a non-Newtonian fluid, most of the investigations carried out in this domain consider the blood as a Newtonian fluid with a constant viscosity. In order to understand the effects of this behavior on the flow patterns, it is essential to investigate the hemorheology using different blood viscosity models. CFD results on the effects of the non-Newtonian Carreau-based model on the pulsatile velocity and WSS distributions within the aortic aneurysm geometry have been analyzed and compared to those of the Newtonian model with constant viscosity. The computations are thereby carried out at any time within the cardiac cycle.

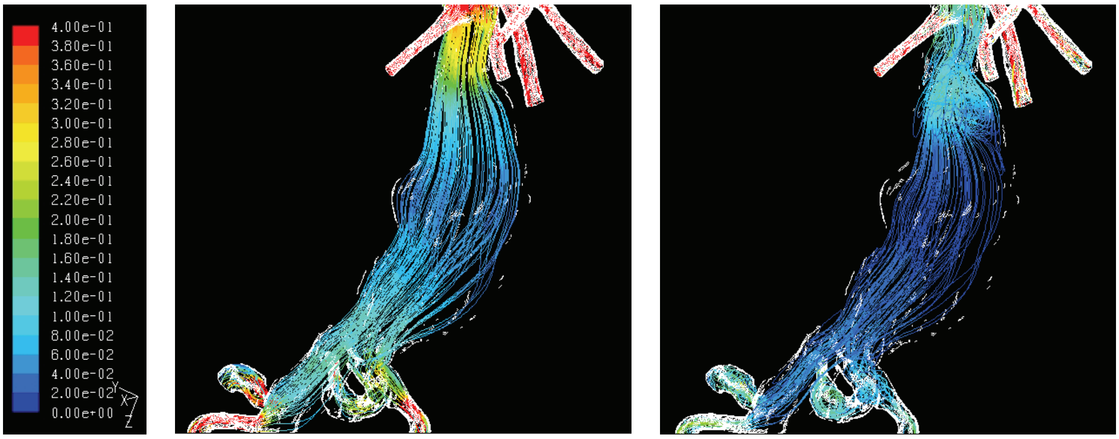
4.00e-01
3.80e-01
3.60e-01
3.40e-01
3.20e-01
3.00e-01
2.80e-01
2.60e-01
2.40e-01
2.20e-01
2.00e-01
1.80e-01
1.60e-01
1.40e-01
1.20e-01
1.00e-01
8.00e-02
6.00e-02
4.00e-02
2.00e-02
0.00e+00
Y
X
Z

(a) Pathlines, t= 0.15 s (b) Pathlines, t= 0.34 s

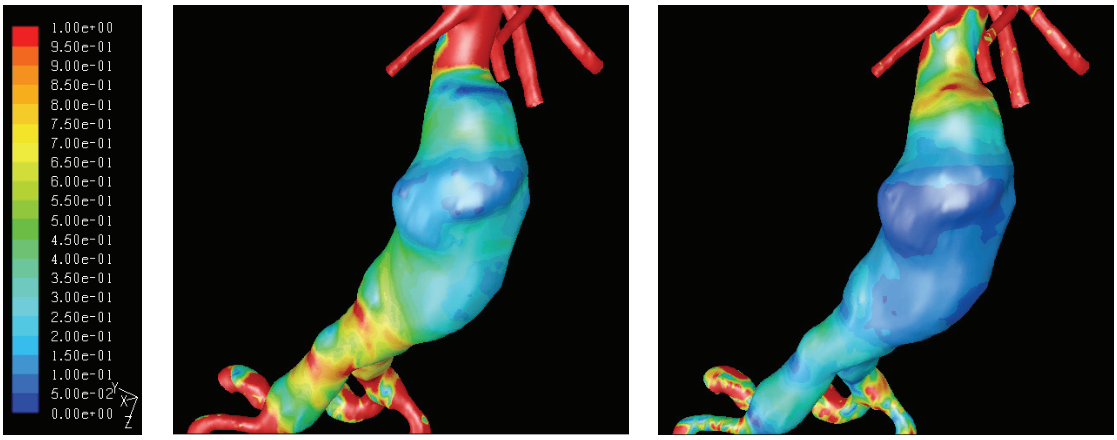
1.00e+00
9.50e-01
9.00e-01
8.50e-01
8.00e-01
7.50e-01
7.00e-01
6.50e-01
6.00e-01
5.50e-01
5.00e-01
4.50e-01
4.00e-01
3.50e-01
3.00e-01
2.50e-01
2.00e-01
1.50e-01
1.00e-01
5.00e-02
0.00e+00
Y
X
Z

(c) WSS, t= 0.15 s (d) WSS, t= 0.34 s

Figure 6.18: Velocity pathlines and corresponding shear stress distributions.

A comparison of both models at the peak systole (t= 0.15 s) and during the diastole (t= 0.34 s) indicates that the unsteady flow parameters are influenced by the non-Newtonian behavior of the blood. The results also show that the effect is more predominant within the small arteries (celiac, mesenteric superior, renal, femoral) than within the main aortic vessel. This is because the red blood cells (RBC) aggregation is also influenced by the size of the domain [CK91] and the shear-thinning behavior of blood is lower in regions of small diameters.

Specifically, the effects on the WSS distributions are marked, in particular within the small vessels but also in the aneurysmal region. The highest WSS is observed in the Carreau model in all cases. This is due to the fact that the viscosity of the non-Newtonian model is higher than that of the Newtonian model along the whole shear rate range. Indeed, the effect is more pronounced in the diastole than in the systole due to the low velocity during diastole resulting in a lower shear-thinning behavior.

The results also show that axial and radial components of the flow velocity patterns, as well as the velocity magnitude in the lumen region face alterations and are affected by the non-Newtonian blood behavior. These results are evaluated along the centerlines L1, L2, L3, L4 and L5 represented in Fig.6.19, and along the lines in the x-direction lying in the planes P50, P110, P150, P220 and Pmes. L5 and Pmes lie inside the mesenteric superior artery. All planes are orthogonal to the flow in the z-direction.

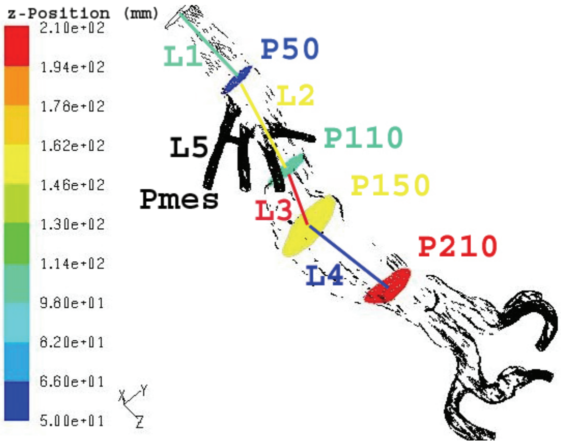

Figure 6.19: Overview: Evaluation sites for the non-Newtonian behavior.

The distribution of the velocity magnitude along the centerlines L3 and L5 is shown in Fig.6.20.a and Fig.6.20.b at peak systole and in Fig.6.20.c and Fig.6.20.d at diastole, respectively. In both cases, the non-Newtonian velocity magnitude showed higher values along these lines. Indeed the effect is predominant along the centreline through the small artery (L5) than that through the aneurysmal region (L3). Similar results were obtained along L1, L2 and L4. Also the dynamic pressure effects take the same course along these lines.
The results of the velocity distribution at the lines in the x-direction lying within the planes P150 and Pmes, orthogonal to the flow in the z-direction, are shown in Fig.6.21.a and Fig.6.21.b at peak systole and in Fig.6.21.c and Fig.6.21.d at diastole, respectively. Compared to the Newtonian velocity, the non-Newtonian computations along these lines show lower values near the wall. Consequently, in order to compensate for the total volume flow, the velocities in the inside increase and show higher values. This also explains the higher non-Newtonian velocities along the centrelines L3 and L5, shown in Fig.6.20. Further, the simulations show that the radial velocity along all lines is in general more affected by the non-Newtonian behavior than the axial velocity.

In summary, the results show that including the non-Newtonian properties is important and cannot be neglected while computing parameters in regions near the wall. The computations agree with experimental results obtained by other in-vivo and in-vitro methods as reported in [GvdVJ99; KGBB06].

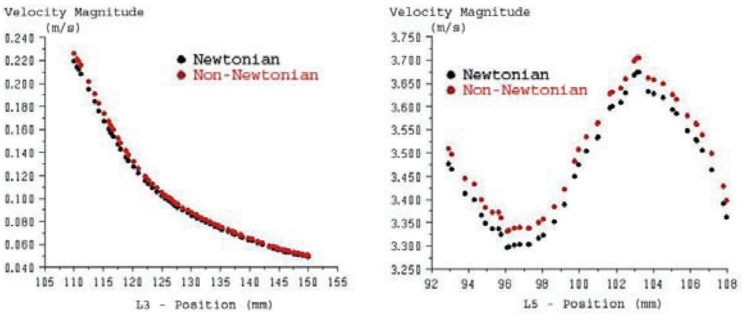

(a) L3, t= 0.15 s (b) L5, t= 0.15 s

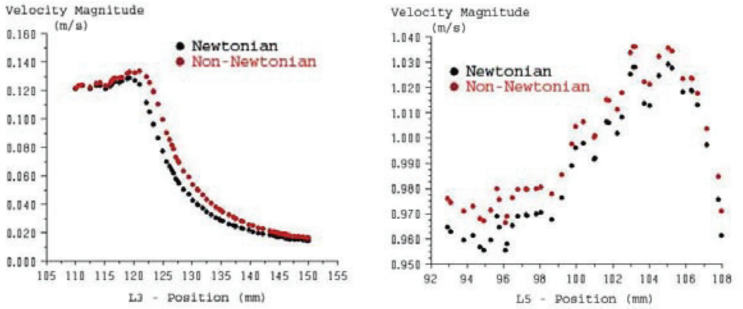

(c) L3, t= 0.34 s (d) L5, t= 0.34 s

Figure 6.20: Velocity magnitudes along the centerlines L3 and L5.

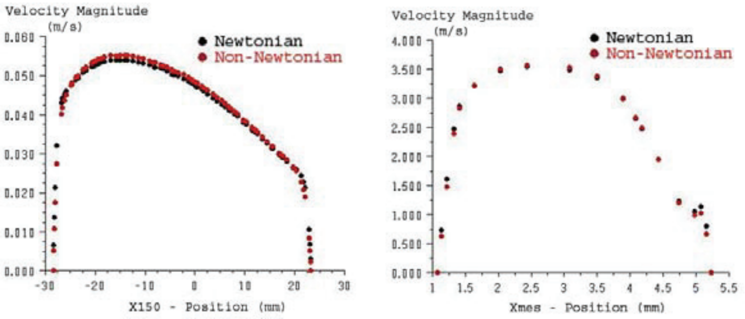

(a) X150, t= 0.15 s (b) Xmes, t= 0.15 s

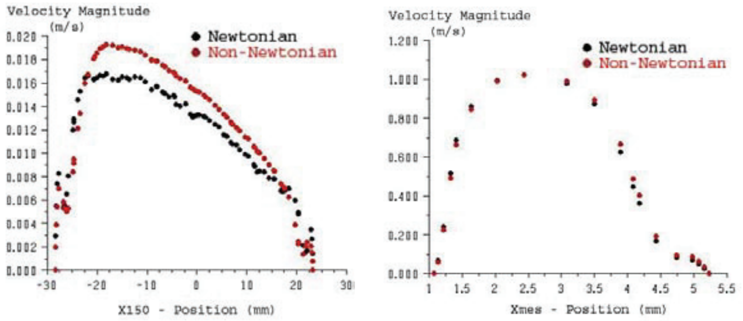

(c) X150, t= 0.34 s (d) Xmes, t= 0.34 s

Figure 6.21: Velocity magnitudes along the lines X150 and Xmes.

6.7.4 Effects of Stent-Graft Implantation using CT-TAA

The thoracic aortic aneurysm model shown in Fig.3.8 originates from a CT scan after stent-graft implantation. Unsteady simulations with outflow rates boundary condition and k-ϵ-based turbulent flow model are considered for the evaluation of the effects of the stent-graft on the flow dynamics in the aorta.

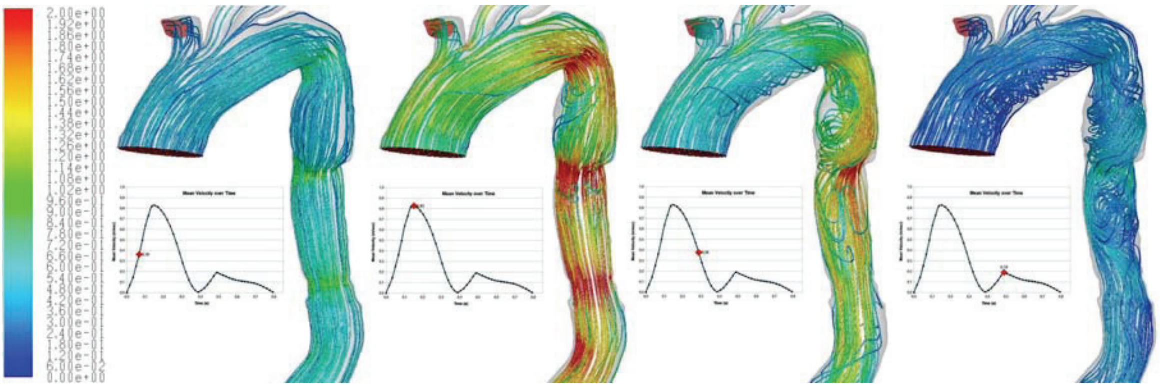
2.00e+00
1.92e+00
1.86e+00
1.80e+00
1.74e+00
1.68e+00
1.62e+00
1.56e+00
1.50e+00
1.44e+00
1.38e+00
1.32e+00
1.26e+00
1.20e+00
1.14e+00
1.08e+00
1.02e+00
9.60e-01
9.00e-01
8.40e-01
7.80e-01
7.20e-01
6.60e-01
6.00e-01
5.40e-01
4.80e-01
4.20e-01
3.60e-01
3.00e-01
2.40e-01
1.80e-01
1.20e-01
6.00e-02
0.00e+00
Mean Velocity over Time
Mean Velocity over Time
Mean Velocity over Time
Mean Velocity over Time

Figure 6.22: Pathlines at early, peak, late systole and peak diastole.

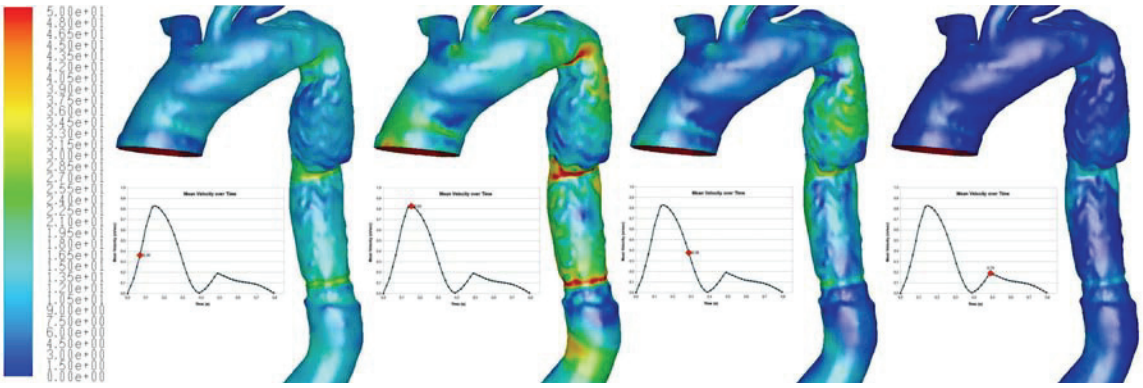
5.00e+01
4.80e+01
4.65e+01
4.50e+01
4.35e+01
4.20e+01
4.05e+01
3.90e+01
3.75e+01
3.60e+01
3.45e+01
3.30e+01
3.15e+01
3.00e+01
2.85e+01
2.70e+01
2.55e+01
2.40e+01
2.25e+01
2.10e+01
1.95e+01
1.80e+01
1.65e+01
1.50e+01
1.35e+01
1.20e+01
1.05e+01
9.00e+00
7.50e+00
6.00e+00
4.50e+00
3.00e+00
1.50e+00
0.00e+00
Mean Velocity over Time
Mean Velocity over Time
Mean Velocity over Time
Mean Velocity over Time

Figure 6.23: WSS at early, peak, late systole and peak diastole.

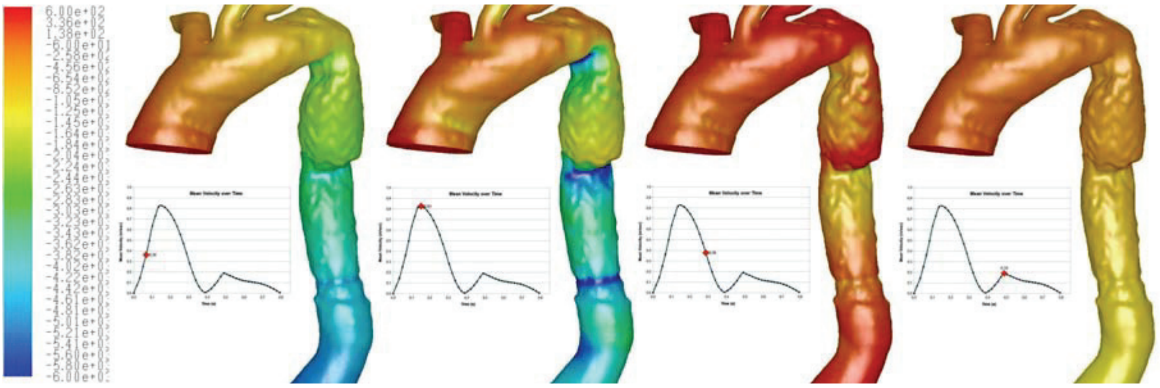
6.00e+02
3.36e+02
1.38e+02
-6.00e+01
-2.58e+02
-4.56e+02
-6.54e+02
-8.52e+02
-1.05e+03
-1.25e+03
-1.45e+03
-1.64e+03
-1.84e+03
-2.04e+03
-2.24e+03
-2.44e+03
-2.63e+03
-2.83e+03
-3.03e+03
-3.23e+03
-3.43e+03
-3.62e+03
-3.82e+03
-4.02e+03
-4.22e+03
-4.42e+03
-4.61e+03
-4.81e+03
-5.01e+03
-5.21e+03
-5.41e+03
-5.60e+03
-5.80e+03
-6.00e+03
Mean Velocity over Time
Mean Velocity over Time
Mean Velocity over Time
Mean Velocity over Time

Figure 6.24: Static pressure at early, peak, late systole and peak diastole.

The results are evaluated at four different times along the cardiac cycle as shown Fig.6.24, Fig.6.22 and Fig.6.23. The flow dynamic is significantly influenced at three marked sites caused by the presence of the stent-graft. These sites are located at the aortic arch where the upper end of the stent is fixed, at the break area in the middle of the stent-graft and at the lower fixed end of the stent. All these sites present a narrowing in the geometry and are therefore associated to high stress gradients at the wall. A flow disruption at high velocities is found at the upper stent-end fixation. The rough surface of the stent enforces the flow disruption and causes additionally high turbulences in the first upper part of the stent-graft. The vortices start to develop right after the peak systolic time as shown in Fig.6.22. The high shear stresses at the wall resulting from the abnormal flow patterns have probably lead to the failure of the stent at these sites. The stent-break in turn resulted in small swirling effects in the following part of the aorta. At the lower stent-end, the turbulences are found at the end of the systole and at the diastole. However, at the end of the diastole, the flow velocities are so small, that the risks associated with the abnormal flow are minimal. Further, the WSS values at the three marked sites show local maxima as illustrated in Fig.6.23. Thus, the wall at these sites is under high stress which may lead to lesions and extend to cause tissue tearing. Fig.6.24 shows the propagation of the pulse wave within the aortic geometry. Thereby, due to the chosen boundary condition, the pressure values are not comparable with real values, and the pressure gradients should be considered instead of the absolute values.

Furthermore, a steady-state simulation with a constant flow rate equal half of the peak velocity is evaluated. The steady-state computations are compared to the unsteady simulations at $t \approx 0.067$ s and $t \approx 0.287$ s, where the velocity is equivalent to 0.37 m/s. Fig.6.25, Fig.6.26 and Fig.6.27 summarize the results of the three simulations. The computations of the unsteady simulation at the early systole are relatively similar to those of the steady-state simulation, since both present accelerating flow. Thereby, the WSS maxima at the critical sites present similar distribution. Consequently, the steady-state approach may be applied for a fast diagnosis of critical sites with high WSS gradients at low computational effort. On the other hand, the results at the late systole, in which the flow is decelerating, present different profiles and show higher local WSS maxima at the upper stent-half and at the stent-break. Also, the significant difference is illustrated through the pathlines, where high turbulences in the late systole start to develop due to the deceleration of the flow velocity. Overall, while the flow behavior in the acceleration phase may be reflected, a steady-state evaluation cannot accurately describe the hemodynamics in the deceleration phase. Consequently, the application of the steady-state simulations should be restricted, where the pulsatile characteristics of the dynamic blood flow cannot be accurately detected.

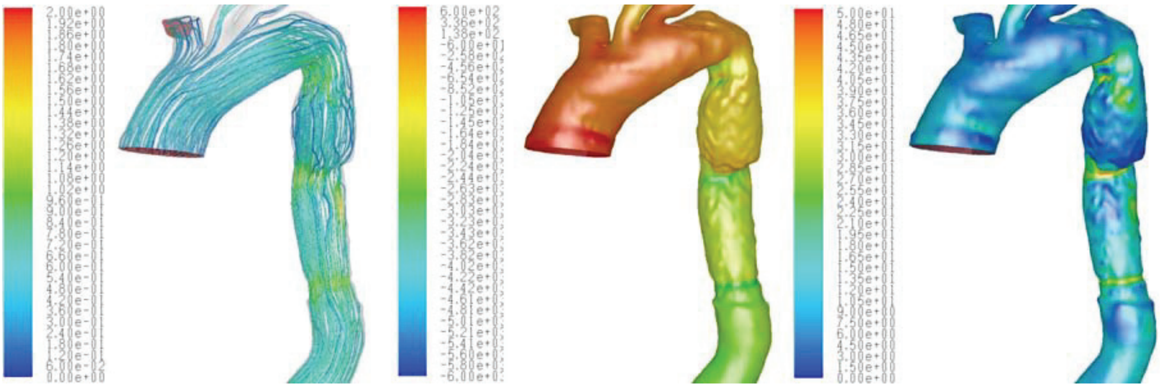
2.00e+00
1.92e+00
1.86e+00
1.80e+00
1.74e+00
1.68e+00
1.62e+00
1.56e+00
1.50e+00
1.44e+00
1.38e+00
1.32e+00
1.26e+00
1.20e+00
1.14e+00
1.08e+00
1.02e+00
9.60e-01
9.00e-01
8.40e-01
7.80e-01
7.20e-01
6.60e-01
6.00e-01
5.40e-01
4.80e-01
4.20e-01
3.60e-01
3.00e-01
2.40e-01
1.80e-01
1.20e-01
6.00e-02
0.00e+00
6.00e+02
3.36e+02
1.38e+02
-6.00e+01
-2.58e+0
-4.56e+0
-6.54e+0
-8.52e+0
-1.05e+0
-1.25e+0
-1.45e+0
-1.64e+0
-1.84e+0
-2.04e+0
-2.24e+0
-2.44e+0
-2.63e+0
-2.83e+0
-3.03e+0
-3.23e+0
-3.43e+0
-3.62e+0
-3.82e+0
-4.02e+0
-4.22e+0
-4.42e+0
-4.61e+0
-4.81e+0
-5.01e+0
-5.21e+0
-5.41e+0
-5.60e+0
-5.80e+0
-6.00e+0
5.00e+01
4.80e+01
4.65e+01
4.50e+01
4.35e+01
4.20e+01
4.05e+01
3.90e+01
3.75e+01
3.60e+01
3.45e+01
3.30e+01
3.15e+01
3.00e+01
2.85e+01
2.70e+01
2.55e+01
2.40e+01
2.25e+01
2.10e+01
1.95e+01
1.80e+01
1.65e+01
1.50e+01
1.35e+01
1.20e+01
1.05e+01
9.00e+00
7.50e+00
6.00e+00
4.50e+00
3.00e+00
1.50e+00
0.00e+00

Figure 6.25: Pathlines, pressure and WSS distribution of the steady-state simulation with velocity of 0.37 m/s.

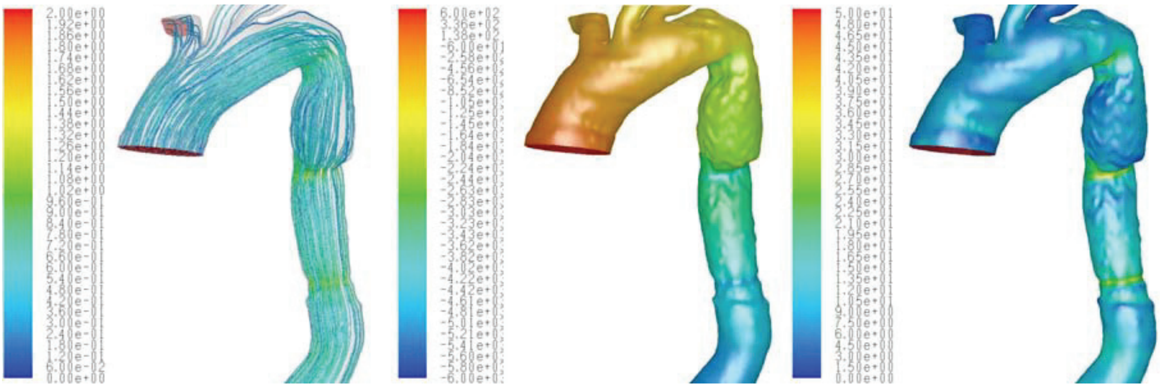
2.00e+00
1.92e+00
1.86e+00
1.80e+00
1.74e+00
1.68e+00
1.62e+00
1.56e+00
1.50e+00
1.44e+00
1.38e+00
1.32e+00
1.26e+00
1.20e+00
1.14e+00
1.08e+00
1.02e+00
9.60e-01
9.00e-01
8.40e-01
7.80e-01
7.20e-01
6.60e-01
6.00e-01
5.40e-01
4.80e-01
4.20e-01
3.60e-01
3.00e-01
2.40e-01
1.80e-01
1.20e-01
6.00e-02
0.00e+00
6.00e+02
3.36e+02
1.38e+02
-6.00e+01
-2.58e+0
-4.56e+0
-6.54e+0
-8.52e+0
-1.05e+0
-1.25e+0
-1.45e+0
-1.64e+0
-1.84e+0
-2.04e+0
-2.24e+0
-2.44e+0
-2.63e+0
-2.83e+0
-3.03e+0
-3.23e+0
-3.43e+0
-3.62e+0
-3.82e+0
-4.02e+0
-4.22e+0
-4.42e+0
-4.61e+0
-4.81e+0
-5.01e+0
-5.21e+0
-5.41e+0
-5.60e+0
-5.80e+0
-6.00e+0
5.00e+01
4.80e+01
4.65e+01
4.50e+01
4.35e+01
4.20e+01
4.05e+01
3.90e+01
3.75e+01
3.60e+01
3.45e+01
3.30e+01
3.15e+01
3.00e+01
2.85e+01
2.70e+01
2.55e+01
2.40e+01
2.25e+01
2.10e+01
1.95e+01
1.80e+01
1.65e+01
1.50e+01
1.35e+01
1.20e+01
1.05e+01
9.00e+00
7.50e+00
6.00e+00
4.50e+00
3.00e+00
1.50e+00
0.00e+00

Figure 6.26: Pathlines, pressure and WSS distribution of the unsteady simulations at early systole.

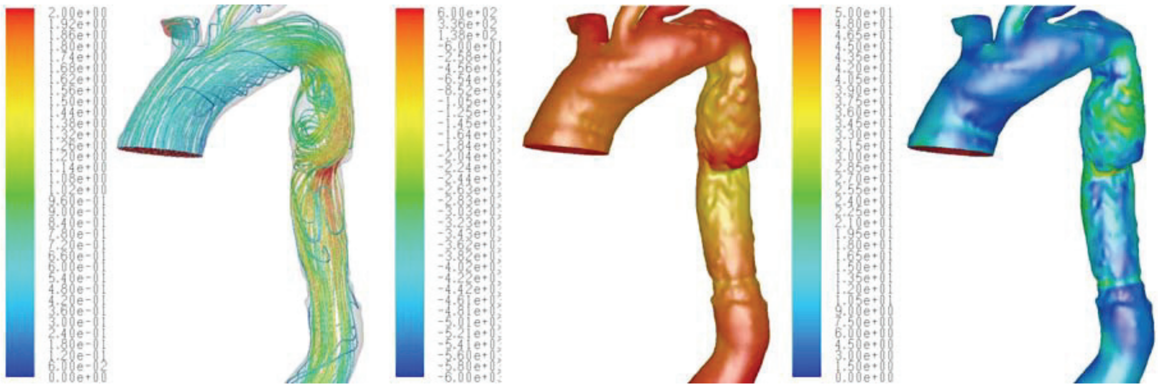
2.00e+00
1.92e+00
1.86e+00
1.80e+00
1.74e+00
1.68e+00
1.62e+00
1.56e+00
1.50e+00
1.44e+00
1.38e+00
1.32e+00
1.26e+00
1.20e+00
1.14e+00
1.08e+00
1.02e+00
9.60e-01
9.00e-01
8.40e-01
7.80e-01
7.20e-01
6.60e-01
6.00e-01
5.40e-01
4.80e-01
4.20e-01
3.60e-01
3.00e-01
2.40e-01
1.80e-01
1.20e-01
6.00e-02
0.00e+00
6.00e+02
3.36e+02
1.38e+02
-6.00e+01
-2.58e+0
-4.56e+0
-6.54e+0
-8.52e+0
-1.05e+0
-1.25e+0
-1.45e+0
-1.64e+0
-1.84e+0
-2.04e+0
-2.24e+0
-2.44e+0
-2.63e+0
-2.83e+0
-3.03e+0
-3.23e+0
-3.43e+0
-3.62e+0
-3.82e+0
-4.02e+0
-4.22e+0
-4.42e+0
-4.61e+0
-4.81e+0
-5.01e+0
-5.21e+0
-5.41e+0
-5.60e+0
-5.80e+0
-6.00e+0
5.00e+01
4.80e+01
4.65e+01
4.50e+01
4.35e+01
4.20e+01
4.05e+01
3.90e+01
3.75e+01
3.60e+01
3.45e+01
3.30e+01
3.15e+01
3.00e+01
2.85e+01
2.70e+01
2.55e+01
2.40e+01
2.25e+01
2.10e+01
1.95e+01
1.80e+01
1.65e+01
1.50e+01
1.35e+01
1.20e+01
1.05e+01
9.00e+00
7.50e+00
6.00e+00
4.50e+00
3.00e+00
1.50e+00
0.00e+00

Figure 6.27: Pathlines, pressure and WSS distribution of the unsteady simulations at late systole.

6.8 Summary

The aim of this chapter was to describe the computational modeling of the blood flow for simulating and analyzing the hemodynamics within individual aortic models. First, the physical fundamentals of the modeling based on the concepts of continuum fluid dynamics were presented. Thereby, the fundamental equations governing the motion of the flow were derived based on the conservation principles. Then, the constitutive material laws necessary to describe the fluid behavior to be modeled were presented. The mathematical relations for the numerical discretization and the resolution of the governing equations based on the finite volume method were then presented. Next, the theoretical steps described in the first three sections were applied to generate computational models for the blood flow in the CFD simulation section. Further, the integration of the blood flow modeling steps into the CFD-Sim component of the MoDiSim simulation system was also described. Thereby, the automation of the steps, the optimization of the individual models as well as the individualization of the CFD simulations were presented. Finally, some simulation results obtained from three individual image-based models are illustrated at the end of this chapter. The effects of various models and physical aspects were thereby also presented.

Chapter 7

Blood-Wall Interaction

7.1 Introduction

In the CFD simulations of the blood flow, the vessel wall was assumed as rigid and thus was not included into the modeling process. In the CSM simulations of the vessel wall, the blood flow was assumed as a known load condition for the modeling. Over a cardiac cycle, the blood dynamics and the wall mechanics are strongly influenced by each other. In fact, the blood forces affect the wall deformation and the wall displacements affect the flow patterns. Therefore, the physical interaction between the vessel wall and the blood flow is a crucial consideration and has to be taken into account for accurate computations. Considering the blood-wall interaction leads to more realistic and reliable simulations for the analysis of cardiovascular diseases. Such a physical interaction may be modeled by means of the Fluid-Structure Interaction (FSI) approach.

7.2 Fluid-Structure Interaction

FSI modeling allows simulating the interaction between a deformable structure with the surrounding fluid. During the interaction, the fluid forces applied on the solid results in its deformation and the resulting solid deformation yields a change in the fluid domain. The complexity of Fluid-Structure problems makes an analytical solution out of question. Numerical FSI problems may therefore be solved by coupling CFD and CSM models describing the fluid and the structure, respectively. The numerical solution of the individual fields may be obtained based on different approaches. However, this would yield to resctrictions on the coupling and iteration methods allowed for the solution.

In the following, the FEM approach is considered for both the fluid and the solid domains to obtain a numerical solution for the FSI problem.

7.2.1 Arbitrary Lagrangian-Eulerian Formulation

When modeling the structural model, the Lagrangian configuration is applied, where the changes in the solid position are observed as it moves in space. The fluid flow is rather analyzed in the Eulerian configuration, where instead of following the fluid particles, the changes taking place at fixed positions in space are observed. However, in FSI analysis, the fluid-structure interface is deformable and the problem includes moving boundary conditions prescribing nodal positions determined by the structural displacements. As a result, the motion of the fluid boundary nodes described along the moving geometric boundary must be described using the Lagrangian coordinates. Elsewhere in the computational domain, the interior fluid nodes may be described in a quite arbitrary configuration as long as they comply to the boundary coordinates, mesh quality and physical requirements. The so called *Arbitrary Lagrangian-Eulerian* (ALE) configuration is shown in Fig.7.1.a.

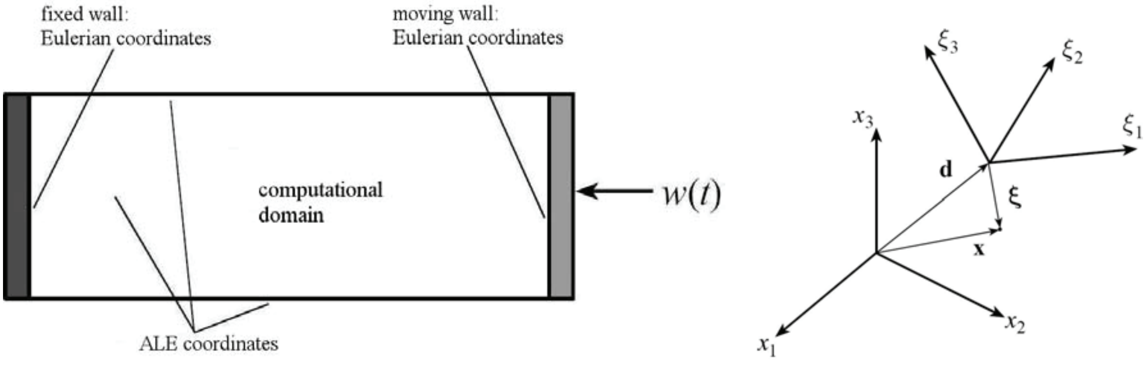

(a) ALE configuration (b) ALE system

Figure 7.1: Illustration of the ALE configuration and coordinate system.

So, solving FSI problems requires that the governing system of equations describing the fluid model must be moved to the ALE coordinate system. An ALE coordinate system may be defined by transforming the moving coordinate system $(\mathbf{x}, t)$ into a new coordinate $(\boldsymbol{\xi}, \tau)$ such that:

$$\mathbf{x}(\boldsymbol{\xi}, \tau) = \boldsymbol{\xi} + \mathbf{d}\left(\boldsymbol{\xi}, \tau\right) \tag{7.1}$$

where $t = \tau$ and $\mathbf{d}$ is the displacement vector representing the arbitrary moving coordinates. The ALE system is illustrated in Fig.7.1.b.

Based on this definition, the time derivative of a given function $f(\mathbf{x}, t) = f(\xi + \mathbf{d}(\xi, \tau), \tau)$ may be written as:

$$\frac{\partial f}{\partial t} = \frac{\partial f}{\partial \tau} - \mathbf{w}.\frac{\partial f}{\partial \mathbf{x}} \tag{7.2}$$

where $\mathbf{w} = \partial \mathbf{x}/\partial \tau = \partial \mathbf{d}/\partial \tau$ denotes the moving coordinate velocity. The ALE system of fluid equations is then obtained by substituting Eq.7.2 into the Eulerian governing equations derived in Chap.6. The non-conservative form of the continuity and momentum equations defined in Eq.6.10 and Eq.6.16 transform in the ALE system respectively to:

$$\frac{\partial \rho}{\partial \tau} + (\mathbf{v} - \mathbf{w}) \nabla \rho + \rho \nabla \mathbf{v} = 0 \tag{7.3}$$

and

$$\rho \frac{\partial v_i}{\partial \tau} + \rho (\mathbf{v} - \mathbf{w}) \nabla v_i - \nabla t_i = \rho f_i \tag{7.4}$$

In these ALE equations, the convective velocity is replaced by the relative velocity. When $\mathbf{w} = 0$ or $\mathbf{w} = \mathbf{v}$, the equations simplify to the Lagrangian or the Eulerian cases, respectively. As for the ALE conservative form of the governing equations derived in terms of the general transport scalar equation described in Eq.6.27, it may be expressed in integral form as:

$$\frac{\partial}{\partial \tau} \int_V \rho \phi dV + \int_S (-\mathbf{w} \rho \phi + (\rho \phi \mathbf{v} - \Gamma \nabla \phi)) \, dS = \int_V q_\phi dV \tag{7.5}$$

Obviously, in an FSI analysis, while the primary variables in the structural model are the displacements, those of the fluid flow include the usual fluid variables as well as the displacements.

7.2.2 Interface Definition

The interaction between the fluid and the solid occurs by exchanging physical variables at a common interface. Defining a valid interface is therefore a crucial factor for obtaining successful solutions of FSI problems. Since the fluid and the solid domains are usually generated using different elements, the discretization of the two meshes on the interfaces is in general incompatible. A coupling is therefore only possible if the distances between the nodal points at the fluid and the solid boundaries do not exceed a certain critical value r_c. The relative distance from the fluid nodes to the solid interface r_f and that from the solid nodes to the fluid interface r_s are defined by:

$$r_f = \max\left\{\frac{d_f}{D_s}\right\} < r_c \qquad \text{and} \qquad r_s = \max\left\{\frac{d_s}{D_f}\right\} < r_c \tag{7.6}$$

where d_f, d_s, D_f and D_s represent the distances from a nodal point to the boundary and the element length for the fluid and the solid respectively, as illustrated in Fig.7.2.b for the case of r_f.

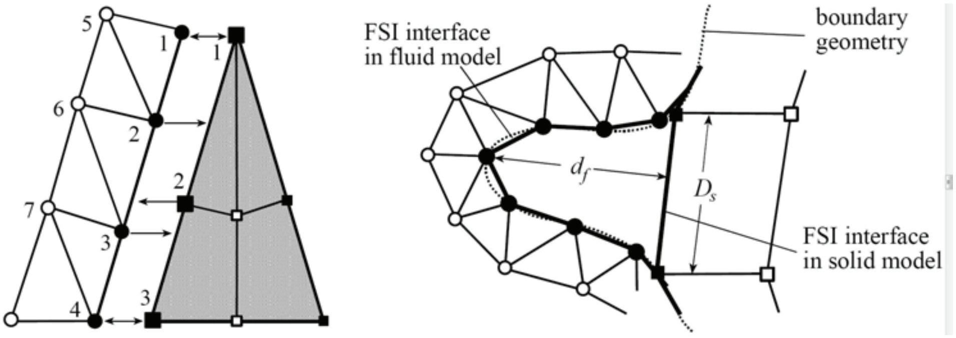

(a) F-S interfaces (b) F-S distances

Figure 7.2: Interfaces and distance measurements between fluid and solid.

The general case of *non-matching grids*, assuming different interface nodal positions for the fluid and solid models is shown in Fig.7.2.a. Exchanging variables at the interfaces is achieved by means of interpolation with the surrounding nodal values. Thus, the displacements at the fluid interface nodes are interpolated from the surrounding nodal displacements at the solid interface. Further, the nodal stresses at the solid interface are interpolated from the fluid traction using the nodal stresses at the fluid interface. In the ideal case of *matching grids* where the interface meshes are compatible, the interpolation at a particular fluid or solid position is achieved using the variables located at the same solid or fluid nodes, respectively.

7.2.3 Equilibrium Conditions

Obviously, common conditions for the fluid and the structure needed to establish exchange equilibrium are defined and applied at the interfaces. These conditions include the displacement compatibility and the traction equilibrium. The displacement compatibility is expressed as the kinematic condition:

$$\mathbf{d}_f = \mathbf{d}_s \tag{7.7}$$

where $\mathbf{d}_f$ and $\mathbf{d}_s$ denote the fluid and solid nodal displacements at the interfaces. As a result of the displacement compatibility, the velocity condition may be derived as well. This is defined in terms of the no-slip or the slip boundary conditions, given respectively by:

$$\mathbf{v} = \dot{\mathbf{d}}_s \qquad \text{and} \qquad \mathbf{n}.\mathbf{v} = \mathbf{n}.\dot{\mathbf{d}}_s \tag{7.8}$$

As for the traction equilibrium, it is expressed by the dynamic condition:

$$\mathbf{t}_f\mathbf{n} = \mathbf{t}_s\mathbf{n} \tag{7.9}$$

where $\mathbf{t}_f$ and $\mathbf{t}_s$ denote the fluid and solid nodal stresses at the interface, respectively. Defining h^d as the virtual solid displacement, the fluid force along the interfaces is derived from the fluid stress such that:

$$\mathbf{F}_f(t) = \int h^d \mathbf{t}_f d\mathbf{S} \tag{7.10}$$

The coupling at the interface is achieved by mapping the fluid nodal displacements according to the kinematic condition and the structure nodal stresses according to the dynamic condition. Given the fluid displacements at the boundary nodes, the internal nodal displacements may be computed based on a special moving mesh procedure such that the initial mesh quality is preserved. Based on the actual fluid nodal positions, the ALE governing equations of the flow domain are solved. Furthermore, the fluid force defined in Eq.7.10 exerted at the nodes of the solid interface includes usually stresses at neighbour solid nodes. As a result, all fluid and solid solution variables at the interfaces are somewhat indirectly coupled together.

7.2.4 Iteration Convergence

A coupled fluid-structure system includes nonlinear fluid equations and is obviously always nonlinear, independent on the linearity of the structure equations. As a result, iterative approaches are needed for the solution of FSI problems. The iteration criteria required to achieved convergence varies depending on the problem definition as well as on issues concerning available time, required accuracy or disposable computational effort and resources. Obviously, since structure displacement and fluid stress represent the exchange variables on the fluid-structure interfaces, convergence criteria based on these variables are generally used.

The displacement convergence conditions r_d is defined in terms of the displacement tolerance ϵ_d such that:

$$r_d \equiv \frac{\left\|\mathbf{d}_s^k - \mathbf{d}_s^{k-1}\right\|}{\max\left\{\left\|\mathbf{d}_s^k\right\|, \epsilon_0\right\}} \leq \epsilon_d \tag{7.11}$$

As for the stress convergence r_t, it is similarly defined in terms of the stress tolerance ϵ_t given by:

$$r_t \equiv \frac{\left\|\mathbf{t}_s^k - \mathbf{t}_s^{k-1}\right\|}{\max\left\{\left\|\mathbf{t}_s^k\right\|, \epsilon_0\right\}} \leq \epsilon_t \tag{7.12}$$

where ϵ_0 denotes a constant tolerance set to a small value and used to avoid overriding very small displacement and stress values.

7.2.5 FEM Coupled Equations

While different numerical approaches may be applied to solve the fields of the coupled system, the allowed solution methods in this case become limited. For instance, the numerical solution of a coupled system in which the finite volume approach is used to solve the fluid domain and the finite element approach to solve the structure domain, is obviously restricted to iterative methods. The use of a unique numerical discretization approach allows overcoming such restrictions and has various advantages [LM01]. Assuming an FEM-based approach as described in Chap.5 to solve the governing conservation equations for both the fluid and the solid domains, the corresponding discretized equations for the individual fields in matrix form may be formulated by:

$$\begin{cases} \mathbf{Q}_f[\mathbf{v}, \dot{\mathbf{v}}, \mathrm{p}] = K_f\mathbf{v} + M_f\dot{\mathbf{v}} + G_f\mathrm{p} \\ \mathbf{Q}_s[\mathbf{d}, \dot{\mathbf{d}}, \ddot{\mathbf{d}}] = K_s\mathbf{d} + D_s\dot{\mathbf{d}} + M_s\ddot{\mathbf{d}} \\ \mathbf{Q}_m[\mathbf{r}] \quad\;\; = K_m\mathbf{r} \end{cases} \tag{7.13}$$

where $\mathbf{r}$ represents the node positions within the ALE mesh domain m. The coupled FSI system is obtained by interpolating the displacement and stress variables at the interface as described above. Denoting $\mathbf{X} = (\mathbf{X}_f, \mathbf{X}_s)$ as the solution vector of the coupled problem, then the coupled FSI system may be written in terms of the fluid and solid finite element equations as:

$$\mathbf{F}[\mathbf{X}] \equiv \begin{bmatrix} \mathbf{F}_f\left[\mathbf{X}_f, \mathbf{d}_s(\mathbf{X}_s)\right] \\ \mathbf{F}_s\left[\mathbf{X}_s, \mathbf{t}_f(\mathbf{X}_f)\right] \end{bmatrix} \tag{7.14}$$

where $\mathbf{X}_f$ and $\mathbf{X}_s$ represent the soltution vectors defined for the fluid and the solid nodes, while $\mathbf{F}_f$ and $\mathbf{F}_s$ are the finite element equations corresponding to $\mathbf{Q}_f$ and $\mathbf{Q}_s$, respectively. A detailled description and the mathematical derivation of these formulations are well explained in [LM01; Bat96]. Obviously, the decoupled FEM system of the fluid and the solid equations follows from Eq.7.14 such that: $\mathbf{F}_f[\mathbf{X}_f, 0] = 0$ and $\mathbf{F}_s[\mathbf{X}_s, 0] = 0$.

Solving the coupled system may occur as a *one-way* or a *two-way* interaction scheme. In the one way coupling, only the fluid stresses are applied on the structure interface while no feedback is given from the structure toward the fluid. A more accurate coupling is achieved based on the two-way scheme, where both the fluid stresses and the structure displacements are exchanged onto the solid and the fluid, respectively.

7.2.6 Time Integration Consistency

It is clear at this point that the systems describing the fluid flow and the solid domain are the same on the fluid-structure interfaces. Consequently, the coupled FSI solution obviously requires a consistent time integration for both system of equations. Furthermore, the fluid and the solid equilibrium is generally satisfied at different times and schemes. Assuming the Euler-alpha method used for the fluid equations $\mathbf{Q}_f[\mathbf{v}, \dot{\mathbf{v}}, \mathrm{p}]$ and that the fluid equilibrium is obtained at time $t+\alpha\Delta t$, then the time integration for the pressure, velocity and acceleration variables may be written as:

$$\begin{cases} \mathrm{p}^{t+\alpha\Delta t} = \mathrm{p}^{t+\Delta t}\alpha + \mathrm{p}^{t}\,(1-\alpha) & \\ \mathbf{v}^{t+\alpha\Delta t} = \mathbf{v}^{t+\Delta t}\alpha + \mathbf{v}^{t}\,(1-\alpha) & \equiv (\mathbf{d}^{t+\Delta t} - \mathbf{d}^{t})/\Delta t \\ \mathbf{a}^{t+\alpha\Delta t} = \mathbf{a}^{t+\Delta t}\alpha + \mathbf{a}^{t}\,(1-\alpha) & \equiv (\mathbf{v}^{t+\Delta t} - \mathbf{v}^{t})/\Delta t \end{cases} \tag{7.15}$$

Further, assuming that the solid equilibrium for the equations $\mathbf{Q}_s[\mathbf{d}, \dot{\mathbf{d}}, \ddot{\mathbf{d}}]$ is obtained at $t + \Delta t$, then the velocity $\mathbf{v}^{t+\Delta t} = \dot{\mathbf{d}}^{t+\Delta t}$ and the acceleration $\mathbf{a}^{t+\Delta t} = \ddot{\mathbf{d}}^{t+\Delta t}$ variables can be derived from Eq.7.15 in terms of the unknown displacement $\mathbf{d}^{t+\Delta t}$. Substituting these equations into the coupled system described in Eq.7.13, the consistent time integration scheme for an FSI problem may be finally expressed as:

$$\begin{cases} \mathbf{Q}_f^{t+\alpha\Delta t} \approx \mathbf{G}_f\left[\mathbf{v}^{t+\alpha\Delta t}, (\mathbf{v}^{t+\alpha\Delta t} - \mathbf{v}^{t})/\alpha\Delta t, \mathrm{p}^{t+\alpha\Delta t}\right] = 0 \\ \mathbf{Q}_s^{t+\Delta t} \approx \mathbf{G}_s\left[\mathbf{d}^{t+\Delta t}, a\mathbf{d}^{t+\Delta t} + b\boldsymbol{\xi}^{t}, \mathbf{d}^{t+\Delta t} + \boldsymbol{\eta}^{t}\right] = 0 \end{cases} \tag{7.16}$$

7.2.7 Coupling Approaches

The main objective of FSI coupling is to analyze the interaction between the fluid and the structure under consideration. A solution may be obtained by simulating the response of a coupled system of both computational models. Many solution approaches exist to achieve such a numerical coupling [Wal99]. From the application point of view, these may be classified into three categories:

- The direct approach
- The iterative approach
- The field elimination

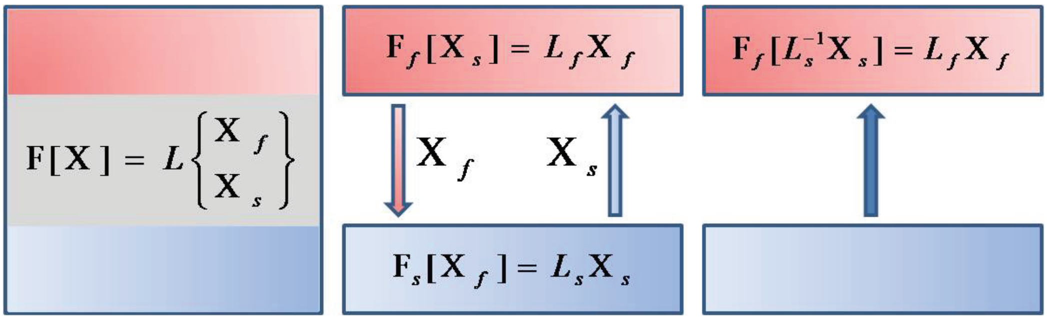
$F[X] = L\begin{Bmatrix} X_f \\ X_s \end{Bmatrix}$
$F_f[X_s] = L_f X_f$
X_f
X_s
$F_s[X_f] = L_s X_s$
$F_f[L_s^{-1} X_s] = L_f X_f$

(a) Direct coupling (b) Iterative coupling (c) Field elimination

Figure 7.3: Various coupling approaches for FSI problems.

The classification and main differences of these approaches are illustrated in Fig.7.3. Thereby, **X** denotes the field variables, L is a differential operator and **F** the right-hand side of the individual fields. Further, the fluid f and solid s domains are represented by the red and blue fields, respectively. In the last, field elimination approach, the solutions within an individual field are assigned to the equations of the other field before the old one is destroyed. The application of this approach is however restricted to simple linear analysis, which misfits the complex demands of most FSI problems. The evaluation of the field elimination after [PF83] states: *'it can be properly characterized as a poor strategy that eventually leads to a computational horror show for more general problems'* [Wal99].

In the following therefore, the direct and the iterative approaches as well as their pros and cons are presented.

Direct Coupling

In the direct approach, the entire problem is defined and solved simultaneously. Thereby, the equations governing the dynamics of the fluid and the mechanics of the structure are combined and solved within one coupled system and using a single solver. The simultaneous formulation includes all physical and numerical dependencies of the field variables. The linearization of the coupled system occurs then in the same way as for the fluid or solid equations being treated apart. The matrix system arising from the coupled fluid and structure equations may be thus expressed as:

$$\begin{bmatrix} \mathbf{A}_{ff} & \mathbf{A}_{fs} \\ \mathbf{A}_{sf} & \mathbf{A}_{ss} \end{bmatrix} \begin{bmatrix} \Delta\mathbf{X}_f^k \\ \Delta\mathbf{X}_s^k \end{bmatrix} = \begin{bmatrix} \mathbf{B}_f \\ \mathbf{B}_s \end{bmatrix} \tag{7.17}$$

and

$$\mathbf{X}^{k+1} = \mathbf{X}^k + \Delta\mathbf{X}^k \tag{7.18}$$

Assuming indeed that the Newton-Raphson method is used to solve the non-linear equations, then:

$$\begin{cases} \mathbf{B}_f & = -\mathbf{F}_f^k & \equiv -\mathbf{F}_f\left[\mathbf{X}_f^k, \lambda_d \mathbf{d}_s^k + (1-\lambda_d)\mathbf{d}_s^{k-1}\right] \\ \mathbf{B}_s & = -\mathbf{F}_s^k & \equiv -\mathbf{F}_s\left[\mathbf{X}_s^k, \lambda_t \mathbf{t}_f^k + (1-\lambda_t)\mathbf{t}_f^{k-1}\right] \\ \mathbf{A}_{ij} & = \partial \mathbf{F_i^k} / \partial \mathbf{X_j} & ; (i,j) = (f,s) \end{cases} \tag{7.19}$$

Thereby, the fluid stress and the solid displacement have been relaxed, using a stress relaxation factor λ_t and a displacement relaxation factor λ_d, respectively.

The unknown solution ${}^{t+\Delta t}\mathbf{X}$ at time $t+\Delta t$ is considered to be derived from ${}^{t}\mathbf{X}$, being the solution at time t. The two-way direct coupling approach yielding a fully coupled solution is demonstrated by the following algorithm [Adi08]:

1. Start with the initial condition: $\mathbf{X}^0 =^t \mathbf{X}$
2. Iterate for $k = 1, 2, \cdots < k_{max}$ to obtain solution at $t + \Delta t$
3. Assemble single fluid $\mathbf{F}_f$ and solid $\mathbf{F}_s$ equations
4. Compute the coupling matrices $\mathbf{A}_{ij}$ for $(i,j) = (f,s)$
5. Solve the linearized coupled system and update the solution
6. Compute the stress r_t and/or displacement residuals r_d for convergence
7. Check converged solution: Yes= jump to (8); No= back to (3) with $k+1$
8. Accept and/or save and/or print solutions ${}^{t+\Delta t}\mathbf{X}$

Steps 1 to 8 are repeated for the entire temporal domain.

Iterative Coupling

In the iterative, or staggered approach, the computational fields are defined and solved separately independent from each other. Thereby, the equations governing the fluid dynamics and the structure mechanics are solved within two systems that are coupled together. The so called partitioned formulation is thus based on separate physical and numerical conditioning of the individual fields and field variables. The interaction of the fluid and the structure is accounted for though the transfer of constraints between the individual fields. This is achieved by using the previous iterated coupling information. The first contribution of iterative methods for coupled analysis originate from [PFD77]. An overview over prediction tools and substitution techniques necessary to achieve such a communication may be found in [FPF98].

Similar to the direct coupling, the unknown solution ${}^{t+\Delta t}\mathbf{X}$ is assumed at time $t+\Delta t$ and has to be derived from the solution ${}^{t}\mathbf{X}$ at time t. The two-way iterative coupling approach also leading to a fully coupled solution is demonstrated by the following algorithm:

1. Start with the initial condition: $\mathbf{d}_s^{-1} = \mathbf{d}_s^0 =^t \mathbf{d}_s$ and $\mathbf{t}_f^0 =^t \mathbf{t}_f$
2. Iterate between fluid and solid for $k = 1, 2, \cdots < k_{max}$
3. Solve the fluid equations for $\mathbf{X}_f^k$ using prescribed displacements $\mathbf{d}_s$:

$$\mathbf{F}_f\left[\mathbf{X}_f^k, \lambda_d \mathbf{d}_s^{k-1} + (1-\lambda_d)\mathbf{d}_s^{k-2}\right] = \mathbf{0}$$

4. Stress convergence is required? Yes= go to (5); No= go to (7)
5. Compute and check the stress residuals r_t
6. Converged solution for $\mathbf{t}$? Yes= go to (7); No= back to (3) with $k+1$
7. Displacement convergence required? Yes= go to (8); No= jump to (10)
8. Solve the structure equations for $\mathbf{X}_s^k$ using prescribed $\mathbf{t}_f$:

$$\mathbf{F}_s\left[\mathbf{X}_s^k, \lambda_t \mathbf{t}_f^k + (1-\lambda_t)\mathbf{t}_f^{k-1}\right] = \mathbf{0}$$

9. Compute the fluid displacements $\mathbf{d}_f^k$ using prescribed conditions:

$$\mathbf{d}_f^k = \lambda_d \mathbf{d}_s^k + (1-\lambda_d)\mathbf{d}_s^{k-1}$$

10. Compute and check the displacement residuals r_d
11. Converged solution for $\mathbf{d}$? Yes= go to (12); No= back to (3) with $k+1$
12. Accept and/or save and/or print solutions ${}^{t+\Delta t}(\mathbf{X}_f, \mathbf{X}_s)$

Thereby, at least one of the convergence criteria is obviously required and must be computed. Finally, steps 1 to 8 are repeated until the entire temporal range of the computations is covered. Here also, relaxation factors are applied and have particular importance in reaching convergence in the iterations.

Parallel and Serial Coupling

Practically, there exist two techniques to realize an iterative coupling for the integration of FSI solutions. The main difference hereby is based on the way, in parallel or in serial, the fields are coupled together.

The iterative algorithm just described above illustrates a two-way partitioned coupling. This kind of coupling is called strong or parallel coupling. Thereby, the governing equations for the fluid and the solid models are solved individually in parallel by using the latest information provided from each other. Equilibrium iterations between the fluid and the solid continue until the solution of the coupled equations is converged [Adi08]. As a result, all coupling conditions between the fields are fulfilled at the end of every timestep and the whole system is in equilibrium at the new time $t + \Delta t$. Therefore, based on this approach, an implicit coupling may be achieved through iteration between the fields within one timestep [CL97]. Consequently, a strong staggered coupling carries in it all advantages of implicit approaches, mainly that of being unconditionally stable, having no restrictions concerning the allowed timestep size that can be used. This may however lead to a relatively high computational cost in terms of the number of iterations required to achieve convergence between the fields.

Alternatively, the iterative approach may be realized as a one-way partitioned coupling. The simple one-way staggered coupling is also known as the weak or the serial approach. In this case, the governing equations for the fluid and the solid models are solved individually in sequence. Thereby, coupling information from the individual solutions of one field is transferred to the other field which is now considered at the next timestep. As a result, such a procedure does not allow a simultaneous satisfaction of all coupling conditions at the interface, in terms of both displacement and velocity. Further, weak coupled integration approaches do not inherit the same numerical properties from their individual fields. So, they are only of first order in Δt, even when the individual fields are based on second or higher-order approaches. Further, being based on a serial procedure, the weak approach includes an explicit part, even when the individual fields are implicit [CL97]. Thus, in general serial coupling is conditionally stable even when both individual fields are unconditionally stable. The latter point represents the major constraint of this approach when used to solve real FSI problems.

An overview on the fundamental approaches and various application fields of parallel and serial iterative coupling may be found in [FPF98]. Furthermore, requirements and optimization strategies are presented in [WMR99].

Direct versus Iterative

Which approach to apply for solving an FSI problem? A suitable choice of a coupling approach depends on many factors. In search of a reasonable answer, in the following, the direct and iterative methods are compared together.

An iterative approach benefits with a modular design allowing to couple two independent models together. In the direct coupling the fluid and the solid equations are solved using a single solver. The partitioned method on the other hand, allows a solution of the governing equations based on two different solvers. In that way, different spacial and temporal discretization techniques may be applied for the fluid and the structure models such that to meet the specific requirements and characteristics of the individual fields. Also, the flexibility in choice of independent solution techniques allows the application of more efficient methods developed particularly for either the fluid or the solid equations. Finally, through the partitioning into individual fields, the differences in the stiffness coefficients of the system equations of the individual fields do not necessarily lead to bad conditioning of the whole problem.

On the other hand, the advantages of iterative methods are not obtained for free. While a partitioned approach allows flexible modification and optimization of the individual techniques, iterative simulations require also the integration of a coupling algorithm. The main disadvantages face to direct methods, concern especially stability and accuracy issues of the whole coupled system. As mentioned above, iterative approaches behave explicitly and are therefore unconditionally stable, even when the individual fields are both based on implicit approaches and thus conditionally stable. Furthermore, since the governing equations are solved simultaneously in one matrix, direct methods are much more robust in terms of accuracy of the results. This property get lost or at least damped through the iterations between the two systems. While a strong iterative approach may lead to similar accuracy level as in the direct method, this can only be achieved at the cost of laborious work and very well formulated algorithms. The direct method is in general faster than the iterative method. On the other side, since the problem is partitioned into two parts, the solution effort is reduced and the iterative method requires less memory than the direct method.

In general, direct coupling is appropriate for small to medium sized problems without contact definition. Whereas, iterative approaches are more suitable for small to large sized problems with or without contact conditions. The direct method has proven efficiency in application for transient analysis, while iterative methods are better when used for steady-state analyses [Adi08].

However, a definitive statement about an exclusive choice is pointless at this level. Obviously, the answer to the above question may be easily formulated now: It all depends on the nature and complexity of the problem to be solved, on the available time and computational resources and of course on the user priority concerning stability and accuracy issues.

7.2.8 Solution Methods

The approach for solving the governing equations consists of two kinds of iterations: the outer and the inner iterations. For the solution of the nonlinear system of equations, incremental iterative approaches are used similar to the decoupled CFD and CSM problems. The segregated and the Newton-Raphson methods, described in Chap.6 and Chap.5, respectively may be used as outer iteration methods for solving FSI problems.

In order to obtain the linear equations in the segregated method, each variable is integrated while considering all other variables to be fixed. This applies for all equations except the continuity equation, for which a pressure-correction relation is derived based on the discretized momentum equations to satisfy velocity corrections. On the other hand, the Newton-Raphson method generally derives the linear flow and structural equations by assuming the entire variables in the fluid and solid domains. Depending on the desired coupling scheme to be used, either the Newton-Raphson or the segregated method may be chosen. The Newton-Raphson method used in the vessel wall modeling can be applied for both direct and iterative FSI coupling approaches. While the segregated method used in the blood flow modeling, in which even the blood equations are not coupled together, cannot be used for direct FSI coupling.

Once the linear systems are derived, a solution of the resulting linearized equations can be then obtained by applying inner iterations based on either direct or iterative methods. When the segregated method is applied to linearize the governing equations, the variables are derived in a certain order in the outer iteration using the linear solver. On the other hand, if the nonlinear system is solved using the Newton-Rapson method, then the linear solver is applied to solve the vector $\mathbf{X}$ containing all solution variables. There exist various forms of such linear solvers. The most famous direct solution may be obtained based on the Gauss elimination method. The iterative solution is usually based on the Gauss-Seidel algorithm. Thereby, the flow problem and structural problem are solved successively until convergence criteria are satisfied.

Gauss-Seidel Relaxation Algorithm

Relaxation methods are used to solve partial differential equations that involve splitting the sparse matrix and then iterating until a solution is found [PFTV92]. The Gauss-Seidel algorithm combined with a scalar algebraic multigrid (AMG) method may be used to solve the linearized scalar equations. Thereby, the N equations of $a_{ij}x_j = b_i$ are solved one by one in sequence by using the previously computed results as soon as they become available.

The point implicit Gauss-Seidel relaxation procedure is based on two sweeps of the unknowns in forward and backward directions. For the scalar system, first a forward sweep is performed such that:

$$x_i^{k+1/2} = \frac{b_i - \sum_{j<i} a_{ij} x_j^{k+1/2} - \sum_{j<i} a_{ij} x_j^{k}}{a_{ii}} \tag{7.20}$$

where $i = 1 \cdots N$ denotes the number of unknowns. Then, a backward sweep follows the forward one which can be written as:

$$x_i^{k+1} = \frac{b_i - \sum_{j<i} a_{ij} x_j^{k+1/2} - \sum_{j<i} a_{ij} x_j^{k+1}}{a_{ii}} \tag{7.21}$$

Since each new iterate component depends upon all previously computed components, the computations in the Gauss-Seidel method are performed in a serial manner. Furthermore, as a result of the serial computations, the new iterate x^k depends upon the order in which the equations are examined and thus their components will be changed if this ordering is changed.

Gauss Elimination Algorithm

Alternatively, the linear system of equations may be solved based on the Gaussian elimination. The algorithm is the standard direct linear solution method and consists of two steps: a Forward Elimination in which the matrix system is reduced to an echelon form based on elementary row operations, followed by a back substitution to solve for the unknown variables. The algorithm involves a matrix decomposition, such as an LDU decomposition, expressing an original matrix A as a product of lower triangular L, upper triangular U and diagonal D invertible matrices, such that:

$$A = LDU \tag{7.22}$$

Since the diagonal elements of L and U are all ones, all the matrices may be stored into the original matrix. Once the decomposition matrices are computed, the equation is solved such that:

$$X = A^{-1}B = U^{-1}D^{-1}L^{-1}B \tag{7.23}$$

The arithmetic operations required to solve an $n \times n$ matrix is of the order of $\mathcal{O}(n^3)$ ($= 2/3n^3$ operations) [Adi08]. For large systems, iterative methods are therefore more efficient. Further, the algorithm has in principle large round-off errors. These can be however resolved by applying matrix pivoting before eliminating any variable. This column and/or row interchanging is very efficient to enhance the numerical stability of the computations though it obviously adds to the total computational cost required to find a solution.

7.3 FSI Simulation Models

Simulating the interaction between the blood flow and the vessel wall provides a significant insight into the underlying real physical behavior of the hemodynamics and the elastomechanics of the vessels. Numerical modeling of the interaction between the fluid and the structure consists of a coupled modeling of CFD and CSM models as described separately in Chap.6 and Chap.5, respectively. The theoretical formulations arising from the coupling problem have been presented in the previous sections of this chapter. Together with the fundamental principles of fluid dynamics and solid mechanics already described, these formulations will now be applied to simulate the blood-vessel interaction problem. The FSI simulation process for computing the physical interaction between the hemodynamics and the elastomechanics is based on the steps described in Sec.3.2 applied to a coupled CFD-CSM problem. Appropriate image-based patient-specific mesh models for the blood volume, the wall volume and the interface domains are thereby generated based on the specific meshing processes established for FSI applications and described in Sec.4.5. The FSI computations of the relevant parameters, such velocity fields, pressure loads, wall stress and strain distributions are based on the finite element approach described in Chap.5 and applied for both the blood and the wall models. For the solution of the fundamental equations governing the blood and the wall domains, the numerical solvers of the software Adina are adopted to obtain FEM-based simulation results.

In the following sections, the physical models, material properties, boundary and initial conditions and mathematical models governing the blood flow and the arterial wall domains and used for performing the FSI simulations are presented. Also, a stability analysis describing the influence of the applied models on the convergence behavior of the simulations will be discussed.

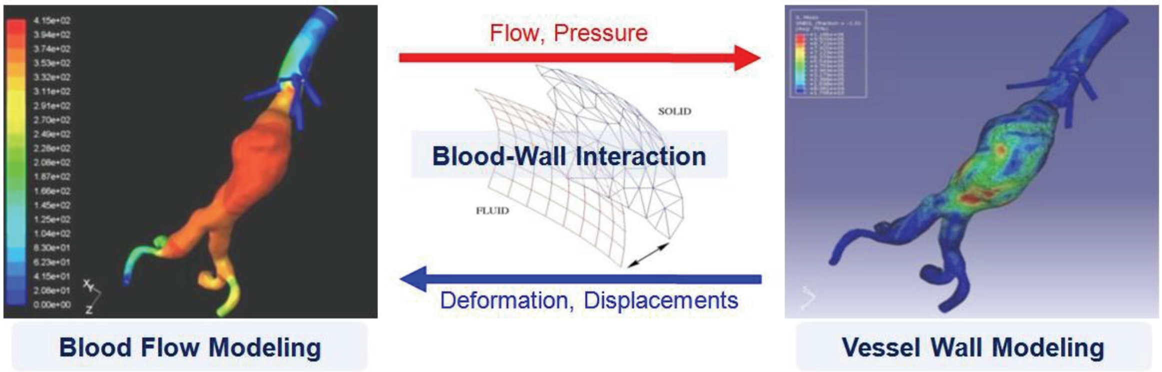
4.15e+02
3.94e+02
3.74e+02
3.53e+02
3.32e+02
3.11e+02
2.91e+02
2.70e+02
2.49e+02
2.28e+02
2.08e+02
1.87e+02
1.66e+02
1.45e+02
1.25e+02
1.04e+02
8.30e+01
6.23e+01
4.15e+01
2.08e+01
0.00e+00
X
Y
Z
Flow, Pressure
SOLID
Blood-Wall Interaction
FLUID
Deformation, Displacements
Blood Flow Modeling
Vessel Wall Modeling

Figure 7.4: Coupling blood flow and vessel wall simulations.

7.3.1 Physical and Constitutive Modeling

Physical modeling of the interaction between the blood flow and the vessel wall includes the description of the behavior of the flow dynamics and the vessel mechanics through the fundamental equations, as well as the description of the material properties of the blood and the wall through their appropriate constitutive equations. The constitutive equations are then substituted into the fundamental equations of the respective domain, before they finally get coupled for the analysis of the interaction together.

Blood Modeling

The three-dimensional equations governing the dynamics of the blood flow were derived in Chap.6 from the mass and momentum conservation laws. Here again, the energy conservation may be neglected assuming small temperature variations along the aorta. The system of governing equations represented by the continuity and the Navier-Stokes equations for a laminar blood flow in the ALE configuration is given by Eq.7.3 and Eq.7.4.
The constitutive equations needed for the description of the physical behavior of the blood as a fluid were also described in Chap.6 based on the material laws. These include mainly incompressible, viscous and turbulent properties required beside the fundamentals equations. Blood incompressibility is determined in terms of the constant mass density ρ= 1050 Kgm^{-3}. The Newtonian viscosity is given in terms of the shear-independent constant μ, while the shear-thinning non-Newtonian behavior of the blood is defined based on the Carreau model given in Eq.6.76. The associated non-Newtonian blood constants characterizing the Carreau model were introduced in Sec.6.5.1. Further, in flow domains where the time-averaged Reynolds number defined in Eq.6.34 is larger than Re_{crit}, the turbulent behavior of the blood is described based on the Reynolds-averaged approach. Thereby, the $k - \epsilon$ two-level model defined in Eq.6.73 and Eq.6.74 is used for the determination of the governing RANS equations. The constant parameters corresponding to the $k - \epsilon$ model were also introduced in Sec.6.5.1.

Wall Modeling

The time-dependent vessel equations governing the elastomechanics of the wall domain are described in Chap.5 based on the Euler-Cauchy principle. These were derived from the Eulerian force and momentum balance equations, represented by the dynamics equations and the symmetry of the Cauchy stress tensor and given in Eq.5.36 and Eq.5.37, respectively.

The wall material properties and the elastomechanical behavior of the vessel are also described in Chap.5 in terms of the wall constitutive equations. Arterial wall constitutive equations involve the description of the elasticity, the anisotropy and the compressibility of the wall. Also here, the vascular tissue is modeled as a non-linear hyperelastic material based on a finite strain constitutive theory assuming that the wall undergoes large displacements prior to rupture. The energy strain function W describing the nonlinear hyperelastic aortic wall as a homogeneous, isotropic and incompressible structure is expressed in terms of the three invariants of the Cauchy-Green dilation tensor given in Eq.5.67. Based on W, the elastomechanical constitutive behavior of abdominal and thoracic aneurysms as well as healthy human and porcine aortic materials is modeled using the hyperelastic models defined in Sec.5.5.1.

7.3.2 Initial and Boundary Conditions

The initial and boundary conditions for the FSI simulations consist of individual conditions involving the separated blood and wall domains, and of interface conditions for the coupled domain.

Blood Conditions

Blood conditions involve velocity-based and pressure-based conditions to be applied at the inlet and the outlets of the blood model. A first set of conditions appropriate for use at the inlet and the outlets of the blood domain was presented in Sec.6.5.2. In search of more accurate computations, two additional conditions have been developed specifically for application to the coupled FSI simulations. These are the *flow-based spatial distribution* and the *pressure-based outlet-specific* conditions. Thus, beside the homogeneous flow-based condition for the inlet and the pressure-based and outflow-rates conditions for the outlets, these two conditions can be alternatively applied to the inlet and the outlet boundaries, respectively.

- **Flow-based spatial distribution:**
  In the homogeneous profiles, the velocity values are considered as constant along the inlet at a given instant of time. Alternatively, the spacial distribution of the inlet flow may be considered for more accurate boundary conditions. The spacial distribution is derived based on the *Womersley* profiles, calculated from known homogeneous pulsatile flow measurements. Thereby, the spacial distribution of the velocity w in the flow direction z is computed as a function of the radius r in the inlet cross-section:

$$\frac{\partial^2 w}{\partial r^2} + \frac{1}{r}\frac{\partial w}{\partial r} - \frac{1}{\nu}\frac{\partial w}{\partial t} = -\frac{1}{\mu}\frac{\partial p}{\partial z} \tag{7.24}$$

A Matlab code has been developed to automatically derive the spatial Womersley distribution by computing the unsteady profiles for each mesh node at the inlet cross-section based on a Fourier analysis. The derivation is illustrated in Fig.7.5. Assuming that $\partial p/\partial z = A^* e^{iwt}$, then:

$$w\left(y = r/R\right) = \frac{A^*}{iw\rho}\left(1 - \frac{J_0\left(\alpha y i^{3/2}\right)}{J_0\left(\alpha i^{3/2}\right)}\right) e^{iwt} \tag{7.25}$$

Obviously, the number of time-functions associated with the boundary conditions is related to the number of mesh nodes at the inlet face. This number varies usually in the range of hundreds of functions. In order to facilitate the processing, the code can optionally save the time-dependent results at each node automatically into the Adina form so that these can be directly applied for running the FSI simulations.

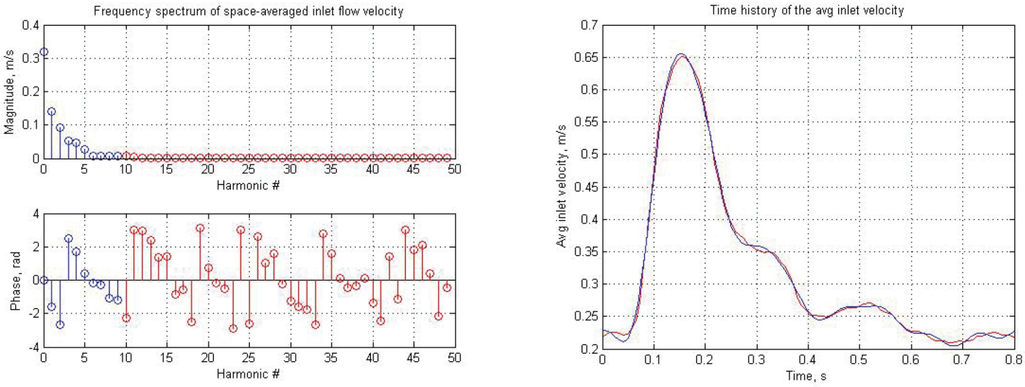

(a) Fourier harmonics (b) Homogeneous inlet velocity

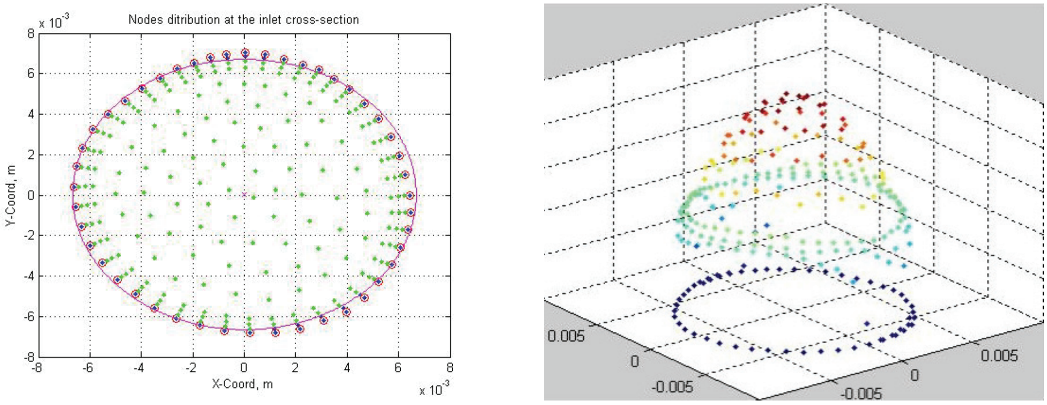

(c) Inlet mesh nodes (d) Peak Womersley profile

Figure 7.5: Computation of the Womersley flow condition for 4D-CT-P2.

- **Pressure-based outlet-specific:**
  While the pressure-based condition assumes the pressure to be the same at all outlets, the application of distinct profiles for the different outlets leads to more accurate modeling. Therefore, another Matlab code has been developed to derive pressure-based outlet-specific conditions based on the mass and energy conservation laws as described in [FKA03]. Thereby, the geometric properties of the aortic model must be accurately pre-measured. In the current implementation, the pressure p_i at a given outlet i and at a given instant of time t expressed in terms of the known velocity v_0 and pressure p_0 profiles at the inlet is derived such that:

$$p_i(t) = p_0(t) + \alpha \frac{v_0^2(t)}{2}\rho - \frac{v_i^2(t)}{2}\rho\left(\alpha + f\frac{L_{0,i}}{D_i}\right) + \rho g\left(z_0 - z_i\right) \qquad (7.26)$$

  Where v_i is the velocity profile at the outlet i, computed for instance from an outflow-based condition, $\alpha = 1/A \int (u/v)^3 dA$ denotes the kinetic correction factor, with u and v being the instantaneous and the spatially-averaged velocity at a cross section, $f = 8\tau_w/\rho v^2$ is a flow-induced WSS dependent friction factor, D_i is the diameter of the outlet and $L_{0,i} = L_0 + L_i$ is the centreline length from the inlet to the outlet i. The code automatically generates the pressure profiles at all outlets by solving p_i for each time t based on a user-defined timestep size Δt and a consistent period T for all given velocity and pressure profiles (Fig.7.6).

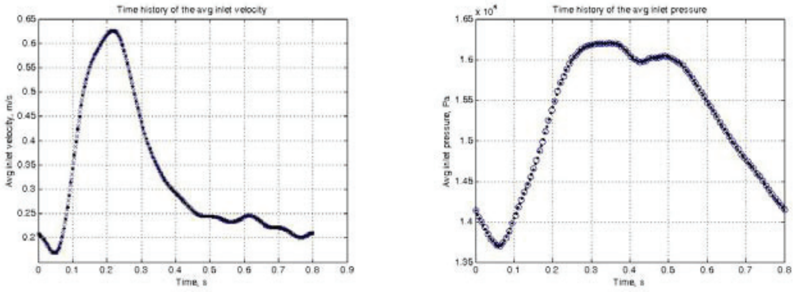

(a) Inlet velocity (b) Inlet pressure

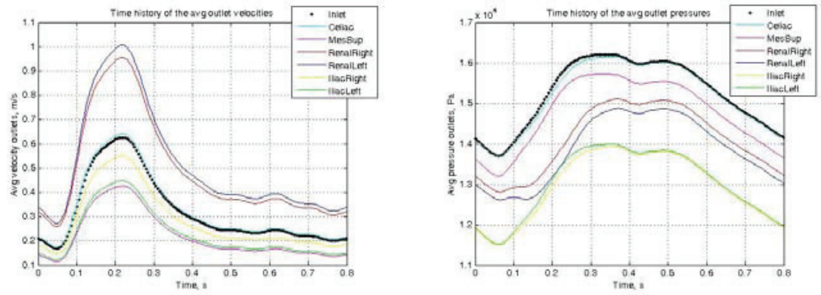

(c) Outlet velocities (d) Outlet-specific pressures

Figure 7.6: Computation of the outlet-specific pressures for 4D-CT-P3.

Wall Conditions

As for the wall boundary conditions, they consist of the Dirichlet condition applied at the boundaries of the solid model. The physical condition is similar to the case of the vessel wall modeling described in Chap.5. Thereby, the aorta is virtually fixed by the surrounding organs by imposing zero translation at its ends. However, since the wall domain for FSI simulations consists of a volume mesh, the definition of the displacement condition in this case of FSI has to be adapted to the application and the software used. Therefore, the constraint condition for all degrees of freedom is defined at the inlet and the outlet faces, determined specifically while generating the FE-Mesh model for application to coupled FSI simulations, as described in Sec.4.7.

Interface FSI Conditions

The particular point characterizing FSI simulations is that no prescribed loads, at least not directly, are defined at the wall of the solid model. Instead, the interaction between the blood flow and the vessel wall is computed at each timestep. Therefore, the Neumann condition applied at the wall in the case of CSM, is replaced here by the special FSI boundary condition applied at the interfaces. In contrast to usual boundary conditions, the special boundary conditions contain unknown variables determining the interaction. These are discretized, assembled and solved into the global system of equations [Adi08]. The definition of the special FSI condition has again to be adapted to the form and the element type of the interfaces being related to the software used. While direct nodes are used for the blood interface, the special FSI condition is applied to the nodes as part of the element faces for the wall interface.

7.3.3 Mathematical and Numerical Modeling

The coupled equations governing the blood flow and the vessel wall domains involve a nonlinear system of partial differential equations. The computational domains are thereby discretized based on the FEM into three dimensional 8-nodes hexahedric elements for the wall domain and 4-nodes tetrahedric elements for the blood domain. Further, the interface consists of two-dimensional 4-nodes quadratic elements, while at the wall-blood transition the blood includes indeed a layer of 3D 5-nodes prisms elements. The associated interpolating shape functions for the discrete node variables within the finite elements are defined based on the polynomial functions described in Sec.5.4.2.

The finite element conservation equations are obtained by integrating the governing equations in their weak form over the individual cells using the Galerkin method. The variational forms of the equations are obtained, depending on the models, in a similar way as derived in Chap.5 for the solid equations. Dynamic equilibrium is solved by interpolating the field variables of the differential equations at the centre of the elements. The Arbitrary Lagrangian-Eulerian formulation is adopted to derive and approximate the nonlinear discretized equations to their incremental forms. All time-dependent differential equations are discretized using implicit formulations based on the Newmark, the Euler and the Composite (see Sec.7.3.4) methods.

The Newton-Raphson approach is adopted to solve the resulting time-dependent system of nonlinear partial differential equations. In this formulation, the entire field variables are assumed together. This approach is used rather than the segregated method, since it enables dealing with both direct and iterative FSI coupling. Nodal equilibrium of the resulting linearized system of governing equations is solved using either a direct iteration approach based on the Gauss Elimination Algorithm or an iterative approach based on the Gauss-Seidel algorithm. In Adina, the direct and the iterative linear solution methods are applied using the sparse and the AMG solvers, respectively. These are adopted depending on the coupling scheme to be used to solve the FSI problem. Finally, the direct coupling algorithm described in Sec.7.2.7 is primarily used to obtain the fluid and structure response by computing the interaction between both domains.

7.3.4 Numerical Stability - Discussion

Numerical stability of the coupled simulations includes the individual stability of the blood flow and vessel wall models as well as stability related to the coupling scheme. Stability issues of the individual simulation models were discussed in Chap.5 and Chap.6 and also apply for the coupled models.

Enhanced stability is first obtained by avoiding discrepancies between the two interfaces. This was achieved by using conformal meshes generated based on the optimized mesh processes described in Chap.4.

Implicit time integration is used for more accurate solutions and to overcome the limitation of explicit methods being conditionally stable and to achieve more accurate solutions. When the implicit Euler method presented in Sec.6.4.5 is used, a necessary condition to obtain stable consistent time integration as described in Eq.7.16 is to have $\alpha \geq 1/2$ [Adi08]. While the trapezoil rule with scheme of $\alpha = 1/2$ is second-order accurate, it is usually unstable when nonlinear equations or non-uniform element size is used. On the other hand, excluding this value, the Euler method is first-order accurate in time.

The Euler backward method with $\alpha = 1$ leads to stable conditions for most real applications, though it is only first-order accurate. For more accurate FSI simulations, a second-order scheme based on two consecutive sub-timesteps is used. Thereby, in the first step the variables are solved at time $t + \gamma \Delta t$ based on the α-Euler method, then solutions at time $t + \Delta t$ are obtained [BZJ99]:

$$u^{t+\gamma\Delta t} = u^t + \gamma\Delta t f\left(u^{t+1/2\gamma\Delta t}\right) \quad \text{and} \tag{7.27}$$

$$u^{t+\Delta t} = u^{t+\beta\gamma\Delta t} + (1-\alpha)\Delta t f\left(u^{t+\Delta t}\right) \quad \text{with} \tag{7.28}$$

$$u^{t+\beta\gamma\Delta t} = (1-\beta)\, u^t + \beta u^{t+\gamma\Delta t},$$

$$\gamma = 2 - 1/\alpha, \quad \beta = \alpha^2/\left(2\alpha - 1\right), \quad 1/2 < \alpha < 1$$

Truncation errors introduced by the second-order time discretization scheme ($(O(t)^2)$) are minimized by using $\alpha = 1/\sqrt{2}$. The composite method needs obviously twice the computational cost per timestep. However, it may provides faster solutions if less number of timesteps overall can be used.
The automatic time stepping method provided in Adina controls the timesteps to enhance convergence in case solutions cannot be reached with the current timestep size. This is particularly important in dynamic computations, where matrix conditioning may be improved by using smaller timesteps and where the application of smaller load increments may be more efficient. Furthermore, the automatic time-stepping allows controlling the accuracy of the dynamic solution. The accuracy criterion based on which accuracy checking is performed after each iteration is defined by:

$$\max\left|U_{im}^{t+\Delta t/2} - U_{ih}^{t+\Delta t/2}\right| \leq \epsilon_d$$

where i denotes the translational degrees of freedom, $U_{ih}^{t+\Delta t/2}$ the displacement at time $t + \Delta t/2$. On the other hand, since the timesteps are successively subdivided until convergence is reached, the initial and the final sizes must be properly controlled otherwise the process can become very expensive if these are far different. Finally, a proper dealing with the way the next timestep following the convergence is further processed (such as to return to the original timestep size, to use the time increment that gave convergence, or to proceed through user-defined time points) is very important.

A weak interaction between the fluid and the solid assumes that the influence of the solid deformation on the fluid is small and thus can be neglected. As a result, a one-way coupling scheme in which only the fluid stress is applied on the structure interface, does not enforce the desired equilibrium within a timestep. Therefore, two-way coupling was applied, in which both the fluid and the structure are influenced by the structure displacement and by the fluid stress, respectively, and yields to more accurate interaction. Thereby, both displacement and stress convergence criteria has to be satisfied for accurate simulations of the interaction. The direct and the iterative FSI coupling schemes in two-ways coupling were presented and compared in Sec.7.2.7. In general, while the direct coupling requires more memory, it is much faster and accurate than the iterative coupling. Thus, when enough memory is available the direct FSI coupling is the scheme of choice.

In general, the memory and solution time needed by the segregated method behave linearly with the mesh size and are less than those needed by the Newton-Raphson method. Nevertheless, since the variables in the segregated solution are not solved simultaneously in one matrix system, it is relatively hard to achieve convergence on each iteration. Under-relaxation algorithms are therefore required and the outer and inner solution processes must be properly controlled. These factors were described in Chap.6 and usually depend on the mesh quality of the computational domain, on the difficulty of the problem and on the solution variables being solved. Furthermore, the use of the Newton-Raphson rather than the segregated method to solve the nonlinear equations also adds to the flexibility in applying coupling FSI schemes. Obviously, when the segregated method is used, in which even the fluid variables are not coupled together, direct FSI cannot be applied. Further, the implicit solution in which the equilibrium equations are considered at an unkwon time configuration is improved by the use of the Newton-Method. Also, when necessary, line searches as implemented in Adina may be used to enforce convergence though they add to the overall cost per iteration [Adi08]. The pros and cons of the full and modified Newton-Raphson iteration schemes discussed in Chap.5 also apply here for the coupled dynamic response.

The stability of an iterative solver requires a proper control of the convergence of the inner iterations. Thereby, the variable and equation residuals r_v^i and r_e^i in the inner iteration i are related to variable and equation scales, v_o and e_o, determined in the outer iteration convergence. The convergence criteria of the inner iteration is then defined such to sastisfy the condition $r_j^i \leq p\sigma_j\epsilon_j$. The right side of the condition denotes a percentage p of the critical residual in outer iteration convergence represented in terms of the variable and equation reduction numbers σ_j and outer tolerances ϵ_j, with $j = v, e$ [Adi08]. The direct solver is more efficient, accurate and stable, though it requires more memory storage than iterative solvers [ZZJ$^+$03]. By using the sparse direct solver, this memory can be efficiently reduced. The sparse solver performs a reordering of the finite element equations while preserving the parsity of the original system matrix. Then, it minimizes the number of fill-ins by performing a symbolic factorization and thus reduces the required time and storage.

7.4 System Integration in *FSI-Sim*

The coupled blood-wall simulation models are integrated in MoDiSim into the component FSI-Sim. FSI-Sim consists of blood and wall functions for generating and performing the simulations. It allows automatic, optimized and individual computations and visualization of blood-wall interaction simulations in patient-specific aortic models at any time. The user-interaction with FSI-Sim is realized through the main interface illustrated in Fig.7.7.

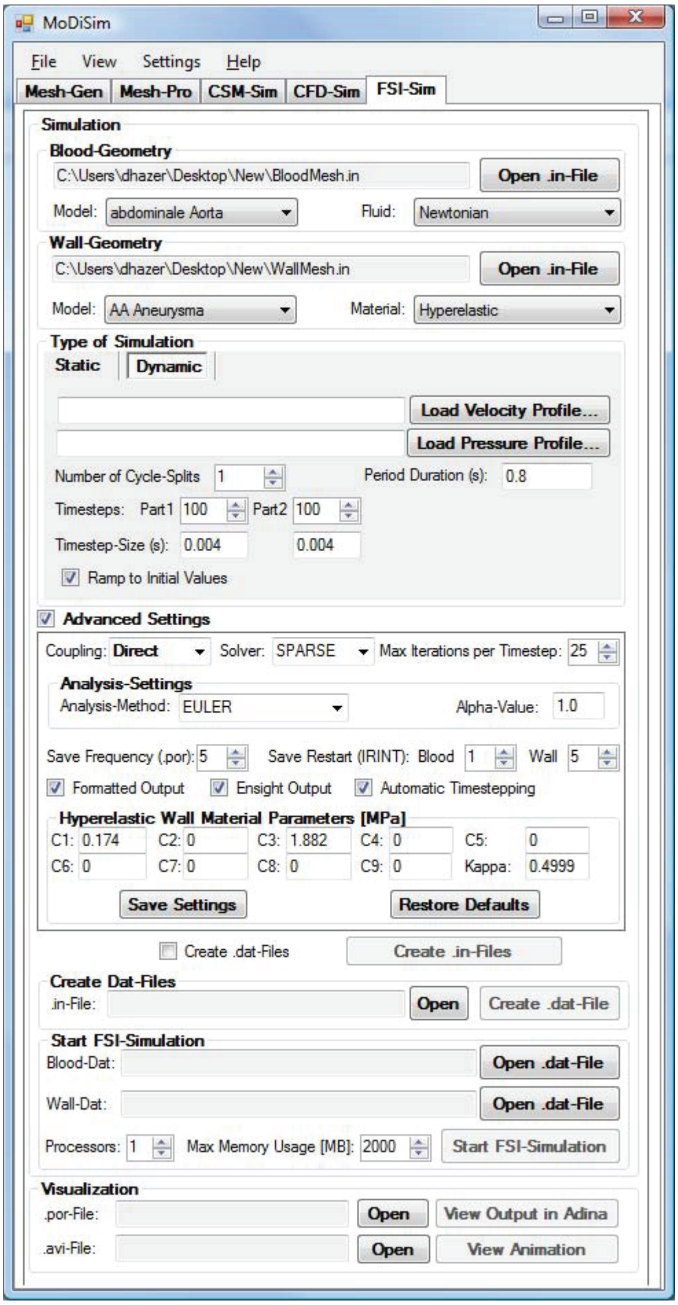
File
View
Settings
Help
Mesh-Gen
Mesh-Pro
CSM-Sim
CFD-Sim
FSI-Sim
Open .in-File
Open .in-File
Static
Dynamic
Load Velocity Profile...
Load Pressure Profile...
Save Settings
Restore Defaults
Create .in-Files
Open
Create .dat-File
Open .dat-File
Open .dat-File
Start FSI-Simulation
Open
View Output in Adina
Open
View Animation

MoDiSim

Simulation

Blood-Geometry

C:\Users\dhazer\Desktop\New\BloodMesh.in

Model: abdominale Aorta
Fluid: Newtonian

Wall-Geometry

C:\Users\dhazer\Desktop\New\WallMesh.in

Model: AA Aneurysma
Material: Hyperelastic

Type of Simulation

Number of Cycle-Splits 1
Period Duration (s): 0.8
Timesteps: Part1 100 Part2 100
Timestep-Size (s): 0.004 0.004
☑ Ramp to Initial Values

☑ Advanced Settings

Coupling: Direct
Solver: SPARSE
Max Iterations per Timestep: 25

Analysis-Settings

Analysis-Method: EULER
Alpha-Value: 1.0

Save Frequency (.por): 5
Save Restart (IRINT): Blood 1 Wall 5
☑ Formatted Output ☑ Ensight Output ☑ Automatic Timestepping

Hyperelastic Wall Material Parameters [MPa]

C1: 0.174 C2: 0 C3: 1.882 C4: 0 C5: 0
C6: 0 C7: 0 C8: 0 C9: 0 Kappa: 0.4999

☐ Create .dat-Files

Create Dat-Files

.in-File:

Start FSI-Simulation

Blood-Dat:
Wall-Dat:
Processors: 1
Max Memory Usage [MB]: 2000

Visualization

.por-File:
.avi-File:

Figure 7.7: User-Interface of the FSI simulation component *FSI-Sim*.

7.4.1 Automation

The automation of the coupled simulations is achieved by integrating the FSI modeling steps for the individual fields into FSI-Sim. These steps are processed by MoDiSim and executed within Adina automatically based on a minimal user interaction through the FSI-Sim user-interface. The most important implemented actions in the FSI-Sim component are sketched in Fig.7.8. These are described below:

- **Generate Simulation Files:**
  The *CreateSimulationInputFiles* method creates first a directory for the entire simulation and in there various subdirectories for each of the required subsimulations (for the static ramp-simulation and for each split-part of the transient simulation). In each of these subdirectories one copy of the *BloodMesh* input file and one copy of the *WallMesh* input file are created. During the processing, the simulation settings are written to these copies.

- **Define Main Settings:**
  The *WriteMasterSection* method generates the corresponding master sections for each of the subsimulations. The master section contains the main simulation settings such as the solvers to be used or the type of the simulation. The definition of the master sections in Adina is different for blood flow and vessel wall simulations and has therefore to be created for each input model apart. For transient (blood) and dynamic (wall) simulations, the *TStart* property for restart options is also adjusted here. Finally, settings defining the type and format of the results output files are determined by the *WritePortholeSection* method.

- **Define Timestpes and Timefunctions:**
  WriteTimestep writes the timesteps for each subsimulation using default values or user-defined inputs given through the FSI-Sim interface. There exist therefore three possible basic constellations: 1) a single static simulation in which the number of timesteps and the timestep size for velocity and pressure are given by the user, 2) a ramp simulation prior a dynamic simulation where the number of timesteps and their size for the ramp to the initial values in the profiles are determined by default values, 3) a dynamic simulation in which the number of timesteps and their size is based on user-defined values. *WriteTimeFunctions* defines in the dynamic case the input time-dependent profiles of the velocity and pressure as single time functions. In the static case, one linear time function for velocity and one for pressure are created. The characteristic points of these functions depend thereby on the defined timestep settings.

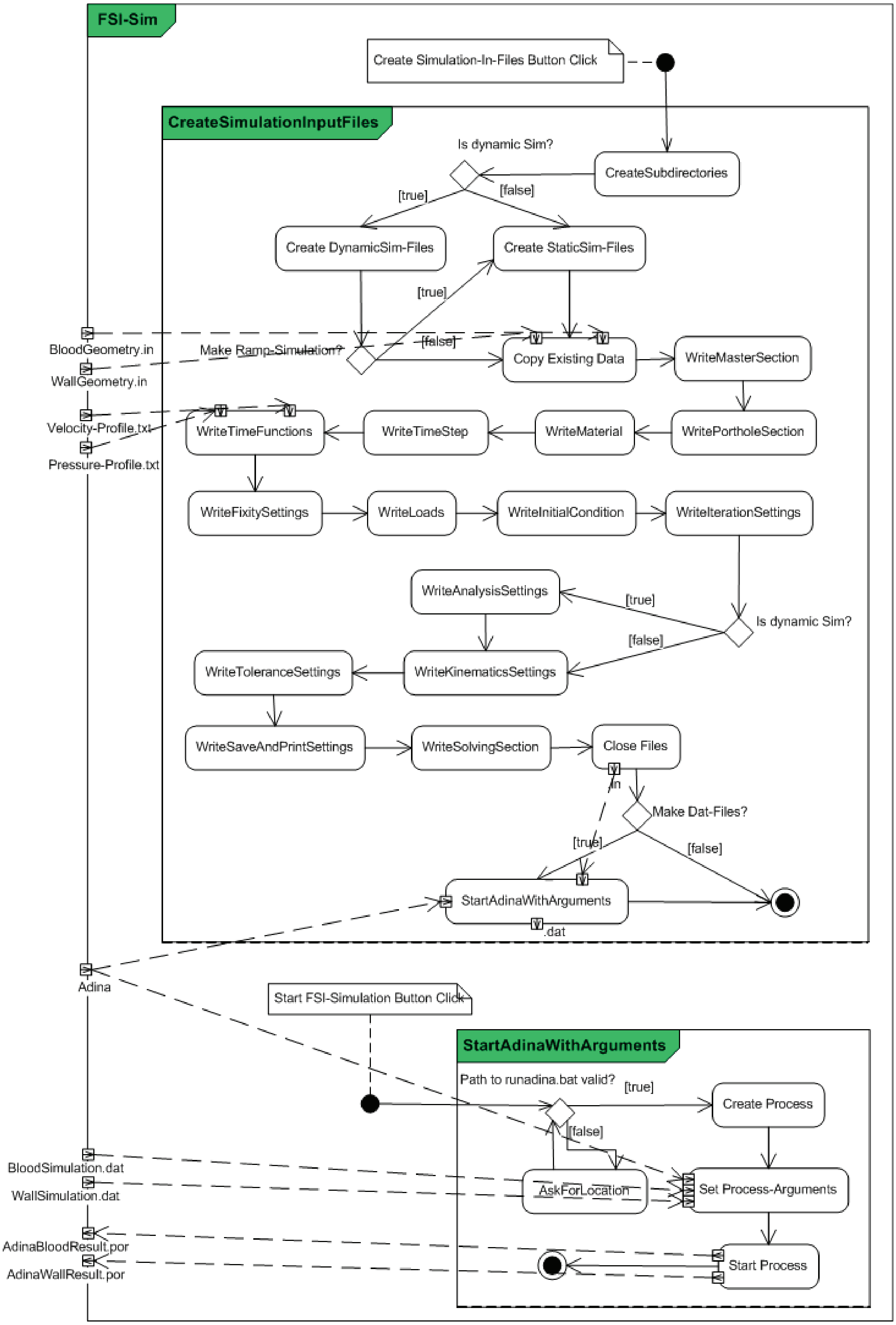
FSI-Sim
Create Simulation-In-Files Button Click
CreateSimulationInputFiles
Is dynamic Sim?
CreateSubdirectories
[true]
[false]
Create DynamicSim-Files
Create StaticSim-Files
[true]
Make Ramp-Simulation?
[false]
Copy Existing Data
WriteMasterSection
BloodGeometry.in
WallGeometry.in
Velocity-Profile.txt
Pressure-Profile.txt
WriteTimeFunctions
WriteTimeStep
WriteMaterial
WritePortholeSection
WriteFixitySettings
WriteLoads
WriteInitialCondition
WriteIterationSettings
WriteAnalysisSettings
[true]
Is dynamic Sim?
[false]
WriteToleranceSettings
WriteKinematicsSettings
WriteSaveAndPrintSettings
WriteSolvingSection
Close Files
.in
Make Dat-Files?
[true]
[false]
StartAdinaWithArguments
.dat
Adina
Start FSI-Simulation Button Click
StartAdinaWithArguments
Path to runadina.bat valid?
[true]
Create Process
[false]
BloodSimulation.dat
WallSimulation.dat
AskForLocation
Set Process-Arguments
AdinaBloodResult.por
AdinaWallResult.por
Start Process

Figure 7.8: Activity diagram of the FSI simulation component *FSI-Sim*.

- **Define Boundary Conditions:**
  WriteFixitySettings writes the constraint boundary condition for the wall simulation. This is defined by fixing the x-, y- and z-coordinates at the inlet and the outlets of the wall domain. *WriteLoads* defines the load boundary conditions in terms of velocity-load for the inlet and pressure-load for the outlets of the blood domain. Thereby, velocity is applied on the nodes in positive z-direction, while pressure is applied as normal traction on the outlets. *WriteInitialCondition* defines the settings of the initial condition for the computations. For all simulations the z-velocity is set to zero within the whole computational domain.

- **Define Material Settings:**
  WriteMaterial defines the compressibility and elastic material properties of the vessel wall domain as well as the compressibility and viscous properties of the blood material. Thereby, all associated parameters are also determined here.

- **Define Solution Approaches:**
  WriteIterationSettings defines the iteration solution method in the simulations. For both the blood and the wall domains, Newton-based methods are used and applied with the necessary parameters. *WriteAnalysisSettings* writes the time-integration approaches for the dynamic simulations. These consist of either the Euler or the Composite method for the blood flow and of the Newmark method for the vessel wall computations. *WriteKinematicsSettings* defines the settings governing the wall kinematics such as large displacement and small strain theories. *WriteToleranceSettings* determines the convergence behavior of the simulations by setting tolerance limits parameters. These are different for static and dynamic simulations and for blood and wall simulations.

- **Define Final Settings:**
  WriteSaveAndPrintSettings writes the settings defining the saving frequency of the results in terms of timestep numbers. Therefore the total timesteps of the particular subsimulation has to be precomputed. *WriteSolvingSection* applies the settings to create the executable files for the simulations. Therefore the filenames with corresponding subdirectory for a particular subsimulation are needed.

- **Start FSI Simulation:**
  For an FSI simulation two executable files are needed, describing the wall and the blood models individually. These files are either created automatically at the end of *CreateSimulationInputFiles* or explicitly by the user in the MoDiSim-UI, in case further processing of the simulation data is still desired.

7.4.2 Optimization

Next, optimization of the automated computations is conducted by extending the integrated models. Consequently, various FSI modeling options are made accessible and depending on the application, the optimal related models are automatically chosen by MoDiSim. The optimization consists of improved models for both the blood and the wall modeling, as described in the individual corresponding chapters. Therefore, only the most important optimization aspects are listed below. These can be directly selected and defined within FSI-Sim.

- Steady-state and dynamic coupled computations of the interaction between the hemodynamics and the wall mechanics are possible.
- Constitutive materials including linear elastic and nonlinear hyperelastic models are integrated for the wall elasticity.
- Further, various polynomial-based models with specific material parameters are implemented for hyperelastic modeling.
- Constitutive behavior of blood viscosity is included by integrating both the Newtonian and the Carreau-based non-Newtonian viscosity models.
- Laminar and $k - \epsilon$-based turbulent modeling are available to simulate the dynamics of the flow.
- Several options for defining the boundary conditions are included, allowing pressure-based, flow-based and DOF constraints conditions. Thereby, the application regions have been appropriately defined in the *Mesh-Pro* component. Also, the interface finite mesh and the moving condition are defined as compatible for both the fluid and the solid models.
- The convergence behavior may be quasi-controlled by adopting various cycle splits and time-stepping options.
- Implicit time integration may be employed based on both the Euler and the Composite discretization schemes.
- Further, the direct sparse and the multigrid iterative linear solvers may be adopted for the fluid and the solid iterations.
- The simulations result can be visualized, providing a realistic insight into the coupled hemodynamics and elastomechanics parameters. Herefore, FSI-Sim includes automatic quantification of various Wall Stresses, deformation, pressure profiles as well as velocity based-pathlines as image sequences for the simulated model.

7.4.3 Individualization

Individual FSI modeling, independent on the vessel region, shape or origin of the aorta is also presented for the Adina-based simulations in FSI-Sim. As a result, thoracic and abdominal, healthy and aneurysmal, human and porcine aortas may be processed. Patient- and region-independent FSI modeling are achieved through the integration of various flow and material constitutive models with appropriate parameters required for performing individual simulations, as described in Chap.5 and Chap.6. Besides the individual geometry, the definition of individual boundary conditions is of great importance for coupled simulations. Therefore, also here, the inlet, outlet and interface conditions may be defined based on physiological pressure and flow data obtained from direct subject-specific measurements. Three individual aortic models have been processed and simulated using FSI-Sim. These are shown in Fig.7.9 and originate from the patient-specific MR-based abdominal aorta (Fig.3.9) and the two 4D-CT-based porcine abdominal aortas (Fig.3.11 and Fig.3.12). Examples of the numerical results are presented in the next section.

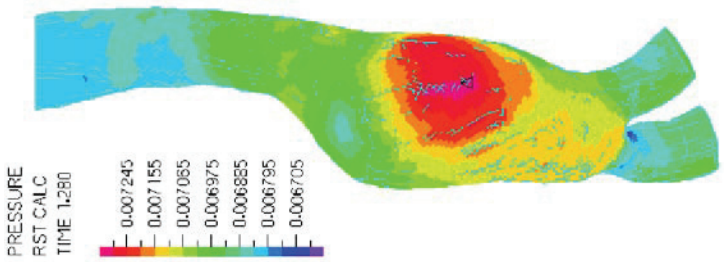

(a) MR-AAA: 3D wall pressure

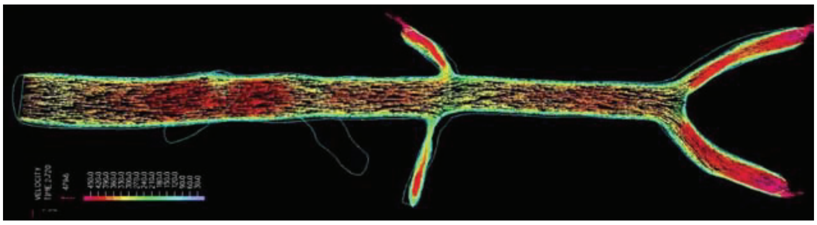

(b) 4D-CT-P2: Velocity vectors within a vertical plane

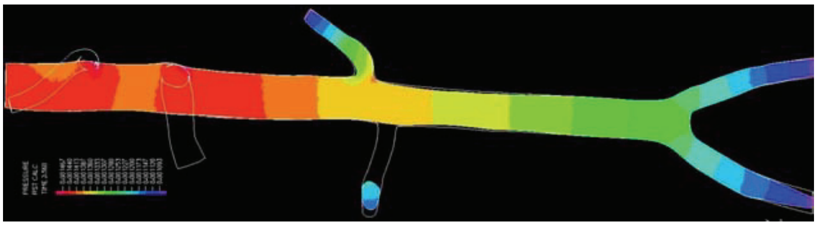

(c) 4D-CT-P3: Pressure contours within a vertical plane

Figure 7.9: FSI simulations with three individual aortic models.

7.5 FSI Simulation Results

Coupled simulation results between the blood flow and the vessel wall were carried out to analyze the physical interaction between the hemodynamics within the blood domain and the elastomechanics along the wall at any time. Some numerical examples of the simulation results of three models are presented below. Compromising between accuracy and computational cost, the simulations were performed using timestep sizes in the order of ts= 0.8 ms to model a cardiac cycle of period T= 0.8 s with the direct coupling scheme.

7.5.1 Coupled vs. Decoupled Results using MR-AAA

In order to evaluate the efficiency of FSI simulations in terms of accuracy, coupled and decoupled simulations were performed and compared. The decoupled computation consists of a CFD simulation followed by a CSM simulation. Thereby, the wall pressure distribution obtained from the CFD is used as wall boundary condition in the CSM. All results are evaluated at the peak systolic time t= 0.28 s. Fig.7.10 shows the velocity magnitudes along a vertical plane for the decoupled CFD (a) and coupled FSI (b) simulations. Fig.7.11 and Fig.7.12 illustrate the 3D wall displacements and stress distributions resulting from the decoupled CSM (a) and coupled FSI (b) simulations.

The velocity contours show similar course in both simulations with slightly higher values found in the decoupled model. More significant is the influence of the coupled approach on the total displacements with maximum values of 5.8 mm for the CSM and 4.5 mm for the FSI computations (including translatory motion). The most significant effect is demonstrated through the wall stress distributions. The decoupled CSM simulation resulted in much higher stresses than the FSI with CSM and FSI peak values equal 1.1 Nmm^{-2} and 0.5 Nmm^{-2}, respectively. These results are in contradiction with previous investigations stating that CSM underestimates the stresses. In fact, our example shows that the primary factor affecting the results is the amplitude of the pressure profile obtained from CFD and applied as boundary condition for CSM. CSM computations utilize a homogeneous profile based on predictions stating that the fluid pressure drop across the aorta is small at 0.1 KPa [WRS$^+$05]. However, the CFD pressure gradients obtained here were higher, which makes a homogeneous assumption inaccurate. Also, the CFD pressure values were much higher than those obtained from the FSI and resulted therefore in higher displacements and wall stress distributions. Consequently, since stresses are the primary indicator for failure of the vessel wall, computations with non-uniform pressure should be adopted for reliable evaluation.

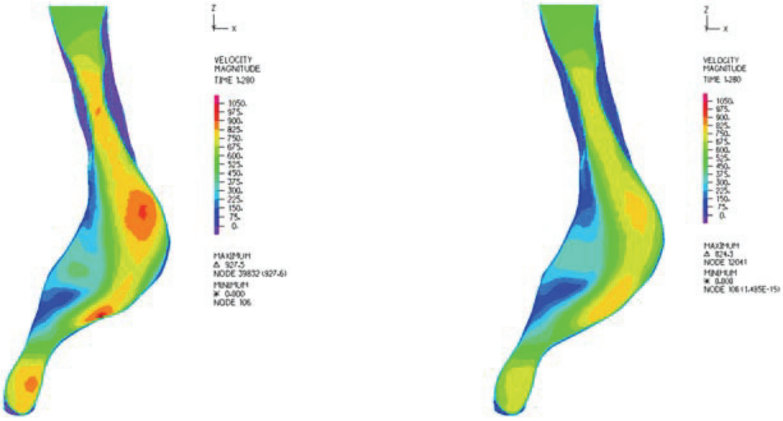
Z
X
VELOCITY MAGNITUDE
TIME 1.280
1050.
975.
900.
825.
750.
675.
600.
525.
450.
375.
300.
225.
150.
75.
0.
MAXIMUM
△ 927.5
NODE 39832 (927.6)
MINIMUM
✱ 0.000
NODE 106
Z
X
VELOCITY MAGNITUDE
TIME 1.280
1050.
975.
900.
825.
750.
675.
600.
525.
450.
375.
300.
225.
150.
75.
0.
MAXIMUM
△ 824.3
NODE 12041
MINIMUM
✱ 0.000
NODE 106 (1.495E-15)

(a) Decoupled (CFD) simulation (b) Coupled (FSI) simulation

Figure 7.10: Velocity magnitudes along a vertical plane from CFD and FSI.

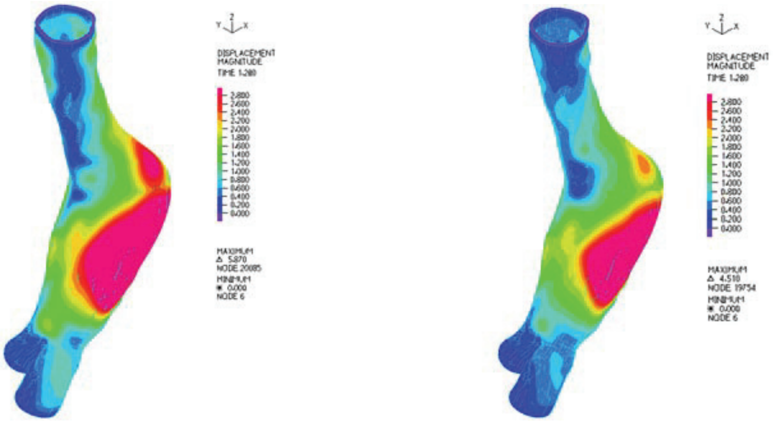
Z
Y
X
DISPLACEMENT MAGNITUDE
TIME 1.280
2.800
2.600
2.400
2.200
2.000
1.800
1.600
1.400
1.200
1.000
0.800
0.600
0.400
0.200
0.000
MAXIMUM
△ 5.870
NODE 20085
MINIMUM
✱ 0.000
NODE 6
Z
Y
X
DISPLACEMENT MAGNITUDE
TIME 1.280
2.800
2.600
2.400
2.200
2.000
1.800
1.600
1.400
1.200
1.000
0.800
0.600
0.400
0.200
0.000
MAXIMUM
△ 4.510
NODE 19754
MINIMUM
✱ 0.000
NODE 6

(a) Decoupled (CSM) simulation (b) Coupled (FSI) simulation

Figure 7.11: 3D displacements of the vessel wall from CSM and FSI.

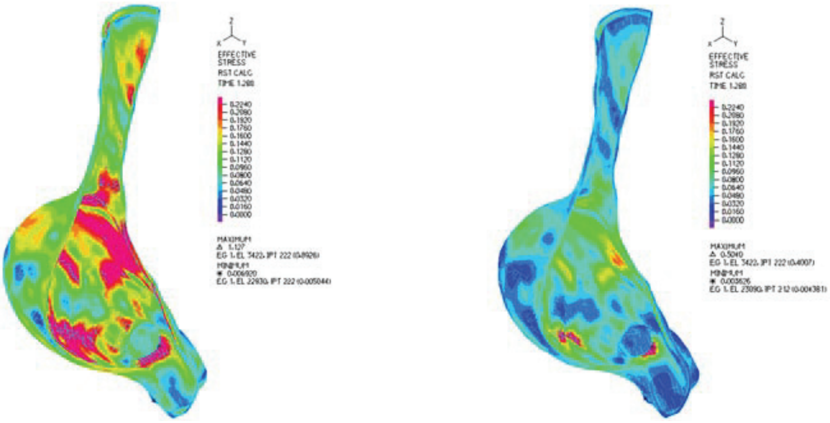
Z
X
Y
EFFECTIVE STRESS
RST CALC
TIME 1.280
0.2240
0.2080
0.1920
0.1760
0.1600
0.1440
0.1280
0.1120
0.0960
0.0800
0.0640
0.0480
0.0320
0.0160
0.0000
MAXIMUM
△ 1.127
EG 1, EL 3422, IPT 222 (0.8926)
MINIMUM
✱ 0.006920
EG 1, EL 22930, IPT 222 (0.005044)
Z
X
Y
EFFECTIVE STRESS
RST CALC
TIME 1.280
0.2240
0.2080
0.1920
0.1760
0.1600
0.1440
0.1280
0.1120
0.0960
0.0800
0.0640
0.0480
0.0320
0.0160
0.0000
MAXIMUM
△ 0.5240
EG 1, EL 3422, IPT 222 (0.4007)
MINIMUM
✱ 0.003626
EG 1, EL 23090, IPT 212 (0.004381)

(a) Decoupled (CSM) simulation (b) Coupled (FSI) simulation

Figure 7.12: 3D stress distributions along the vessel wall from CSM and FSI.

7.5.2 FSI from in-vivo Experiment using 4D-CT-P2

The 4D-CT-P2 abdominal model, obtained from a dynamic CT-scan and from in-vivo measurements performed on a porcine aorta was simulated to quantify and validate the elastomechanics and the hemodynamics over several cardiac cycles. Measured velocity and pressure profiles above the celiac artery were used for the inlet and outlets boundary conditions, respectively. Fig.7.13, Fig.7.14 and Fig.7.15 show the cross-sectional wall stress and strain distributions, the 3D wall pressure contours and recirculation zones around the celiac artery, respectively.

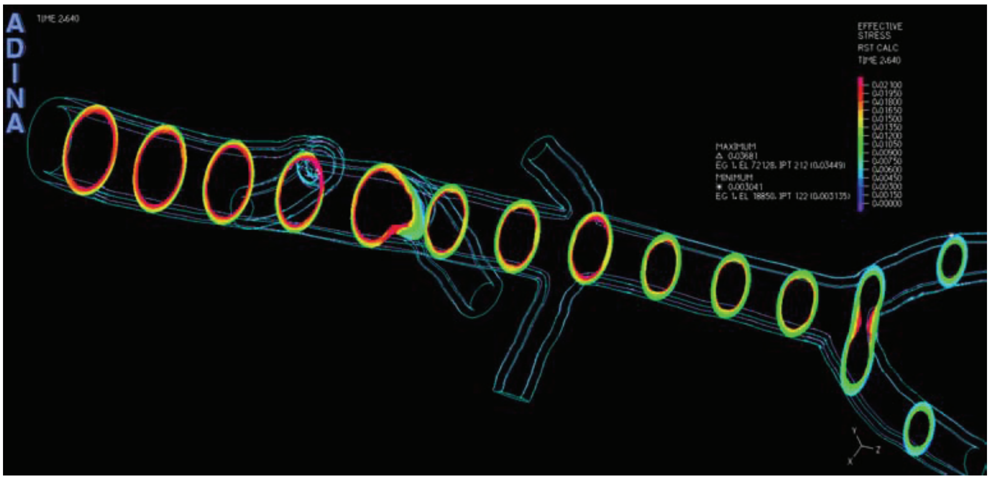

(a) Cross-sectional wall stress (t= 0.24 s)

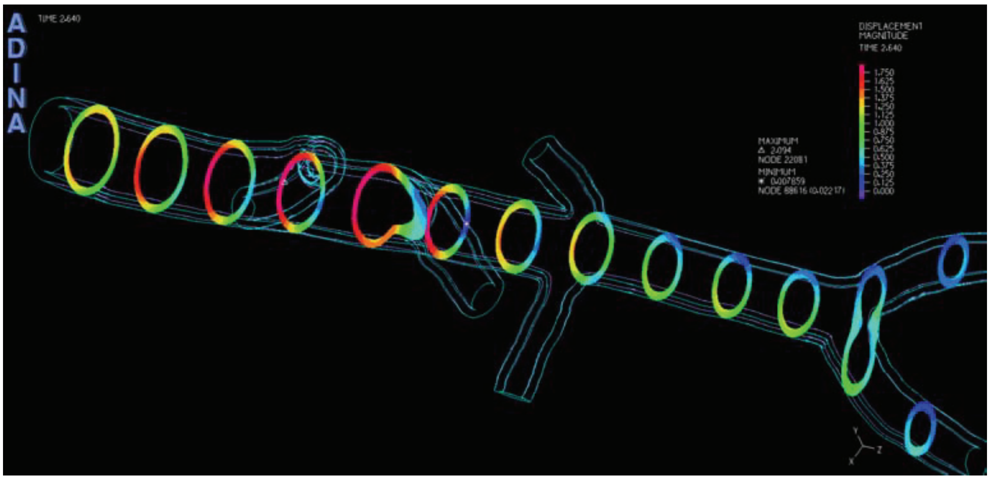

(b) Cross-sectional wall strain (t= 0.24 s)

Figure 7.13: Peak stress and strain distributions across the wall.

The quantification of the wall deformation and of the blood pressure and flow profiles used for the validation of the FSI simulations will be presented in details in Chap.8.

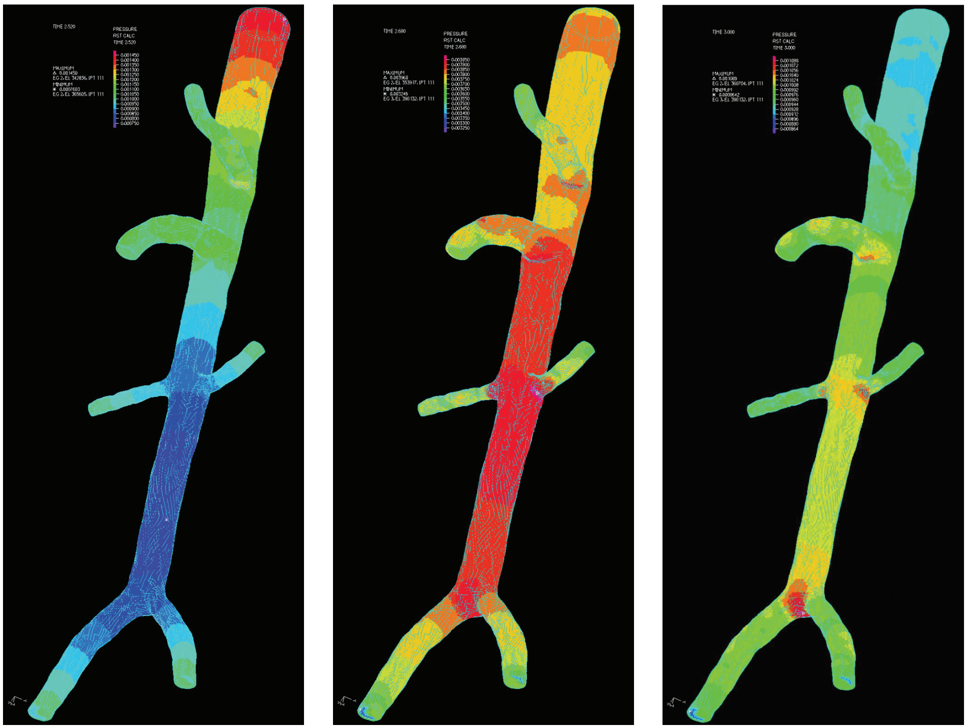

(a) t= 0.12 s (b) t= 0.28 s (c) t= 0.60 s

Figure 7.14: 3D wall pressure contours.

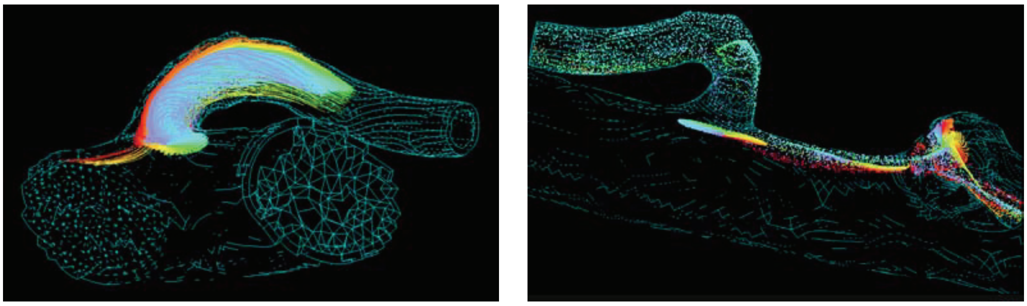

(a) Vortices inside the celiac (b) Particle trace from the celiac

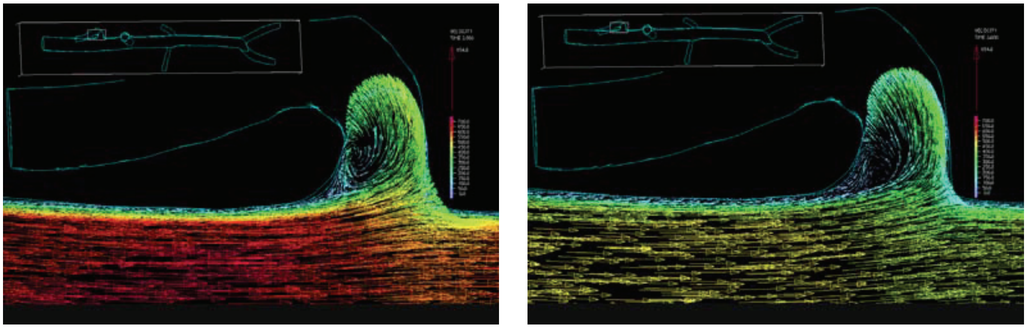

(c) Velocity vectors (t= 0.16 s) (d) Velocity vectors (t= 0.20 s)

Figure 7.15: Turbulence and recirculation zones around the celiac artery.

7.5.3 FSI from in-vivo Experiment using 4D-CT-P3

The 4D-CT-P3 porcine model is obtained in a similar way as the 4D-CT-P2 model and is also used for the validation of the FSI simulations. The inlet and outlets boundary conditions are also defined from velocity and pressure measurements, respectively, obtained above the celiac artery. A detailed evaluation of the results based on the quantification of the wall deformation and the pressure and flow profiles is presented in Chap.8. Fig.7.16, Fig.7.17 and Fig.7.18 show the 3D wall stress distribution, the pathlines injected from the inlet and the velocity vectors at the aortic bifurcation, respectively.

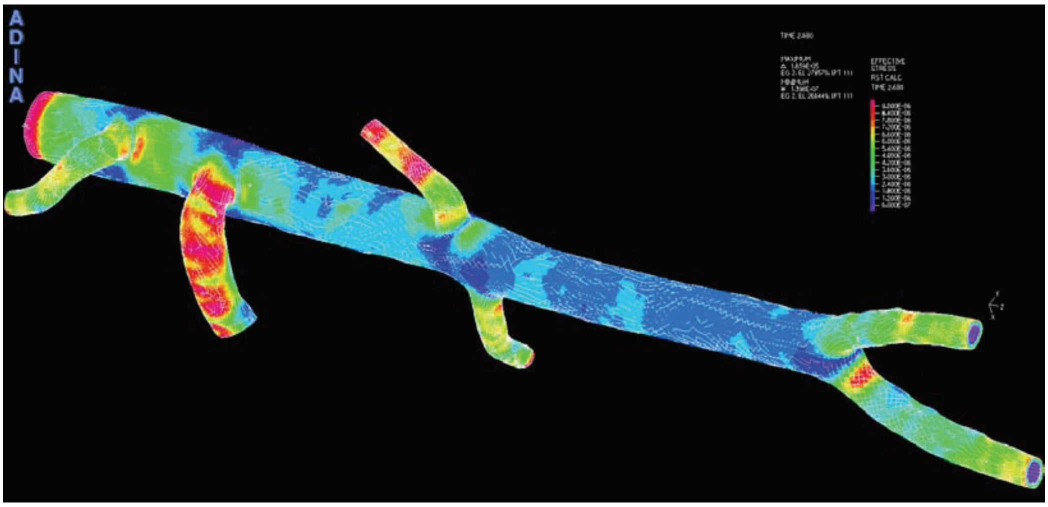

(a) Systolic wall stress distribution at t= 0.28 s

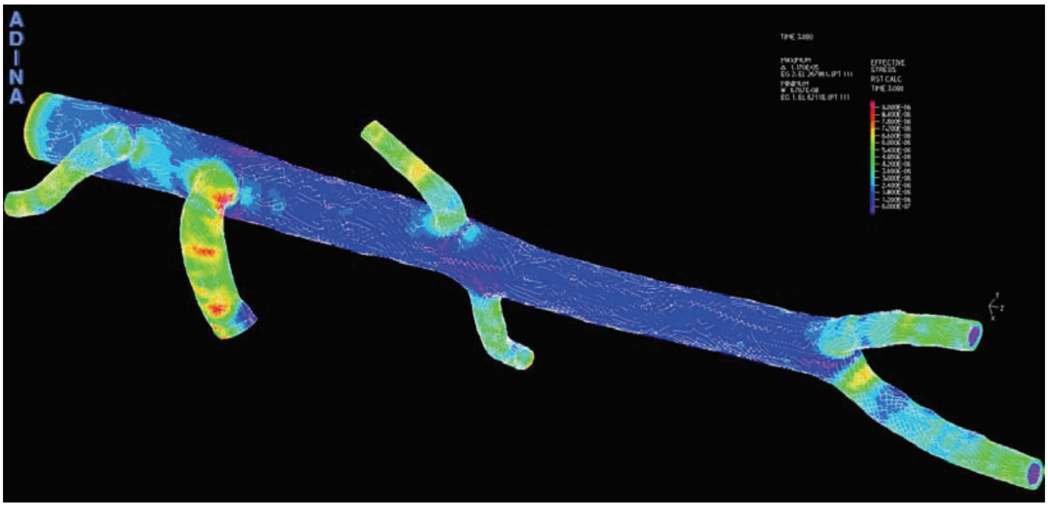

(b) Diastolic wall stress distribution at t= 0.68 s

Figure 7.16: Effective 3D stress distribution along the wall.

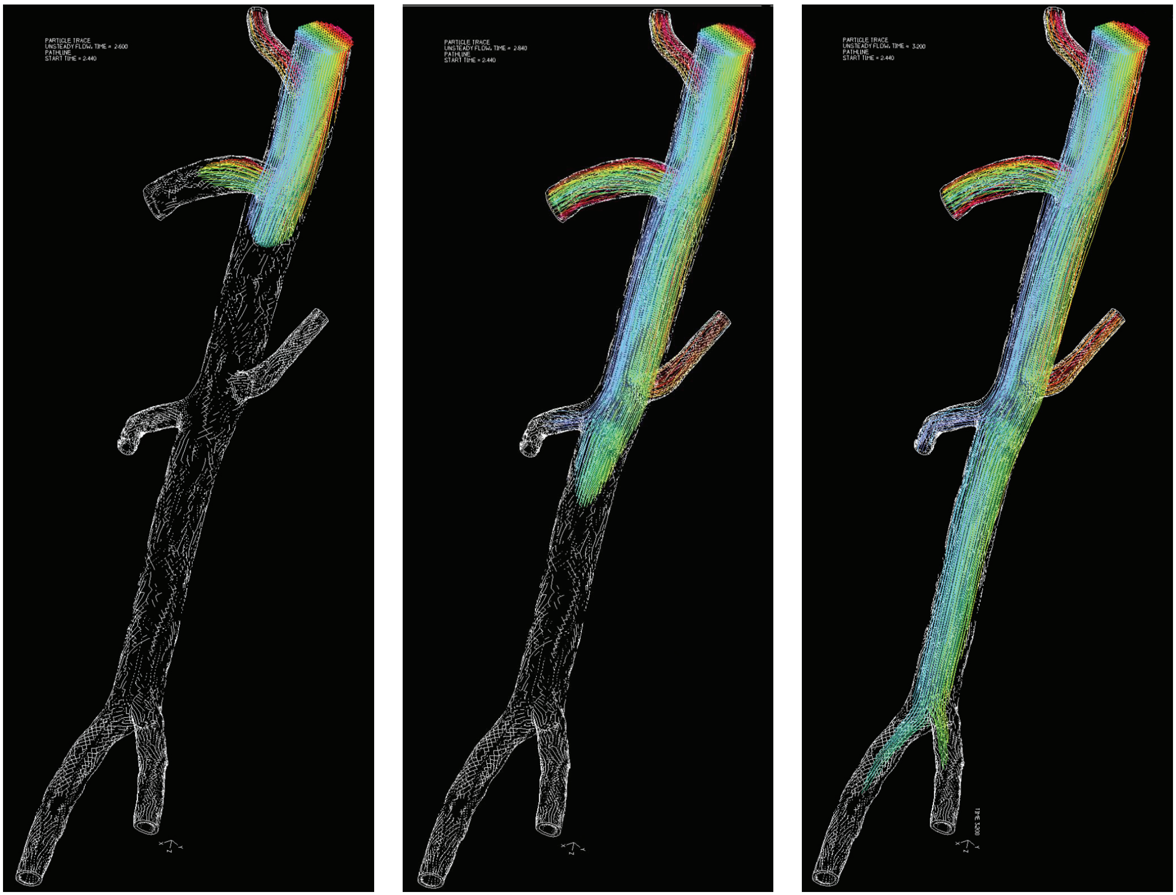
PARTICLE TRACE
UNSTEADY FLOW, TIME = 2.600
PATHLINE
START TIME = 2.440
PARTICLE TRACE
UNSTEADY FLOW, TIME = 2.840
PATHLINE
START TIME = 2.440
PARTICLE TRACE
UNSTEADY FLOW, TIME = 3.200
PATHLINE
START TIME = 2.440

(a) after 0.20 s (b) after 0.44 s (c) after 0.80 s

Figure 7.17: 3D pathlines injected from the inlet.

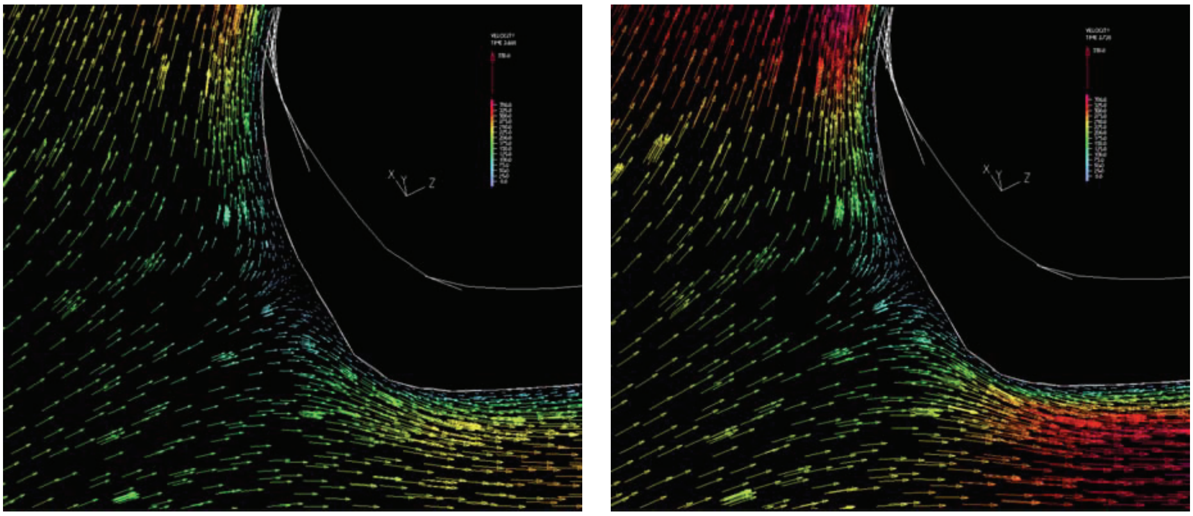

(a) t= 0.20 s (b) t= 0.32 s

Figure 7.18: Velocity vectors at the aortic bifurcation.

7.6 Summary

In summary, this chapter describes computational modeling and implementation of the blood-wall interaction within patient-specific aortic vessels. The mutual physical interaction between the blood flow and the vessel wall along the cardiac cycle is the primary reasons why FSI simulations are necessary for real modeling. This is why this part was indeed included in this work besides the separate blood flow and vessel wall modelings. First, the main aspects and requirements concerning the field of Fluid-Structure Interaction were presented. These include general modeling definitions, coupling approaches and solution techniques. The explanation of these aspects is based on the knowledge of the physical fundamentals governing the blood flow and the vessel wall as well as the mathematical fundamentals necessary for the derivation of FEM-based solutions. Then, the models applied to perform the FSI simulations using the developed workflow for patient-specific modeling are presented. Next, the integration of the blood-wall interaction simulation steps into the FSI-Sim component of the MoDiSim system was described. Thereby, the automation of the simulations, the optimization of the models as well as the individualization of the computations were presented. Finally, some examples from the FSI simulation results obtained from three individual image-based models are shown at the end of this chapter.

Chapter 8

Experimental Validation

8.1 Introduction

An experimental validation is necessary for the evaluation and the clinical implementation of computational systems [KHK^{+}07]. Based on predictions originating from validated models, individual biomechanical analysis can be conducted providing a reliable tool to understand the underlying biomechanics of vascular pathologies. In the present chapter, we implement in-vivo morphological and physiological data acquired from experiments performed on porcine abdominal aortas to:

1. Generate computational models from in-vivo data to simulate the biomechanics of the vessels.
2. Validate the simulations by quantifying and comparing the results with the experimental data.
3. Evaluate the efficiency of fully coupled simulations compared to decoupled simulations.

All experiments have been performed at the University Hospital of Heidelberg, Department of Diagnostic Radiology within the medical thesis of cand. med. M. Kostrzewa under the supervision of Prof G.M. Richter. The generation of the computational models has been conducted during a research internship at the Carnegie Mellon University (CMU) in Pittsburgh, PA, under the supervision of Prof E.A. Finol at the Biomedical Engineering Department, Vascular Biomechanics and Biofluids Laboratory. While the processing and the evaluation of the simulations have been conducted at the University of Karlsruhe, Institute of Anthropomatics, chair Prof R. Dillmann.

8.2 Experimental Setting and Data

For the validation of the simulations, an experimental methodology has been developed and implemented in [Kos09]. In-vivo experiments were conducted on the 25 kg minipigs 4D-CT-P1 (Fig.3.10), 4D-CT-P2 (Fig.3.11) and 4D-CT-P3 (Fig.3.12), with the objective of acquiring morphological and physiological data required for executing and evaluating the simulations. The data consist of 4D high-resolution, ECG-triggered, dual source CT images, in-vivo measured catheter-based pressure and ultrasound-based velocity profiles. The setting of the experimental environment in the angiography room is shown in Fig.8.1.

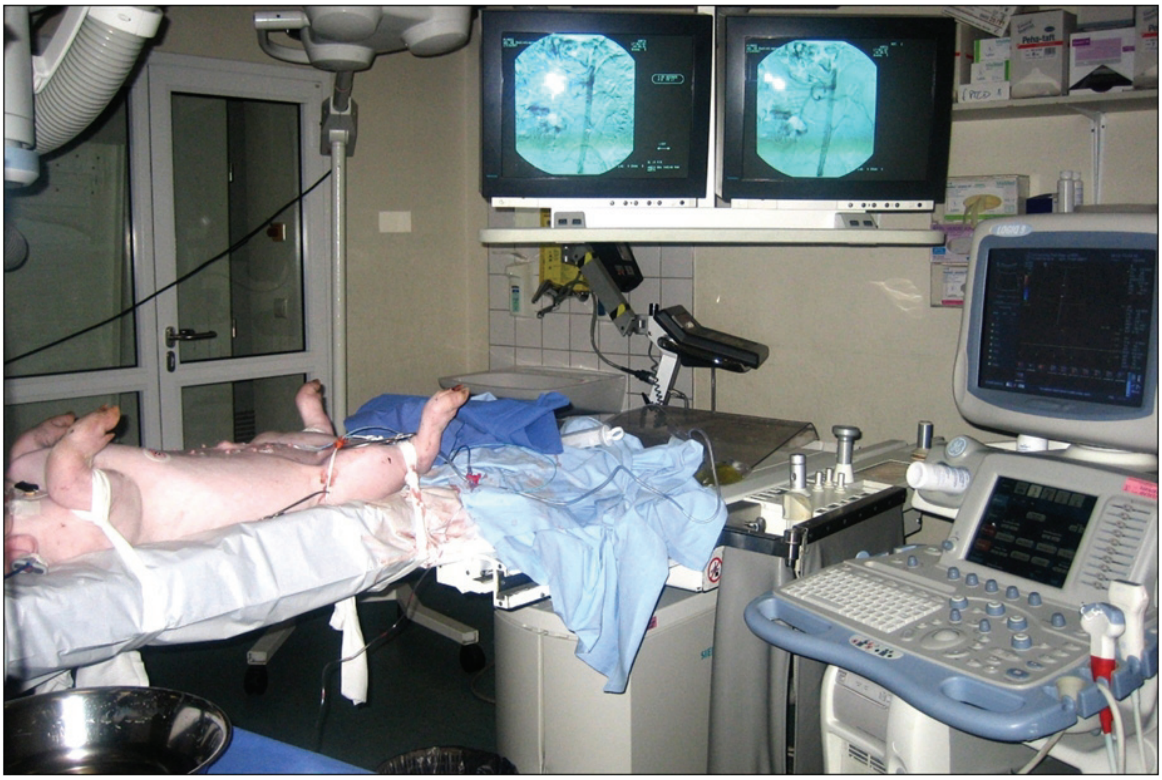

Figure 8.1: Experimental setup in the angiography room.

Furthermore, models 4D-CT-P2 and 4D-CT-P3 have been subject to an infrarenal stent implantation with different designs, thus all measurements are available pre- and post-stent implantation. In this work, only pre-stent data are adapted for the validation of the simulations. Details on all experiments and protocols performed are described in [Kos09]. The experiments workflow is illustrated in Fig.8.2.

(a) Dynamic CT (b) Artery preparation

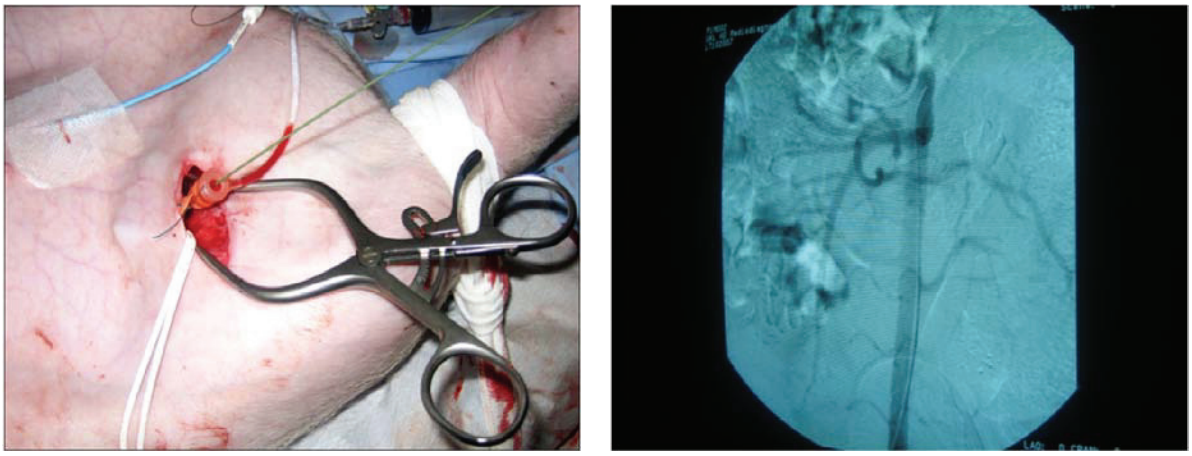

(c) Gate placement (d) Angiographic control

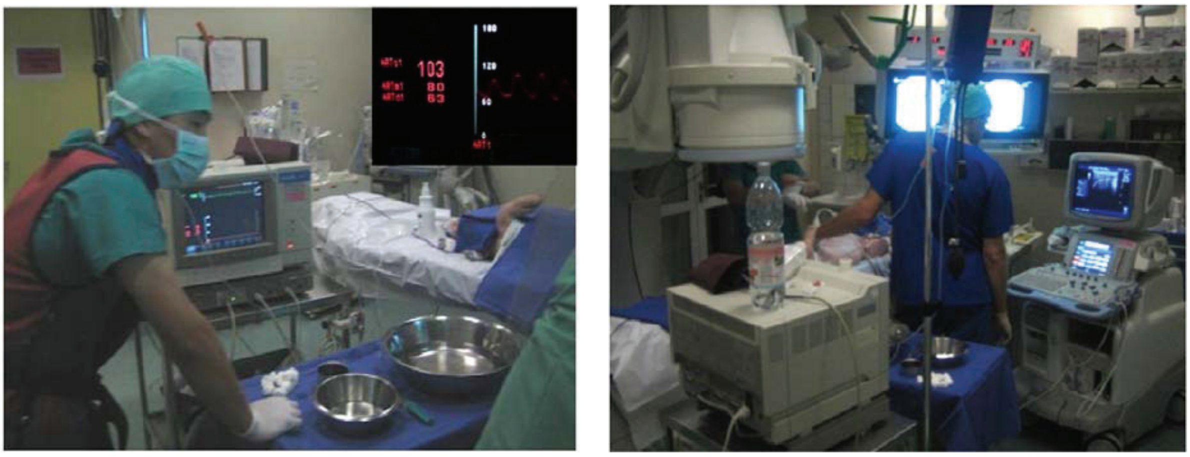

(e) In-vivo pressure measurements (f) Ultrasound flow measurements

Figure 8.2: Experimental validation: Workflow.

8.2.1 Dynamic 4D-CT with Contrast Medium

The dynamic (4D) CT image datasets provide the 4D geometry of the aortic models. The 4D-CT images were acquired using the dual source CT by Siemens, Somatom Definition (Fig.8.2.a), allowing the reconstruction of highly accurate 3D vessel models at various times. The CT images were ECG-triggered and reconstructed with a slice thickness of 0.9 mm for 4D-CT-P1 and 4D-CT-P2 and of 1 mm for 4D-CT-P3. The 2D image size, pixel size and resolution of the individual three models have been described in Tab.3.1. Further, the images were acquired at 5 % intervals yielding 21 phases in the cardiac cycle with periods equal T= 0.8 s. While only one -the diastolic- phase is needed to reconstruct the geometry, the other 20 phases are used to compute the change in the geometry over time. These changes can be compared to the strain fields obtained from the numerical simulations and hence used for the validation of the vessel wall computations. Fig.8.3 shows one transversal cross-section taken at various times with the aorta marked in pink.

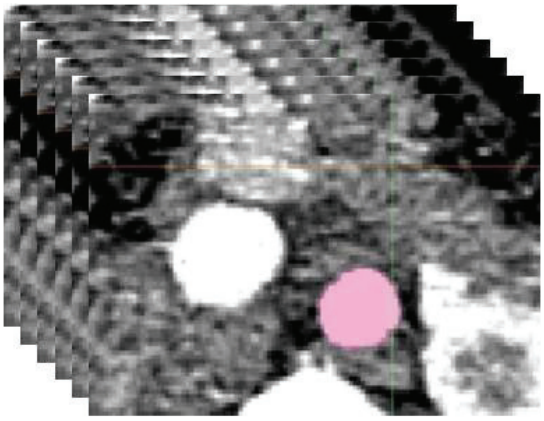

Figure 8.3: Dynamic CT images.

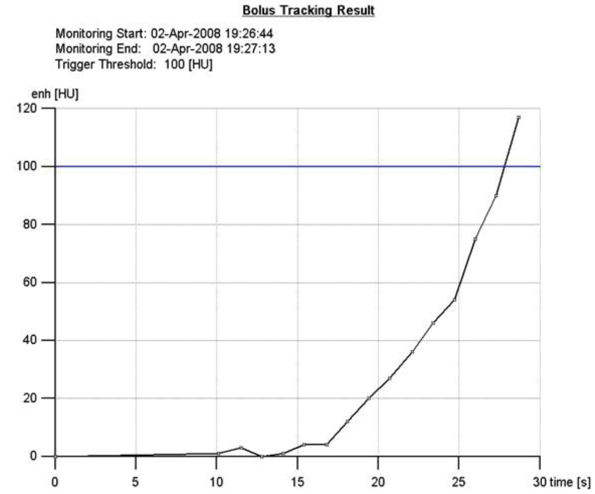

Figure 8.4: Bolus track [Kos09].

The dynamic CT was performed under respiratory arrest in order to avoid artifacts due to breathing motion. Further, for a better detection of the aorta, 50 ml contrast medium (Imeron 400, Byk Gulden, ultravist 370, shering) followed by 50 ml NaCl-Bolus was injected and monitored. Through repeated 1-slice-scan at the level of the *H. aortae*, the contrast enhancement could be observed over time. At a contrasting higher than 100 HU, the triggering of the CT data was automatically started, as illustrated in Fig.8.4 [Kos09].

8.2.2 Catheter-based in-vivo Pressure Measurements

Under the guidance of a Polystar Top angiography system (Fig.8.2.d), a pressure probe was introduced into the abdominal aorta through a gate (Fig.8.2.c) placed in the femoral artery after its preparation (Fig.8.2.b). Pressure profiles including several cycles were then generated by invasive measurements (Fig.8.2.e) 2 cm proximal to the celiac trunk (TC) for all three models and 1 cm proximal to the aortic bifurcation (AB) for 4D-CT-P2 and 4D-CT-P3. Positions TC and AB are shown in Fig.8.8. The measured pressure profiles are used as parameters for the boundary conditions as well as for the validation of the FSI simulations previously described in Sec.7.5.2 and Sec.7.5.3.

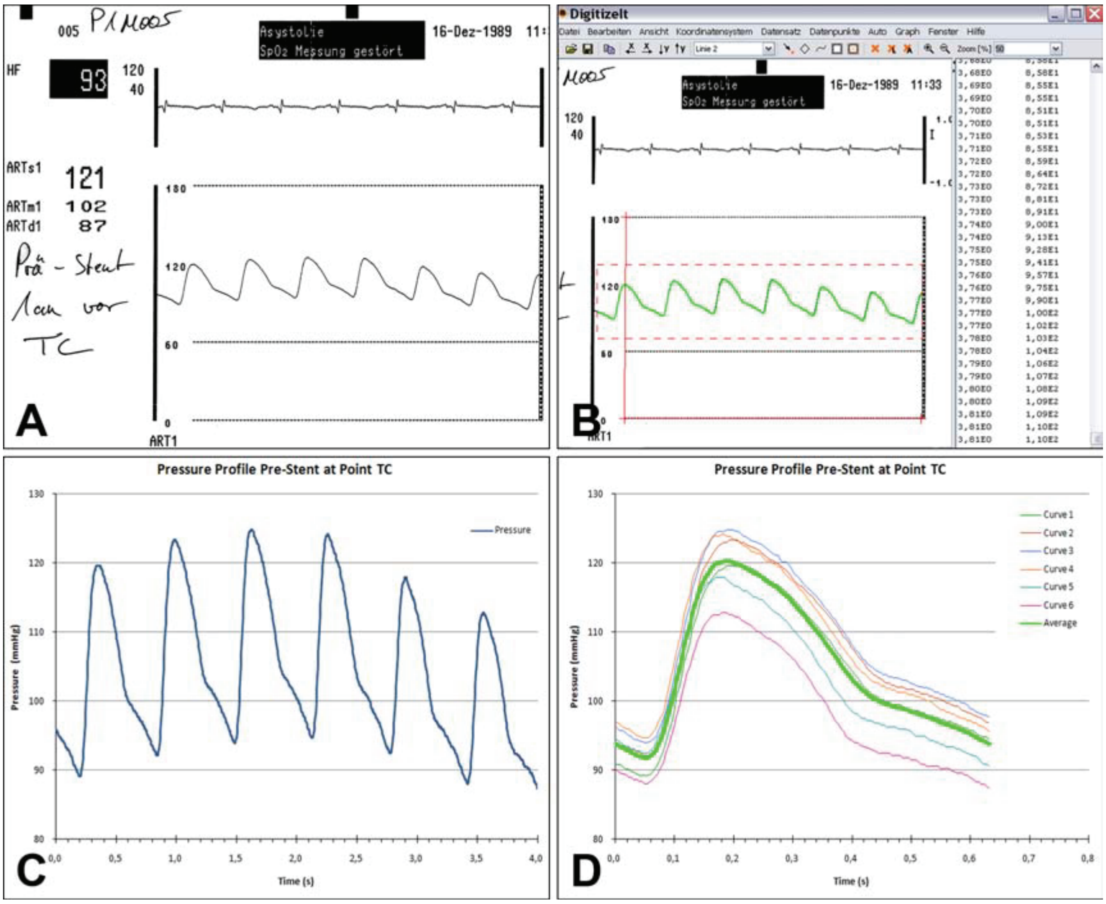

```
3,68E0      8,58E1
3,69E0      8,55E1
3,69E0      8,55E1
3,70E0      8,51E1
3,70E0      8,51E1
3,71E0      8,53E1
3,71E0      8,55E1
3,72E0      8,59E1
3,72E0      8,64E1
3,73E0      8,72E1
3,73E0      8,81E1
3,73E0      8,91E1
3,74E0      9,00E1
3,74E0      9,13E1
3,75E0      9,28E1
3,75E0      9,41E1
3,76E0      9,57E1
3,76E0      9,75E1
3,77E0      9,90E1
3,77E0      1,00E2
3,77E0      1,02E2
3,78E0      1,03E2
3,78E0      1,04E2
3,79E0      1,06E2
3,79E0      1,07E2
3,80E0      1,08E2
3,80E0      1,09E2
3,81E0      1,09E2
3,81E0      1,10E2
3,81E0      1,10E2
```

Figure 8.5: Digitization process of the pressure measurements [Kos09].

Since there was no digital output and in order to obtain the measured profiles in a digital X-Y form, the obtained pressure curves were first printed from the monitor to *thermo-sensitiv* paper and the images were scanned (A). Using the software DigitizeIt, the curves were digitized by giving the X- and Y- scale values (B) and plotted (C). The so resulting pressure curves include about 920 data points and about 5 cardiac cycles from which an average profile was generated for each measurement (D) [Kos09].

8.2.3 Ultrasound-based Flow Measurements

Following the invasive pressure measurements, ultrasound-based measurements were performed using a General Electric Logiq 9 device to additionally obtain individual flow information (Fig.8.2.f). The measurements were acquired at the same TC and AB positions shown in Fig.8.8, where the pressure measurements were acquired, that is, 2 cm proximal to the celiac trunk and 1 cm proximal to the aortic bifurcation. The measured flow profiles are used as additional parameters for the boundary conditions as well as for the validation of the FSI simulations previously described in Sec.7.5.2 and Sec.7.5.3.

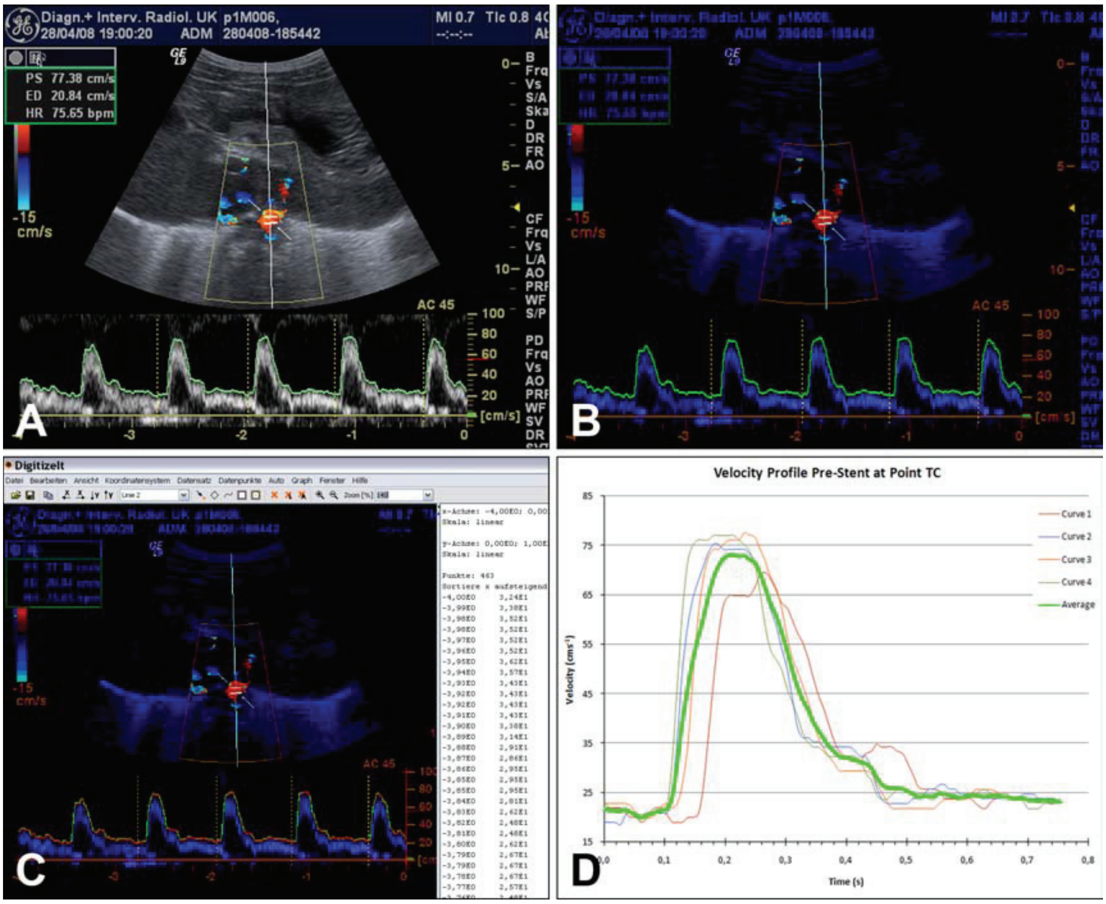
Diagn.+ Interv. Radiol. UK p1M006,
28/04/08 19:00:20 ADM 280408-185442
MI 0.7 TIc 0.8
PS 77.38 cm/s
ED 20.84 cm/s
HR 75.65 bpm
-15 cm/s
AC 45
100
80
60
40
20
[cm/s]
-3
-2
-1
0
A
B
C
DigitizeIt
D
Velocity Profile Pre-Stent at Point TC
Curve 1
Curve 2
Curve 3
Curve 4
Average
Velocity (cms⁻¹)
85
75
65
55
45
35
25
15
0,0
0,1
0,2
0,3
0,4
0,5
0,6
0,7
0,8
Time (s)

Figure 8.6: Digitization process of the flow measurements [Kos09].

Also here, the digitization of the flow data presented a problem, since the ultrasound device did not allow a data point export. Fig.8.6 illustrates the flow digitization process as adopted by [Kos09]. Thereby, the data were first exported as images (A). Contrast enhancement was then applied by adopting various image processing filters using Adobe Photoshop (B) based on which the profiles could be digitized in DigitizeIt (C). The resulting flow curves consist of about 460 data points and about 5 cardiac cycles from which an average profile was generated for each measurement (D).

8.3 Simulations and Evaluation Approach

Based on the experiments, individual biomechanical simulations have been performed on the three models and the computations were evaluated for comparison with the acquired experimental data. FSI simulations are computationally much more expensive compared to decoupled simulations. In order to evaluate the efficiency of these approaches in terms of accuracy, two kinds of simulations were performed:

- CSM as a decoupled approach on 4D-CT-P1 as described in Chap.5.
- Fully coupled FSI simulations on 4D-CT-P2 and 4D-CT-P3 as described in Chap.7.

The segmented 3D geometrical models of 4D-CT-P1, 4D-CT-P2 and 4D-CT-P3 are illustrated in Fig.3.10, Fig.3.11 and Fig.3.11, respectively and the corresponding simulation results were presented in Sec.5.7 and Sec.7.5. In the following, the results of 4D-CT-P1 are used to evaluate the wall deformation obtained from CSM simulations, while the results of 4D-CT-P2 and 4D-CT-P3 are used for the evaluation of FSI simulations in terms of wall deformation as well as pressure and flow computations.

8.3.1 Wall Deformation Simulations

For the evaluation of the wall deformation, the following approach is adopted:

Identification of the cross-sections:

For the validation of the wall deformation in 4D-CT-P1, 5 cross-sections were chosen including 2 suprarenal (Z1= 33.4 mm and Z2= 51.4 mm) and 3 infrarenal (Z3= 100.0 mm, Z4= 113.5 mm and Z5= 127.9 mm) datasets as shown in Fig.8.7. Thereby, the reference origin with zero coordinates was defined at the centre of the inlet cross-section. On the other hand, since 4D-CT-P2 and 4D-CT-P3 were subject to a stent implantation, the location of the cross-sections was chosen related to the position of the implanted stent as shown in Fig.8.8.a on the example of 4D-CT-P2. These include:

- the suprarenal SR cross-section located at mid-distance between the T. coeliacus and the Aa. renales,
- the infrarenal IR cross-section located directly above the stent,
- the mid-stent MS cross-section located at mid-distance of the stent, and
- the cross-section AB located 1 cm proximal to the aortic bifurcation

Isolation of the cross-sections:

The isolation of the above listed cross-sections from the complete dynamic CT dataset was performed based on the identification of the slice position in a transversal view. For 4D-CT-P2 and 4D-CT-P3, the slice positions were first identified in the post-stent datasets and the same locations were assigned to the pre-stent images as shown in Fig.8.8.b. Finally, the corresponding slice position as saved in the Dicom header of the CT images was used to extract the same cross-sections in the computational models as illustrated in Fig.8.8.c. Thereby, the clipped geometrical part at the inlet and outlet boundaries of the aorta obtained from processing the geometrical models as described in Sec.3.2 had to be taken into account. Therefore, the clipped geometry size was substracted from the original geometry while calculating the exact cross-sectional positions in the simulated models.

Evaluation Times:

The dynamic CT measurements were performed over the whole cardiac cycle (100 %) in 5 % steps. As a result, each cross-sectional set was composed of 21 images allowing the evaluation at 21 different times. With a period T= 0.80 s for all three models, the evaluation times corresponding to 0.04 s timesteps were t= 0.00 s, 0.04 s, . . . , 0.76 s, 0.80 s.

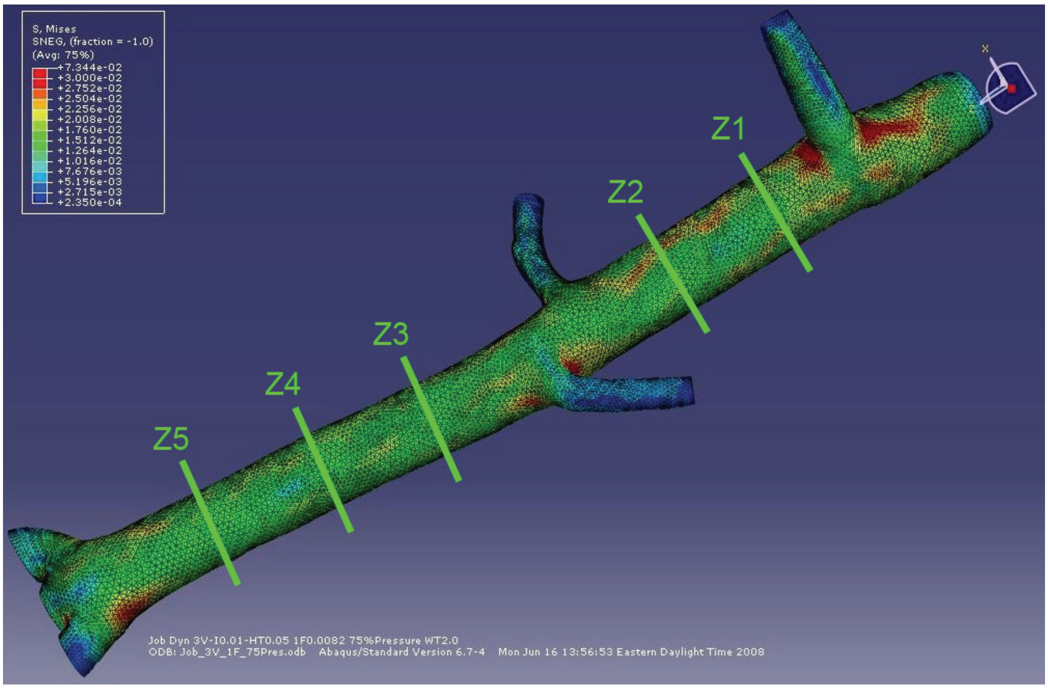
S, Mises
SNEG, (fraction = -1.0)
(Avg: 75%)
+7.344e-02
+3.000e-02
+2.752e-02
+2.504e-02
+2.256e-02
+2.008e-02
+1.760e-02
+1.512e-02
+1.264e-02
+1.016e-02
+7.676e-03
+5.196e-03
+2.715e-03
+2.350e-04
Z1
Z2
Z3
Z4
Z5
Job Dyn 3V-I0.01-HT0.05 1F0.0082 75%Pressure WT2.0
ODB: Job_3V_1F_75Pres.odb Abaqus/Standard Version 6.7-4 Mon Jun 16 13:56:53 Eastern Daylight Time 2008

Figure 8.7: Cross-sections used to evaluate the wall deformation in model 4D-CT-P1 based on CSM simulations.

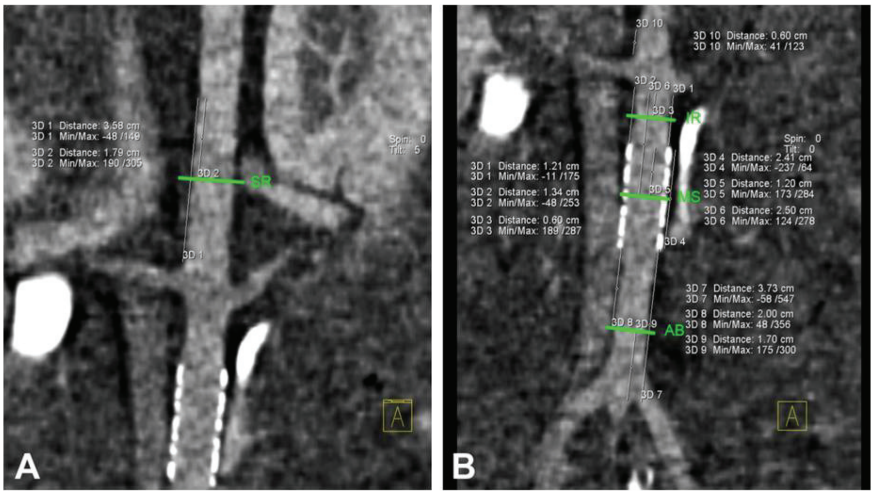
3D 1 Distance: 3.58 cm
3D 1 Min/Max: -48 /149
3D 2 Distance: 1.79 cm
3D 2 Min/Max: 190 /305
3D 2
SR
3D 1
Spin: 0
Tilt: 5
A
A
3D 10
3D 10 Distance: 0.60 cm
3D 10 Min/Max: 41 /123
3D 1 Distance: 1.21 cm
3D 1 Min/Max: -11 /175
3D 2 Distance: 1.34 cm
3D 2 Min/Max: -48 /253
3D 3 Distance: 0.60 cm
3D 3 Min/Max: 189 /287
IR
MS
Spin: 0
Tilt: 0
3D 4 Distance: 2.41 cm
3D 4 Min/Max: -237 /64
3D 5 Distance: 1.20 cm
3D 5 Min/Max: 173 /284
3D 6 Distance: 2.50 cm
3D 6 Min/Max: 124 /278
3D 7 Distance: 3.73 cm
3D 7 Min/Max: -58 /547
3D 8 Distance: 2.00 cm
3D 8 Min/Max: 48 /356
3D 9 Distance: 1.70 cm
3D 9 Min/Max: 175 /300
AB
3D 7
A
B

(a) Dynamic CT post-stent [Kos09]

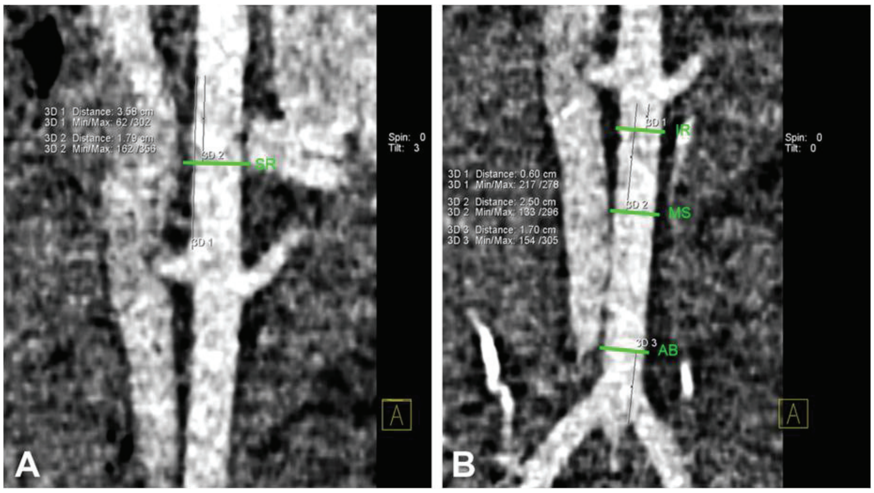
3D 1 Distance: 3.58 cm
3D 1 Min/Max: 62 /302
3D 2 Distance: 1.79 cm
3D 2 Min/Max: 162 /366
3D 2
SR
3D 1
Spin: 0
Tilt: 3
A
A
3D 1
IR
3D 1 Distance: 0.60 cm
3D 1 Min/Max: 217 /278
3D 2 Distance: 2.50 cm
3D 2 Min/Max: 133 /296
3D 3 Distance: 1.70 cm
3D 3 Min/Max: 154 /305
3D 2
MS
3D 3
AB
Spin: 0
Tilt: 0
A
B

(b) Dynamic CT pre-stent [Kos09]

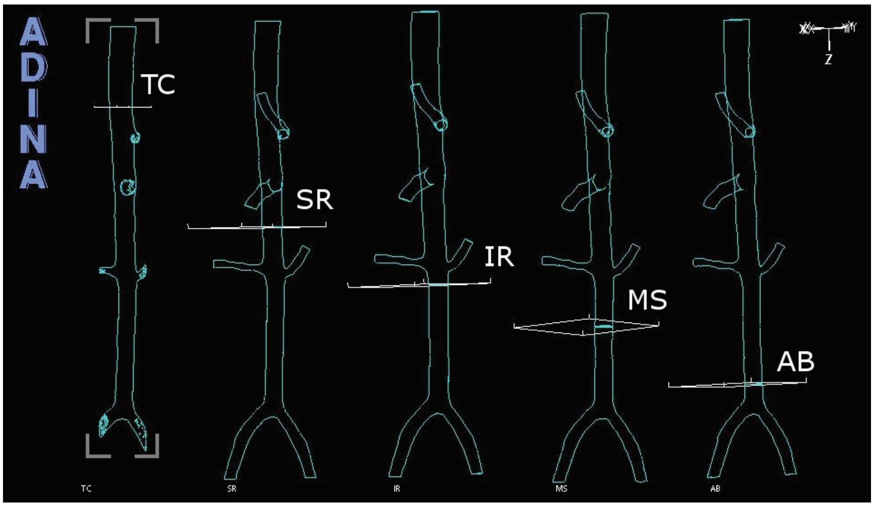
ADINA
TC
SR
IR
MS
AB
Z
TC
SR
IR
MS
AB

(c) Corresponding cross-sections in the computational model

Figure 8.8: Cross-sections used to evaluate the wall deformation (SR, IR, MS, AB) and the pressure and flow computations (TC, AB) for models 4D-CT-P2 and 4D-CT-P3 based on FSI simulations.

Quantification of the Deformation:

At the selected cross-section locations represented by Z1, Z2, Z3, Z4 and Z5 for 4D-CT-P1 and by SR, IR, MS and AB for 4D-CT-P2 and 4D-CT-P3, the deformation of the aorta was evaluated. Each cross-section is composed of 21 images representing the dynamic motion of the vessel at this cross-section for the cardiac cycle. Thus, a total of 105 simulation images were examined for 4D-CT-P1 and 84 for each 4D-CT-P2 and 4D-CT-P3. The dynamic displacement in each slice was quantified in terms of the hydraulic diameter (D_h). The hydraulic diameter is commonly used in the field of hydrodynamics to deal with fluids flowing in noncircular domains. It is calculated based on area (A) and perimeter (P) measurements for each phase such that:

$$D_h = 4\frac{A}{P}$$

The quantification of the wall deformation in each cross-section and for each image is illustrated in Fig.8.9 on the example of 4D-CT-P3. The areas and perimeters are measured by delineating the wall boundary for each cross-sectional image using the Digimizer image analysis software as shown in Fig.8.9.b. Prior the measurements, a calibration of the simulation images into Digimizer is performed (Fig.8.9.a). Finally, the hydraulic diameter profile (Fig.8.9.d) for each cross-section is derived from the resulting area and perimeter profiles (Fig.8.9.c) after performing the measurements on all the 21 images.

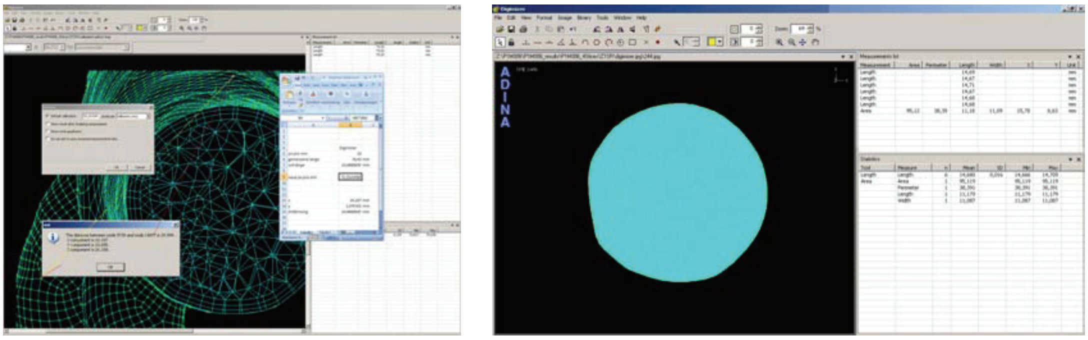

(a) Image calibration (b) Cross-sectional measurements

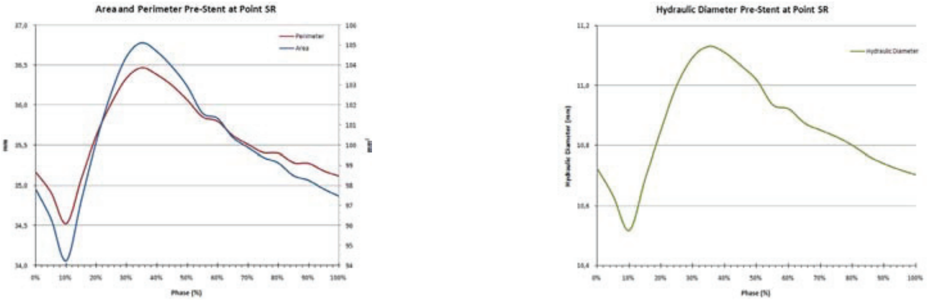

(c) Area and perimeter profiles (d) Hydraulic diameter profile

Figure 8.9: Quantification of the wall deformation in each cross-section.

Similar evaluation for the same cross-sections and the same images have been performed in [Kos09] for the CT data. The CT and the simulations were then compared by analyzing the sequences at 5 % increments. Fig.8.10 shows an example of the measurements performed on the dynamic CT data and on the CSM simulations results for the same cross-section (Z3) and the same image at t= 0.41 s for model 4D-CT-P1.

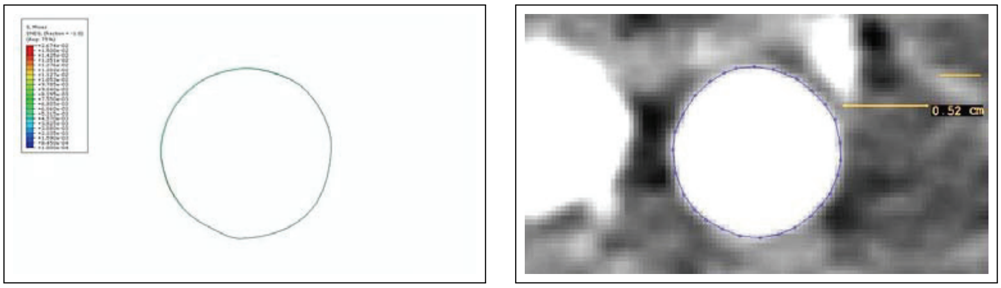

(a) Simulations (b) CT

Figure 8.10: Wall deformation in 4D-CT-P1 at Z3= 100.0 mm and t= 0.41 s for both the dynamic CT and the CSM simulations.

8.3.2 Blood Pressure Simulations

Further, an additional TC cross-section located 2 cm above the celiac trunk was identified and isolated as shown on the left-hand side of Fig.8.8.c. Cross-sections TC and AB are then used for the evaluation of the pressure and the flow results of the FSI simulations, being the positions at which the experimental measurements were performed.

Fig.8.11 and Fig.8.12 show the contours of the pressure results obtained from the FSI simulations at cross-sections TC and AB for 4D-CT-P2 and 4D-CT-P3, respectively. Pressure profiles over time of the area-weighted cross-sectional values are then derived for comparison with the catheter-based in-vivo measured profiles as presented in Sec.8.4.

8.3.3 Blood Flow Simulations

In a similar way, the flow simulations were evaluated. The velocity distributions at the TC and AB cross-sections obtained from the FSI simulations for models 4D-CT-P2 and 4D-CT-P3 are shown in Fig.8.13 and Fig.8.14, respectively. The corresponding average profiles over time are similarly extracted for comparison with the ultrasound-based flow measurements and will be presented in Sec.8.4.

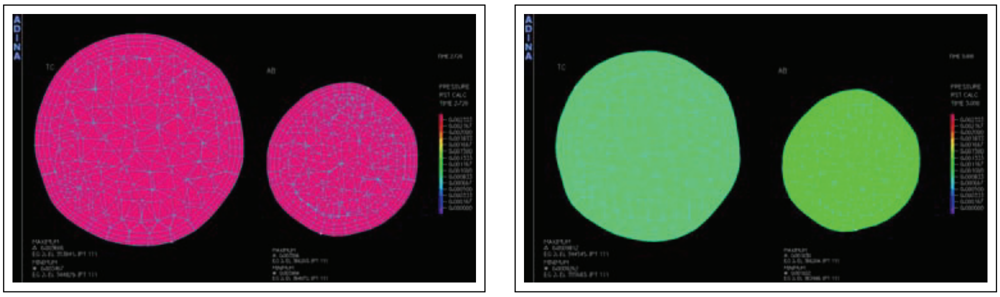

(a) t= 2.72 s (b) t= 3.00 s

Figure 8.11: Pressure simulations (FSI) in TC and AB for 4D-CT-P2.

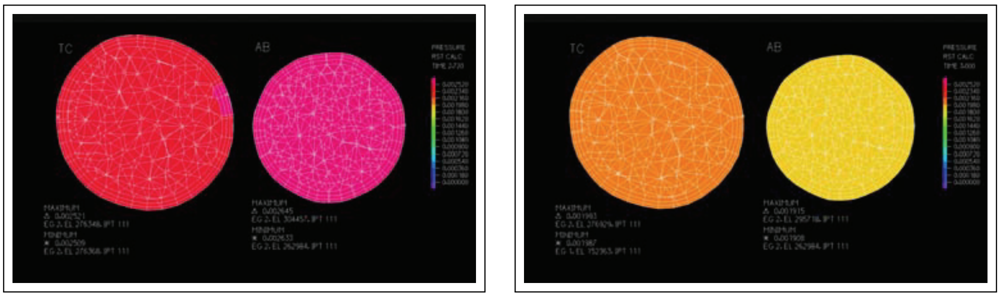

(a) t= 2.72 s (b) t= 3.00 s

Figure 8.12: Pressure simulations (FSI) in TC and AB for 4D-CT-P3.

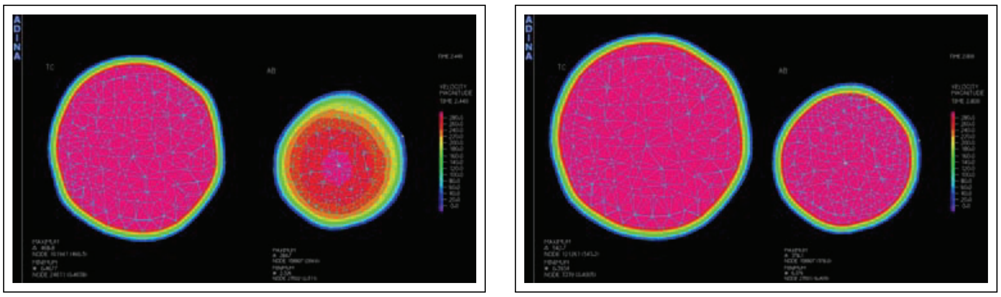

(a) t= 2.44 s (b) t= 2.80 s

Figure 8.13: Velocity simulations (FSI) in TC and AB for 4D-CT-P2.

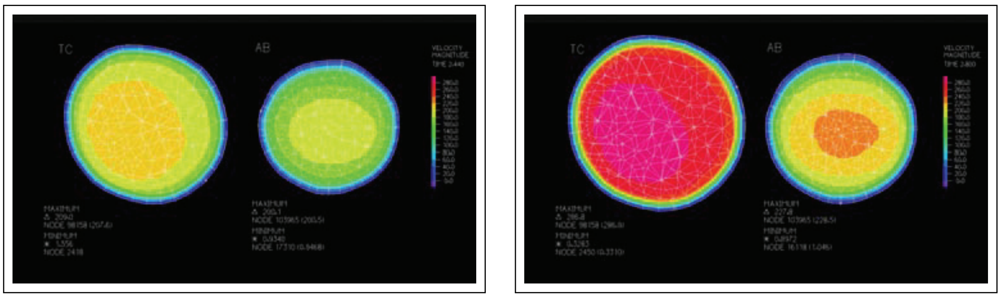

(a) t= 2.44 s (b) t= 2.80 s

Figure 8.14: Velocity simulations (FSI) in TC and AB for 4D-CT-P3.

8.4 Experiments vs. Simulations

The computations are evaluated by comparing the simulations to the in-vivo measurements obtained from the above described experiments. The dynamic CT data are used to evaluate the simulated wall deformation in 4D-CT-P1, 4D-CT-P2 and 4D-CT-P3, while the ultrasound-based flow and catheter-based pressure measurements are used to evaluate the numerical flow and pressure fields computed from the FSI simulations for 4D-CT-P2 and 4D-CT-P3. In the following, the obtained results for all three models are presented. All dynamic simulation results represented below are evaluated at the fourth cardiac cycle, ensuring convergence and periodicity. They were simulated with a homogeneous wall thickness of 2 mm and with the hyperelastic material model for porcine abdominal aortic tissue described in Sec.5.5.1.

8.4.1 4D-CT-P1 (Experiment 1 with CSM)

As mentioned before, CSM simulations were performed on 4D-CT-P1 and the dynamic CT are used to validate the wall deformation. As a boundary condition for the CSM simulations, the pressure profile measured at location equivalent to TC and shown in Fig.8.15 is applied at the inner aortic wall.

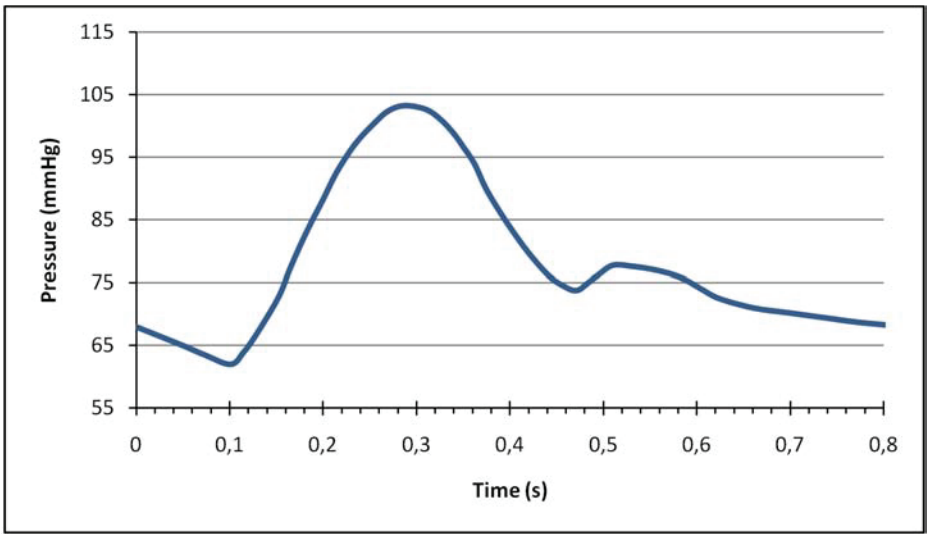

Figure 8.15: In-vivo measured pressure profile used for the boundary conditions of the CSM simulations for the 4D-CT-P1 model.

Wall Deformation Profiles

The wall deformation over the cardiac cycle for 4D-CT-P1 is validated along the depicted five cross sections of the aorta Z1, Z2, Z3, Z4 and Z5, obtained from lateral cuts orthogonal to the z-direction.

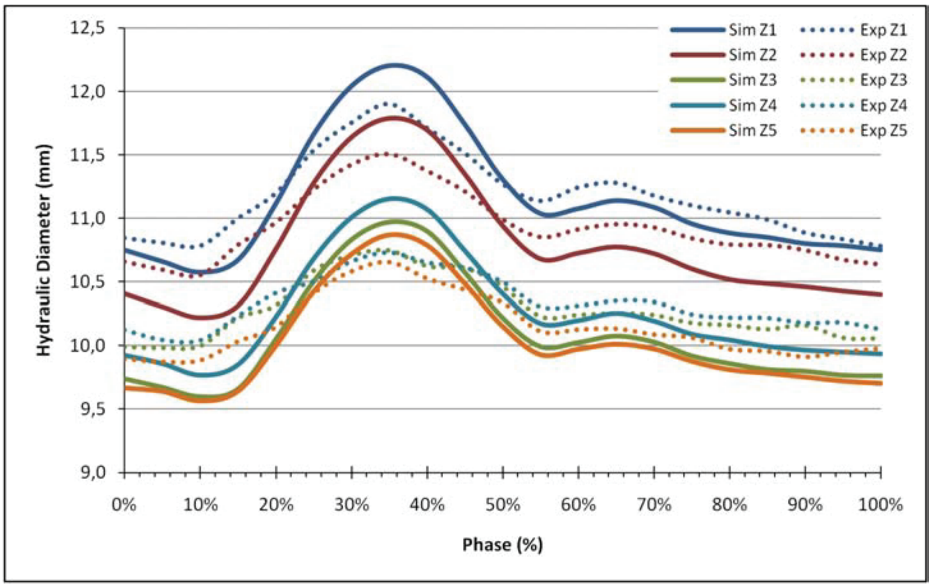

Figure 8.16: Wall deformation at the cross-sections Z1, Z2, Z3, Z4 and Z5 for model 4D-CT-P1 based on CSM.

Fig.8.16 presents the measured hydraulic diameters for 4D-CT-P1 as a function of the cardiac cycle phase for the five cross-sections from the 4D-CT images and the computational results. The transient deformation resulting from the simulations follows similar profiles to those found in the 4D-CT images, with lower hydraulic diameter values obtained at the beginning and the end of the cardiac cycle, and higher values during systole. The Root Mean Square (RMS) errors of the hydraulic diameter for sections Z1, Z2, Z3, Z4, and Z5 are 0.188, 0.252, 0.280, 0.237, and 0.204 mm, respectively. This is equivalent to an error of 0.327, 0.438, 0.487, 0.412, and 0.354 pixels. Relative to the time-averaged hydraulic diameter measured for each 4D-CT slice (11.178 mm, 10.923 mm, 10.284 mm, 10.333 mm and 10.145 mm), this is equivalent to an error of 1.7 %, 2.3 %, 2.7 %, 2.3 %, and 2.0 %, respectively. The maximum hydraulic diameter is obtained for all slices at t= 0.287 s (35 % phase) for both simulations and 4D-CT. The maximum deformation is obtained at the upper suprarenal slice Z1. The displacements decreased towards the iliac arteries where a minimal vessel diameter change is found at the lower infrarenal slice Z5.

8.4.2 4D-CT-P2 (Experiment 2 with FSI)

The FSI simulations of 4D-CT-P2 are validated in terms of the wall deformation as well as the pressure and the flow profiles.

Wall Deformation Profiles

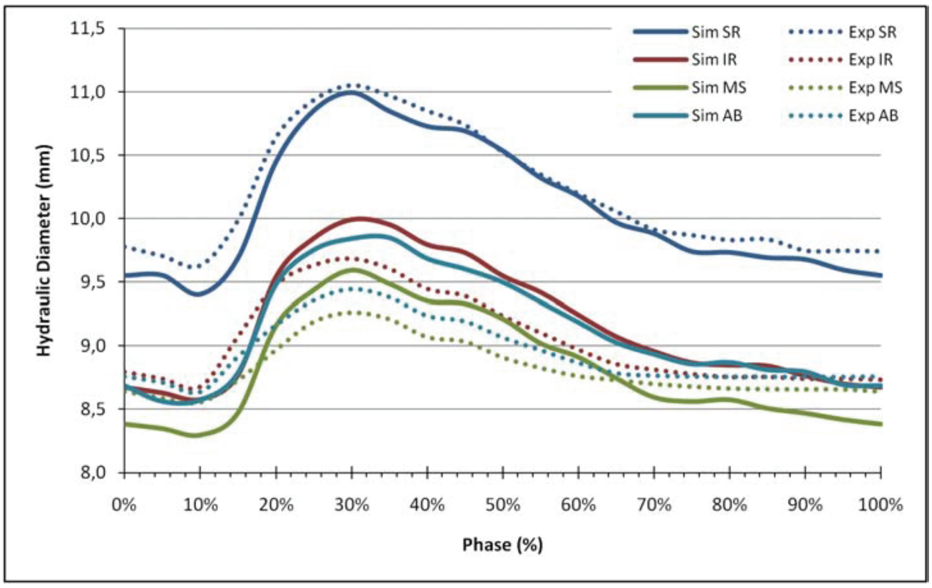

Figure 8.17: Wall deformation at the cross-sections SR, IR, MS and AB for model 4D-CT-P2 based on FSI.

Fig.8.17 presents the measured hydraulic diameters for 4D-CT-P2 as a function of the cardiac cycle phase for the four cross-sections from the 4D-CT images and the computational results. Here also, the transient deformation resulting from the simulations follows similar profiles to those found in the 4D-CT images, with lower hydraulic diameter values obtained at the beginning and the end of the cardiac cycle, and slightly higher values during systole. The Root Mean Square (RMS) errors of the hydraulic diameter for sections SR, IR, MS and AB are 0.14 mm, 0.219 mm, 0.227 mm and 0.276 mm respectively. This is equivalent to an error of 0.931, 1.46, 1.511 and 1.839 pixels. Relative to the time-averaged hydraulic diameter measured for each 4D-CT slice (10.193 mm, 9.048 mm, 8.816 mm and 8.943 mm), this is equivalent to an error of 1.4 %, 2.4 %, 2.6 %, and 3.1 %, respectively. The maximum hydraulic diameter is obtained for all slices at the 30 % phase for both simulations and 4D-CT. The maximum deformation is obtained at the upper suprarenal slice SR. However, the displacements did not decrease continuously downwards and the minimal vessel diameter change is found at cross-section MS rather than the lower AB position.

Blood Pressure Profiles

The RMS errors of the blood pressure are equivalent to 1.451 mmHg at TC and 7.433 mmHg at AB. Relative to the time-averaged in-vivo pressure measured for TC and AB (104.294 mmHg and 113.475 mmHg), this is equivalent to an error of 1.4 % and 6.6 %, respectively.

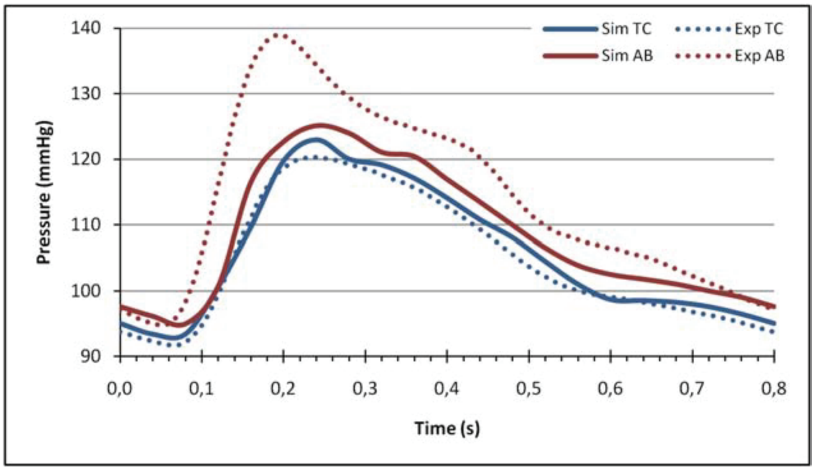

Figure 8.18: Pressure profiles at cross-sections TC and AB for 4D-CT-P2.

Blood Flow Profiles

The RMS errors of the blood flow in terms of velocity are equivalent to 68.176 mms^{-1} at TC and 117.508 mms^{-1} at AB. Relative to the time-averaged ultrasound-based flow measured for TC and AB (338.593 mms^{-1} and 274.266 mms^{-1}), this is equivalent to an error of 20.1 % and 42.8 %, respectively.

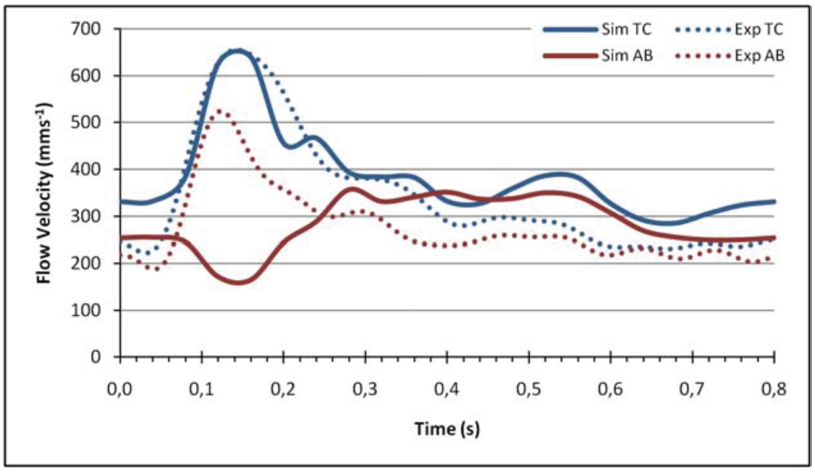

Figure 8.19: Velocity profiles at cross-sections TC and AB for 4D-CT-P2.

8.4.3 4D-CT-P3 (Experiment 3 with FSI)

Similar to 4D-CT-P2, the FSI simulations of 4D-CT-P3 are validated in terms of the wall deformation as well as the pressure and the flow profiles.

Wall Deformation Profiles

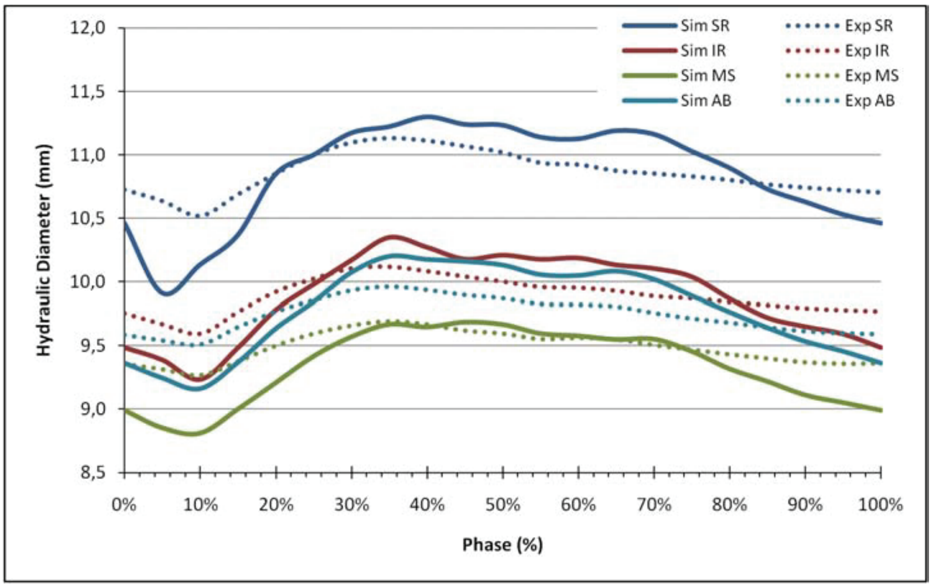

Figure 8.20: Wall deformation at the cross-sections SR, IR, MS and AB for model 4D-CT-P3 based on FSI.

Fig.8.20 presents the measured hydraulic diameters for 4D-CT-P3 as a function of the cardiac cycle phase for the four cross-sections from the 4D-CT images and the computational results. Again, the transient deformation resulting from the simulations follows similar, somehow flat, profiles to those found in the 4D-CT images with lower hydraulic diameter values obtained at the beginning and the end of the cardiac cycle, and slightly higher values during systole. The Root Mean Square (RMS) errors of the hydraulic diameter for sections SR, IR, MS and AB are 0.203 mm, 0.208 mm, 0.237 mm and 0.218 mm, respectively. This is equivalent to an error of 1.015, 1.038, 1.184 and 1.091 pixels. Relative to the time-averaged hydraulic diameter measured for each 4D-CT slice (10.856 mm, 9.887 mm, 9.485 mm and 9.738 mm), this is equivalent to an error of 1.9 %, 2.1 %, 2.5 %, and 2.2 %, respectively. The maximum hydraulic diameter is obtained for all slices at the 35 % phase for both simulations and 4D-CT. Also here, the maximum deformation is obtained at the upper suprarenal slice SR. Similar to 4D-CT-P2, the displacements did not decrease continuously towards the iliac arteries and the minimal vessel diameter change is found at cross-section MS.

Blood Pressure Profiles

The RMS errors of the blood pressure are equivalent to 1.174 mmHg at TC and 5.28 mmHg at AB. Relative to the time-averaged in-vivo pressure measured for TC and AB (114.375 mmHg and 109.836 mmHg), this is equivalent to an error of 1.0 % and 4.8 %, respectively.

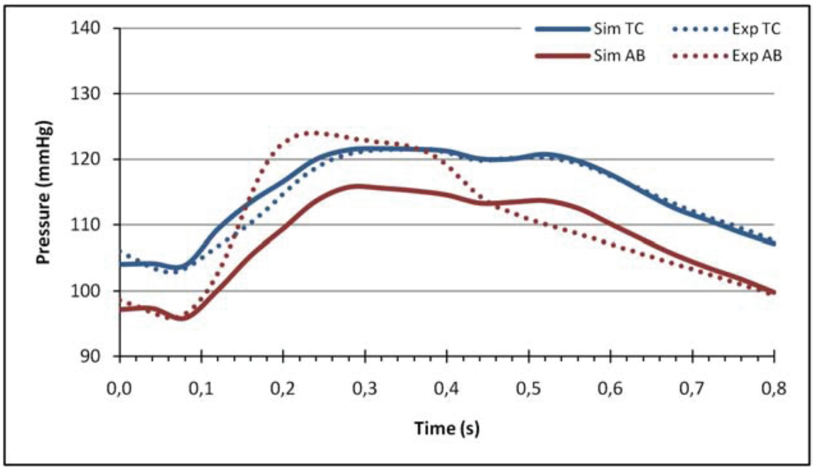

Figure 8.21: Pressure profiles at cross-sections TC and AB for 4D-CT-P3.

Blood Flow Profiles

The RMS errors of the blood flow in terms of velocity are equivalent to 21.508 mms^{-1} at TC and 109.274 mms^{-1} at AB. Relative to the time-averaged ultrasound-based flow measured for TC and AB (317.881 mms^{-1} and 234.419 mms^{-1}), this is equivalent to an error of 6.8 % and 46.6 %, respectively.

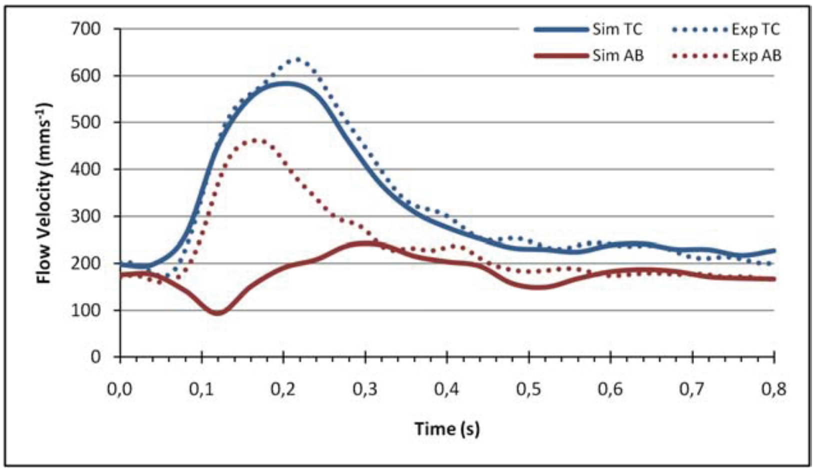

Figure 8.22: Velocity profiles at cross-sections TC and AB for 4D-CT-P3.

8.5 Discussion

Subject-specific biomechanical simulations and validation based on in-vivo experiments performed on three porcine aorta are presented. This work is a first attempt to numerically simulate and experimentally validate the biomechanics in the aorta based on real morphological data and boundary conditions. By using the actual vessel geometry and implementing physiological in vivo-based pressure and flow boundary conditions in the computations, a necessary step towards realistic patient-specific modeling could be taken. An experimentally validated patient-specific simulation system based on realistic geometrical and physical data can be implemented clinically and presents a reliable tool in evaluating non-invasively individual therapies and treatment strategies in the field of minimally invasive surgery. The accuracy of the computations is evaluated based on the quantification of the vessel deformation and of the intraluminal pressure and flow profiles in both the simulations and the acquired experimental data.

8.5.1 Wall Deformation Results

The wall motion was validated by measuring the dynamic hydraulic diameter from the biomechanical simulations and from the 4D-CT data at 21 phases of the cardiac cycle, for various specific cross-sections of the aorta. The computation of the wall mechanics is based on CSM simulations for the first porcine model 4D-CT-P1 obtained by computing the arterial wall response to a realistic measured pulsatile aortic pressure, and on FSI simulations with coupled blood flow for models 4D-CT-P2 and 4D-CT-P3. The results show that accurate vessel wall modeling is possible using FEM-based CSM simulations for which RMS errors varying between 1.7 % and 2.7 % based on the time-averaged hydraulic diameter estimated at five cross-sections for model 4D-CT-P1 were obtained. Although computations that are more reliable should be obtained when also incorporating the fluid dynamics into the numerical model by means of FSI, the FSI simulations showed very similar results, with RMS errors varying between 1.9 % to 2.5 % for model 4D-CT-P2 and between 1.4 % to 3.1 % for model 4D-CT-P3. Obviously, since larger amount of input data is necessary to conduct FSI simulations, the sources of error become also higher. Further, the maximum diameters of all cross-sections were found at the same cardiac phase within each model, indicating that the pulse wave was significantly reduced on its way to the abdominal aorta. Finally, in contrast to the FSI results, the CSM systolic deformation was always higher than that obtained from the dynamic CT. This demonstrates that CSM is strongly influenced by the pressure profile applied at the wall boundary.

8.5.2 Blood Pressure Results

The obtained RMS errors of the blood pressure are equivalent to 1.4 % and 6.6 % for 4D-CT-P2 and 1.0 % and 4.8 % for 4D-CT-P3, calculated relative to the time-averaged in-vivo pressure measured for TC and AB, respectively. These results show that the pressure profiles based on FSI simulations can be accurately computed, as being compared to precise in-vivo and individual measured pressure profiles.

8.5.3 Blood Flow Results

On the other hand, the RMS errors of the blood flow do not imply good results, especially for the lower cross-section AB. From the numerical point of view, AB is located directly above a stagnation point in which the flow should be relatively low due to the high local pressure values. However, in contrast to the human anatomy (Fig.2.4), the porcine Aa. iliacae internae branches out directly from the aorta abdominalis. Consequently, the porcine aorta does not include a stagnation point at the aortic bifurcation, which explains the higher experimental values and thus the difference in the results. Another reason may be due to difficulties in the definition of the exact position at which the ultrasound measurements were performed; probably, the flow measurements reported at AB were taken at some higher level along the aorta.

8.6 Summary

The experimental validation of the numerical simulations were presented in this chapter. The experiments performed on three porcine aortas and the data acquired to generate the computational models and to experimentally validate the biomechanical simulations were first described. The experimental data consisting of morphological images acquired by dynamic 4D-CT and physiological pressure and flow profiles generated by catheter-based invasive and ultrasound-based flow measurements were thereby presented. Further, the approach followed to evaluate the computations in terms of quantification of the vessel wall deformation, and of the pressure and velocity profiles as well as the FEM-based simulations were presented. Then, the computed vessel wall deformation, the pressure profiles and the velocity profiles of the three porcine models are validated by comparing the provided experimental data with the simulation results. Finally, the experimental and simulation results as well as the efficiency of the CSM and the FSI computational methods were discussed.

Chapter 9

Conclusions

9.1 Summary and Discussion

Patient-specific computational modeling of biomechanics based on medical imaging provides a physical and realistic insight into the blood hemodynamics and the wall elastomechanics and enables accurate predictive simulations of development, growth and failure of cardiovascular pathologies. In spite of all technological advancements in computational methods, a clinically implementable system allowing reliable modeling was not available up to now. The primary objective of the present work was to establish a numerical approach to non-invasively help the diagnosis of patients with vascular pathologies on an individual basis.

The patient-specific FEM-/FVM-based simulation system MoDiSim, has been therefore designed, developed and evaluated to automatically simulate the hemodynamics and the elastomechanics as well as their interaction within CT/MRI image-based vessel models. MoDiSim represents a tool for the detection of regions with pathological hemodynamics and elastomechanics and for the evaluation of associated risks.

For the computation of blood flow and vessel wall biophysical parameters, a simulation workflow has been first developed, applied for CSM, CFD and FSI applications and finally integrated into MoDiSim. The process chain for the simulations was therefore generated, consisting of a fine segmentation, the creation of 3D geometrical models, the generation and processing of controlled surface and volume meshes, the setting of realistic boundary conditions and of the computations using appropriate physical models and mathematical solvers leading to stable and accurate solutions.

Due to the significant effects of patient-specific geometry and pathology shape, of high-quality meshes, of accurate physics, of realistic boundary conditions and of coupled and decoupled modeling on the simulation results, great care was taken while building the elements of the individual process chains. Furthermore, the effects of pulsatile dynamic modeling, of material blood and wall constitutive relations, of the impact of physiological boundary conditions and of stent-graft implantation on the hemodynamics and the elastomechanics have been evaluated.

The effects of different mesh configurations on the computed parameters have been investigated to determine the properties of the meshes that result in stable simulations. Based on these results, automatic generation of stable patient-specific mesh geometries was made possible. Further, a numerical tool to automatically process and convert the finite mesh models as required for CSM, CFD and FSI applications within patient-specific vessels has been developed and integrated into MoDiSim.

The CSM computations simulate the arterial wall response to an applied predefined pressure load. The CFD computations simulate the hemodynamics while assuming a rigid vessel wall. Coupling the hemodynamics and the elastomechanics by means of FSI allows more reliable simulations of the physical interaction between both models. FSI simulations are however computationally demanding. MoDiSim includes therefore CSM, CFD and FSI modeling, while keeping the freedom and flexibility for the user to choose the application method depending on the available time and computational resources.

For the validation of the computational results, in-vivo experiments have been performed on porcine aortas to experimentally evaluate the results based on morphological data obtained from dynamic 4D-CT imaging, catheter-based in-vivo pressure and ultrasound-based flow measurements. The simulation results were compared, discussed and evaluated.

After all, the most important contribution of this work remains in the individualized, optimized and especially automated feature of MoDiSim, being essential for performing reliable, efficient and fast evaluation and hence for a clinical implementation. By accounting for individual geometry and conditions as well as implementing optimized physical models, a necessary step towards realistic patient-specific modeling could be taken. MoDiSim provides an individual computational analysis of potential predictions on the assessment of the pathological state for various pathologies and vessel regions and was evaluated using various aortic models. The expendable features of MoDiSim allow for flexible integration of further components such as extending its application for predictive simulations with endovascular devices for optimal planning.

9.2 Future Developments

Finally, future developments and further research activities in regard to segmentation and endovascular devices are shorty outlined below:

Automatic Segmentation and Detection of Wall Thickness

The segmentation of the CT and MRI images performed in a semi-automatic way showed good results, but was time consuming. In order to facilitate a clinical implementation of this step, further development in the segmentation techniques and the application of more sophisticated, vessel-specific and especially automated algorithms are needed to improve the results in terms of accuracy and speed.

Furthermore, a homogeneous wall thickness was assumed in this work, which in general underestimates the wall stresses compared to variable thickness. An accurate modeling of the variable wall thickness is a crucial factor affecting the computation of wall stresses. A more reliable modeling requires therefore the detection of the real non-homogeneous wall thickness from the patient images. This in turn requires further development and improvement in the imaging techniques and resolution quality.

Ongoing research on automatic segmentation of patient-specific aortic models as well as automatic detection of patient-specific wall thickness from CT and MRI images is conducted by [SDG$^+$08] and [MDMA$^+$09].

Computational Design and Optimization of Stents and Stent-Grafts

The work is a milestone towards a numerical methodology for the computational design and optimization of stents and stent-grafts in the prefield of the intervention for patients with vascular pathologies on an individual basis.

In face of the advantages of minimally invasive surgery in treating cardiovascular pathologies, complications following endovascular treatments show that further advances in stent-graft development are needed. Post-repair complications include endoleaks formation, stent migration or even failure of the stent material. These may have fatal consequences on the patient. An endovascular treatment with individual awareness in terms of design geometry and material characteristics is therefore a crucial issue for efficient therapies.

An optimal treatment may be achieved when associated to an individual choice of the stent or stent-graft design. The design of a stent-graft can be primarily defined by material and geometry parameters. The choice of the optimal design highly depends on the shape and the size of the pathology, as well as on the wall biomechanics and the blood flow characteristics inside the vessel. Thus the knowledge of such parameters, considering the patient-specific geometry, elastomechanics and hemodynamics, may be helpful in the field of minimally invasive surgery to predict optimal therapies and improve individual treatments.

The future vision is to conduct research on the quantitative variables for design optimization of endovascular devices that best fulfill the patient's needs based on FSI simulations. Fully coupled simulations including virtual endovascular models should be developed to study the interaction between stent-grafts, vessel wall and blood flow within patient-specific vascular models. From the FSI simulations variables, such as flow patterns, fluid pressure, wall stresses and strains can be obtained. Based on these, parameters describing endovascular device geometry and material characterization providing optimal biomechanical conditions for the blood flow and the vessel wall can be derived for each individual patient.

This can be achieved by quantifying the changes in the vascular morphology (diameter, volume, curvature etc.) due to the different stent-graft designs (diameter, strut number, width, thickness and elastic material properties), which in turn influences the hemodynamics and the wall mechanics as well as the interaction between them. The design of the endovascular devices may be then evaluated by studying the relation between the vessel size and the stent-graft design, and by analyzing the effects of the device geometry and material characterization on the flow, pressure, strain and stress distributions of the various stented and of the pre- and post-stented models. Consequently, by precisely adapting endovascular devices to the patient's anatomic conditions, therapies and treatment strategies can be optimized as an assessment tool for optimal placement and improved device design to minimize post-procedural complications.

References

[AAL$^+$04] Luis A. Alicea, José I. Aviles, Iris A. López, Luis E. Mulero, and Luis A. Sánchez. Mechanics biomaterials: Stents. *Application of Engineering Mechanics in Medicine*, 2004.

[ABH05] F. Abraham, M. Behr, and M. Heinkenschloss. Shape optimization in steady blood flow a numerical study of non-newtonian effects. *Comput Methods Biomech Biomed Eng*, 8(2), 2005.

[ABK$^+$05] M. Alizadeh, G. Benderoth, S. Kasseckert, M. Rzepka, M. Stanull, S. Vogt, R. Moosdorf, and G. Silber. Calculation of haemorheological properties for vascular diagnosis based on ultra sound measurements of velocity profiles. *Cardiovasc Eng*, 10(1):81–93, 2005.

[Adi08] Inc. Adina. Adina 8.5 - theory and modeling guide, 2008.

[AWWL06] S. Amornsamankul, B. Wiwatanapataphee, Y.H. Wu, and Y. Lenbury. Effect of non-newtonian behaviour of blood pulsatile flows in stenotic arteries. *Int. J. Biomed Sciences*, 1(1):42–46, 2006.

[Bat96] K.J. Bathe. *Finite element procedures.* Englewood Cliffs, NJ: Prentice Hall, 1996.

[BBK06] R. Berguer, J. Bull, and K. Khanafer. Refinements in mathematical models to predict aneurysm growth and rupture. *Annals of the New York Academy of Sciences*, 87(11-12):110–116, 2006.

[BDZ07] A. Benninghoff, D. Drenckhahn, and W. Zenker. *Anatomie: makroskopische Anatomie, Embryologie und Histologie des Menschen.* Urban & Schwarzenberg, 2007.

[BE08] K. Bauer and J. Ennker. *Aortenchirurgie: Ein Patientenratgeber.* Steinkopff-Verlag Darmstadt, 2008.

[Bec91] G.J. Becker. Intravascular stents. general principles and status of lower-extremity arterial applications. *Circulation*, 83:I122–I136, 1991.

[BJ89] T.J. Barth and D. Jespersen. The design and application of upwind schemes on unstructured meshes. *AIAA 27th Aerospace Sciences Meeting*, 89(0366), 1989.

[BKMH78] W. Bleifeld, C. Kramer, and K. Meyer-Hartwig. *Klinische Physiologie*. Gerhard Witzstrock, Baden-Baden, Köln, New York, Bd. II, 1978.

[BPC06] R. Benard, R. Perrault, and D. Coisne. Computational approach to estimating the effects of blood properties on changes in intra-stent flow. *A. Biomed Eng*, 34(8):1259–1271, 2006.

[BZJ99] K.J. Bathe, H. Zhang, and S. Ji. Finite element analysis of fluid flows fully coupled with structural interactions. *Computers and Structures*, 72:1–16, 1999.

[CK91] Y.I. Cho and K.R. Kensey. Effect of the non-newtonian viscosity of blood on flows in a diseased arterial vessel. *Biorheology*, 28(3-4):241–262, 1991.

[CL97] J.R. Cebral and R. Lohner. Fluid-structure coupling - extensions and improvements. *AIAA-97-0858*, 1997.

[Coo03] Cook. Zenith, suggested instructions for use. 2003.

[Cow07] M.G. Cowling. *Vascular Interventional Radiology: Current Evidence in Endovascular Surgery; angioplasty, Stenting, Thrombolysis and Thrombectomy*. Springer, 2007.

[CSM02] A. Colombo, G. Stankovic, and J.W. Moses. Selection of coronary stents. *Journal of the American College of Cardiology*, 40(6):1021–1033, 2002.

[DB00] B.L. Dolmatch and U. Blum. *Stent-grafts: current clinical practice*. Thieme Medical Pub, 2000.

[DMGF$^+$01] E.S. Di Martino, G. Guadagni, A. Fumero, G. Ballerini, R. Spirito, P. Biglioli, and A. Redaelli. Fluid-structure interaction within realistic threedimensional models of the aneurysmatic aorta as a guidance to assess the risk of rupture of the aneurysm. *Med Eng Phys*, 23(9):647–655, 2001.

[DMV03] E.S. Di Martino and D.A. Vorp. Effect of variation in intraluminal thrombus constitutive properties on abdominal aortic aneurysm wall stress. *A. Biomed Eng*, 31(7):804–809, 2003.

[EKH$^+$07] H. Eichstädt, W. Kübler, R. Hetzer, R. Sommerfeld, J. Sommerfeld, H. Siniawski, L. Lehmkuhl, and T. Störk. Operationszeitpunkt bei thorakalen aortenaneurysmen und bei dissektionen. *Herzmedizin 24*, 4:162–174, 2007.

[FI06] Fluent-Inc. Fluent 6.3 documentation, 2006.

[FKA03] E.A. Finol, Marra K.G., and C.H. Amon. Analytical estimation of flow-induced forces in endovascular grafts and design methodology for a tissue-engineered endovascular attachment mechanism. *Biomedicine*, 2003.

[FMRK03] M.F. Fillinger, S.P. Marra, M.L. Raghavan, and F.E. Kennedy. Prediction of rupture risk in abdominal aortic aneurysm during observation: wall stress versus diameter. *J. Vasc Surg*, 37(4):724–732, 2003.

[FP08] J.H. Ferziger and M. Peric. *Numerische Strömungsmechanik.* Springer, Berlin, 2008.

[FPF98] C.A. Felippa, K.C. Park, and C. Farhat. Partitioned analysis of coupled systems. *Computational Mechanics*, 1998.

[Gam06] Gambit. *Gambit User's Guide, Fluent Inc.* 2006.

[Geb07] J.O. Gebbers. Atherosclerosis, cholesterol, nutrition and statins - a critical review. *GMS German Medical Science*, 2007.

[GvdVJ99] F. Gijsen, F. van de Vosse, and J. Janssen. The influence of the non-newtonian properties of blood on the flow in large arteries: Unsteady flow in a 90 degrees curved tube. *J. Biomech*, 32:705–713, 1999.

[HBK$^+$07] D. Hazer, O. Bondarenko, R. Kröger, R. Dillman, and G.M. Richter. Grid analysis for mesh-independent and stable cfd simulations in the aorta. *Proc. 6. CURAC*, pages 129–132, 2007.

[HFK$^+$09] D. Hazer, E.A. Finol, M. Kostrzewa, M. Kopaigorenko, G.M. Richter, and R. Dillmann. Computational biomechanics and experimental validation of vessel deformation based on 4d-ct imaging of the porcine aorta. *Proc. SPIE*, 7262:72621F–72621F–9, 2009.

[HKU$^+$07] D. Hazer, R. Kröger, R. Unterhinninghofen, P. Kurz, R. Dillman, and G.M. Richter. Cfd simulations: Effects of non-newtonian blood behaviour in individual aortic aneurysms. *Proc. Surgetica*, 2007.

[HO03] G.A. Holzapfel and R.W. Ogden. *Biomechanics of soft tissue in cardiovascular systems.* Springer, 2003.

[HRL66] G. Heberer, G. Rau, and H.H. Löhr. *Aorta und große Arterien: Pathophysiologie, Klinik, Röntgenologie und Chirurgie.* Springer Berlin Heidelberg, 1966.

[HSU$^+$08] D. Hazer, E. Schmidt, R. Unterhinninghofen, G.M. Richter, and R. Dillman. Automatic generation of individual finite-element models for computational fluid dynamics and computational structure mechanics simulations in the arteries. *Proc. ICCMSE*, 2008.

[Hug00] T.J.R. Hughes. *The finite element method - linear static and dynamic finite element analysis.* Englewood Cliffs, NJ: Prentice-Hall, 2000.

[HUK$^+$06a] D. Hazer, R. Unterhinninghofen, M. Kostrzewa, H.U. Kauczor, R. Dillman, and G.M. Richter. Wall shear stress simulations in a ct based human abdominal aortic model. *GMS German Medical Science*, 2006.

[HUK$^+$06b] D. Hazer, R. Unterhinninghofen, M. Kostrzewa, H.U. Kauczor, R. Dillman, and G.M. Richter. A workflow for computational fluid dynamics simulations using patient-specific aortic models. *Proc. 24. CADFEM Users' Meeting*, 2006.

[IN01] H. Ince and C.A. Nienaber. Endovaskuläre stentgraft-prothesen beim aortenaneurysma. *Zeitschrift für Kardiologie*, 90:67–72, 2001.

[KBB07] K. Khanafer, J. Bull, and R. Berguer. Fluid structure interaction of turbulent pulsatile flow within a flexible wall axisymmetric aortic aneurysm model. *Eur J. Mech - B/Fluids*, 28(1):88–102, 2007.

[KGBB06] K. Khanafer, P. Gadhoke, R. Berguer, and J. Bull. Modeling pulsatile flow in aortic aneurysms: Effect of non-newtonian properties of blood. *Biorheology*, 43:661–679, 2006.

[KHK$^+$07] M. Kostrzewa, D. Hazer, P. Kurz, H. von Tengg-Kobligk, and G.M. Richter. Doppler measurements of blood flow in the aorta - an evaluation method for a computational fluid dynamic model - preliminary results. *Proc. BMT*, 83:I122–I136, 2007.

[Kle89] M. Kleiber. *Incremental Finite Element Modeling in Non-linear Solid Mechanics.* Ross. Chichester: Ellis Horwood, 1989.

[Kos09] M. Kostrzewa. Entwicklung einer validierungsmethodik für ein simulationsmodell des blutflusses und der wanddeformation der aorta. Universität Heidelberg, Medizinischen Fakultät, Dissertation, 2009.

[LBBJ+07] M. Li, J. Beech-Brandt, L. John, P. Hoskins, and W. Easson. Numerical analysis of pulsatile blood flow and vessel wall mechanics in different degrees of stenoses. *J. Biomech*, 40(16):3715–3724, 2007.

[LC87] W. Lorensen and H. Cline. Marching cubes: A high resolution 3d surface reconstruction algorithm. *Computer Graphics*, 21(4):163–169, 1987.

[Lei74] H. Leipholz. *Theory of Elasticity.* New York: Dekker, 1974.

[LK05a] Z. Li and C. Kleinstreuer. Blood flow and structure interactions in a stented abdominal aortic aneurysm model. *Med Eng Phys*, 27(5):369–382, 2005.

[LK05b] Z. Li and C. Kleinstreuer. Fluid-structure interaction effects on sac blood pressure and wall stress in a stented aneurysm. *J. Biomech Eng*, 127(4):662–671, 2005.

[LK05c] Z. Li and C. Kleinstreuer. Fluid-structure interaction effects on sac-blood pressure and wall stress in a stented aneurysm. *J. Biomech Eng*, 127:662, 2005.

[LK06a] Z. Li and C. Kleinstreuer. Computational analysis of type ii endoleaks in a stented abdominal aortic aneurysm model. *J. Biomech*, 39(14):2573–2582, 2006.

[LK06b] Z. Li and C. Kleinstreuer. Effects of major endoleaks on a stented abdominal aortic aneurysm. *J. Biomech Eng*, 128(1):59–68, 2006.

[LM90] B.P. Leonard and S. Mokhtari. Ultra-sharp nonoscillatory convection schemes for high-speed steady multidimensional flow. *NASA TM 1-2568 (ICOMP-90-12)*, 1990.

[LM01] P. LeTallec and J. Mouro. Fluid structure interaction with large structural displacements. *Comput Methods Appl Mech Eng*, 190(24):3039–3068, 2001.

[Lut07] B. Luther. *Kompaktwissen Gefäßchirurgie differenzierte Diagnostik und Therapie.* Springer ed 8. Berlin, Heidelberg, New York, 2007.

[LWC^{+}06] J.H. Leung, A.R. Wright, N. Cheshire, J. Crane, S.A. Thom, A.D. Hughes, and Y. Xu. Fluid structure interaction of patient specific abdominal aortic aneurysms: a comparison with solid stress models. *Biomed Eng Online*, 33(5):647–655, 2006.

[LWJ^{+}02] F.A. Lederle, S.E. Wilson, G.R. Johnson, D.B. Reinke, F.N. Littooy, C.W. Acher, D.J. Ballard, L.M. Messina, I.L. Gordon, E.P. Chute, W.C. Krupski, S.J. Busuttil, G.W. Barone, S. Sparks, L.M. Graham, J.H. Rapp, M.S. Makaroun, G.L. Moneta, R.A. Cambria, R.G. Makhoul, D. Eton, H.J. Ansel, J.A. Freischlag, and D. Bandyk. Immediate repair compared with surveillance of small abdominal aortic aneurysms. *N Engl J Med*, 346(19):1437–1444, 2002.

[MDMA^{+}09] G. Martufi, E.S. Di Martino, C.H. Amon, S.C. Muluk, and A. Finol, E. Three dimensional geometrical characterization of abdominal aortic aneurysms. *J. Biomech Eng*, *131*(061015), 2009.

[Meda] Johnson Metthey Medical. Nitinol technical properties.

[Medb] Medtronic. Valiant thoracic stent graft system.

[MGF01] A. Machraoui, P. Grewe, and A. Fischer. *Koronarstenting.* Steinkopff, 2001.

[MS91] A.K. Mal and S.J. Singh. *Deformation of elastic solids.* Englewood Cliffs, NJ:Prentice-Hall, 1991.

[OBD09] H. Oertel, M. Böhle, and U. Dohrmann. *Strömungsmechanik: Grundlagen - Grundgleichungen - Lösungsmethoden - Softwarebeispiele.* Vieweg + Teubner, Wiesbaden, 5. ed. edition, 2009.

[Ogd84] R.W. Ogden. *Non-linear Elastic Deformations.* Chichester: Ellis Horwood / New York: John Wiley & Sons, 1984.

[OKM^{+}95] J. Oshinski, D. Ku, J. Mukundan, F. Loth, and R. Pettigrew. Determination of wall shear stress in the aorta with the use of mr phase velocity mapping. *J. Magn Reson Imaging*, 5(6):640–647, 1995.

[OS89] J.T. Oden and J.M. Steele. *Finite Elements of Non-linear Continua.* New York: Dekker, 1989.

[Par98] The UK Small Aneurysm Trial Participants. Mortality results for randomised controlled trial of early elective surgery or ultrasonographic surveillance for small abdominal aortic aneurysms. *The Lancet*, 352(9141):1649–1655, 1998.

[Pat80] S.V. Patankar. *Numerical Heat Transfer and Fluid Flow.* Hemisphere, Washington, DC, 1980.

[PE01] S. Prakash and C.R. Ethier. Requirements for mesh resolution in 3d computational hemodynamics. *J. Biomed Eng*, 123(2):134–144, 2001.

[PF83] K.C. Park and C.A. Felippa. Partitioned analysis of coupled systems. *Computational Methods for Transient Analysis*, 1983.

[PFD77] K.C. Park, C.A. Felippa, and J.A. DeRuntz. Stabilization of staggered solution procedures for fluid structure interaction analysis. *Computational Methods for Fluid Structure Interaction Problems*, 26:95–124, 1977.

[PFTV92] W.H. Press, B.P. Flannery, S.A. Teukolsky, and W.T. Vetterling. Relaxation methods for boundary value problems. *Numerical Recipes in FORTRAN - The Art of Scientific Computing*, pages 863–871, 1992.

[PLD+03] P.J. Prendergast, C. Lally, S. Daly, A.J. Reid, T.C. Lee, D. Quinn, and F. Dolan. Analysis of prolapse in cardiovascular stents: A constitutive equation for vascular tissue and finite-element modelling. *J. Biomech Eng*, 125:692–699, 2003.

[PMW+09] H. Perea, H. Methe, E. Wintermantel, et al. *Magnetoseed - Vasculäres 24 Tissue Engineering.* Springer Berlin Heidelberg, 2009.

[PPR+05] S. Petersen, V. Peto, M. Rayner, J. Leal, R. Luengo-Fernandez, and A. Gray. European cardiovascular disease statistics / british heart foundation. Research report, 2005.

[QTV00] A. Quarteroni, M. Tuveri, and A. Veneziani. Computational vascular fluid dynamics: problems, models and methods. *Computing and Visualization in Science*, 2(4):163–197, 2000.

[RBY91] R.D. Rauch, J.T. Batira, and N.T. Yang. Spatial adaption procedures on unstructured meshes for accurate unsteady aerodynamic flow computations. *Technical Report AIAA-91-1106*, 1991.

[RC83] C.M. Rhie and W.L. Chow. Numerical study of the turbulent flow past an airfoil with trailing edge separation. *AIAA Journal*, 21(11):1525–1532, 1983.

[Rem99] W. Remmele. *Pathologie. 1. Rechtsfragen in der Pathologie; Einführung in die bioptische Diagnostik; Herz und Gefäßsystem; Hämatologie; Milz; Thymus*. Springer, 1999.

[RLD96] J.W. Rohen and E. Lütjen-Drecoll. *Funktionelle Histologie*. Schattauer Stuttgart, 1996.

[RV00] M.L. Raghavan and D.A. Vorp. Toward a biomechanical tool to evaluate rupture potential of abdominal aortic aneurysm: identification of a finite strain constitutive model and evaluation of its applicatibility. *J. Biomech*, 33(4):475–482, 2000.

[RWV96] M.L. Raghavan, M.W. Webster, and D.A. Vorp. Ex-vivo biomechanical behavior of abdominal aortic aneurysm: assessment using a new mathematical model. *A. Biomed Eng*, 33(4):475–482, 1996.

[SBRH02] C.A.J. Schulze-Bauer, P. Regitnig, and G.A. Holzapfel. Mechanics of the human femoral adventitia including the high-pressure response. *American Journal of Physiology- Heart and Circulatory Physiology*, 282(6):2427–2440, 2002.

[SC05] S. Shibeshi and W. Collins. The rheology of blood flow in a branched arterial system. *Appl Rheol.*, 15(6):398–405, 2005.

[Sch91] H.R. Schwarz. *Methode der finiten Elemente*. Teubner, 1991.

[Sch07] R.F. Schmidt. *Physiologie des Menschen : mit Pathophysiologie*. Springer Medizin Verlag Heidelberg, Berlin, Heidelberg, 30., neu bearb. und aktualisierte aufl. edition, 2007.

[SDG$^+$08] J. Shum, E.S. DiMartino, A. Goldhammer, D. Goldman, L. Acker, G. Patel, G. Martufi, and E.A. Finol. Semi-automatic vessel wall detection and quantification of wall thickness in ct images of human abdominal aortic aneurysms. *Medical Image Analysis, submitted*, 2008.

[SDW$^+$07] A. Schomig, A. Dibra, S. Windecker, J. Mehilli, J. Suarez de Lezo, C. Kaiser, S.J. Park, J.J. Goy, J.H Lee, E. Di Lorenzo, J. Wu, P. Juni, M. Pfisterer, B. Meier, and A. Kastrati. A meta-analysis of 16 randomized trials of sirolimus-eluting stents versus paclitaxel-eluting stents in patients with coronary artery disease. *J. Am Coll Cardiol*, 50(14), 2007.

[SF07] C.M. Scotti and E.A. Finol. Compliant biomechanics of abdominal aortic aneurysms: A fluid-structure interaction study. *Computers and Structures*, 85(11-14):628–644, 2007.

[Sie06] J.R. Siewert. *Chirurgie*. Springer, 2006.

[SIK$^+$01] K. Suzuki, T. Ishiguchi, S. Kawatsu, H. Iwai, K. Maruyama, and T. Ishigaki. Dilatation of evgs by luminal pressures: experimental evaluation of polytetrafluorothylene (ptfe) andwoven polyester grafts. *Cardiovascular and Interventional Radiology*, 24:94–98, 2001.

[SK07] T.H. Schiebler and H.W. Korf. *Anatomie: Histologie, Entwicklungsgeschichte, makroskopische und mikroskopische Anatomie, Topographie*. Springer, 2007.

[SL00] S. Silbernagl and F. Lang. *Color Atlas of Pathophysiology*. Thieme, Stuttgart, New York, 2000.

[SL09] D.S. Sankar and U. Lee. Mathematical modeling of pulsatile flow of non-newtonian fluid in stenosed arteries. *Commun Nonlinear Sci Numer Simulat*, 14(7):2971–2981, 2009.

[Sny72] R.W. Snyder. Large deformation of isotropic biological tissue. *J. Biomech*, 5:601–606, 1972.

[Sok07] D.P. Sokolis. Passive mechanical properties and structure of the aorta: segmental analysis. *Acta Physiol*, 190(6):277–289, 2007.

[SSMF05] C.M. Scotti, A.D. Shkolnik, S.C. Muluk, and E.A. Finol. Fluid-structure interaction in abdominal aortic aneurysms: Effects of asymmetry and wall thickness. *Biomed Eng Online*, 4(1):64, 2005.

[SvdLK$^+$06] S. Spring, B. van der Loo, E. Krieger, B. Amann-Vesti, V. Rousson, and R. Koppensteiner. Decreased wall shear stress in the common carotid artery of patients with peripheral arterial disease or abdominal aortic aneurysm. *J. Vasc Surg*, 43(1):56–63, 2006.

[TBM$^+$09] F. Tan, A. Borghi, R. Mohiaddin, N. Wood, S. Thom, and X. Xu. Analysis of flow patterns in a patient-specific thoracic aortic aneurysm model. *Computers and Structures*, 87(11-12):680–690, 2009.

[TCE$^+$02] C. Taylor, C. Cheng, L. Espinosa, B. Tang, D. Parker, and R. Herfkens. In vivo quantification of blood flow and wall shear stress in the human abdominal aorta during lower limb exercise. *A. Biomed Eng*, 30:402–408, 2002.

[TL90] H. Tennekes and J.L. Lumley. *A First Course in Turbulence.* Butterworth, 13. ed. edition, 1990.

[VFM+04] A.K. Venkatasubramaniam, M.J. Fagan, T. Mehta, K.J. Mylankal, B. Ray, G. Kuhan, I.C. Chetter, and P.T. McCollum. A comparative study of aortic wall stress using finite element analysis for ruptured and non-ruptured abdominal aortic aneurysms. *Eur J. Vasc Endovasc Surg*, 28(2):168–176, 2004.

[VG05] D.A. Vorp and J.P. Geest. Biomechanical determinants of abdominal aortic aneurysm rupture. *Arterioscler Thromb Vasc Biol*, 25(8):1558–1566, 2005.

[VGSV04] J.P. Vande Geest, M.S. Sacks, and D.A. Vorp. Age dependency of the biaxial biomechanical behavior of human abdominal aorta. *J. Biomech Eng*, 126(6):814–822, 2004.

[VRW98] D.A. Vorp, M.L. Raghavan, and M.W. Webster. Mechanical wall stress in abdominal aortic aneurysm: influence of diameter and asymmetry. *J. Vasc Surg*, 27(4):632–639, 1998.

[VSE+03] D.A. Vorp, B.J. Schiro, M.P. Ehrlich, T.S. Juvonen, M.A. Ergin, and B.P. Griffith. Effect of aneurysm on the tensile strength and biomechanical behavior of the ascending thoracic aorta. *A. Thorac Surg*, 75(4):1210–1214, 2003.

[WA09] J.F. Wendt and J.D. Anderson. *Computational Fluid Dynamics.* Springer Berlin Heidelberg, 2009.

[Wal99] W.A. Wall. *Fluid-Struktur-Interaktion mit stabilisierten Finiten Elementen.* Universität Stuttgart, Dissertation, 1999.

[WF99] R.A. White and T.J. Fogarty. *Peripheral endovascular interventions.* Springer, 1999.

[WMR99] W.A. Wall, D.P. Mok, and E. Ramm. Partitioned analysis approach for the transient, coupled response of viscous fluids and flexible structures. *Proc. ECCM 99, European Conference on Computational Mechanics: Solids, Structures and Coupled Problems*, 1999.

[WMWV02] D.H. Wang, M.S. Makaroun, M.W. Webster, and D.A. Vorp. Effect of intraluminal thrombus on wall stress in patient-specific models of abdominal aortic aneurysm. *J. Vasc Surg*, 36(3):598–604, 2002.

[WRS+05] B.J. Wolters, M.C. Rutten, G.W. Schurink, U. Kose, J. de Hart, and F.N. van de Vosse. A patient-specific computational model of fluid-structure interaction in abdominal aortic aneurysms. *Med Eng Phys*, 27:871–883, 2005.

[YB04] B.A. Younis and S.A. Berger. A turbulence model for pulsatile arterial flows. *J. Biomech Eng*, 126(5):578–584, 2004.

[Zie89] O.C. Zienkiewicz. *The finite element method.* 4th ed. McGraw-Hill London, 1989.

[ZT06] O.C. Zienkiewicz and R.L. Taylor. *The finite element method for solid and structural mechanics.* 6th ed. Elsevier Butterworth-Heinemann, 2006.

[ZZJ$^+$03] H. Zhang, X. Zhang, S. Ji, Y. Guo, G. Ledezma, N. Elabbasi, and H. deCougny. Recent development of fluid structure interaction capabilities in the adina system. *Computers and Structures*, 81:1071–1085, 2003.

List of Figures

2.1 Heart and blood circulation. 10
2.2 Cardiac cycle: Systole with isovolumetric contraction (I) and ejection (IIa and IIb) phases; Diastole with isovolumetric relaxation (III) and filling (IVa and IVb) phases [SL00]. 12
2.3 Vessel wall layers: Intima, media and adventitia [HO03]. 14
2.4 Anatomy of the thoracic (top) and the abdominal (bottom) aorta [HRL66]. 15
2.5 Atherosclerotic change of the vessel wall [SL00]. 16
2.6 Vascular pathologies: Consequences of atherosclerosis [SL00]. . . 17
2.7 Aneurysms classification after their position [BE08]. 18
2.8 Endovascular intevention: Stent-graft implantation [Medb]. . . . 22
2.9 Endovascular therapy for AAA [Sie06]. 23
2.10 Endovascular devices: Stent and stent-graft. 23
2.11 Reactions on grafts with PET and ePTFE materials [DB00]. . . 25

3.1 Simulation workflow. 29
3.2 Patient-specific segmentation step. 30
3.3 3D model generation and preprocessing steps. 31
3.4 MoDiSim: Components in the main interface. 38
3.5 MoDiSim: Components overview. 40
3.6 CT-AA: Patient CT-based Abdominal Aorta. 43
3.7 CT-AAA: Patient CT-based Abdominal Aortic Aneurysm. . . . 44
3.8 CT-TAA: Patient CT-based Thoracic Aortic Aneurysm. 44
3.9 MR-AAA: Patient MR-based Abdominal Aortic Aneurysm. . . . 45
3.10 4D-CT-P1: Porcine1 4D-CT-based Abdominal Aorta. 45
3.11 4D-CT-P2: Porcine2 4D-CT-based Abdominal Aorta. 45
3.12 4D-CT-P3: Porcine3 4D-CT-based Abdominal Aorta. 45

4.1 Applied boundary layers (BL). 50
4.2 Boundary layers uniform algorithm [Gam06]. 52
4.3 Curvature size function definition. 53
4.4 Curvature size function effects on the wall and thrombus. 53

4.5 Meshed size function effects within the blood. 54
4.6 The finest AAA wall surface mesh model based on the curvature size function, and the inlet of the AAA with the finite boundary layers and volume mesh elements. 56
4.7 Idealized mesh models with four BL of various first layer size. . 57
4.8 MR-AAA: Boundary surface and interface mesh models. 63
4.9 4D-CT-P1: Wall surface mesh model (4D-CT-P1-SMesh). 64
4.10 4D-CT-P2: Interface mesh model (4D-CT-P2-IMesh). 64
4.11 4D-CT-P3: Interface mesh model (4D-CT-P3-IMesh). 64
4.12 Blood mesh cross-section showing the resulting FSI elements. . . 65
4.13 CT-AA: Boundary surface and blood volume mesh models. . . . 66
4.14 CT-AAA: Boundary surface and blood volume mesh models. . . 66
4.15 CT-TAA: Boundary surface and blood volume mesh models. . . 66
4.16 Outer wall generation from the inner boundary surface. 67
4.17 MR-AAA: Blood and wall volume mesh models. 68
4.18 4D-CT-P2: Blood, wall and combined volume mesh models. . . 68
4.19 4D-CT-P3: Blood, wall and combined volume mesh models. . . 68
4.20 User-Interface of the mesh generation component *Mesh-Gen*. . . 71
4.21 User-Interface of the mesh processing component *Mesh-Pro*. . . 72
4.22 Activity diagram of the mesh generation component *Mesh-Gen*. 74
4.23 Activity diagram of the mesh processing component *Mesh-Pro*. . 75

5.1 Lagrangian and Eulerian configurations. 79
5.2 Full and modified Newton-Raphson iterations [Kle89]. 108
5.3 Stress distribution. 109
5.4 Strain analysis. 109
5.5 Constitutive evaluation of material parameters. 109
5.6 Evaluation of the thoracic porcine model from testdata. 112
5.7 Stress-Strain curves for both porcine material models. 112
5.8 CFD simulations: Wall pressure distribution at various times. . 114
5.9 Load boundary conditions: Static and dynamic pressure profiles. 114
5.10 User-Interface of the CSM simulation component *CSM-Sim*. . . 117
5.11 Activity diagram of the CSM simulation component *CSM-Sim*. . 119
5.12 CSM simulations with four individual vessel wall aortic models. 121
5.13 Static (left) and dynamic (right) von Mises wall stress computations at peak systole for the elastic model. 123
5.14 Static (left) and dynamic (right) von Mises wall stress computations at peak systole for the hyperelastic model. 123
5.15 Elastic (left) and hyperelastic (right) von Mises stresses at t= 0.17 s (top), t= 0.30 s (middle) and t= 0.52 s (bottom). 124
5.16 Maximum stress profile over time and peak cross-sectional deformation in the aneurysm for all thicknesses. 125

5.17 Stresses at five different elements at peak pressure time with elements overview. 126
5.18 Static (left) and dynamic (right) von Mises stresses for the 1.0, 1.2, 1.5, 1.8 and 2.0 mm wall thicknesses shown from the top to the bottom, respectively. 127
5.19 Wall stress distribution *without stent-graft* at t= 0.287 s. 128
5.20 Stress distribution in the aorta of the simulation *with stent* at t= 0.287 s (scale: 0 Nmm^{-2} in blue, 0.1 Nmm^{-2} in red). 129
5.21 Stress distribution in the stent of the simulation *with stent* at t= 0.287 s (scale: 0 Nmm^{-2} in blue, 7 Nmm^{-2} in red). 129
5.22 Histological cross-section from [DB00] compared to the generated aorta (red), stent (grey) and graft (blue). 130
5.23 Stress distribution in the aorta of the simulation *with stent-graft* at t= 0.287 s (scale: 0 Nmm^{-2} in blue, 0.1 Nmm^{-2} in red). . . . 130
5.24 Stress distribution in the graft (a) and stent (b) of the simulation *with stent-graft* at t= 0.287 s (scale (a): 0 Nmm^{-2} in blue, 2 Nmm^{-2} in red; scale (b): 0 Nmm^{-2} in blue, 7 Nmm^{-2} in red). 131
5.25 Stress distribution in the aorta of the simulation *with stent-graft-equivalent* from measurements at t= 0.287 s (scale: 0 Nmm^{-2} in blue, 2 Nmm^{-2} in red). 132
5.26 Stress distribution in the aorta of the simulation *with stent-graft-equivalent* from manufacturer's data at t= 0.287 s (scale: 0 Nmm^{-2} in blue, 2 Nmm^{-2} in red). 132
5.27 Stress distribution and cross-sectional strain analysis. 133

6.1 Finite and infinitesimal control volumes within fixed and moving configurations [WA09]. 137
6.2 Surface forces acting on a fluid element [WA09]. 142
6.3 LES and DNS turbulence motions and their velocity components [FP08]. 150
6.4 RANS: Steady and unsteady averaging processes [FP08]. 152
6.5 FVM: Control volumes [WA09]. 155
6.6 Illustration of the QUICK scheme: 1D control volume [FI06]. . . 158
6.7 Velocity pathlines, vectors and vortices in the thoracic aorta. . . 166
6.8 Pressure and wall shear stress (WSS) distributions. 166
6.9 Newtonian and non-Newtonian blood viscosity models. 169
6.10 Flow-based and pressure-based boundary conditions. 170
6.11 Mapping the flow rates at the existing outlets. 172
6.12 User-Interface of the CFD simulation component *CFD-Sim*. . . 175
6.13 Activity diagram of the CFD simulation component *CFD-Sim*. . 177
6.14 CFD simulations with three individual blood flow aortic models. 179
6.15 Velocity vectors and corresponding shear stress distributions. . . 180

6.16 Shear stress distribution on the wall (left) and in the flow z-direction (right) at five different times. 182
6.17 Dynamic and static pressures along a vertical plane at t= 0.34 s. 183
6.18 Velocity pathlines and corresponding shear stress distributions. . 184
6.19 Overview: Evaluation sites for the non-Newtonian behavior. . . 185
6.20 Velocity magnitudes along the centerlines L3 and L5.
186
6.21 Velocity magnitudes along the lines X150 and Xmes. 186
6.22 Pathlines at early, peak, late systole and peak diastole. 187
6.23 WSS at early, peak, late systole and peak diastole. 187
6.24 Static pressure at early, peak, late systole and peak diastole. . . 187
6.25 Pathlines, pressure and WSS distribution of the steady-state simulation with velocity of 0.37 m/s. 189
6.26 Pathlines, pressure and WSS distribution of the unsteady simulations at early systole. 189
6.27 Pathlines, pressure and WSS distribution of the unsteady simulations at late systole. 189

7.1 Illustration of the ALE configuration and coordinate system. . . 192
7.2 Interfaces and distance measurements between fluid and solid. . 194
7.3 Various coupling approaches for FSI problems. 198
7.4 Coupling blood flow and vessel wall simulations. 205
7.5 Computation of the Womersley flow condition for 4D-CT-P2. . . 208
7.6 Computation of the outlet-specific pressures for 4D-CT-P3. . . . 209
7.7 User-Interface of the FSI simulation component *FSI-Sim*. 214
7.8 Activity diagram of the FSI simulation component *FSI-Sim*. . . 216
7.9 FSI simulations with three individual aortic models. 219
7.10 Velocity magnitudes along a vertical plane from CFD and FSI. . 221
7.11 3D displacements of the vessel wall from CSM and FSI. 221
7.12 3D stress distributions along the vessel wall from CSM and FSI. 221
7.13 Peak stress and strain distributions across the wall. 222
7.14 3D wall pressure contours. 223
7.15 Turbulence and recirculation zones around the celiac artery. . . 223
7.16 Effective 3D stress distribution along the wall. 224
7.17 3D pathlines injected from the inlet. 225
7.18 Velocity vectors at the aortic bifurcation. 225

8.1 Experimental setup in the angiography room. 228
8.2 Experimental validation: Workflow. 229
8.3 Dynamic CT images. 230
8.4 Bolus track [Kos09]. 230
8.5 Digitization process of the pressure measurements [Kos09]. . . . 231
8.6 Digitization process of the flow measurements [Kos09]. 232

8.7 Cross-sections used to evaluate the wall deformation in model 4D-CT-P1 based on CSM simulations. 234
8.8 Cross-sections used to evaluate the wall deformation (SR, IR, MS, AB) and the pressure and flow computations (TC, AB) for models 4D-CT-P2 and 4D-CT-P3 based on FSI simulations. . . 235
8.9 Quantification of the wall deformation in each cross-section. . . 236
8.10 Wall deformation in 4D-CT-P1 at Z3= 100.0 mm and t= 0.41 s for both the dynamic CT and the CSM simulations. 237
8.11 Pressure simulations (FSI) in TC and AB for 4D-CT-P2. 238
8.12 Pressure simulations (FSI) in TC and AB for 4D-CT-P3. 238
8.13 Velocity simulations (FSI) in TC and AB for 4D-CT-P2. 238
8.14 Velocity simulations (FSI) in TC and AB for 4D-CT-P3. 238
8.15 In-vivo measured pressure profile used for the boundary conditions of the CSM simulations for the 4D-CT-P1 model. 239
8.16 Wall deformation at the cross-sections Z1, Z2, Z3, Z4 and Z5 for model 4D-CT-P1 based on CSM. 240
8.17 Wall deformation at the cross-sections SR, IR, MS and AB for model 4D-CT-P2 based on FSI. 241
8.18 Pressure profiles at cross-sections TC and AB for 4D-CT-P2. . . 242
8.19 Velocity profiles at cross-sections TC and AB for 4D-CT-P2. . . 242
8.20 Wall deformation at the cross-sections SR, IR, MS and AB for model 4D-CT-P3 based on FSI. 243
8.21 Pressure profiles at cross-sections TC and AB for 4D-CT-P3. . . 244
8.22 Velocity profiles at cross-sections TC and AB for 4D-CT-P3. . . 244

List of Tables

3.1 Summary of all processed models. 43

4.1 Results of the velocity (V) and WSS computations and the corresponding relative errors (%) obtained at transitions between the different mesh configurations within the idealized models. . . 58
4.2 Results of the velocity (V), WSS computations and the corresponding relative errors obtained at transitions between the different configurations, at systole (S) and diastole (D). 59
4.3 Parameters for the curvature and the meshed size functions obtained from all boundary layers mesh configurations described above within the patient-specific CT-AAA model. 59
4.4 Summary of all generated mesh models. 62
4.5 Summary of the generated surface mesh models. 63
4.6 Summary of the generated mesh models for the blood domain. . 65
4.7 Summary of the generated mesh models for the wall domain. . . 67
4.8 Conversion library: Various surface (S) and volume (V) meshes. 69
4.9 Overview: FE-sets generation. 70

5.1 Maximum, minimum and mean von Mises values at peak systole for the various simulations. 122
5.2 Maximum, mean and minimum stresses over the cardiac cycle. . 126

Curriculum Vitae

Dilana Hazer
born on 1982 in Beirut

Oct 05 – today	Research assistant, Universität Karlsruhe, Germany Institute of Anthropomatics, Chair Prof. Dillmann
	Research assistant, Univ. Hospital Heidelberg, Germany Department of Diagnostic Radiology
	Member of Graduiertenkolleg 1126: ”Intelligent Surgery”
	Research Internship (6 months), CMU, Pittsburgh, PA, USA
	PhD Thesis: ”Automated Patient-Specific Modeling of Blood Flow and Vessel Wall Mechanics in Aortic Pathology”
Oct 00 – Sept 05	Study of Engineering Physics, Universität Oldenburg, Germany Degree Master of Science (1.4)
	Master Thesis at Siemens Medical Solutions, Heidelberg, Germany Subject: ”Leaf sequencing algorithm for a multileaf collimator”
	Bachelor Thesis at CNRS, Lyon, France Subject: ”Modélisation de la cochlée”
	Erasmus (1 year), Université UCBL Lyon1, France Degree Bachelor of Engineering (1.4)
Oct 99 – Aug 99	Université Libanaise, Faculté de Génie, Beirut, Lebanon
Oct 84 – June 99	Collège St-Elie Btina, Beirut Degree Baccalauréat, série Mathématiques (good)
	Ecole St-Elie Moussaitbeh, Beirut Degree Brevet (good)
Languages	Arabic, French, English, German, Spanish